applied sciences

Special Issue Reprint

Advanced Welding Technology and Its Applications

Edited by
Radosław Winiczenko

mdpi.com/journal/applsci

MDPI

Advanced Welding Technology and Its Applications

Advanced Welding Technology and Its Applications

Guest Editor

Radosław Winiczenko

MDPI

Basel • Beijing • Wuhan • Barcelona • Belgrade • Novi Sad • Cluj • Manchester

Guest Editor
Radosław Winiczenko
Institute of Mechanical
Engineering
Warsaw University of Life
Sciences
Warsaw
Poland

Editorial Office
MDPI AG
Grosspeteranlage 5
4052 Basel, Switzerland

This is a reprint of the Special Issue, published open access by the journal *Applied Sciences* (ISSN 2076-3417), freely accessible at: https://www.mdpi.com/journal/applsci/special_issues/67V179AJ4J.

For citation purposes, cite each article independently as indicated on the article page online and as indicated below:

Lastname, A.A.; Lastname, B.B. Article Title. *Journal Name* **Year**, *Volume Number*, Page Range.

ISBN 978-3-7258-8639-5 (Hbk)
ISBN 978-3-7258-8640-1 (PDF)
https://doi.org/10.3390/books978-3-7258-8640-1

© 2026 by the authors. Articles in this reprint are Open Access and distributed under the Creative Commons Attribution (CC BY) license. The reprint as a whole is distributed by MDPI under the terms and conditions of the Creative Commons Attribution-NonCommercial-NoDerivs (CC BY-NC-ND) license (https://creativecommons.org/licenses/by-nc-nd/4.0/).

Contents

About the Editor . . . . . **vii**

Radosław Winiczenko
Advanced Welding Technology and Its Applications
Reprinted from: *Appl. Sci.* **2026**, *16*, 6391, https://doi.org/10.3390/app16136391 . . . . . **1**

Eli J. da Cruz, Junior, Francisco M. F. A. Varasquim, Fábio O. Carvalho, Luiz F. F. Santiago, Bruno F. Gianelli, et al.
Hot-Wire Gas Tungsten Arc Welding Cladding of Super Austenitic Stainless Steel on Low Carbon Steel
Reprinted from: *Appl. Sci.* **2026**, *26*, 1527, https://doi.org/10.3390/app16031527 . . . . . **6**

Rodolphe Bolot, Alexandre Mathieu, Hichem Aberbache, Mohamed-Achref Karoui and Frédéric Bernard
Wire Arc Additive Manufacturing of Complex-Shaped Capsules for HIP Sintering of Powder
Reprinted from: *Appl. Sci.* **2026**, *16*, 179, https://doi.org/10.3390/app16010179 . . . . . **20**

Martyna Zemlik, Beata Białobrzeska, Mateusz Stachowicz and Łukasz Konat
The Effect of Heat Treatment on the Abrasive Wear Resistance of Boron-Alloyed Armor Steel Welded Joints
Reprinted from: *Appl. Sci.* **2025**, *15*, 12860, https://doi.org/10.3390/app152412860 . . . . . **39**

Karthik Ravi Krishna Murthy, Reza Sanei, Abhay Sharma, Simon Olschok and Uwe Reisgen
Impact of Beam Shape and Frequency on Weld Seam Geometry and Penetration Depth Using a Coherent Beam Combining Laser
Reprinted from: *Appl. Sci.* **2025**, *15*, 9432, https://doi.org/10.3390/app15179432 . . . . . **60**

Ivica Garašić, Mislav Štefok, Maja Jurica, Davor Skejić and Mato Perić
Mechanical Properties Analysis of WAAM Produced Wall Made from 6063 Alloy Using AC MIG Process
Reprinted from: *Appl. Sci.* **2025**, *15*, 6740, https://doi.org/10.3390/app15126740 . . . . . **78**

Radosław Winiczenko, Andrzej Skibicki and Paweł Skoczylas
Multi-Objective Optimisation of Welding Parameters for AZ91D/AA6082 Rotary Friction Welded Joints
Reprinted from: *Appl. Sci.* **2025**, *15*, 1477, https://doi.org/10.3390/app15031477 . . . . . **93**

Mingoo Cho, Jinsu Gim, Ji Hoon Kim and Sungwook Kang
Development of an Artificial Neural Network Model to Predict the Tensile Strength of Friction Stir Welding of Dissimilar Materials Using Cryogenic Processes
Reprinted from: *Appl. Sci.* **2024**, *14*, 9309, https://doi.org/10.3390/app14209309 . . . . . **110**

Wiesław Czapiewski, Stanisław Pałubicki, Jarosław Plichta and Krzysztof Nadolny
State of Knowledge in the Field of Regenerative Hardfacing Methods in the Context of the Circular Economy
Reprinted from: *Appl. Sci.* **2026**, *16*, 792, https://doi.org/10.3390/app16020792 . . . . . **126**

Wenji Liu, Qing Li, Jianfeng Yue, Peng Zhu and Bing Li
Research Status and Progress of All-Position Narrow-Gap GMAW for Pipelines
Reprinted from: *Appl. Sci.* **2025**, *15*, 2270, https://doi.org/10.3390/app15052270 . . . . . **156**

About the Editor

Radosław Winiczenko

Radosław Winiczenko is a professor in the Institute of Mechanical Engineering at the Warsaw University of Life Sciences. He was born in 1971 in Płock, where he completed a five-year technical secondary school specialising in mechanics. In 1997, he graduated from the Faculty of Mechanical Engineering at the Bydgoszcz University of Science and Technology. After his studies, he worked as a process engineer at the Harvesting Machinery Factory in Płock. In 2001, he completed his doctoral studies at the Foundry Division at the Warsaw University of Technology. From 2002, he worked as an assistant and subsequently as an assistant professor at the Faculty of Production Engineering at the Warsaw University of Life Sciences. In 2019, he obtained the habilitation in engineering and technical sciences from the University of Warmia and Mazury in Olsztyn. He is the author or co-author of dozens of scientific publications, comprising original research papers published in JCR-indexed journals. Dr Winiczenko is also a co-author of academic books. His research findings have been presented at numerous international conferences. His research focused primarily on the structure and mechanical properties of friction-welded dissimilar metals, utilising both light and electron microscopy. He developed durable friction-welded joints between various materials, such as ductile cast iron–austenitic stainless steel; tungsten heavy alloy–aluminium alloy; and magnesium alloys–aluminium alloys. In 2025, he completed a research internship at the Faculty of DET of the Polytechnic University of Turin.

applied sciences

MDPI

Editorial

Advanced Welding Technology and Its Applications

Radosław Winiczenko

Institute of Mechanical Engineering, Warsaw University of Life Sciences, Nowoursynowska 164, 02-787 Warsaw, Poland; radoslaw_winiczenko@sggw.edu.pl

1. Introduction

Welding technology is crucial to modern manufacturing, construction, and structural engineering. As industrial demands evolve toward higher performance, greater efficiency, and improved sustainability, the field continues to push the boundaries—embracing artificial intelligence, additive manufacturing, novel energy sources, and surface engineering strategies. Advanced welding technologies (AWTs) are driving fabrication efficiencies by reducing heat input, minimising distortion, and enabling the joining of dissimilar materials. Key advancements include friction stir welding (FSW) for aerospace light alloys, Hybrid Laser-Arc welding and AI-integrated robotic welding for real-time consistency.

Solid-state friction stir welding (SSFSW) is a solid-state joining method that is increasingly reviewed in AWT for its ability to join materials without melting them. This prevents defects commonly found in fusion welding and is ideal for aerospace and automotive parts. A comprehensive review of friction stir welding of metal matrix composites for automotive applications is presented in paper [1]. The review combines findings on mechanical properties and high-strain-rate behaviour to establish process–property–performance relationships relevant to crashworthy, lightweight vehicle applications. Solid-state friction stir techniques encompass both the joining operations of friction stir welding (FSW) and the layer-by-layer fabrication of Friction Stir Additive Manufacturing (FSAM). FSAM, derived from FSW, achieves layer-by-layer material deposition through solid-state bonding of the rotating tool. As an emerging solid-state additive manufacturing (AM) process, FSAM holds significant potential for large-scale AM of metals and composites [2].

Hybrid Laser-Arc welding bridges the gap between the deep penetration of lasers and the low cost of arc welding, enabling high-speed fusion of stainless and mild steel. Laser-arc hybrid welding (LAHW) offers the advantages of large penetration, high efficiency, and minimal deformation compared to laser welding. The study [3] demonstrates that synchronous wire-powder feeding combined with beam oscillation is a promising approach for achieving high-performance welded joints in high-strength aluminium alloys. The LAHW process is 50–100% faster than the autogenous laser welding. According to the review paper [4], a small joint gap is beneficial for hybrid welding, and the maximum welding speed is achieved for a gap of 0.6–1 mm. The 25 mm thick steel plates are successfully welded in a single pass using a LAHW at 1 m/min. The major applications of LAHW are found in the automobile and shipbuilding industries. Laser-arc hybrid welding has also found its application in the aerospace industry and other manufacturing industries. Recent studies have increasingly emphasised the role of advanced process control and hybrid welding techniques in improving the weldability of titanium alloys [5]. Compared with traditional arc welding methods, Laser–MIG hybrid welding provides better control of heat input, droplet transfer dynamics, and melt pool stability. Advanced welding techniques, such as Laser–MIG hybrid welding, play a significant role in improving compatibility.

Their lower, more controlled heat input reduces the thickness of the intermetallic layer and residual stresses [6]. In recent years, the oscillating laser-arc hybrid welding (OLAHW) has attracted increasing attention due to its remarkable porosity-suppression capability. The study [7] provides a comprehensive understanding of the dynamic mechanisms of pore formation during OLAHW of aluminium alloy.

The rapid development of AWTs means that modern solutions for welding equipment are now appearing on the market, enabling the robotisation and automation of the welding process. Artificial intelligence and machine learning are systems that analyse data in real time to make micro-adjustments during the welding process. Using AI reduces the risk of human error and ensures highly repeatable welds in automated environments. Robots like COBOTs are gaining popularity in the welding industry, ensuring safe and effective collaboration with humans. An overview of collaborative robot applications in welding and additive manufacturing (AM) is described in the paper [8]. In the manufacturing sector, the use of COBOTs is significantly impacting welding and additive manufacturing. In welding, COBOTs can work alongside welders to perform repetitive or physically demanding tasks, while allowing skilled workers to focus on more complex aspects such as welding parameter selection, inspection, and quality control [9]. Furthermore, these robots have been found to improve welding precision, particularly in multi-pass welding on non-horizontal and curved surfaces, and to maintain process consistency, reducing distortion and defects and increasing productivity.

This Special Issue, titled "Advanced Welding Technology and Its Applications", presents nine original contributions, divided into five thematic sections: solid-state friction welding process, wire arc additive manufacturing, gas metal arc welding, hot-wire gas tungsten arc welding, and laser welding. The final thematic group brings together contributions addressing the surface performance of welded and overlaid components, with a shared emphasis on durability and sustainability. These papers collectively reflect the current state of the art across the most dynamic borders of welding science and engineering.

2. An Overview of Published Articles

2.1. Solid-State Friction Welding Process Optimisation

Cho et al. (Contribution 1) developed an artificial neural network (ANN) model to predict the tensile strength of friction stir welding (FSW) joints between dissimilar aluminium–copper combinations processed under cryogenic conditions. They incorporated heat transfer analysis outputs—specifically the maximum temperature and temperature gradient—as ANN inputs. Using the Hyperband tuner for model optimisation, the authors achieved tensile strength predictions with an average error of only 5.4%. This work underscores the potential of data-driven approaches to replace or substantially reduce the cost of experimental campaigns in FSW process development. Winiczenko et al. (Contribution 2) addressed the multi-objective optimisation of rotary friction welding (RFW) parameters for dissimilar AZ91D magnesium–AA6082 aluminium alloy joints, a material combination important for lightweight structural applications. They used a hybrid strategy combining ANNs with genetic algorithms. The authors simultaneously maximised tensile strength and minimised material loss (shortening) during welding, achieving a joint strength improvement from 24 to 81 MPa and a reduction in shortening from 8.25 to 0.23 mm. Together, these two studies highlight the power of AI-assisted methodologies in advancing friction welding of multi-material systems.

2.2. Wire Arc Additive Manufacturing

The second thematic group focuses on wire arc additive manufacturing (WAAM), an increasingly prominent technology for the near-net-shape fabrication of medium- and

https://doi.org/10.3390/app16136391

large-scale metal components. Garašić et al. (Contribution 3) investigated the influence of current type and AC polarity balance on the mechanical and microstructural properties of 6063 aluminium alloy walls produced by WAAM using an AC MIG process. Employing a TiB_2-refined Al–Mg–Si filler wire, the study demonstrated that polarity balance critically governs wall geometry, porosity, grain structure, and residual stress distribution, with the highest tensile strength of 172 MPa recorded in DC-MIG samples near the substrate—a region benefiting from accelerated cooling. These insights are fundamental for tailoring process parameters to achieve consistent part quality in aluminium WAAM.

Extending the application scope of WAAM to a more specialised domain, Bolot et al. (Contribution 4) examined the fabrication of complex-shaped sealed capsules from AISI 316L stainless steel for use in hot isostatic pressing (HIP) sintering of powder. The study demonstrated the feasibility of a hybrid WAAM–HIP manufacturing route by addressing robot trajectory generation from CAD models, characterising WAAM mechanical properties (UTS between 540 and 600 MPa), and confirming that HIP processing restores a fully austenitic structure. The proposed technology is identified as a promising candidate for medium-scale component manufacturing in the nuclear sector, illustrating how WAAM can serve as an enabling platform for advanced hybrid processes.

2.3. Gas Metal Arc Welding and Hot-Wire Gas Tungsten Arc Welding

The third thematic group addresses arc welding in two key industrial areas: all-position pipeline welding and protective cladding of structural steels. Liu et al. (Contribution 5) reviewed the status and technological advances in all-position narrow-gap gas metal arc welding (GMAW) for pipelines. This process is challenging due to frequent sidewall and interlayer lack-of-fusion defects, especially in non-flat positions. The review synthesises recent findings on droplet transfer, arc morphology, and molten pool behaviour in different welding positions. It also outlines optimisation strategies, including parameter adjustment, control of the external magnetic field, and laser-arc hybrid welding. The paper offers practical guidance for pipeline construction engineers and a structured research agenda for the welding community.

Regarding surface protection, da Cruz Jr. et al. (Contribution 6) explored the use of hot-wire gas tungsten arc welding (HW-GTAW) to clad low-carbon steel substrates with super-austenitic stainless steel. By comparing cold-wire (CW-GTAW) and hot-wire conditions, the authors demonstrated that the hot-wire configuration reduced dilution—a key advantage for preserving clad-layer integrity—while achieving competitive corrosion and wear resistance. This contribution underscores the relevance of HW-GTAW as an efficient and versatile cladding process for surface engineering applications.

2.4. Laser Welding

The fourth thematic area is devoted to laser welding, with a particular focus on the opportunities offered by dynamic beam control. Krishna Murthy et al. (Contribution 7) explored the influence of beam shape and modulation frequency on weld seam geometry, penetration depth, and capillary behaviour using a coherent beam combining (CBC) laser system. Three intensity distributions—single point, line–point–line, and boomerang—were applied at modulation frequencies of 1, 10, and 100 kHz during welding of duplex and austenitic stainless steels. High-speed imaging revealed significant effects of both beam shape and frequency on capillary stability and penetration characteristics. These findings position CBC laser technology as a versatile and highly controllable platform for precision welding, with important implications for the welding of advanced high-performance steels.

https://doi.org/10.3390/app16136391

2.5. The Surface Performance of Welded Components

The fifth and final thematic group brings together contributions addressing the surface performance of welded and overlaid components, with a shared emphasis on durability and sustainability. Zemlik et al. (Contribution 8) investigated the restoration of abrasive wear resistance in welded joints of boron-alloyed martensitic armour steel (500 HBW nominal hardness) through post-weld heat treatment (PWHT). Combining metallographic analysis with tribological testing on a T-07 tribotester, the study demonstrated that PWHT increased wear resistance by 55% compared to the as-welded condition—results of direct relevance not only to defence applications but also to the mining, construction, and transportation sectors where such steels operate under intense abrasive loading.

By broadening the scope, Czapiewski et al. (Contribution 9) conducted a systematic review of regenerative hardfacing methods applied to steel substrates. The review maps process–structure–property (PSP) relationships across arc-based hardfacing techniques and identifies measurable indicators—energy input, dilution, bead geometry, heat-affected zone characteristics—as the principal levers governing weld structure and functional properties, including hardness, wear resistance, and fatigue life. A dedicated PSP table is proposed as a practical framework for process optimisation, and research gaps are identified regarding standardisation of energy metrics and the definition of technology windows within welding procedure specifications (WPS/WPQR). By framing regenerative hardfacing explicitly within the circular economy paradigm, this review highlights welding's underappreciated role as a sustainability-enabling technology.

3. Future Perspectives

Advanced technologies will continue to improve welding quality through better process control, eliminating defects, and improving the final product. It is worth noting that these technologies also improve occupational safety by automating processes, thereby minimising employee exposure to hazardous substances. Technological transformation can bring numerous benefits to both welders and end consumers. Key changes may include optimising material consumption, improving quality control, and reducing occupational health and safety costs. AI will play an important role in these changes. Investing in modern welding technologies increases the efficiency and productivity of production processes. Also, AM technologies will play a key role. Currently, they are gaining popularity in many industries. AM welding technology primarily encompasses processes such as laser metal deposition and electric arc additive manufacturing. Their advantage is the ability to create complex parts directly from digital data, layer by layer. This enables the production of components with custom shapes and functionalities.

The nine contributions assembled in this Special Issue collectively reflect the breadth and vitality of current research in advanced welding technology. Across solid-state and fusion welding, additive manufacturing, laser processing, and surface engineering, common threads emerge: the pursuit of superior mechanical performance, the integration of intelligent computational tools, and an increasing awareness of sustainability imperatives.

The Guest Editor trusts that this welding collection will serve as a valuable reference for researchers and engineers working in welding science and will stimulate further inquiry into the many open questions that remain in this technologically rich and industrially critical field.

The Guest Editors gratefully acknowledge the contributions of all authors, reviewers, and the editorial team of *Applied Sciences* MDPI for their efforts in bringing this Special Issue to completion.

Conflicts of Interest: The author declares no conflicts of interest.

https://doi.org/10.3390/app16136391

List of Contributions:

1. Cho, M.; Gim, J.; Kim, J.H.; Kang, S. Development of an Artificial Neural Network Model to Predict the Tensile Strength of Friction Stir Welding of Dissimilar Materials Using Cryogenic Processes. *Appl. Sci.* **2024**, *14*, 9309. https://doi.org/10.3390/app14209309.
2. Winiczenko, R.; Skibicki, A.; Skoczylas, P. Multi-Objective Optimisation of Welding Parameters for AZ91D/AA6082 Rotary Friction Welded Joints. *Appl. Sci.* **2025**, *15*, 1477. https://doi.org/10.3390/app15031477.
3. Garašić, I.; Štefok, M.; Jurica, M.; Skejić, D.; Perić, M. Mechanical Properties Analysis of WAAM Produced Wall Made from 6063 Alloy Using AC MIG Process. *Appl. Sci.* **2025**, *15*, 6740. https://doi.org/10.3390/app15126740.
4. Bolot, R.; Mathieu, A.; Aberbache, H.; Karoui, M.-A.; Bernard, F. Wire Arc Additive Manufacturing of Complex-Shaped Capsules for HIP Sintering of Powder. *Appl. Sci.* **2026**, *16*, 179. https://doi.org/10.3390/app16010179.
5. Liu, W.; Li, Q.; Yue, J.; Zhu, P.; Li, B. Research Status and Progress of All-Position Narrow-Gap GMAW for Pipelines. *Appl. Sci.* **2025**, *15*, 2270. https://doi.org/10.3390/app15052270.
6. da Cruz, E.J., Junior; Varasquim, F.M.F.A.; Carvalho, F.O.; Santiago, L.F.F.; Gianelli, B.F.; Ventrella, V.A.; Pigato, M.; Calliari, I. Hot-Wire Gas Tungsten Arc Welding Cladding of Super Austenitic Stainless Steel on Low Carbon Steel. *Appl. Sci.* **2026**, *16*, 1527. https://doi.org/10.3390/app16031527.
7. Krishna Murthy, K.R.; Sanei, R.; Sharma, A.; Olschok, S.; Reisgen, U. Impact of Beam Shape and Frequency on Weld Seam Geometry and Penetration Depth Using a Coherent Beam Combining Laser. *Appl. Sci.* **2025**, *15*, 9432. https://doi.org/10.3390/app15179432.
8. Zemlik, M.; Białobrzeska, B.; Stachowicz, M.; Konat, Ł. The Effect of Heat Treatment on the Abrasive Wear Resistance of Boron-Alloyed Armor Steel Welded Joints. *Appl. Sci.* **2025**, *15*, 12860. https://doi.org/10.3390/app152412860.
9. Czapiewski, W.; Pałubicki, S.; Plichta, J.; Nadolny, K. State of Knowledge in the Field of Regenerative Hardfacing Methods in the Context of the Circular Economy. *Appl. Sci.* **2026**, *16*, 792. https://doi.org/10.3390/app16020792.

References

1. Shrivastava, P.; Msomi, V.; Mabuwa, S. Friction stir welding of metal matrix composites for automotive applications: A comprehensive review. *Mater. Today Commun.* **2026**, *52*, 114987. [CrossRef]
2. Yao, Y.; Cao, X.; Liu, X.; Zhang, Z.; Xu, W.; Wen, H. A comprehensive review of solid-state friction stir processing robots: Design, dynamics and control for enabling applications in additive manufacturing. *J. Manuf. Process.* **2025**, *149*, 1151–1165. [CrossRef]
3. Meng, Y.; Hou, Z.; Wang, L.; Deng, A.; Hu, D.; Yang, X.; Yang, Z.; Zhu, Z.; Chen, H. Oscillating laser-arc hybrid welding of aluminum alloy via synchronous wire-powder feeding: Microstructure evolution and mechanical properties. *Mater. Des.* **2026**, *265*, 116056. [CrossRef]
4. Acherjee, B. Hybrid laser arc welding: State-of-art review. *Opt. Laser Technol.* **2018**, *99*, 60–71. [CrossRef]
5. Patel, P.; Dutta, A.; Ghosh, A.; Basak, S.; Sahoo, S.K.; Sahoo, N.; Shrivastava, P.; Das, A.; Msomi, V. Advances in welding of titanium and its alloys using CMT, MIG, and laser-MIG hybrid processes: A comprehensive review. *Mater. Today Commun.* **2026**, *53*, 115264. [CrossRef]
6. Xu, J.; Zhao, S.; Jiang, L.; Cen, L.; Shi, L.; Gao, M. Porosity formation and suppression mechanisms in oscillating laser-arc hybrid welding of aluminum alloys. *Int. J. Heat Mass Transf.* **2026**, *261*, 128528. [CrossRef]
7. Xu, X.; Cui, H.; Lan, L.; Shao, C.; Wang, Y.; Lu, F. Improvement of weld formation and mechanical properties in high-speed spiral oscillating laser–arc hybrid welding of medium-thick Al–Mg–Er–Zr alloy. *Mater. Sci. Eng. A* **2026**, *958*, 149999. [CrossRef]
8. Mohammad, A.; Tuhin, M. A review of applications of collaborative robot in welding and additive manufacturing. *Robot. Comput.-Integr. Manuf.* **2026**, *100*, 103256. [CrossRef]
9. Zhang, R.; Lv, Q.; Li, J.; Bao, J.; Liu, T.; Liu, S. A reinforcement learning method for human-robot collaboration in assembly tasks. *Robot. Comput.-Integr. Manuf.* **2022**, *73*, 102227. [CrossRef]

Disclaimer/Publisher's Note: The statements, opinions and data contained in all publications are solely those of the individual author(s) and contributor(s) and not of MDPI and/or the editor(s). MDPI and/or the editor(s) disclaim responsibility for any injury to people or property resulting from any ideas, methods, instructions or products referred to in the content.

applied sciences

MDPI

Article

Hot-Wire Gas Tungsten Arc Welding Cladding of Super Austenitic Stainless Steel on Low Carbon Steel

Eli J. da Cruz, Junior [1,*], Francisco M. F. A. Varasquim [1], Fábio O. Carvalho [1], Luiz F. F. Santiago [1], Bruno F. Gianelli [1], Vicente A. Ventrella [2], Mirko Pigato [3] and Irene Calliari [3]

[1] Department of Industy, São Paulo Federal Institute of Education, Science and Technology, Campus Itapetininga, Av. João Olímpio de Oliveira 1561, Itapetininga 18202-000, SP, Brazil; franciscomateus@ifsp.edu.br (F.M.F.A.V.); fabiocarvalho@ifsp.edu.br (F.O.C.); frezzatti@ifsp.edu.br (L.F.F.S.); prof.gianelli@ifsp.edu.br (B.F.G.)
[2] Department of Mechanical Engineering, Sao Paulo State University, Avenue Brasil 56, Ilha Solteira 15385-000, SP, Brazil; vicente.ventrella@unesp.br
[3] Department of Industrial Engineering, University of Padua, Via Gradenigo, 6/a, 35131 Padova, Italy; mirko.pigato@unipd.it (M.P.); irene.calliari@unipd.it (I.C.)
* Correspondence: dacruz.eli@ifsp.edu.br

Abstract

Arc welding techniques for applying austenitic stainless steel cladding to low-carbon steels are common. Cladding enhances surface properties, increases corrosion resistance, improves product performance, extends service life, and reduces maintenance costs associated with surface corrosion. The hot-wire gas tungsten arc welding (HW-GTAW) method offers several benefits, making it appealing for cladding applications. This research investigates the use of HW-GTAW to clad low-carbon steels with super-austenitic stainless steel, examining macro and microstructures, mechanical strength, corrosion resistance, and wear performance. Two conditions were tested: one without a hot-wire, called CW-GTAW (cold-wire), and one with a hot-wire, called HW-GTAW. The HW-GTAW process reduced the dilution rate, thereby benefiting cladding. Microstructural analysis showed that both conditions exhibited elongated columnar dendrites in the heat-affected zone and a shallow region of equiaxed dendrites near the surface. The HW-CL condition displayed slight improvements in corrosion and wear resistance, but both samples outperformed the uncoated base material. These findings support the expanded application of super austenitic stainless steels and HW-GTAW in cladding processes.

Keywords: super austenitic stainless steel; low-carbon steel; HW-GTAW; corrosion resistance; mechanical properties; dilution; microstructure

1. Introduction

Industries like petrochemical, pulp and paper, and offshore operations operate in highly corrosive environments, requiring materials with excellent corrosion resistance [1]. Among stainless steels, super austenitic grades are notable for their superior corrosion resistance [2]. However, these super austenitic stainless steels usually have high nickel content, which typically increases their cost.

For applications such as pressure vessels operating at high temperatures and pressures, and under corrosive conditions, constructing the entire structure from austenitic stainless steel is impractical [3]. Instead, it is typical to build the structure using low-carbon steel and add a layer of austenitic stainless steel on the surface. This technique, called cladding,

not only improves surface properties but also enhances overall product performance, extends service life, and lowers maintenance costs caused by surface material loss and corrosion [4–6].

Recent studies indicate that arc welding is frequently used for stainless steel cladding because of its cost-effective equipment [7,8]. Di Schino and Testani [9] employed submerged-arc welding (SAW) to clad low-carbon steel with austenitic stainless steel AISI 316. Hou et al. [3] examined stainless steel cladding using twin-electrode gas tungsten arc welding (GTAW). Kumar, Singh, and Uppal [10] applied GTAW to clad AISI 316L stainless steel onto a low-carbon steel base. Jayavelu et al. [11] explored depositing austenitic 316L stainless steel onto carbon steel with constant current gas metal arc welding (GMAW). Peng et al. [12] investigated cladding austenitic 308 stainless steel on low-carbon steel via GMAW with ultrasonic vibration. Da Cruz et al. [13] researched cladding super austenitic stainless steel onto low-carbon steel using a specific process, GTAW.

Among arc welding methods, GTAW (Gas Tungsten Arc Welding) is notable for producing high-quality, defect-free welds [14]. A variant of GTAW involves preheating the filler wire, called hot-wire gas tungsten arc welding (HW-GTAW). This heating is achieved by applying an electrical potential between the wire feed and the workpiece. When the wire contacts the molten weld pool, the circuit closes, and resistance heating rapidly raises the wire's temperature. Although common, this approach can cause arc deflection, which may weaken the weld integrity bead [15].

Another approach to preheat the filler wire in GTAW involves an indirect heating system, which does not electrically connect to the workpiece. In this method, the wire is preheated using a resistive or inductive system linked to the wire feeder, with heating occurring just prior to contact with the molten pool. Since the heating system is not connected to the workpiece, this indirect technique avoids arc deflection [15].

HW-GTAW provides several benefits over traditional GTAW, including lower porosity and fewer welding defects, along with a higher deposition rate that boosts productivity and results in better-quality weld beads. Additionally, a significant advantage, especially important in cladding processes, is HW-GTAW's ability to achieve lower dilution rates [16–18].

Dilution describes the change in the cladding alloy composition caused by mixing with the molten matrix. Excessive dilution can modify the clad's composition, diminishing its mechanical and corrosion resistance. Conversely, too little dilution results in weak fusion between the substrate and the clad. Therefore, managing dilution levels is essential for producing high-quality weld cladding [19,20].

A new class of austenitic stainless steels, called super austenitic stainless steels, has become an important part of high-performance steel development. They have a more advanced chemical composition than traditional austenitic steels, featuring higher amounts of chromium, nickel, and molybdenum, which enhances their corrosion resistance. In environments with highly aggressive corrosive conditions, super austenitic stainless steels are increasingly replacing conventional austenitic steel grades [21].

Although GTAW is well established for cladding austenitic stainless steels onto low-carbon steels, supported by numerous studies highlighting its effectiveness and advantages, and HW-GTAW has documented benefits over traditional GTAW, its application for cladding super austenitic stainless steels remains unclear.

This study focuses on applying HW-GTAW to clad low-carbon steels with super austenitic stainless steels. It includes macro- and microstructural analysis of the coatings, along with assessments of their mechanical strength, corrosion resistance, and wear properties. The research also aims to broaden the use of super austenitic stainless steels and the HW-GTAW process in cladding applications technology.

https://doi.org/10.3390/app16031527

2. Materials and Methods

The base metal was ASTM A516 Gr. 70 (TENAX, Rio de Janeiro, Brazil), commonly used for pressure vessels [22,23], in plates measuring 150 mm by 150 mm and 12.7 mm (1/2 inch) thick. For the cladding, AWS ER385 (AISI 904L—MJV Soldas, São Paulo, Brazil) filler metal was used. A low-carbon filler was chosen to prevent sensitization in the cladding. The compositions of both the base and filler metals are detailed in Table 1, as provided by the supplier.

Table 1. Chemical composition of the base and filler metals.

	C	Si	Mn	Ni	Cr	Mo	Cu	N
ASTM 516 Gr. 70	≤0.28	0.15–0.40	0.85–1.2	-	-	-	-	-
AWS ER385	≤0.02	0.7	4.7	25.4	20	6.2	1.5	0.23

The cladding system consisted of a 2-axis CNC table, a CNC drive system, a GTAW welding machine, a wire feeder, and a hot-wire system. The welding trajectory, travel speed, welding current, and wire feed rate were controlled by a computer. A Data Acquisition System (DAQ), comprising a measuring shunt and an oscilloscope, was used to monitor the welding current.

An inductive hot-wire system was used, in which a coil preheats the filler wire, raising its temperature via inductive heating shortly before immersion in the weld pool. The wire outlet temperature was controlled by the power applied to the inductive heating system. A power source set to 24 V and 30 A (720 W) was used. The experimental setup is shown in Figure 1.

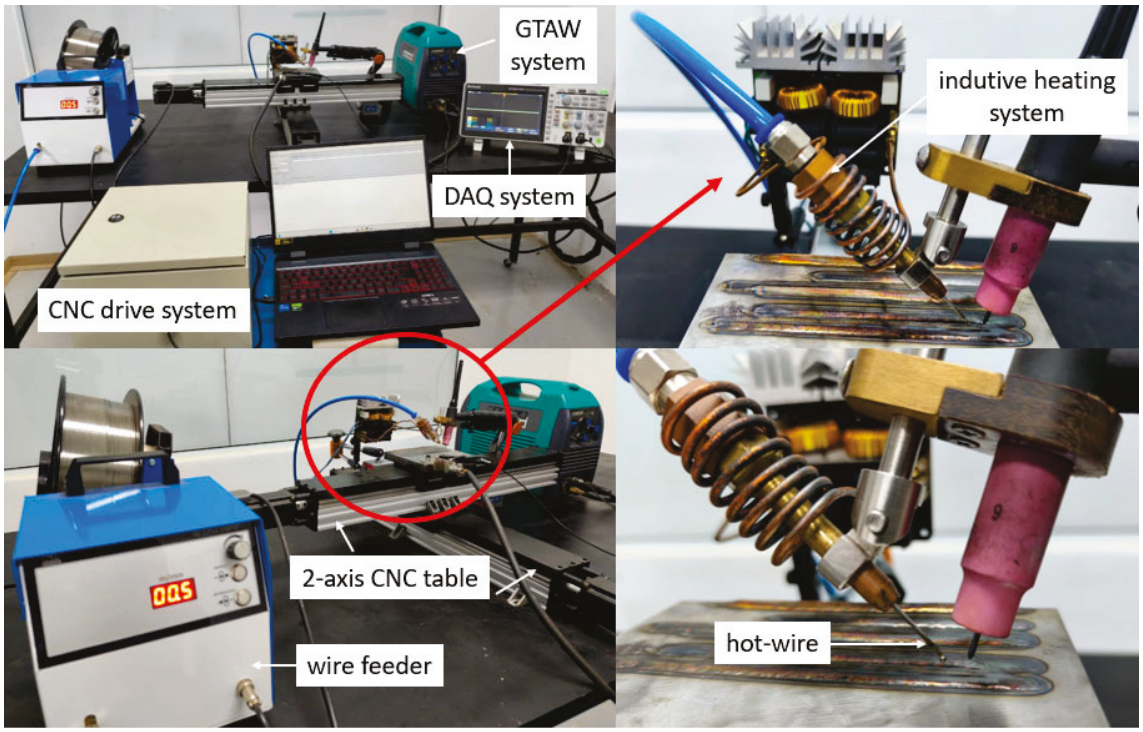

Figure 1. Experimental setup of the HW-GTAW cladding system.

A thoriated tungsten electrode, labeled AWS EW7H2, with a 1.6 mm diameter and a 75° angle to the surface, was employed. It was placed 1.5 mm from the plate. Shielding was provided by argon gas at a flow rate of 15 L per minute.

Several preliminary tests without the hot-wire system were conducted to determine suitable welding parameters, mainly focusing on heat input, and to evaluate cladding quality by analyzing dilution levels and welding defects. The best parameters resulted in a cladding layer with minimal dilution and no visible defects. After setting these parameters, two conditions were tested: one without the hot-wire system (cold-wire cladding, CW-CL) and another with it (hot-wire cladding, HW-CL). For each condition, four test specimens measuring 150 × 150 mm were prepared.

For both conditions, a welding voltage of 30 V, a current of 180 A, a travel speed of 300 mm/min, and a wire feed rate of 0.5 mm/min were applied. The machine was set for high-frequency welding. A 40% overlap rate was used between beads in the cladding layers. Figure 2 shows the current signal obtained with the DAQ system.

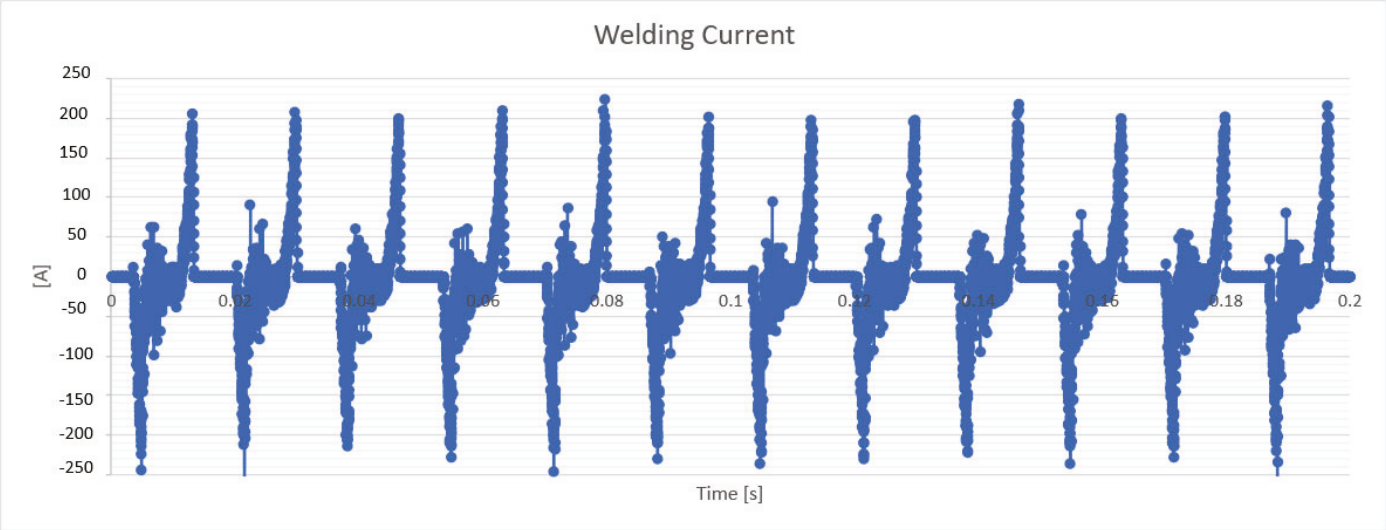

Figure 2. Welding current signal.

The waveform of the electric current generated by the welding machine shows oscillations caused by the machine's control system. Even though the machine was set to 180 V, the measured welding current was approximately 220 V.

After cladding tests, the samples were cut transversely and embedded in Bakelite for further analysis. The samples were sanded manually, alternating their position by 90° for each change. The sandpaper grits used followed the sequence: 220, 320, 400, 600, 1000, and 1200. For polishing, alumina particles measuring 1.0 and 0.3 µm were employed. For macro and microstructural evaluation, aqua regia served as the reagent, with an average etching time of 15 s per sample. Structural analysis was carried out with optical microscopy, using a Zeiss AxioLab.A1 microscope (Jena, Germany) and a ZEISS Axiocam ERc 5s digital camera (Jena, Germany), connected to an AxioVision Rel. 4.8 image analysis system. Additionally, a ZEISS Stemi DV4 stereo microscope was used to enhance the examination.

The dilution ratio of the cladding materials was determined from the captured macrographs. Dilution is the ratio of the cross-sectional area of the melted base material to the total cross-sectional area of the fusion zone, as shown in Figure 3. It is expressed as the percentage of base material in the final clad-layer deposit.

Vickers microhardness testing was carried out using an EMCO TEST Duravision device with a 1 kgf load. Measurements were taken across five distinct areas of the cladding: the base metal, the Heat-Affected Zone (HAZ), the boundary between the HAZ and the Fusion Zone (FZ), the FZ featuring a columnar microstructure, and the FZ with an equiaxed microstructure. In each region, 15 depth measurements were recorded, ensuring

that the minimum spacing between indentations was at least three times the indentation value diagonal.

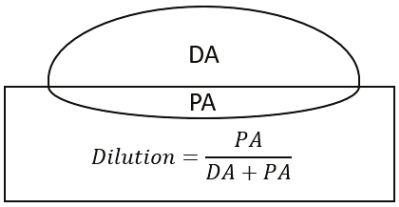

Figure 3. Dilution calculation.

The coefficient of friction of the coating layer was measured using fatigue reciprocating friction tests (Anton Paar TRB^3). The coating surface was polished. The test utilized reciprocating dry friction as the mode of friction. The applied load was 100 N, with a slide distance of 6 mm, a friction duration of 50 min, and a linear speed of 5×10^{-2} m/s. A steel (100Cr6) grinding ball with a diameter of 6 mm was used for the test. Temperature and humidity were maintained at 27.8 ± 1.3 °C and 55 ± 4%, respectively.

Bending tests followed ASME IX QW-160 standards [24]. The specimens were bent to 180°, and both the surface and tension side were examined.

The corrosion resistance was evaluated for CW-CL, HW-CL conditions, and the base metal. Additionally, a rolled AISI 904L plate was tested to compare the coatings' resistance against a reference material. The tests complied with ASTM G1 standards [25]. A surface area of 1 cm^2 was immersed in a 3.5% NaCl electrolyte solution under corrosive conditions. For electrochemical measurements, a silver/silver chloride (Ag/AgCl) reference electrode with 3 M KCl and a platinum (Pt) auxiliary electrode served as the counter electrode. These electrochemical tests were conducted at room temperature using an AMETEK VersaSTAT 4 potentiostat (Princeton Applied Research, Oak Ridge, TN, USA), with a scanning rate of 1 mV/s across all samples. The results were analyzed with Origin software 2025 for comprehensive interpretation.

3. Results and Discussions

3.1. Macrostructure

Figure 4 shows the coating surface for the CW-CL (a) and HW-CL (b) conditions. Visual inspection revealed good coat continuity, with no apparent weld defects. No significant changes were observed in the bead surfaces between the conditions.

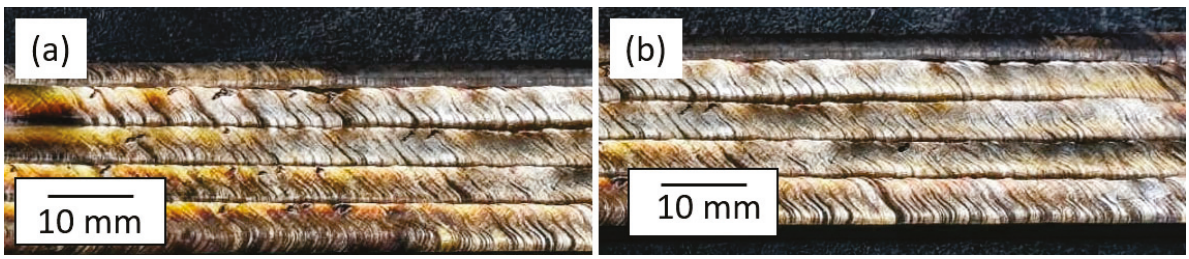

Figure 4. Coating surface for (**a**) CW-CL and (**b**) HW-CL.

Figure 5 shows the cross-sectional macrostructures of single beads produced under CW-CL (a) and HW-CL (b) conditions. The HW-CL process significantly altered the bead geometry, making a wider bead (W—6.1 mm vs. 5.8 mm) and a greater reinforcement height (H—1.2 mm vs. 1.0 mm). Consequently, the average penetration depth decreased (D—0.3 mm vs. 0.5 mm). This geometric shift was accompanied by a notable reduction in the dilution rate, from 26.7% (CW-CL) to 19.8% (HW-CL).

https://doi.org/10.3390/app16031527

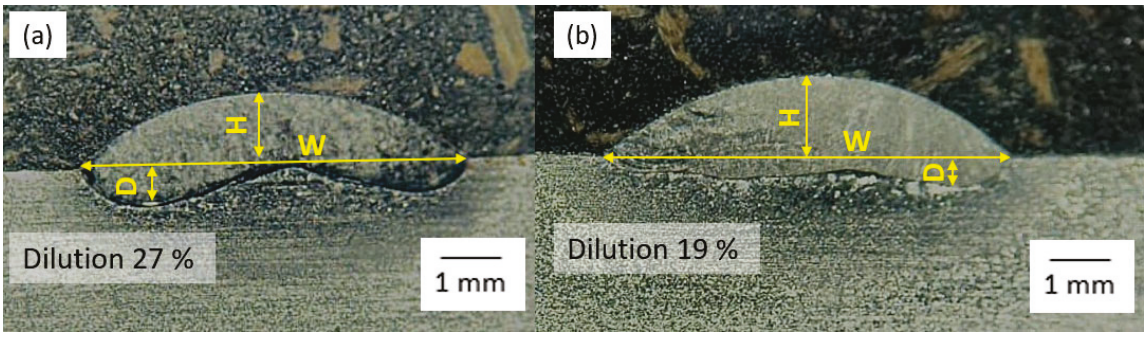

Figure 5. Macrostructure of (**a**) CW-CL and (**b**) HW-CL.

The deposited weld bead consists of both the base metal and the wire metal. During cladding welding, the welding pool comprises droplets of molten metal from the welding wire and melted base metal. The weld forms through the ongoing process of pool formation and solidification. Dilution refers to the change in the cladding alloy composition resulting from mixing the molten matrix [26]. It is a key process-control parameter for producing high-quality cladding. Maintaining a low dilution is essential because it improves reinforcement quality and increases clad width, thereby providing greater substrate coverage. Additionally, low dilution helps retain the essential elements within the clad layers [19].

The hot-wire technique reduces the dilution rate by preheating the filler wire. This preheating reduces the energy required by the main arc, thereby minimizing melting of the base metal. Since indirect heating was used, preheating could be separated from the GTAW process [15,16]. This allowed the penetration and reinforcement height to be determined independently of the GTAW arc. With welding parameters such as travel speed, wire feed rate, and welding current kept constant in both cases, the additional heat from wire preheating mainly melted the filler wire. This resulted in a higher reinforcement-to-penetration ratio and produced a dilution level better suited to cladding applications.

3.2. Microstructure

Figure 6 presents the microstructure for the CW-CL (a) and HW-CL (b) conditions. No significant differences were observed between the two conditions. The microstructure resembles that of wire-arc additive manufacturing (WAAM), characterized by elongated columnar dendrite grains extending from the heat-affected zone and a shallow zone of equiaxed dendrite grains near the bead surface [27–29].

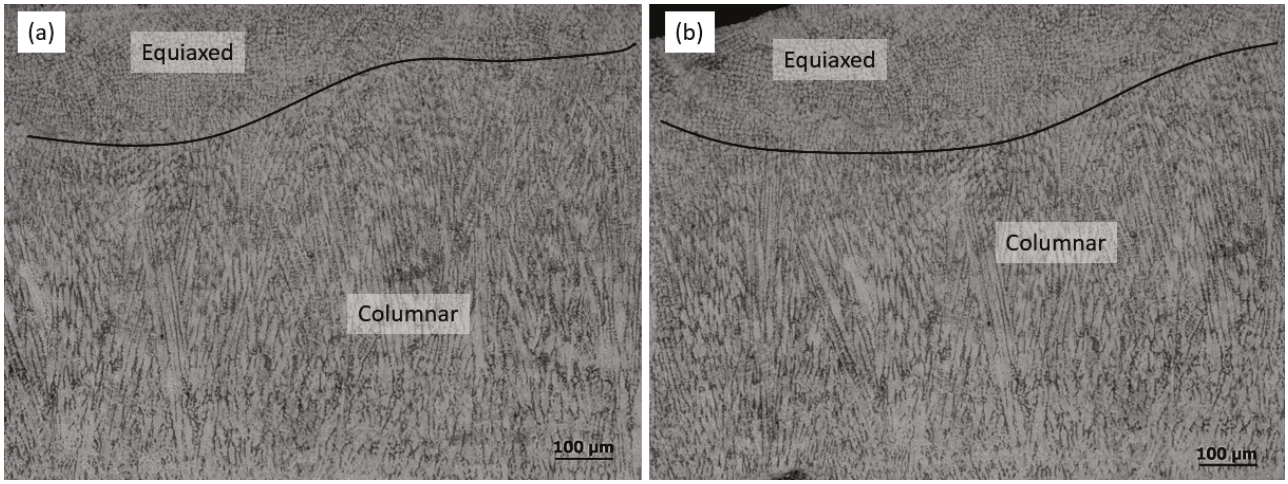

Figure 6. Microstructure of (**a**) CW-CL and (**b**) HW-CL.

The thermal cycles during cladding influence the bead's microstructure development. Factors such as temperature distribution during welding, heating rate, and cooling rate shape the resulting microstructure. These thermal cycles and cooling rates cause variations in grain shape and phase distribution. Near the Heat-Affected Zone (HAZ), heat is conducted away from the molten pool to the base metal. Near the coating surface, heat transfer occurs via convection and radiation [30]. Cooling rates are higher near the HAZ and decrease toward the coating surface. The slower cooling near the surface allows equiaxed austenite grains to grow. At the boundary between the HAZ and the coating, where cooling is fastest, grains tend to grow in the direction of the greatest temperature difference, resulting in columnar dendrites [27].

Since the microstructures for both conditions were similar, Figure 7 presents the microstructure for the HW-CL condition (a), with details of the equiaxial (b) and columnar (c) regions. The equiaxial region exhibited a microstructure predominantly of γ-austenite in combination with δ-ferrite on the grain boundaries. The columnar region also showed a microstructure predominantly of γ-austenite with acicular ferrite mode.

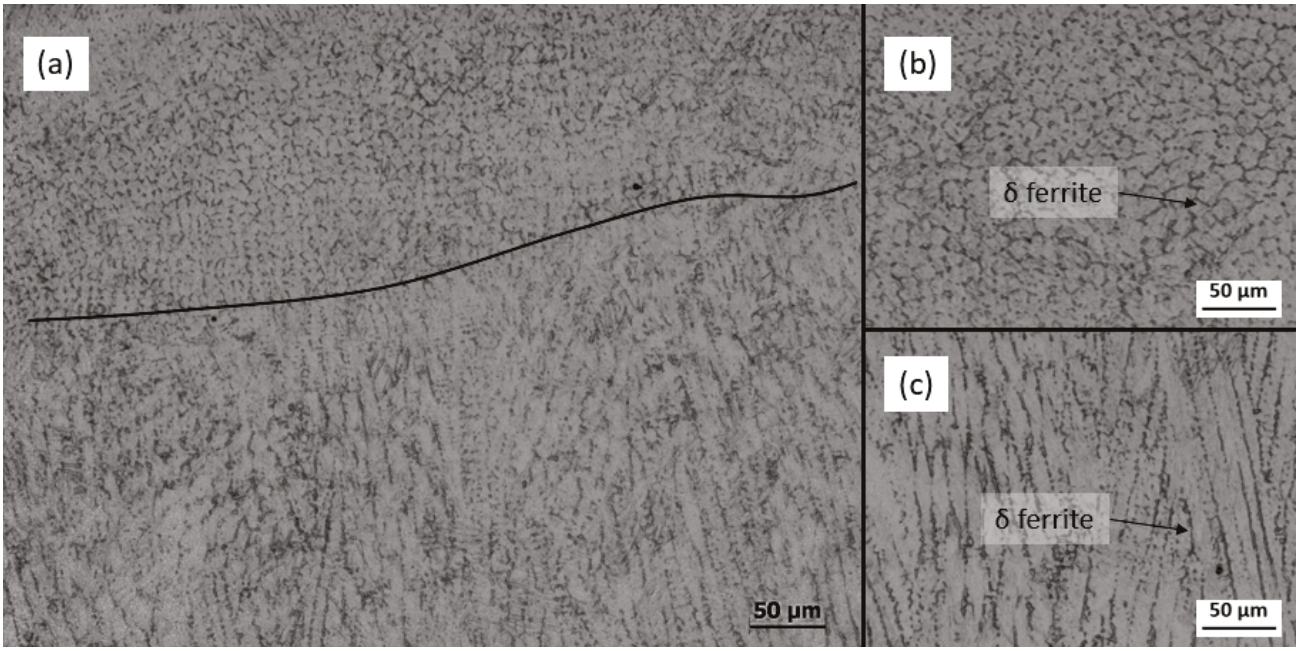

Figure 7. Microstructure of (**a**) HW-CL (**b**) columnar region and (**c**) equiaxed region.

During cooling, δ-ferrite dissolves into the austenitic matrix via a solid-state reaction, leading to a predicted fully austenitic microstructure. However, a high cooling rate can inhibit this phase transformation, preventing complete diffusion solid-state dissolution of δ-ferrite. As a result, some δ-ferrite remains stable within the microstructure. It tends to form at grain boundaries and resists transforming into austenite during cooling because it is already enriched with ferrite-promoting elements due to segregation during solidification [31]. The δ-ferrite volume fraction can reach up to 8%, depending on the conditions [28].

The presence of δ-ferrite in the austenitic matrix of stainless steel welds is essential to lower the risk of hot cracking during solidification. Fully austenitic stainless steel weld deposits tend to develop microfissures upon cooling after solidification. A minimum amount of δ-ferrite helps to dissolve harmful phase elements [10].

Similar to the microstructure of the clad layer, which showed no significant differences between the CW-CL and HW-CL conditions, the HAZ microstructures were also similar. Figure 8 presents the microstructure of the HAZ (a), the area near the HAZ/fusion zone

(FZ) transition (b), and the interior of the HAZ at a higher magnification (c) for the HW-CL condition. The HAZ microstructure exhibits a gradient of hardened phases, likely due to varying cooling rates across the depth profile. Near the fusion boundary, high-carbon martensite forms due to carbon migration from the steel into the dilute stainless melt pool during welding, thereby influencing its hardness and crack susceptibility. As the distance from the interface increases, the HAZ shows zones of coarse-grained martensite, fine-grained martensite, and a tempered region (ferrite and cementite), eventually transitioning into the unaffected ferrite-pearlite base metal. The presence of ferrite and cementite near the unaffected base material can be attributed to lower cooling rates and higher peak temperatures, whereas martensite forms near the fusion boundary due to accelerated cooling rates [3,13,21].

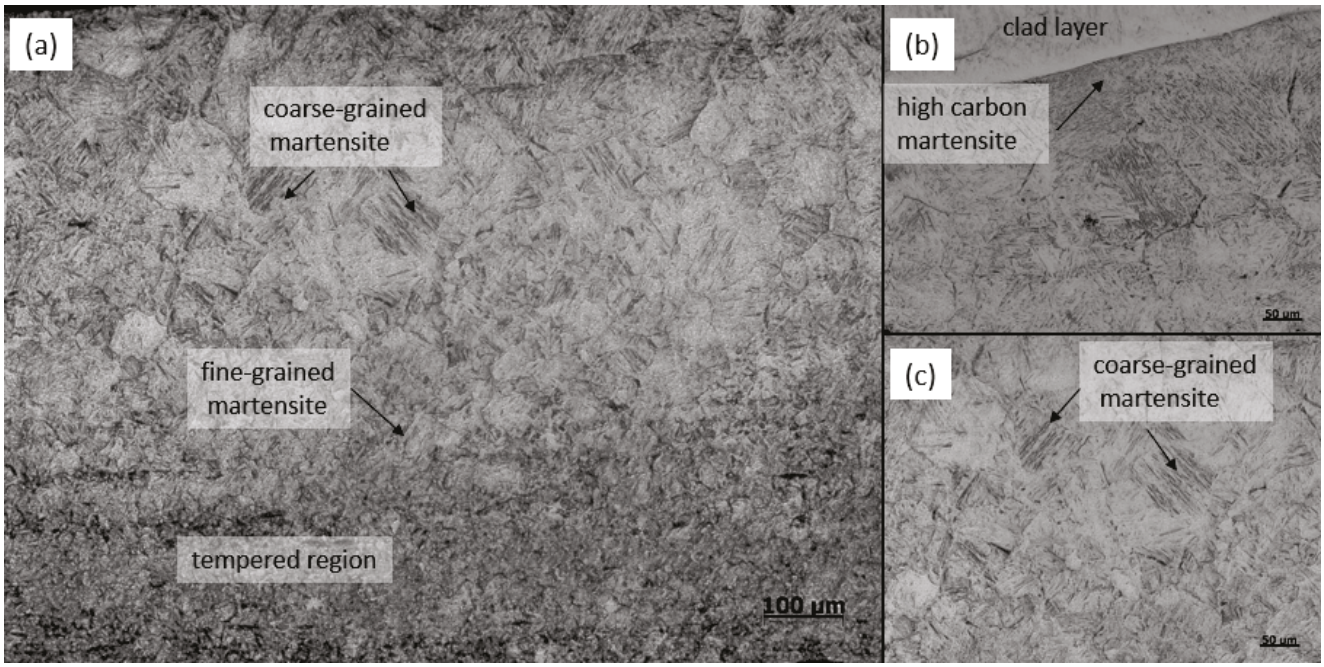

Figure 8. (**a**) Microstructure of HAZ for HW-CL (**b**) HAZ-FZ transition (**c**) HAZ with high magnification.

3.3. Microhardness

Figure 9 illustrates a schematic of the regions where microhardness measurements were taken, along with the microhardness values for the CW-CL and HW-CL conditions. In both cases, a hardness variation is evident in the HAZ, with the peak hardness near the boundary between the HAZ and the FZ. The microstructures in the HAZ Figure 8 exhibit a gradient of hardened phases, with high-carbon austenite forming near the HAZ/FZ interface, resulting in higher hardness in that region than in the remainder of the HAZ.

Regarding microhardness, in both conditions, a pattern is observed in which regions with a columnar dendritic austenitic microstructure generally exhibit slightly higher hardness than regions with an equiaxed dendritic austenitic microstructure. As noted by Chamim et al. [31] in their study on the influence of welding thermal cycles on δ-ferrite evolution in austenitic stainless steel produced by WAAM-GTAW, the presence of coarse acicular ferrite in the columnar region contributes to increased hardness compared to the equiaxed region. Additionally, Xu et al. [32] report that the columnar dendritic austenitic structure typically exhibits slightly higher as-built hardness than the equiaxed dendritic structure, primarily due to greater internal strain and distinct segregation patterns.

https://doi.org/10.3390/app16031527

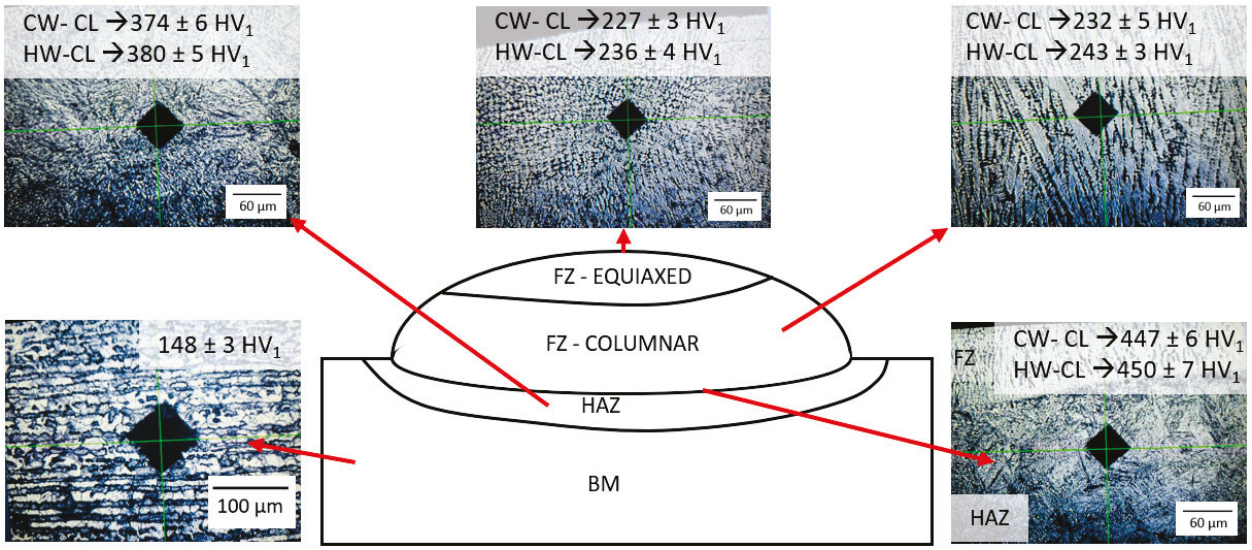

Figure 9. Schematic of the microhardness measurements.

Compared with the CW-CL condition, hardness was higher in the HW-CL condition. In the HAZ, differences were more subtle, with intervals in which values were within the standard deviation, indicating minimal influence of the hot-wire in this region. Conversely, in the fusion zone, differences were more noticeable, showing a tendency toward higher hardness in the HW-CL condition. As previously noted, the additional heat from wire preheating primarily melted the filler wire, resulting in slightly higher cooling rates in the HW-CL fusion zone. While this did not alter the microstructural morphology, it likely caused a slightly higher internal strain than in the CW-CL condition.

3.4. Coefficient of Friction

Figure 10 shows the coefficient of friction (COF) results for the base metal, CW-CL, and HW-CL. During the early wear stage, contact between the sample surface and the contact surface creates an unstable condition. As wear progresses, contact between the sample surface and the grinding balls stabilizes and remains steady for the remainder of the test. The base metal had the highest coefficient of friction. The HW-CL condition showed the lowest coefficient, about 5% lower than CW-CL. Because a higher COF indicates greater wear potential, both CW-CL and HW-CL conditions exhibited greater wear resistance than the base metal, with HW-CL showing the greatest wear resistance. The wear resistance followed the same pattern as the microhardness, particularly in the fusion zone. Its higher hardness improves resistance to plastic deformation, thereby enhancing wear resistance [33].

3.5. Bending Tests

Figure 11 shows the samples after the bending tests. The bending tests revealed no visible cracks in either the CW-CL or HW-CL conditions, including at the interface with the substrate. All tests were approved; no cracking was observed, and a strong metallurgical bond was indicated. Additionally, the cladding layer did not peel from the base metal, and the lack of cracks and fusion defects showcases the excellent toughness of the clad layers [34].

3.6. Corrosion Resistance

Figure 12 displays the Tafel polarization results for CW-CL, HW-CL, base metal, and a rolled plate of AISI 904L stainless steel (Realum, São Paulo, Brazil). The key parameters, corrosion potential (Ecorr) and corrosion current (Icorr), are derived from potentiodynamic

polarization curves and relate to the thermodynamics and kinetics of corrosion, respectively. Ecorr indicates the open-circuit potential at equilibrium, reflecting the material's tendency to oxidize: more positive (higher) Ecorr values imply greater nobility and reduced corrosion likelihood. Conversely, Icorr measures the true rate of oxidation; lower Icorr values denote slower corrosion rates and thus, improved material performance in the given environment [35,36].

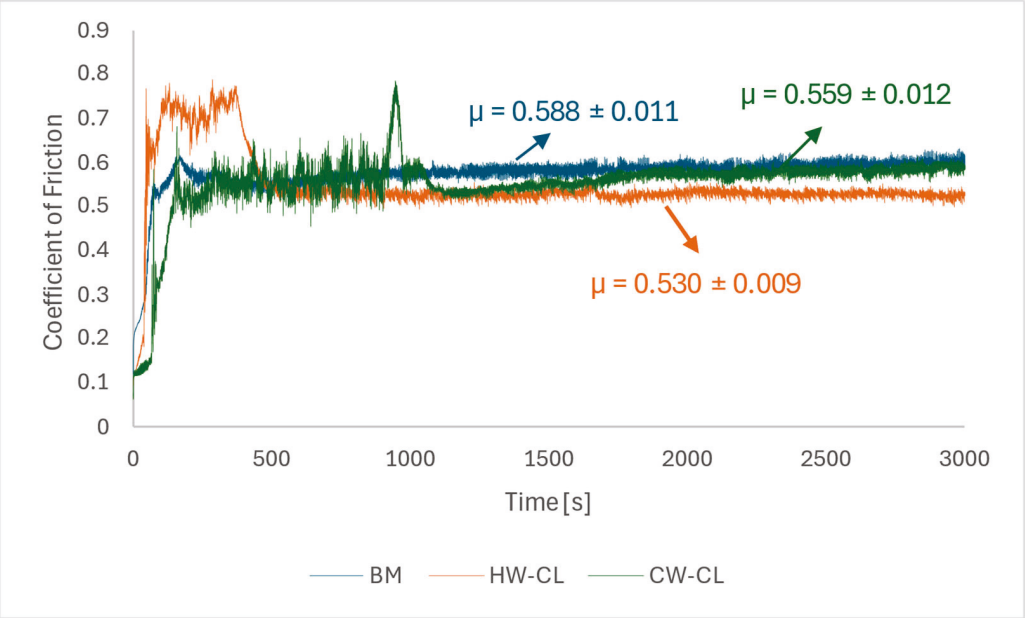

Figure 10. Coefficient of friction results.

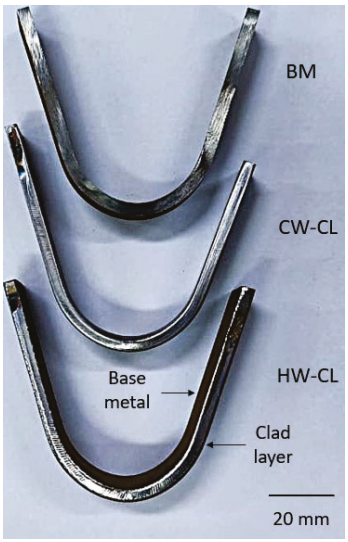

Figure 11. Bending test samples.

The results show a clear enhancement in corrosion resistance for both CW-CL and HW-CL conditions compared to the base metal. The base metal's Ecorr was −625 mV with an Icorr of 5.7 μA. In contrast, CW-CL and HW-CL displayed Ecorr values of −365 mV and −351 mV, and Icorr values of 1.1 μA and 1.9 μA, respectively. Both conditions resulted in higher Ecorr and lower Icorr, signifying improved corrosion resistance.

Among the conditions, HW-CL exhibited a slight enhancement in corrosion resistance compared to CW-CL. This minor improvement is associated with the lower dilution rate in HW-CL, which affects the cladding alloy composition by reducing the mixing of the molten

matrix. A lower dilution rate helps maintain the original chemical composition of the 904L alloy, thereby enhancing its corrosion resistance [37].

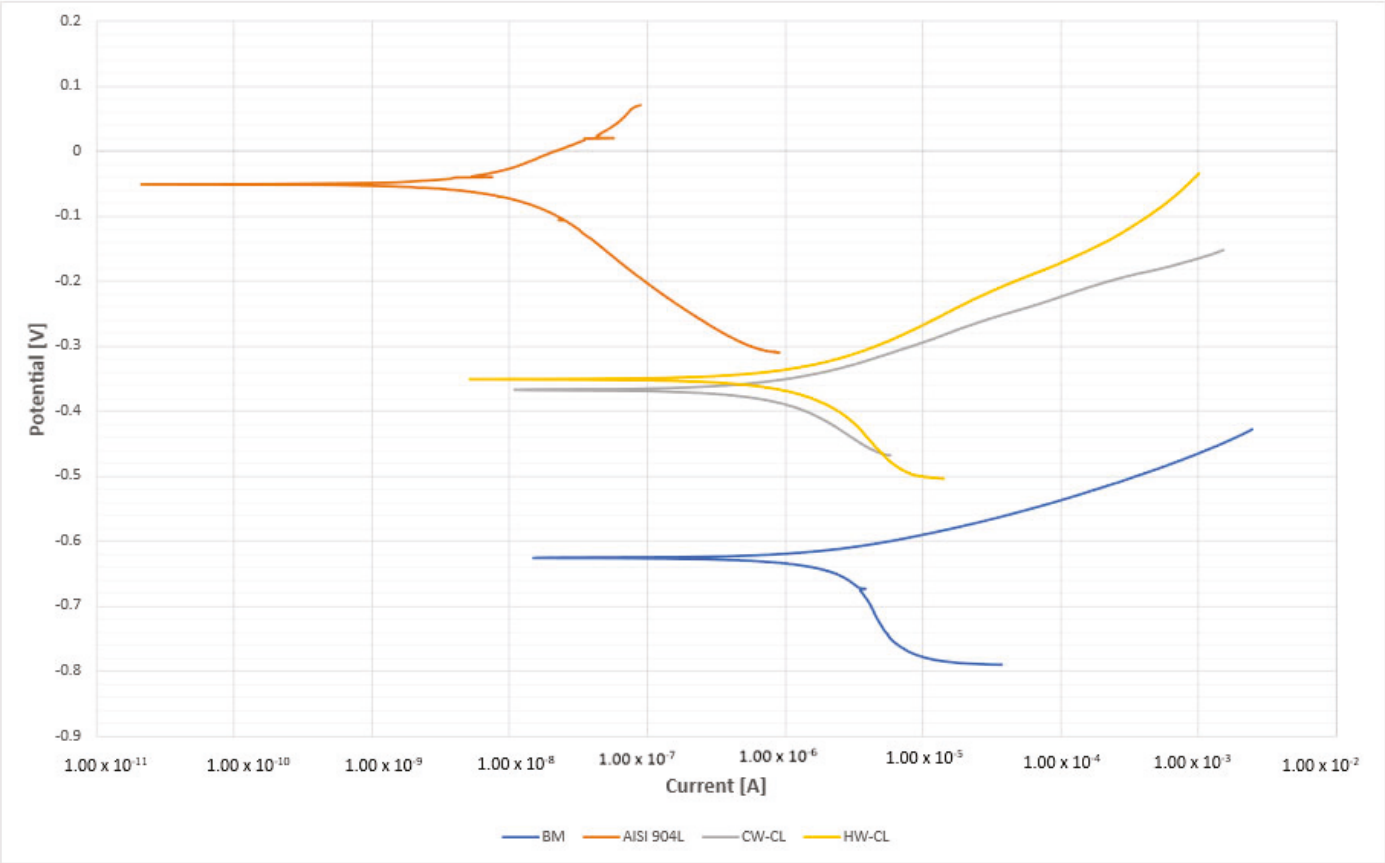

Figure 12. Tafel polarization curves.

Although they did not match the corrosion resistance of the wrought AISI 904L plate (used as a reference), both conditions showed a significant improvement over the base metal, achieving the goal of super austenitic stainless steel cladding on low-carbon steel.

4. Conclusions

1. Hot-wire GTAW is a method suitable for cladding super austenitic stainless steels onto low-carbon steels. It creates weld beads with excellent surface adhesion, defect-free quality, and mechanical and corrosion resistance appropriate for corrosive environments.
2. Hot-wire GTAW decreased dilution from 27% to 19% compared to the traditional CW-GTAW method, enhancing its suitability for cladding applications.
3. In both conditions, the microstructure of the clad layer featured elongated columnar dendrite grains that extend from the heat-affected zone, along with a shallow region of equiaxed dendrite grains near the bead surface, similar to what is observed in wire-arc additive manufacturing.
4. In both conditions, the HAZ microstructure shows a gradient of hardened phases, featuring higher hardness near the HAZ/FZ interface because of high-carbon martensite, which diminishes towards the unaffected base metal.
5. Hot-wire GTAW showed slightly better wear resistance than CW-GTAW, mainly because of its higher hardness across the entire clad layer. Additionally, hot-wire GTAW also exhibited better corrosion resistance compared to CW-GTAW, which is

linked to its lower dilution. For both conditions, the corrosion resistance exceeded that of the base metal.
6. Both conditions successfully passed the bending test, showing no cracks and maintaining a strong metallurgical bond.

Author Contributions: Conceptualization, E.J.d.C.J., F.M.F.A.V. and L.F.F.S.; methodology, E.J.d.C.J., F.M.F.A.V. and F.O.C.; validation, I.C. and V.A.V.; formal analysis, B.F.G. and M.P.; writing—original draft preparation, E.J.d.C.J., F.M.F.A.V., L.F.F.S., F.O.C., B.F.G., V.A.V., I.C. and M.P.; writing—review and editing, I.C. and V.A.V.; supervision, E.J.d.C.J.; project administration, E.J.d.C.J.; funding acquisition, E.J.d.C.J. and F.M.F.A.V. All authors have read and agreed to the published version of the manuscript.

Funding: This research was funded by FAPESP—São Paulo Research Foundation, Brazil (Grant: 2023/16993-0) and São Paulo Federal Institute of Education, Science and Technology (Grant: 60/2024).

Institutional Review Board Statement: Not applicable.

Informed Consent Statement: Not applicable.

Data Availability Statement: The original contributions presented in this study are included in the article. Further inquiries can be directed to the corresponding author.

Acknowledgments: To São Paulo Research Foundation (FAPESP) and São Paulo Federal Institute of Education, Science and Technology, Brazil, for the financial support for the development of the research. To Anton Parr Brazil for supporting the tribological tests. To the Center for Research and Innovation in Materials and Structures (CEPIMATE) for the technical support.

Conflicts of Interest: The authors declare no conflicts of interest.

References

1. Saravanan, S.; Raghukandan, K.; Sivagurumanikandan, N. Pulsed Nd: YAG laser welding and subsequent post-weld heat treatment on super duplex stainless steel. *J. Manuf. Process.* **2017**, *25*, 284–289. [CrossRef]
2. Huang, Z.; Zhang, J.; Ma, Z.; Yuan, S.; Yang, H. Research Progress on the Relationship Between Microstructure and Properties of AISI 321 Stainless Steel. *Appl. Sci.* **2024**, *14*, 10196. [CrossRef]
3. Hou, Z.; Fu, K.; Fang, D.; Wang, J. Microstructure and Mechanical Performances of Stainless Steel Cladding by Twin-Electrode GTAW. *Mater. Trans.* **2021**, *62*, 995–1000. [CrossRef]
4. de Paula, H.O.; de Castro, L.A.S.; Cavalcante, D.R.; Pinheiro, C.M.; Carneiro, J.R.G. Study on HW-GTAW cladding of super austenitic stainless steel on low-carbon steel: Microstructure and mechanical properties. *Mater. Res.* 2025, *advance online publication*. [CrossRef]
5. Murkute, P.; Pasebani, S.; Isgor, O.B. Production of corrosion-resistant 316L stainless steel clads on carbon steel using powder bed fusion-selective laser melting. *J. Mater. Process. Technol.* **2019**, *273*, 116243. [CrossRef]
6. Aslam, M.; Sahoo, C.K. Numerical and experimental investigation for the cladding of AISI 304 stainless steel on mild steel substrate using Gas Metal Arc Welding. *CIRP J. Manuf. Sci. Technol.* **2022**, *37*, 378–387. [CrossRef]
7. Li, C.; Qin, G.; Tang, Y.; Zhang, B. Microstructures and mechanical properties of stainless steel clad plate joint with diverse filler metals. *J. Mater. Res. Technol.* **2020**, *9*, 2522–2534. [CrossRef]
8. Prakash Pasupulla, A.; Agisho, H.A.; Seetharaman, S.; Vijayakumar, S. Characterization and analysis of TIG welded stainless steel 304 alloy plates using radiography and destructive testing techniques. *Mater. Today Proc.* **2022**, *51*, 935–938. [CrossRef]
9. Di Schino, A.; Testani, C. Corrosion Behavior and Mechanical Properties of AISI 316 Stainless Steel Clad Q235 Plate. *Metals* **2020**, *10*, 552. [CrossRef]
10. Kumar, M.; Singh, J.; Uppal, A.S. Improvement in corrosion resistance of AISI 316L stainless steel weld cladding using GTA remelting technique. *Mater. Today Proc.* **2022**, *65*, 3224–3228. [CrossRef]
11. Jayavelu, M.; Kasi, S.; Visvalingam, B.; Bellamkonda, P.N.; Dara, S. Wear properties and microstructural characteristics of mild steel cladded with AISI 316L stainless steel using constant current gas metal arc welding process. *Mater. Today Proc.* 2023, *in press*. [CrossRef]

12. Peng, C.; Gao, T.; Fu, P.; Zhu, R.; Xuan, H.; Duan, L.; Zhao, K.; Yuan, B.; Zhang, L.; Xie, Z. Ultrasonic vibration-assisted gas metal arc welding for 308 stainless steel cladding layers: Microstructure, mechanical properties, and corrosion resistance. *Mater. Today Commun.* **2025**, *49*, 114106. [CrossRef]
13. da Cruz Junior, E.J.; Varasquim, F.M.F.A.; De Mendonça, V.R.; Ventrella, V.A.; Gonçalves, A.C.; Fagundes Junior, J.G.; Zambon, A.; Calliari, I. Impact of Heat Input on the Cladding of Super Austenitic Stainless Steel Through the Gas Tungsten Arc Welding Process on ASTM A516 Grade 70 Steel. *Coatings* **2024**, *14*, 1356. [CrossRef]
14. Hedaiat, F.; Dehmolaei, R.; Khorasanian, M.; Lotfi, B. Long-term oxidation behaviour and thermal stability of heat-resistant stainless steel claddings deposited on AISI 316 stainless steel by the GTAW process. *Surf. Coat. Technol.* **2021**, *424*, 127605. [CrossRef]
15. Ungethüm, T.; Spaniol, E.; Hertel, M.; Füssel, U. Analysis of metal transfer and weld geometry in hot-wire GTAW with indirect resistive heating. *Weld. World* **2020**, *64*, 2109–2117. [CrossRef]
16. Zhang, Z.; Kong, F.; Kovacevic, R. Laser hot-wire cladding of Co-Cr-W metal cored wire. *Opt. Laser Eng.* **2020**, *128*, 105998. [CrossRef]
17. Chen, Y.; Zhang, X.; Cheng, T.; Yang, C. Effect of hot-wire method on microstructure and mechanical properties of wire arc additive repaired superalloy. *Mater. Sci. Eng. A* **2024**, *916*, 147359. [CrossRef]
18. Hassel, T.A.; Sørby, K.; Brøtan, V. Effect of preheat in DED-LB/wire of Ni-base, Cu-base and Fe-base alloys. *Procedia CIRP* **2024**, *126*, 674–679. [CrossRef]
19. Majid, M.; Goel, L.; Saxena, A.; Srivastava, A.K.; Singh, G.K.; Verma, R.; Bhutto, J.K.; Hussein, H.S. Firefly Algorithm and Neural Network Employment for Dilution Analysis of Super Duplex Stainless Steel Clads over AISI 1020 Steel Using Gas Tungsten Arc Process. *Coatings* **2023**, *13*, 841. [CrossRef]
20. Gao, S.; Fu, Q.; Li, M.; Huang, L.; Liu, N.; Cui, C.; Yang, B.; Zhang, G. Optimization of Laser Cladding Parameters for High-Entropy Alloy-Reinforced 316L Stainless-Steel via Grey Relational Analysis. *Coatings* **2024**, *14*, 1103. [CrossRef]
21. Matias, J.V.S.; Lourenço, M.J.C.; Jorge, J.C.F.; de Souza, L.F.G.; Farneze, H.N.; Mendes, M.C.; da Silva, C.L.A.; Araújo, L.S. Behavior of a superaustenitic stainless steel weld cladding deposited by the gas metal arc welding process. *Mater. Today Commun.* **2023**, *34*, 104978. [CrossRef]
22. Coêlho, G.d.C.; Silva, A.A.; dos Santos, M.A.; Machado, J.J.M.; Tavares, J.M.R.S. Ductile Fracture Behavior of ASTM A516 Gr.70 Pressure Vessel Steel by ASTM and ISO Fracture Toughness Standards. *Metals* **2023**, *13*, 867. [CrossRef]
23. Lee, S.-H.; Choi, B.-J. Mechanical Properties of ASTM A572 Grades 50 and 60 Steels at High Temperatures. *Appl. Sci.* **2021**, *11*, 11833. [CrossRef]
24. ASME IX QW-160. Available online: https://www.scribd.com/document/645452520/02-ASME-IX-QW-160-2010-pdf (accessed on 31 January 2026).
25. *ASTM G1*; Standard Practice for Preparing, Cleaning, and Evaluating Corrosion Test Specimens. ASTM: West Conshohocken, PA, USA, 2025.
26. Bazychowska, S.; Panasiuk, K.; Starosta, R. The Influence of Variable Plasma Welding Parameters on Weld Geometry, Dilution Factor, and Microhardness. *Appl. Sci.* **2024**, *14*, 7248. [CrossRef]
27. Rahimi, A.; Yazdizadeh, M.; Ara, M.V.; Pouranvari, M. CMT wire-arc additive manufacturing of 310 austenitic stainless steel: Microstructure-properties relationships. *J. Mater. Res. Technol.* **2025**, *35*, 881–891. [CrossRef]
28. Kondratev, N.; Podsedertsev, A.; Bezverkhy, D.; Sharifullina, E.; Olshanskaya, T.; Trushnikov, D. Multilevel Prediction of Mechanical Properties of Samples Additively Manufactured from Steel 308LSi. *Metals* **2026**, *16*, 8. [CrossRef]
29. Jin, W.; Zhang, C.; Jin, S.; Tian, Y.; Wellmann, D.; Liu, W. Wire Arc Additive Manufacturing of Stainless Steels: A Review. *Appl. Sci.* **2020**, *10*, 1563. [CrossRef]
30. Lu, L.; Cai, Z.; Yang, J.; Liang, Z.; Sun, Q.; Pan, J. Study on Key Parameters of Dilution Ratio of the Bead Deposited by GTAW Method for Nuclear Components. *Metals* **2022**, *12*, 1506. [CrossRef]
31. Chamim, M.; Darmadi, D.B.; Purnowidodo, A.; Widodo, T.D.; Ismail, Z. Influence of the welding thermal cycle on δ-ferrite evolution in the first layer of austenitic stainless steel (ASS) 308L produced by WAAM-GTAW. *Case Stud. Therm. Eng.* **2024**, *64*, 105489. [CrossRef]
32. Xu, X.; Ganguly, S.; Ding, J.; Guo, S.; Williams, S.; Martina, F. Microstructural evolution and mechanical properties of maraging steel produced by wire+arc additive manufacture process. *Mater. Charact.* **2018**, *143*, 152–162. [CrossRef]
33. Zhang, D.; Li, H.; Liu, Y.; Jiang, J.; Gao, Y. An Investigation of the Microstructure and Wear Resistance of Laser Clad 316 Stainless Steel/TiC Coatings Containing Different LaB_6 Contents. *Ceramics* **2025**, *8*, 121. [CrossRef]
34. Yoon, J.-H.; Kim, J.H.; Shin, G.; Kim, C. Characterization of nickel cladding on type 316H stainless steel for enhanced corrosion resistance in molten chloride salts. *Nucl. Eng. Technol.* **2025**, *57*, 103276. [CrossRef]
35. Amiri, E.; Ostovan, F.; Toozandehjani, M.; Shafiei, E.; Mohamed, I.F. Study and selection of most appropriate filler rod for GTAW of S32750 super duplex steel joints: A comprehensive study on microstructural, mechanical and corrosion properties. *Mater. Chem. Phys.* **2021**, *270*, 124839. [CrossRef]

36. Wang, Q.; Gu, G.; Jia, C.; Li, K.; Wu, C. Investigation of microstructure evolution, mechanical and corrosion properties of SAF 2507 super duplex stainless steel joints by keyhole plasma arc welding. *J. Mater. Res. Technol.* **2023**, *22*, 355–374. [CrossRef]
37. Cunha, A.B.; Vatavuk, J.; Lima, C.R.C. Investigating the Effects of Iron Dilution on the Corrosion Resistance of Inconel 625 Welding Overlay on Carbon Steel. *Materials* **2025**, *18*, 5574. [CrossRef] [PubMed]

Disclaimer/Publisher's Note: The statements, opinions and data contained in all publications are solely those of the individual author(s) and contributor(s) and not of MDPI and/or the editor(s). MDPI and/or the editor(s) disclaim responsibility for any injury to people or property resulting from any ideas, methods, instructions or products referred to in the content.

applied sciences

MDPI

Article

Wire Arc Additive Manufacturing of Complex-Shaped Capsules for HIP Sintering of Powder

Rodolphe Bolot *, Alexandre Mathieu, Hichem Aberbache, Mohamed-Achref Karoui and Frédéric Bernard

ICB UMR 6303 CNRS, Université de Bourgogne Europe, 21078 Dijon, France;
alexandre.mathieu@u-bourgogne.fr (A.M.); mohamed-achref.karoui@u-bourgogne.fr (M.-A.K.);
frederic.bernard@u-bourgogne.fr (F.B.)
* Correspondence: rodolphe.bolot@ube.fr; Tel.: +33-(0)3-85-73-10-42; +33-(0)6-87-17-53-40

Featured Application

A new hybrid process for prototyping medium-size metal components with enhanced mechanical properties, especially within the framework of the nuclear industry.

Abstract

This work focuses on wire arc additive manufacturing for the rapid prototyping of shell-type parts such as sealed containers/capsules required in the manufacturing of metal components using hot isostatic pressing (HIP) of powder. The selected material was AISI 316L. The automatic generation step of robot trajectories from the CAD design of the part to be manufactured was addressed first. The mechanical and metallurgical properties of WAAM samples were then evaluated. Finally, a hollow cylindrical capsule manufactured by WAAM was used for the HIP sintering of powder to demonstrate the relevance of the hybrid technology. The main results are as follows: 1. The Ultimate Tensile Strength (UTS) of AISI 316L WAAM samples was measured be-19 tween 540 MPa (longitudinal direction) and 600 MPa (transverse direction). 2. The as-manufactured WAAM parts present a residual (δ) ferrite content of 5–7%. 3. HIP processing permitted to reset a fully austenitic structure within the WAAM wall/shell. 4. The grain size was found to be coarser in the WAAM walls and finer in the core of the part (made of sintered powder). Finally, the suggested hybrid process may become an alternative technology for the manufacture of medium-size metal components in the nuclear industry.

Keywords: wire arc additive manufacturing; WAAM; metal additive manufacturing; slicer; automatic offline programming of robot trajectories

1. Introduction

Hot isostatic pressing of powder is a promising technology for the future of prototyping large metal components. Expectations regarding the direct manufacturing of parts by hot isostatic pressing (HIP) of metal powder are particularly high, especially with regard to the design of new small modular nuclear reactors (SMRs), for which the technology might represent an alternative to casting and forging. It notably allows for the manufacturing of geometrically complex single-piece parts with a fine-grained microstructure. Depending on the process, a hollow shell-type preform (called a capsule) has to be manufactured first. This preform is then filled with metallic powder, followed by being vacuumed and sealed before the entire assembly is subjected to hot isostatic pressing. The HIP processing, which is carried out at up to 2000 bars and 2000 °C (or even more depending on the type

of material), then results in the closure of all initially existing cavities/voids between the powder grains. Finally, the manufactured parts ultimately exhibit a relative density that can exceed 99.9%. Of course, the initial preform (capsule) must remain perfectly sealed and gastight throughout the sintering process. Otherwise, the gas pressure applied in the chamber would propagate inside the capsule, resulting in a low-quality sintering process that would be unable to close the voids between the powder grains. Until now, the gastight capsules required for the process have been manufactured using conventional welding mechanic processing (including multiple operations of cutting, stamping, and welding). These steps can be extremely time-consuming, depending on the geometrical complexity of the part to be manufactured. Hence, the cost of the conventional welding mechanic processing of the capsule, including its removal, may represent up to 45% of the final cost of an HIP part [1]. There is thus huge interest in simplifying the steps of manufacturing the capsule.

In this context, wire arc additive manufacturing (WAAM) technology has been developed as a specific process for manufacturing gastight containers (capsules). Indeed, WAAM has proved to be particularly suitable for printing large metal components. The WAAM shell printing technique is thus presented first in this work. Wire arc additive manufacturing has great potential for manufacturing blanks of large metal parts. It benefits from various advantages such as the absence of a closed chamber under inert gas and its high deposition rate (up to about 3 kg/h). On the other hand, the resolution of the manufactured parts is significantly lower in comparison with the laser powder bed fusion (LPBF) additive manufacturing process, for example (several-millimeter-wide cords/beads in WAAM versus around 50 μm for LPBF). It can therefore be used to produce rough parts quickly; these will then have to undergo surface finishing, particularly to eliminate large-scale waves on the external surface, which are inherent in the process. It can also be used to locally manufacture material additions on larger parts, thus simplifying the initial design of the part in question. At the present time, there are no fully integrated standard solutions provided by the manufacturers of welding tools, as is the case for LPBF; therefore, laboratories and companies generally carry out their own homemade developments, at the software level. However, some SMEs have recently specialized in the integration of virtual robotic cells, and automatic offline programming of robot trajectories for WAAM applications. Among these enterprises, ADAXIS may be cited for commercializing the ADAONE software. The first step of the present work was to develop a complete tool meeting our specifications, and adapted to our available equipment (KUKA KR6, KR8, and KR60 robots; FRONIUS Cold Metal Transfer (CMT) welding workstation). Throughout this work, the specific developments made (CAD slicer, automation of trajectories generation, deposition strategy, and examples of printed parts) are described first. The main objective was to quickly create a simple, easy-to-use, and effective solution for the manufacture of blanks with potentially complex geometries.

Many studies devoted to wire arc additive manufacturing (WAAM) are concerned with the characterization of the material properties, so that simple straight walls are often manufactured in this context. Horgar et al. [2] built aluminum alloy parts (AA5183, i.e., Al4.5MgMn alloy) and produced tensile specimens oriented differently regarding the aligned welds. In all cases, the Ultimate Tensile Strength (UTS) of their samples was a little below 300 MPa, with maximum strains in the range of 22–29% depending on the sample's orientation. Fuchs et al. [3] studied the machining allowance of Ti6Al4V near-net shaped WAAM parts in the context of the aeronautic industry. They developed a process chain that consisted of WAAM and milling, and their objective was to minimize the deviation between the WAAM part and the model. Rodrigues et al. [4] compared conventional GMAW WAAM and UC-WAAM (ultracold wire–arc additive manufacturing), in which

https://doi.org/10.3390/app16010179

the electric arc is established between the wire feedstock material and a non-consumable tungsten electrode. According to the authors, a potential advantage of UC-WAAM was that the layers can be deposited on a non-conductive material, which can allow for the production of overhang structures without any support; this advantage can be useful when manufacturing complex structures. Pizano et al. [5] applied HIP and heat treatment to Ni-based superalloy (HAYNES 282) parts manufactured by WAAM. HIP was found to reduce the porosity level to about 1%, facilitated the tailoring of the microstructure and improved the mechanical properties of the WAAM parts. Mclean et al. [6] used HIP to close pores and reduce the pore size in Al 2319 parts manufactured by WAAM. Experimentally, the volume of pores is reduced but the resulting pressure inside the pores is strongly increased after HIP. They further applied post-HIP heat treatment at atmospheric pressure, and showed that the overall porosity after post-HIP heat treatment is reduced by 95% in comparison with the initial porosity level in as-built specimens. Shiyas et al. [7] presented a review on the post-processing techniques of additively manufactured metal parts, intended to improve the surface finish, fatigue lifetime, and mechanical properties. Similarly, Motallebi et al. [8] performed a review on the post-processing heat treatment methods of lightweight magnesium fabricated by additive manufacturing. HIP may be useful to close pores especially in LPBF parts; in particular, HIP allowed a decrease in the pore level, from 3.4% in an as-built specimen to 0.7% after HIP treatment. However, depending on the application, other sintering processes can be interesting. For example, Teixera et al. [9] used two distinct sintering methods, and showed that microwave sintering was a good alternative to conventional sintering, to manufacture NiTi samples with controlled porosity level and pore sizes. In their study, microwave sintering was considered as very promising as it allowed for the formation of interesting intermetallic phases and homogeneous pores in a very short time. Hence, HIP is useful to improve the properties of AM parts [5–8], especially when pores must be closed. However, in the case of AISI 316L, the quasi-absence of porosity is achieved in the parts manufactured by WAAM. Gurcik and Kovanda [10] used a FANUC robot with offline programming to generate their trajectories. They illustrated the problem of trajectory defaults, as well as those of defects caused by the variation in the wire feeding speed. However, they finally manufactured quite simple parts (cylinders with a height of almost 60 mm) that could have been efficiently produced with a few lines of robot commands defining a circle by just three vertices, and including a repeating loop. Schmitz et al. [11] used multidirectional WAAM additive manufacturing (i.e., the possibility of building up layers in all directions) without providing concrete examples of part manufacturing. He et al. [12] recently discussed the architecture of an open-source software dedicated to the printing of parts by WAAM. They provided some details and showed a few parts manufactured with the suggested software/method, among which were several axisymmetric parts. Their robotic cell included two Yaskawa robots and a positioner. Baccomo et al. [13] suggested a method to analyze the influence of the kinematic of the robot on the WAAM process. They printed a sort of "tulip" part, observed some defects such as variation in the wall thickness, and suggested a method to investigate/explain the reasons of these defects.

In the present work, special interest was taken in the case of shell-type parts, for which concrete applications are more particularly expected, such as the manufacture of complex shape capsules for the hot isostatic pressing (HIP) of powder. Concerning this specific topic, Riehm et al. [14,15] combined additive manufacturing (LBPF) and hot isostatic pressing (HIP) to manufacture near net-shape composite components. In their study, LPBF was used to print the capsule, which was then filled with powder, and HIP was then applied to provide a dense solid part. In their study, they anticipated the distortion and shrinkage of the capsule due to HIP, and compensated by optimizing the capsule

https://doi.org/10.3390/app16010179

shape based on finite element modeling of the HIP process. Bieske et al. [16] developed (or used) a two-step manufacturing process of titanium–aluminide (TiAl) parts, which consisted of filling a gastight non-porous capsule with powder, with the whole being obtained by Electron Beam Powder Bed Fusion (EB-PBF). The produced parts were then treated by HIP to eliminate the pore content and provide dense parts. In the same vein, Farkoush et al. [17] also manufactured titanium–aluminide (TiAl) capsule specimens by EB-PBF. In their manufacturing process, the parts are initially composed of a porous core made of powder treated with low energy parameters, whereas the porous core is coated by a gastight 3 mm thick dense wall treated with higher energy parameters. Low energy parameters facilitate the avoidance of Al losses, which are detrimental to mechanical properties. HIP was then applied to obtain a full dense part, with a nearly 100% relative density. According to their results, after HIP, the parts manufactured with low energy parameters in the core exhibited much lower pore contents than the parts that contained non-treated powder in the core. Finally, their process allowed them to manufacture dense parts without any change in the Al content.

In the present work, the question of path planning in WAAM is discussed, as well as interfacing with the CAD of the part to print. In particular, the intersection between triangular faces described in an STL file, with a horizontal plane, results in a polygonal cross-section of the component along this plane. Depending on the part complexity, the result may either be a single polygonal line or multiple polygons separated from each other or imbricated one in the other (in the case of a hollow part). For a multidirectional slicing strategy, some parts of the geometry may be sliced in one direction, whereas some other parts are scanned in a different direction. Among the works cited by Schmitz et al., one can mention that of Ding et al. [18], which addressed the slicing of STL models for WAAM purposes. They showed a typical sequence of instructions in ASCII STL files created by software products such as CREO or FreeCAD. In their work, they subdivided the geometry into multiple volumes to allow them to apply different slicing directions depending on the considered subpart. In another article [19], Schmitz et al. used their method to print a simple elliptical half shell. Concerning welding, Fang et al. [20] used CAD data to define the path of the weld in the case of Y-type intersection of ducts. Venturini et al. [21] discussed the strategy for the manufacture of T-crossing features. Knezovic et al. showed several parts concerned with this strategy [22]. However, one can notice that the geometrical complexity is moderate for this type of part, since all deposited layers show the same shape, so that a loop can be used with a progressive upgrade/increase in the Z coordinate. The strategy consists of selecting the most adapted sequence of the alternating path. Ali et al. [23] studied the effect of different paths when manufacturing a flat part from juxtaposed welds. They showed that the resulting Von Mises stress and displacement fields differ depending on the selected scanning trajectories. Reisgen et al. [24] tested different cooling methods and showed their influence on the $t_{8/5}$ time (i.e., the time it takes for the weld seam to cool from 800 °C down to 500 °C). The results were then correlated to the Vickers hardness. Finally, Rodrigues et al. [25] established the status and perspectives of WAAM in terms of processes (variants and declinations), in situ cooling, substrates' preheating strategies, material types, deposition strategy, residual stresses, post heat treatments, and, of course, applications. It is worth mentioning that many studies presently draw about WAAM. For example, the WAAM topic in web of science regroups more than 3000 references, more than 300 per year from 2022, and more than 600 in 2024. For this reason, not all of them can be cited.

The aims of the first part of the present study may be summarized as follows:

- Development of a slicer that can provide directly the robot program (sequence of instructions) in KRL format (case of KUKA robots) from the CAD design of the part to be printed;

https://doi.org/10.3390/app16010179

- Ilustration of the capabilities of the developed program (slicer/robot trajectories) through presentation of two examples, including the corresponding printed parts.

The next steps will be focused on the mechanical properties of flat samples cut in straight WAAM walls, and using a gastight cylindrical capsule filled of powder to obtain a dense solid part after HIP (the voids between the powder grains are closed during HIP treatment).

2. Materials and Methods

2.1. Slicing Software Development

As preliminary part of the work, an in-house offline programming (OLP) tool was first developed to generate automatically the command files of the robot/welder system from the CAD file of the part to print. Once this part has been designed and converted into STL format, the in-house slicer tool allows the automatic generation of the successive vertices defining the part contours and the corresponding robot trajectories. The automatic generation of the robot program is then performed including displacement instructions written in KRL (KUKA Robot Language), as well as commands related to starts and stops of the welding device. The different steps in the offline programming pre-treatment process are first described. Up to now, the case of shell-type parts has been considered, since they present several applications, especially in terms of the objective of parts' weight reduction and the manufacture of powder containers for the HIP process. The objective of the present part of the work was thus to show the different steps of the OLP software (i.e., STL file, slicer, trajectories, and robot/welding device command files). The present solution is certainly very similar to that developed by Schmitz et al. between 2020 and 2021 [11,19]. The first step concerned the choice of CAD package used to import or draw the part. In this work, free and open-source software was used, and FreeCAD [26] was selected. It allows the use of solid modeling, functional modeling, and surface modeling. In addition, it allowed us to export the designed parts in ASCII STL files, which were quite easy to read with any programming language, such as C.

Figure 1 shows a typical list of definition instructions within an ASCII STL file. All triangular faces are defined individually from the Cartesian coordinates of three vertices. It is thus easy to read such a file and to define the three edges connecting the vertices. In principle, only one other face is connected to each edge (i.e., only two faces share a common edge). It is also easy to calculate the coordinates of the two vertices defining the intersection with a horizontal plane (if it exists). Finally, the intersection of a horizontal plane with a solid defined in a STL file consists of connected edges forming at least one closed polygon (and possibly several ones).

```
facet normal 0.000000 0.000000 -1.000000
  outer loop
    vertex 25.520000 -0.000000 -0.000000
    vertex -20.645252 15.000000 -0.000000
    vertex 7.886443 24.270510 0.000000
  endloop
endfacet
facet normal -0.000000 -0.000000 -1.000000
  outer loop
    vertex -20.645252 -15.000000 0.000000
    vertex -20.645252 15.000000 -0.000000
    vertex 25.520000 -0.000000 -0.000000
  endloop
endfacet
```

Figure 1. Typical list of definition instructions within an ASCII STL file.

https://doi.org/10.3390/app16010179

It is thus possible to define the different polygons corresponding to the intersection of solids defined in the STL file, with a series of slices (for example, a series of Z altitudes). Finally, it is the role of the slicer to do this work, and to provide the different polygons through a series of successive vertices. In a second step, it is possible to convert the series of vertices into a series of KRL instructions [27] defining the contour of the part and the robot trajectories (in the case of a KUKA robot). In addition, it is possible to add instructions for arc ignition (start of a polygon) and arc extinction (end of a polygon). The connection between two successive polygons may be defined by an additional straight line, and the corresponding displacement instruction may be added; during this connection, the arc of the welder is off. In the present state of development, the proposed technique is thus able to print the contours of the part designed with the CAD software package, which is perfectly suitable for the rapid manufacturing of powder containers (capsules) for the hot isostatic pressing (HIP) of powder. A new HIP facility was just installed in Le Creusot in 2025, with a maximum heating temperature of 1400 °C and a maximum isostatic pressure of 200 MPa. This machine, financed in the frame of EQUIPEX+ ANR-21-ESRE-0039, will allow for the manufacture of parts with a diameter as large as 0.420 m and a height of 1 m, which corresponds to an intermediate scale for the nuclear industry.

The different preprocessing steps to derive the robot program in KRL format (in the case of a Kuka robot) from the CAD design of the part are summarized in a flowchart (Figure 2). The FreeCAD software is used to provide an ASCII STL file of the considered part. The in-house tool provides slices that can be viewed with SCILAB software. In the second step, the in-house tool generates the robot program from edges defined by slicing. This robot program also contains commands to stop and start the welding process managed by the FRONIUS device.

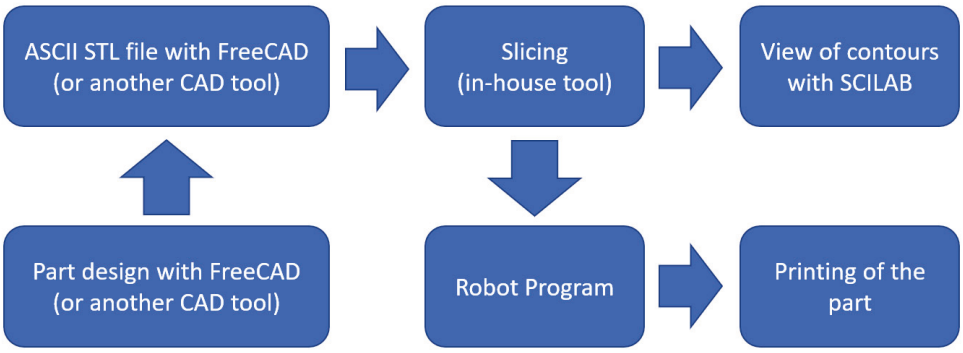

Figure 2. Flowchart of the successive steps, including the use of free software products.

2.2. WAAM Cell and Deposition Parameters

The test/printing rig used for the experiments was composed of a six-axis KUKA KR6 robot carrying a CMT welding torch associated with a CMT ADVANCED source from FRONIUS, within an open cell (roof), and equipped with gas/vapor extraction devices. Figure 3 shows the KR6 robot (left) and the FRONIUS source with the wire dispenser on its top (right). The parts were printed on a one-meter-high steel table, where the ground connector clamp of the welding source was fixed. All parts were manufactured with AISI 316L stainless steel (on thick supporting plates made of 316L too). The filler wire had a diameter of 0.8 mm.



Figure 3. Photographs of the six-axis KUKA KR6 robot (controller KR C2) carrying the CMT torch (**left**), and of the CMT ADVANCED FRONIUS source, with the root of the new KUKA KR8 robot (controller KR C5) (used from February 2023) (**right**).

The retained deposition parameters are listed in Table 1.

Table 1. Deposition parameters.

Material (wire)	AISI 316 L
Wire diameter (mm)	0.8
Wire feed rate (m/min)	12.5
Average current intensity * (A)	128
Average voltage * (V)	16
Welding gas	Argon
Welding mode	CMT
Welding speed (m/s)-(m/min)	0.0125–0.75

* Average values when using the default synergy curve for stainless steel 316L for the present conditions.

2.3. Characterization Techniques

2.3.1. Ferrite Content Analysis

A ferrite meter (MF300F-P10 model from SOFRANEL) was used to estimate the ferrite contents in the WAAM parts. All the measurements were taken after machining, and especially after the preparation of the tensile specimens.

2.3.2. Mechanical Testing

The tensile specimens were manufactured in straight WAAM walls. The milling of the wall faces was performed first, and wire electric discharge machining (EDM) was then used to cut the specimens. The total length of each specimen was 120 mm, whereas their useful length was 60 mm, which allowed an extensometer to be placed. Tensile tests were performed with an MTS machine.

2.4. Hot Isostatic Pressing of Powder with a WAAM Capsule

The HIP of powder with the WAAM capsule was performed with a QIH 15L press from QUINTUS. This HIP press integrates an intermediate-sized chamber (186 mm in diameter and 500 mm in height), and may reach a maximal temperature level of 2000 °C and a pressure of 200 MPa. From 2025, a new HIP facility (QUINTUS QIH 60-URC2) has been available. This new device was purchased in the frame of the CALHIPSO

EQUIPEX+ program ANR-21-ESRE-0039 and integrates a larger chamber (1 m in height and 420 mm in diameter).

The HIP sintering operations comprised the following steps:

- Filling the AISI 316L capsule with AISI 316L powder on a vibrating plate;
- Positioning a filter (to avoid suction of the powder);
- Vacuum draw, and heating at 300 °C;
- Pinching the filling tube, and welding;
- HIP sintering with the following parameters:
    - Two cycles of vacuum draw/argon filling of the chamber.
    - Pressurization at 10 MPa.
    - Heating up to 1200 °C, 102 MPa, with two speeds (10 °C/min, and then 5).
    - 4h sintering at 1200 °C/102 MPa.
    - Natural cooling, and decompression from 150 °C.

3. Results and Discussions

3.1. Slicing Results and Typical Structure of the Robot Programs

Figure 4 shows a concrete example for the case of a simple part composed of a brick, a cylinder, and a conical part. The STL mesh generated by FreeCAD is shown on the left, and the corresponding slices are shown on the right (plot of the successive lines with SCILAB [28], including connecting lines between successive slices). Even if all slice contours look like circles in the top part, these circles are made of straight edges, forming closed polygons. In the present case, the different slices are formed by a little more than 2200 straight edges.

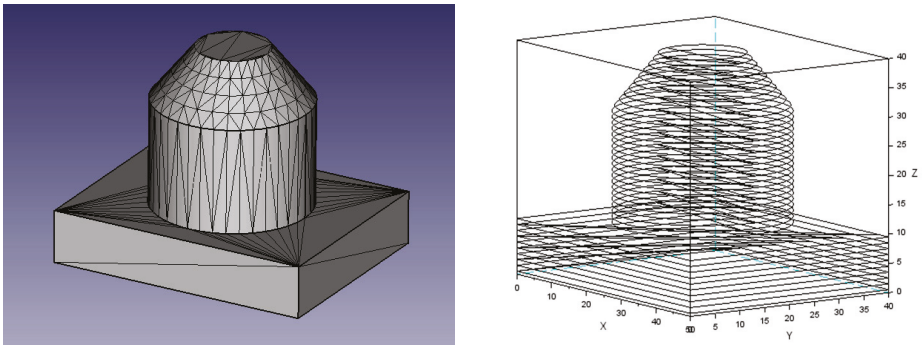

Figure 4. Simple CAD part viewed in FreeCAD (**left**) and corresponding slices viewed with SCILAB (**right**), including connecting lines, allowing us to start the next layer on the opposite side of the part.

Figure 5 shows a typical sequence of instructions in a KRL src file (in the case of a KUKA robot) automatically generated by the OLP tool. The part that is shown is just between two successive polygons. First, each displacement between successive points of a polygon is achieved with a LIN command that displaces the TCP (Tool Center Point) linearly from the current position to the specified point. In the example, POSREF represents a reference position, corresponding to the origin position of the part in the CAD model, which will be located on the welding table. In addition, the C_DIS option of LIN commands avoids stops at each intermediate point (with subsequent slowdown), and permits the continuous displacing with the specified speed. When the contour of a polygon is finished, the arc is switched off and the welder displacement is stopped at the last point during a time lapse of a few seconds (during which the gas of the welding device contributes to cooling down the part). Then, the welder moves linearly from the current position to the first point of the next polygon, the arc is then ignited again, and the welder moves linearly to successive points of the next polygon. Finally, the suppression of short edges along

https://doi.org/10.3390/app16010179

the polygons is not required but may just allow for a decreasing number of points and size of files. One may remark that the three angles defining the tool orientation at each point are kept unchanged, meaning that the welding device remains vertically aligned; this choice allows for the avoidance of strong accelerations where the skeleton of the part shows directional changes. However, it is desired (in the near future) to follow the wall's orientation for some types of parts, and especially for parts presenting smooth variations in the curvature without any abrupt directional changes.

```
LIN POSREF:{X -10.247248,Y -35.087479,Z 5.319844, A 90.0,B 0.0,C 135.0} C_DIS
LIN POSREF:{X -40.450851,Y -13.143278,Z 5.319844, A 90.0,B 0.0,C 135.0} C_DIS
LIN POSREF:{X -36.536751,Y -1.096916,Z 5.319844, A 90.0,B 0.0,C 135.0} C_DIS
LIN POSREF:{X -25.000000,Y 34.409550,Z 5.319844, A 90.0,B 0.0,C 135.0} C_DIS
PRE_ARC_OFF_MSD(AMDWW1)
ARC_OFF_MSD()
WAIT SEC TPOSTGAS
;ENDFOLD SPLINE S3

; FOLD SPLINE S4
$BWDSTART = FALSE
LDAT_ACT=LCPDAT1
FDAT_ACT=FP1
BAS(#CP_PARAMS,VSOUD)
LIN POSREF:{X 40.450851,Y -13.143278,Z 6.835469, A 90.0,B 0.0,C 135.0}
PRE_ARC_ON_MSD(AMDSS,#UNSYNC_ARC)
ARC_ON_MSD(AMDSS)
WAIT SEC TWAIT1
LIN POSREF:{X 30.029228,Y 18.931175,Z 6.835469, A 90.0,B 0.0,C 135.0} C_DIS
LIN POSREF:{X 25.000000,Y 34.409550,Z 6.835469, A 90.0,B 0.0,C 135.0} C_DIS
LIN POSREF:{X -8.725075,Y 34.409550,Z 6.835469, A 90.0,B 0.0,C 135.0} C_DIS
LIN POSREF:{X -25.000000,Y 34.409550,Z 6.835469, A 90.0,B 0.0,C 135.0} C_DIS
```

Figure 5. Typical sequence of instructions in a KRL src file automatically generated from successive slices (i.e., polygons such as those shown in Figure 2), and including arc ignition/extinction commands, as well as waiting instructions.

Figure 6 shows the design of two parts manufactured with the slicer method. The first one (Figure 6a) consists of a part with a regular pentagon basis (5 $\times$ 50 mm edges at the bottom; 5 $\times$ 108° between five successive edges). The total height of the part is 97 mm: the bottom part is 21 mm + 2 $\times$ 38 mm in the upper part. In addition, the dimension of the five edges at the largest section is 63.5 mm. The left picture (Figure 6a) shows the simplest STL file that can be generated in the present case: each quadrangle is split in two triangles, whereas the bottom and top pentagons are split with three triangles, resulting in a total number of 36 triangular faces (i.e., 15 $\times$ 2 + 2 $\times$ 3). The slicing of this part with horizontal planes results in a series of polygons composed of ten edges, with one intermediate vertex along each straight edge of the pentagon (Figure 6b). The second part (Figure 6c) consists of a double square to circular transition part (i.e., square to circular transition, followed by a circular to square transition). The dimensions of the bottom and top square sections are 80 $\times$ 80 mm, whereas the diameter of the circular part at mid height is 60 mm. The total height of the part is 150 mm. This part is thus much more complex, including nonplanar curved surfaces. The resulting robot trajectories (Figure 6d) include connecting edges between successive slices: these edges are used to alternate the successive positions of the starting point for each weld bead. The resulting number of vertices, edges, and displacement instructions in the robot file is as high as 7155 for this example.

https://doi.org/10.3390/app16010179

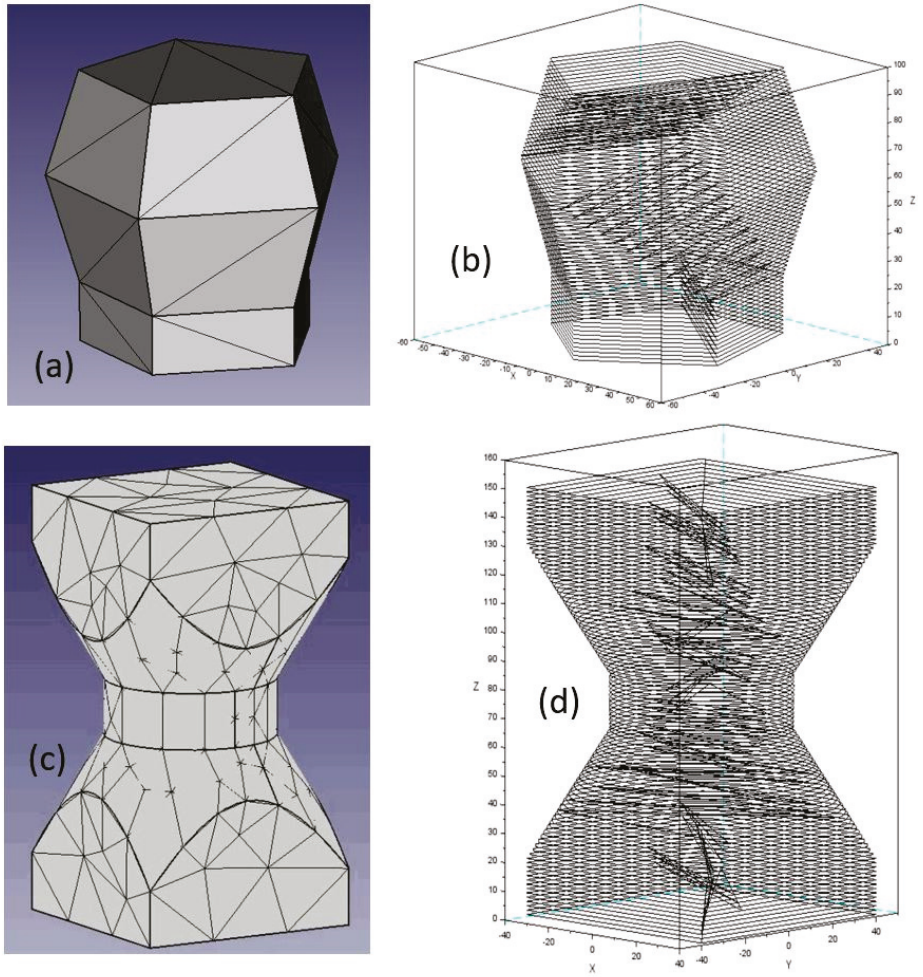

Figure 6. Design of parts manufactured by WAAM (**a**,**c**), and corresponding robot trajectories provided by the slicer software (**b**,**d**).

Direct in situ coding of the robot program required to print these two parts would be complex for the top one (Figure 6a,b), and almost impossible for the bottom one (Figure 6c,d). In contrast, the OLP tool generates the corresponding list of instructions in less than one second, once the STL file is produced. With that tool, there are only few parameters to adjust, such as the height of slicing (Z distance between successive slices). In addition, the another advantage relates to the reliability of the process: the generated list of instructions is always free of bugs once the program has been tested and validated. Once back on the real robot cell, only the POSREF position must be defined by the in situ learning of the printing position on the welding table. The corresponding robot trajectories (Figure 6b,d) are herein viewed with SCILAB software and include the connecting lines between successive slices (starting at the opposite side for two successive slices). The starting point of each slice is always one of the vertices along the trajectory (i.e., one of the ten vertices defining each pentagon for the first part, or more for the second one). For the first part, it may thus either be one of the pentagon corners, or the single intermediate point on each straight edge of the pentagon. These points are thus often aligned or regularly staggered. To avoid this, a simple strategy can be implemented, consisting of increasing the number of triangles in the STL file; for example, by forcing a maximum edge length of 10 or 20 mm for triangles. By doing so, the more points there are along a slice/contour, the lower the probability that the starting point (where the arc ignition takes place) will be regularly aligned regarding the previous layers.

https://doi.org/10.3390/app16010179

3.2. Wire Arc Additive Manufacuring of Capsules

The deposition parameters shown in Table 1 were used to print these parts. When neglecting material losses, the expected value of the cross-section of individual weld beads may be estimated from the following:

$$S_{weld} = S_{wire}\frac{V_{wire}}{V_{weld}} = \frac{\pi 0.8^2}{4}\frac{12.5}{0.75} = 8.4\ \text{mm}^2$$

Considering an average wall width of 6 mm, the expected height of each weld bead is thus 1.4 mm. Experimentally, this value was effectively observed when applying a short waiting time between successive welds/layers. Specifically, the part temperature remains high during the deposition process, and the beads are large. When a higher waiting time was applied (typically 10 s or more), the part cooling was increased, and the average height of each deposited bead was about 1.5 mm, corresponding to the retained slicing distance. This value is not so different from the expected one, and the weak difference is certainly related to a small overestimation of the average thickness of the wall, which has dips and bumps.

3.2.1. Printing of Complex Shape Capsules with the Slicing Method

The printing of the two parts of Figure 6 was thus considered with the parameter set of Table 1. The objective was to show the feasibility of the automated manufacturing process.

The first part is shown at different steps during the WAAM printing process (Figure 7). The part was manufactured by applying an alternative direction strategy:

- The starting point of a polygon at the opposite side to the previous one;
- The inversion of the rotation direction for each layer.

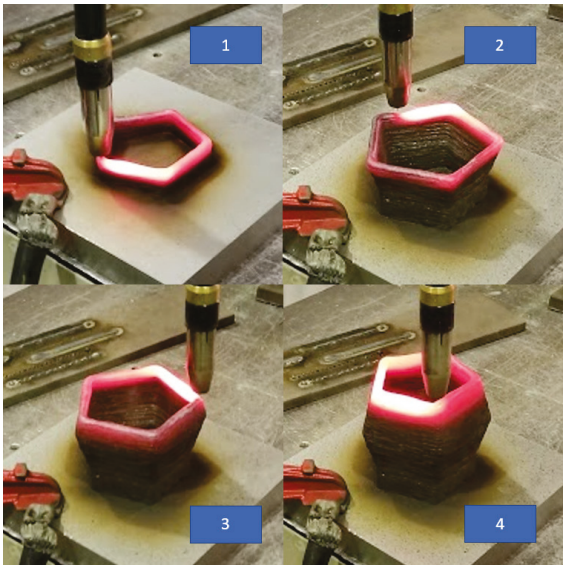

Figure 7. View of the part at four different steps during the manufacturing process (1–3 clockwise rotating direction; 2–4 counterclockwise direction).

Specifically, the weld gun turned clockwise for subfigures 1 and 3 of Figure 7 (left), and in the counterclockwise direction for subfigures 2 and 4 (right).

The corresponding printed parts are shown on Figure 8. The part of Figure 8b was brushed more efficiently. Depending on the application, only functional faces could be machined at this step, whereas some other faces could remain as raw. If all surfaces must be machined, the existing CAD file of the part could be used to perform the corresponding machining using a CNC machining center. The potential applications of this technology

are numerous. One of them relates to the rapid fabrication of complex shape capsules for the hot isostatic pressing technology of powder. Consequently, the hollow WAAM part could be closed with a plate (for this example), and then filled with powder to provide a solid part after HIP.

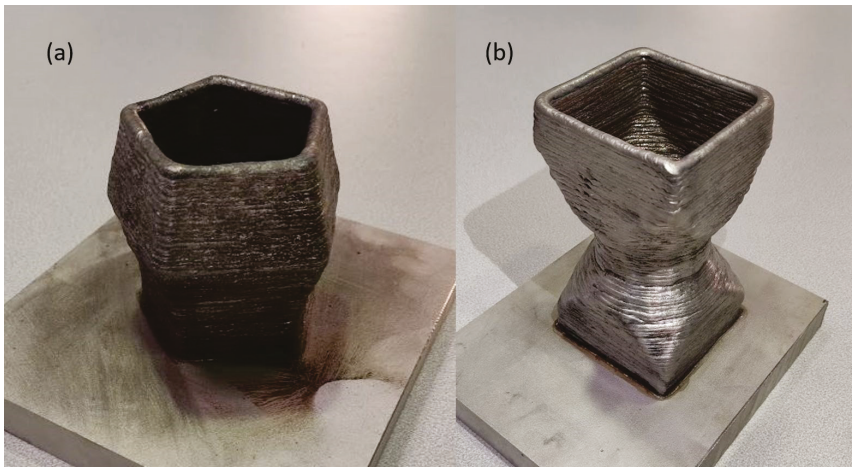

Figure 8. Wire Arc Additive Manufacturing parts corresponding to (**a**) CAD and robot trajectories of Figure 6a, (**b**) CAD and robot trajectories of Figure 6c, and printed with the parameter set of Table 1.

Up to now, one of the remaining challenges has concerned the accuracy of the thickness of each layer, in relation to initial expectations. For the first case exposed, the total height of the first printed part was slightly lower in comparison with that which was initially expected (i.e., about 95 mm instead of 97 mm in the CAD model). A lengthening of the waiting time between layers allowed us to correct this small mismatch in a second step (i.e., second printing of the same part). However, it would be preferable to avoid iterative printing. One idea to meet this challenge consists of the implementation of an online control system for the deposited thickness of each layer, or at least an online control system for the parts' height during the deposition process, not necessary at each layer. Specifically, the robot program could be slightly modified, in order to allow repeating several times a layer if required (i.e., if the part height after a given layer is lower than the expected one). Another subsequent default correlated to the same reason is the progressive increase in the stick-out (i.e., the distance between the contact tip and the part) if the deposited thickness becomes lower than the expected one; this drawback would also be offset by the online control of the part height. However, some other complementary experiments showed that the thickness of the deposited weld bead is dependent on the sublayer material's temperature (i.e., the bead thickness decreases somewhat if the sublayer temperature is too high). The first step before any control of the part height is thus the in situ control of the part temperature; the idea could thus be to automatically adjust the waiting time between the manufacture of successive weld beads in order keep the part temperature unchanged during the whole manufacturing process.

3.2.2. Printing of Simple Cylindrical Capsules with Direct Programming (No Slicing)

A different printing strategy was considered while printing capsules such as like-cylinder ones. For printing the solid bottom, the best results were obtained by superposing several layers formed by a spiral-type robot path (Figure 9a). This may be achieved by programming a parametric function of the following type:

$$x(t) = A\ t\cos(t)$$

$$y(t) = A\ t\ sin(t)$$

in which the value of A must be calculated to provide an accurate distance between juxtaposed beads, and parameter t ranges between 0 (or a higher value) and $2\pi\ n$, in which n is the required number of rounds depending on the diameter of the part/cylinder. When printing the cylindrical part, the starting point of each cylindrical layer/bead must be shifted to avoid the superposition of defaults. In the present case, the corresponding predefined shift angles were set in an array. For printing the half-spherical top, a progressive slicing refinement must be implemented, such as is illustrated in Figure 9b. Finally, the resulting capsule is shown in Figure 9c.

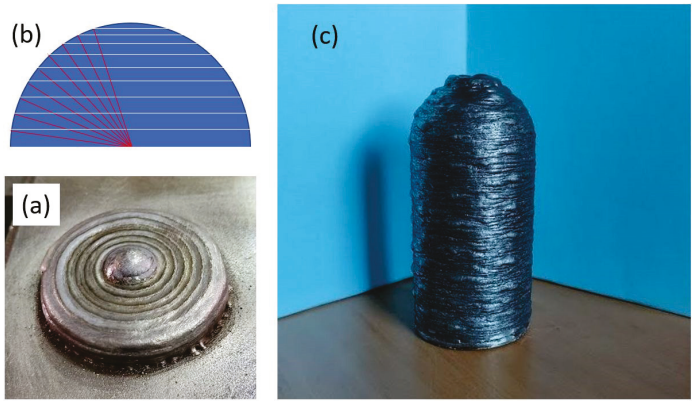

Figure 9. Printing of the bottom with a spiral path (**a**), the strategy of slicing refinement for printing the half-sphere dome (**b**), and the resulting cylindrical capsule for HIP testing (**c**).

3.3. Characterization of Materials' Properties

3.3.1. Microstructure and Ferrite Content of WAAM Samples

Simple experiments showed that the printed parts (Figure 8) are weakly magnetic, which confirmed that the superposed welds are not composed exclusively of austenitic γ-phase.

Specifically, the δ-ferrite phase can form at high temperatures and probably appeared during the manufacturing process. This phase may decrease the risk of hot cracking if its content is lower than 8%. However, it can be detrimental to corrosion resistance if its content becomes higher than 10%. According to the Schaeffler diagram [29], the ferrite content of AISI 316L steel after solidification and cooling should be about 5%. The typical microstructure of the AISI 316L samples manufactured by WAAM with the parameters provided in Table 1 is shown in Figure 10.

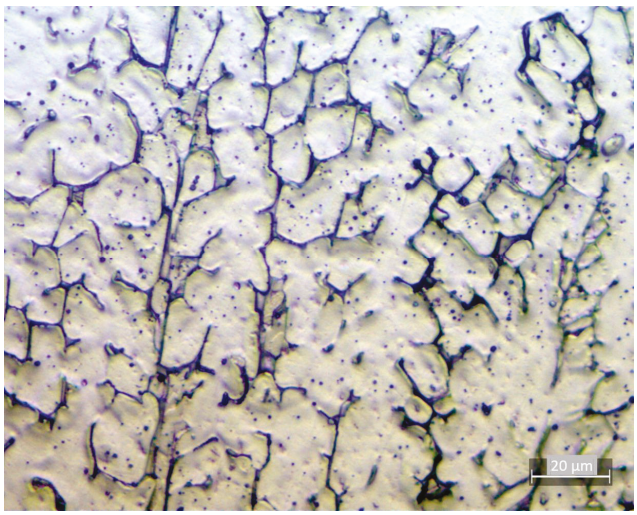

Figure 10. Typical microstructure of an AISI 316L part manufactured by WAAM.

The main phase is the austenitic γ-phase. However, a skeleton composed of δ-ferrite is also clearly observed. The ferrite content was measured in the range 5–7%, and varies only slightly with the position (i.e., top or bottom of a part).

3.3.2. Mechanical Properties of WAAM Parts

Once the printing method has been described and validated, showing the potential of the WAAM technology for the manufacture of complex shape hollow parts, the mechanical properties of materials manufactured with this method were evaluated. Straight walls were first manufactured (Figure 11a) with the objective of evaluating the mechanical properties in both the longitudinal/horizontal and transverse/vertical directions. These walls were then machined (milling of faces first), and the tensile specimens were then cut by wire electric discharge machining. The corresponding specimens after tensile tests are shown in Figure 11b. The Ultimate Tensile Strength (UTS) was measured at 540 MPa for samples manufactured along the horizontal direction (Figure 12 left), and 585 MPa for samples manufactured along the vertical direction (Figure 12 right). In addition, the maximum engineering strain was 40% for the horizontal samples (Figure 11b, bottom), and 34% for the vertical ones (Figure 11b, top). In all cases, ductile behavior was observed. The true stress curves are also reported on the figures, as well as different-type fitting curves: the true stress–strain curves take the striction of the specimens into account. If $\sigma_e = F/S_0$ stands for the engineering stress and σ_t for the true stress, then $\sigma_t = (1+e)\sigma_e$ and $\varepsilon_t = \ln(1+e)$, in which $e = \Delta l/l_0$. The true stress/strain curves were used to derive some constitutive behavior law of the as-deposited material assuming two different models:

- A bilinear model with a Yield stress, and tangent modulus;
- The Hollomon law, commonly used to predict the strain hardening behavior.

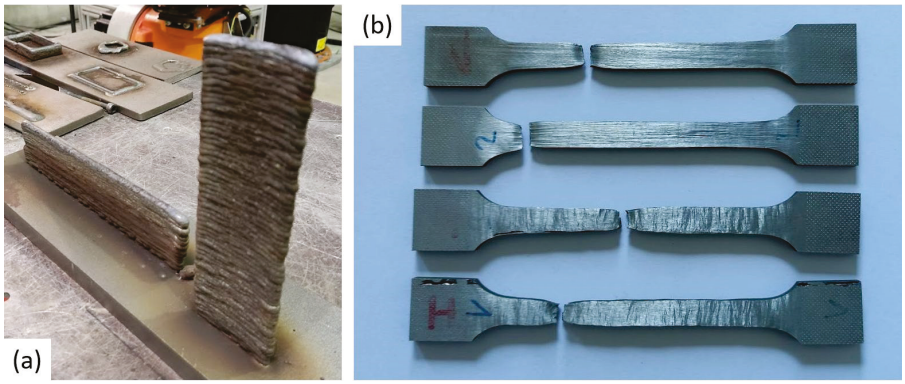

Figure 11. (**a**) Straight walls manufactured by WAAM to cut tensile specimen in the horizontal and vertical directions, and (**b**) corresponding samples after tensile tests (top; two vertical specimens/bottom and two horizontal specimens).

According to the results, the as-built WAAM material was found to be slightly anisotropic. Specifically, the tangent modulus derived for the horizontal direction is 1.5 GPa (i.e., slope of 1496 MPa as derived from the corresponding linear interpolation curve plotted in Figure 12, left) considering a strain range of [0.01…0.25], whereas the tangent modulus is about 1.7 GPa for the vertical direction. In addition, since the elastic curve is almost vertical in this type of graph, the value of 332 MPa reported for the ordinate origin in the linear interpolation (H direction) may be considered as the Yield stress (334 MPa considering the intersection point of the elastic and plastic curves, assuming $E = 200$ GPa for the elastic domain). Again, the ordinate origin is somewhat higher for the vertical direction (365 MPa against 332), corresponding to a Yield stress of 368 MPa.

https://doi.org/10.3390/app16010179

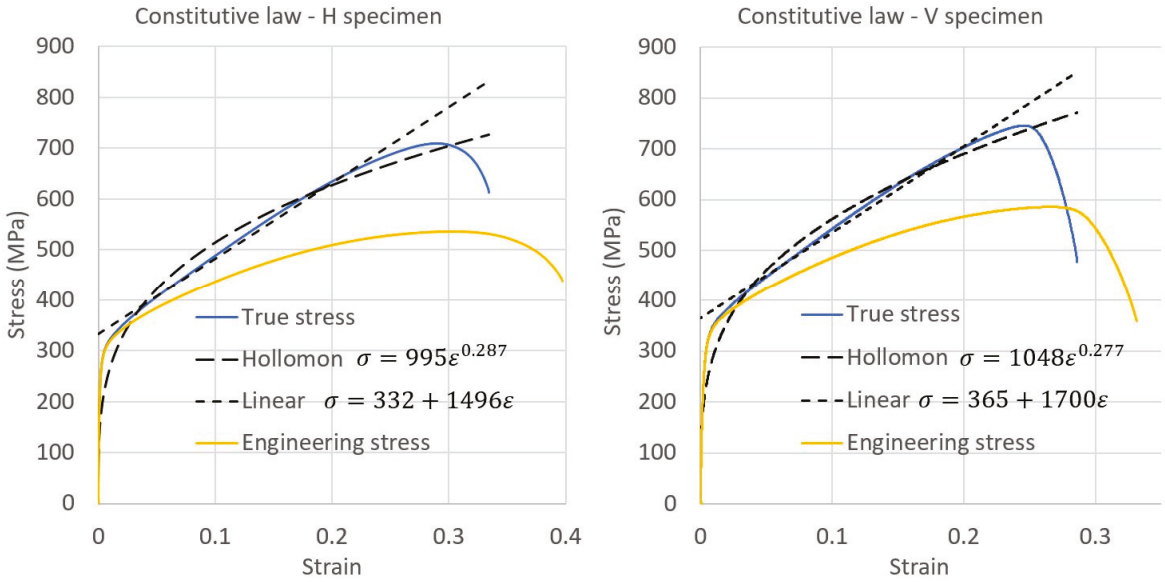

Figure 12. Tensile tests' loading curves in both horizontal (**left**) and vertical (**right**) directions, and engineering stress (orange color), and true stress (blue color), with the corresponding Hollomon and bilinear fitting curves.

Considering a Young modulus of 200 GPa, the ratio E_t/E is thus about 0.75% for the horizontal direction, and 0.85% for the vertical direction.

Concerning the Hollomon law (power law), the best fit was obtained with $\sigma = 995\varepsilon^{0.287}$ (strain range [0.05...0.3]) for the horizontal direction, and $\sigma = 1048\varepsilon^{0.277}$ (strain range [0.05...0.24]) for the vertical one.

Table 2 summarizes the main mechanical properties measured from the tensile tests. The higher UTS (and Yield stress) for the vertical direction attests for the perfect metallurgical continuity and subsequent excellent cohesion between successive layers/beads. A possible explanation is that the grains are more elongated in the vertical direction, which is the preferred cooling and solidification direction, and thus the preferred orientation of grains. For this reason, the number of grain boundaries along the specimen length could be higher for the horizontal direction, giving rise to a higher maximum strain and lower UTS. As observed in Figure 11b, bottom, the horizontal specimens show streaks across the vertical direction after the tensile tests.

Table 2. Summary of mechanical properties measured for both the horizontal and vertical directions/samples.

			Bilinear Law		**Hollomon Law**	
Orientation	**UTS (MPa)**	**Max Strain (%)**	**Ys (MPa)**	***Et* (GPa)**	**σ_0 (MPa)**	***n***
H direction	540	40	334	1.5	995	0.287
V direction	585	34	368	1.7	1048	0.277

In all cases, the results derived for the two different behavior laws will be useful to simulate the deposition/welding process with an FEM package.

3.4. HIP of Powder with a Capsule Manufacured by WAAM

First, experiments validating the new hybrid WAAM/HIP manufacturing process for the prototyping of a solid part from a hollow WAAM capsule were performed. The case of a cylindrical part was considered for these first experiments. A two-step process was used to manufacture the WAAM cylinder, printing a flat bottom first, and printing the cylinder just

after. An AISI 316L cover, including a cylindrical tube (for powder filling), was then welded onto the WAAM capsule (Figure 13). The part was then filled with AISI 316L powder (i.e., the same material as the WAAM capsule) on a vibrating plate, to densify the powder. The HIP processing parameters are summarized in Section 2.4. HIP treatment allowed all the voids between the powder grains to be closed, thus providing a solid part with smaller dimensions. A sectioning of the part was then performed after HIP processing, and the surface was then prepared/polished before chemical etching with Kalling reagent was performed, to reveal the granular microstructure. The results showed perfect continuity from the WAAM capsule to the sintered powder, with a finer microstructure in the core of the sample (sintered powder). According to the Hall–Petch relationship, this fineness of grains is favorable to achieve high mechanical properties.

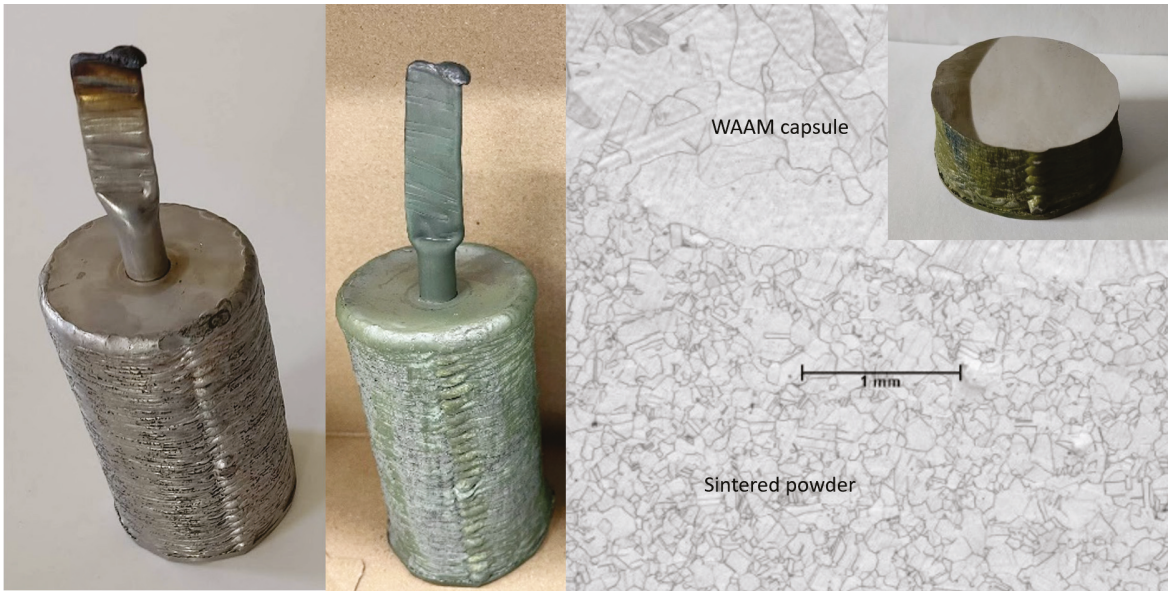

Figure 13. As-built cylindrical capsule manufactured by WAAM, filled with powder, and sealed (**left**); corresponding part after HIP treatment (**middle**); view of the grains after cutting a slice, surface polishing, and chemical etching (**right**); and polished surface of a complete slice (top right corner).

4. Conclusions

The first aim of the present study was to develop a slicer able to provide the printing robot program from the STL file of the CAD part to be printed, and to illustrate the capacities of the corresponding in-house OLP (offline programming) tool, through several examples. The methods that provided directly the list of instructions for the robot program required to manufacture a part by WAAM, from the CAD file of the corresponding part in STL format, were first described. The functionalities of this tool are certainly very similar to those of the tool developed by Schmitz in 2020–2021 [11,19]. Nevertheless, additional information, advice, and examples were provided. The present tool produces very clean files and always applies the same method, which reinforces the robustness and interest of the method. The case of a deposition process managed by a KUKA robot was considered, so that the OLP tool provides a suitable list of instructions in KRL format. Of course, all robot manufacturers have their own input language. However, they often all have the same functionalities, so it is highly probable that one will find corresponding instructions for each robot manufacturer. It is thus highly probable that the present tool could be used to generate programs for several robot manufacturers, including only small changes (i.e., probably only the export function would have to be changed). The case of shell-type parts was considered in the present work, since it already is of particular interest, especially

https://doi.org/10.3390/app16010179

for the printing of large powder containers for the HIP sintering process. The mechanical properties of the samples were evaluated and the exceptional cohesion between successive beads in WAAM parts was confirmed. Finally, a new hybrid WAAM/HIP process was developed, involving using WAAM to manufacture a gastight capsule and applying HIP to provide the corresponding solid part from the capsule filled with powder.

Supplementary Materials: A video of the manufacturing of one layer of the first part is available at https://www.linkedin.com/feed/update/urn:li:activity:7057308642076700672/, accessed on 10 October 2025. This video was recorded using an advanced visualization technology including pulsed lighting with a laser diode from CAVITAR Ltd. (500 W peak power, infrared domain at a wavelength of 810 nm), and using a synchronized Phantom camera from AMETEK. The arc plasma emits only slightly at this range of wavelength so that images are not saturated. One may thus clearly observe the molten pool at the rear of the arc region.

Author Contributions: R.B. and A.M. contributed equally to the development of the automatic robot trajectories generation tool, to the manufacturing of the parts, and to the redaction of the article. H.A. did a post doctorate in the frame of the project, and contributed to the characterization of the HIP part. M.-A.K. joined the team as part of his master's internship, and was in charge of FEM modeling. F.B. was in charge of HIP operations. All authors have read and agreed to the published version of the manuscript.

Funding: This work was supported by the EIPHI Graduate School (Grant number ANR 17-EURE-0002) and Bourgogne-Franche-Comté Region. The HIP facility was funded by ANR EQUIPEX+, grant number ANR-21-ESRE-0039.

Institutional Review Board Statement: Not applicable.

Informed Consent Statement: Not applicable.

Data Availability Statement: The original contributions presented in this study are included in the Supplementary Material. Further inquiries can be directed to the corresponding author.

Conflicts of Interest: The authors declare no conflicts of interest.

Abbreviations

The following abbreviations are used in this manuscript:

WAAM	Wire Arc Additive Manufacturing
HIP	Hot Isostatic Pressing
UTS	Ultimate Tensile Strength
CAD	Computer-Aided Design
SMR	Small Modular Reactor
LPBF	Laser Powder Bed Fusion
EB-PBF	Electron Beam Powder Bed Fusion
CMT	Cold Metal Transfer
SMEs	Small- and Medium-Sized Enterprises
GMAW	Gas Metal Arc Welding
OLP	Offline Programming
STL	Standard Triangle (or Tesselation) Language
KRL	KUKA Robot Language
TCP	Tool Center Point

References

1. Bernard, F.; Château-Cornu, J.-P.; Bolot, R.; Mathieu, A.; Lamesle, P.; Frayssines, P.-É.; Lemarquis, L. Une application thermo-industrielle du futur au Creusot «Métallurgie des Poudres et Compression Isostatique à Chaud»: La plateforme EquipeX+/CALHIPSO. In *Chaleur, Énergie, Thermodynamique, Le Message de Carnot Aujourd'hui… 200 Ans Après*; Ed Éditions Universitaires de Dijon: Dijon Cedex, France, 2025.

2. Horgar, A.; Fostervoll, H.; Nyhus, B.; Ren, X.; Eriksson, M.; Akselsen, O.M. Additive manufacturing using WAAM with AA5183 wire. *J. Mater. Process. Technol.* **2018**, *259*, 68–74. [CrossRef]
3. Fuchs, C.; Baier, D.; Semm, T.; Zaeh, M.F. Determining the machining allowance for WAAM parts. *Prod. Eng.* **2020**, *14*, 629–637. [CrossRef]
4. Rodrigues, T.A.; Duarte, V.R.; Miranda, R.M.; Santos, T.G.; Oliveira, J.P. Ultracold-Wire and arc additive manufacturing (UC-WAAM). *J. Mater. Process. Technol.* **2021**, *296*, 117196. [CrossRef]
5. Pizano, L.F.L.; Sridar, S.; De Vecchis, R.R.; Wang, X.; Biddlecom, J.; Pataky, G.J.; Sudbrack, C.; Xiong, W. Recrystallization behavior and mechanical properties of Haynes 282 fabricated by wire-arc additive manufacturing with post-heat treatment. *J. Manuf. Process.* **2024**, *119*, 781–789. [CrossRef]
6. Mclean, N.; Bermingham, M.J.; Colegrove, P.; Sales, A.; Soro, N.; Ng, C.H.; Dargusch, M.S. Effect of Hot Isostatic Pressing and heat treatments on porosity of Wire Arc Additive Manufactured Al 2319. *J. Mater. Process. Technol.* **2022**, *310*, 117769. [CrossRef]
7. Shiyas, K.A.; Ramanujam, R. A review on post processing techniques of additively manufactured metal parts for improving the material properties. *Mater. Today-Proc.* **2021**, *46*, 1429–1436. [CrossRef]
8. Motallebi, R.; Savaedi, Z.; Mirzadeh, H. Post-processing heat treatment of lightweight magnesium alloys fabricated by additive manufacturing: A review. *J. Mater. Res. Technol.* **2022**, *20*, 1873–1892. [CrossRef]
9. Teixeira, R.D.S.; Oliveira, R.V.D.; Rodrigues, P.F.; Mascarenhas, J.; Neves, F.C.F.P.; Paula, A.D.S. Microwave versus Conventional Sintering of NiTi Alloys Processed by Mechanical Alloying. *Materials* **2022**, *15*, 5506. [CrossRef]
10. Gurčík, T.; Kovanda, K. Waam technology optimized by off-line 3d robot simulation. *Acta Polytech.* **2019**, *59*, 312–321. [CrossRef]
11. Schmitz, M.; Wiartalla, J.; Gelfgren, M.; Mann, S.; Corves, B.; Hüsing, M. A Robot-Centered Path-Planning Algorithm for Multidirectional Additive Manufacturing for WAAM Processes and Pure Object Manipulation. *Appl. Sci.* **2021**, *11*, 5759. [CrossRef]
12. He, H.L.; Lu, C.L.; Ren, J.H.; Dhar, J.; Saunders, G.; Wason, J.; Samuel, J.; Julius, A.; Wen, J.T. Open-source software architecture for multi-robot Wire Arc Additive Manufacturing (WAAM). *Appl. Eng. Sci.* **2025**, *22*, 100204. [CrossRef]
13. Baccomo, A.; Chanal, H.; Duc, E.; Limousin, M. A method for analyzing the kinematic influence of a robot on the WAAM process. *Int. J. Adv. Manuf. Technol.* **2025**, *136*, 4239–4255. [CrossRef]
14. Riehm, S.; Kaletsch, A.; Broeckmann, C.; Friederici, V.; Wieland, S.; Petzoldt, F. Tailor-Made Net-Shape Composite Components by Combining Additive Manufacturing and Hot Isostatic Pressing. In *Hot Isostatic Pressing: Hip'17 (Materials Research Proceedings)*; Materials Research Forum LLC: Millersville, PA, USA, 2019; Volume 10, pp. 203–209.
15. Riehm, S.; Friederici, V.; Wiel, S.; Deng, Y.; Herzog, S.; Kaletsch, A.; Broeckmann, C. Tailor-made functional composite components using additive manufacturing and hot isostatic pressing. *Powder Metall.* **2021**, *64*, 295–307. [CrossRef]
16. Bieske, J.; Franke, M.; Schloffer, M.; Körner, C. Microstructure and properties of TiAl processed via an electron beam powder bed fusion capsule technology. *Intermetallics* **2020**, *126*, 106929. [CrossRef]
17. Farkoush, H.B.; Marchese, G.; Bassini, E.; Aversa, A.; Biamino, S. Microstructure of TiAl Capsules Processed by Electron Beam Powder Bed Fusion Followed by Post-Hot Isostatic Pressing. *Materials* **2023**, *16*, 5510.
18. Ding, D.; Pan, Z.; Cuiuri, D.; Li, H.; Larkin, N.; van Duin, S. Multi-direction slicing of STL models for robotic wire-feed additive manufacturing. In *Solid Freeform Fabrication Symposium*; The University of Texas at Austin: Austin, TX, USA, 2015; pp. 1059–1069.
19. Schmitz, M.; Weidemann, C.; Corves, B.; Hüsing, M. Trajectory Planning Strategy for Multidirectional Wire-Arc Additive Manufacturing. In *ROMANSY 23—Robot Design, Dynamics and Control*; Springer: Berlin/Heidelberg, Germany, 2020; pp. 467–475.
20. Fang, H.C.; Ong, S.K.; Nee, A.Y.C. Robot path planning optimization for welding complex joints. *Int. J. Adv. Manuf. Technol.* **2017**, *90*, 3829–3839. [CrossRef]
21. Venturini, G.; Montevecchi, F.; Scippa, A.; Campatelli, G. Optimization of WAAM Deposition Patterns for T-crossing Features. *Procedia CIRP* **2016**, *55*, 95–100. [CrossRef]
22. Knezovic, N.; Topic, A. Wire and Arc Additive Manufacturing (WAAM)—A New Advance in Manufacturing. *New Technol. Dev. Appl.* **2019**, *42*, 65–71.
23. Ali, M.H.; Han, Y.S. Effect of Phase Transformations on Scanning Strategy in WAAM Fabrication. *Materials* **2021**, *14*, 7871. [CrossRef]
24. Reisgen, U.; Sharma, R.; Mann, S.; Oster, L. Increasing the manufacturing efficiency of WAAM by advanced cooling strategies. *Weld. World* **2020**, *64*, 1409–1416. [CrossRef]
25. Rodrigues, T.A.; Duarte, V.; Miranda, R.M.; Santos, T.G.; Oliveira, J.P. Current Status and Perspectives on Wire and Arc Additive Manufacturing (WAAM). *Materials* **2019**, *12*, 1121. [CrossRef] [PubMed]
26. The FREECAD Team 2023, FREECAD Website. Available online: https://www.freecad.org/ (accessed on 10 October 2025).
27. KUKA Roboter GmbH, KRL Reference Guide Release 4.1. Available online: http://robot.zaab.org/wp-content/uploads/2014/04/KRL-Reference-Guide-v4_1.pdf (accessed on 10 October 2025).

28. Scilab, Dassault Systèmes 2023. Available online: https://www.scilab.org/ (accessed on 10 October 2025).
29. Franco-Rendón, C.M.; León-Henao, H.; Bedoya-Zapata, A.D.; Santa, J.F.; Giraldo, J.E. Failure analysis of fillet welds with premature corrosion in 316L stainless steel slide gates using constitution diagrams. *Rev. UIS Ing.* **2020**, *19*, 141–148. [CrossRef]

Disclaimer/Publisher's Note: The statements, opinions and data contained in all publications are solely those of the individual author(s) and contributor(s) and not of MDPI and/or the editor(s). MDPI and/or the editor(s) disclaim responsibility for any injury to people or property resulting from any ideas, methods, instructions or products referred to in the content.

applied sciences

MDPI

Article

The Effect of Heat Treatment on the Abrasive Wear Resistance of Boron-Alloyed Armor Steel Welded Joints

Martyna Zemlik [1,*], Beata Białobrzeska [1,*], Mateusz Stachowicz [2] and Łukasz Konat [1]

[1] Department of Vehicle Engineering, Faculty of Mechanical Engineering, Wroclaw University of Science and Technology, Wybrzeże Wyspiańskiego 27 Str., 50-370 Wrocław, Poland; lukasz.konat@pwr.edu.pl
[2] Department of Light Elements Engineering, Foundry and Automation, Faculty of Mechanical Engineering, Wrocław University of Science and Technology, Wybrzeże Wyspiańskiego 27 Str., 50-370 Wrocław, Poland; mateusz.stachowicz@pwr.edu.pl
* Correspondence: martyna.zemlik@pwr.edu.pl (M.Z.); beata.bialobrzeska@pwr.edu.pl (B.B.)

Abstract

As a result of welding processes in boron-alloyed martensitic armor steels, unfavorable microstructural changes occur, leading to a significant reduction in the mechanical properties of both the weld metal and the base material. The dendritic structure of the weld metal and the partial tempering in the heat-affected zone contribute to the decreased durability of structural components, thereby deteriorating their performance. This issue is particularly important since such steels are widely used not only in the defense industry but also in the mining, construction, transportation, and metallurgical sectors, where they operate under conditions of intensive abrasive wear. For this reason, the authors attempted to improve the mechanical properties of welded joints of boron-alloyed martensitic armor steel (with a nominal hardness of 500 HBW) through post-weld heat treatment. The welded joint was evaluated based on metallographic examinations using light microscopy and scanning electron microscopy, as well as abrasive wear tests carried out on a T-07 tribotester. The conducted investigations demonstrated that, under loose abrasive conditions (using electrofused alumina), heat treatment increased the wear resistance of the joints by 55% compared to the as-welded condition. The obtained results were compared with selected grades of Hardox steel commonly used in industrial applications.

Keywords: MAG welding; martensitic steel; heat treatment; abrasive wear

1. Introduction

Armor steels represent a key group of engineering materials primarily applied in defense and ballistic protection, as well as in areas where high mechanical strength must be combined with increased resistance to abrasive wear. Their predominantly martensitic microstructure provides high strength while maintaining acceptable ductility. These properties make armor steels attractive not only for military purposes but also for civilian applications, including components of machinery operating under severe abrasive conditions.

One of the key technological challenges associated with the use of armor steels is the ability to produce their welded joints. Although welding enables the fabrication of complex structures, it is accompanied by localized thermal effects that lead to the formation of a heat-affected zone (HAZ) and a weld metal region, both exhibiting properties distinct from those of the base material. In the case of high-strength martensitic steels, to which armored steels belong, this issue becomes particularly critical. Welding of high-strength martensitic

steels invariably results in a reduction in mechanical properties, both within the weld metal and across the extensive HAZ strength properties. For instance, the tensile strength (R_m) of Armox 440T steel is approximately 1250 MPa, while for Armox 500T it reaches about 1400 MPa. Even higher mechanical parameters are reported for Armox 600T, where R_m exceeds 2000 MPa. According to data provided by manufacturers of welding consumables, the maximum achievable strength of commercially available filler metals does not exceed 1000 MPa. This leads to the conclusion that welding martensitic steels—even those with the lowest strength levels—inevitably results in a reduction in tensile strength in the weld metal by nearly 30% compared to the base material. Moreover, as the strength grade of the joined material increases, this difference becomes progressively more pronounced.

Previous research has focused on developing methods to mitigate the adverse effects of welding high-strength martensitic steels. These approaches include optimizing technological parameters, selecting appropriate filler materials, and applying post-weld heat treatment (PWHT). Particular attention has been given to restoring a favorable microstructure within the weld metal and reducing residual stresses, which can significantly enhance the durability of components operating under dynamic loading and abrasive wear conditions. For example, welding trials on Hardox 400 and Hardox 500 steels have shown that a properly selected filler material and welding parameters can yield welded joints with tensile strengths (R_m) of 615 MPa and 663 MPa, respectively—representing approximately 50% and 43% of the base material strength [1]. In the case of Hardox 450 steel, TIG (Tungsten Inert Gas) welding using Filler Rod E 7018 wire and a powder additive enriched with tungsten and cobalt resulted in a maximum tensile strength of 775 MPa [2], whereas submerged arc welding (using flux OK Autrod 13.43 + OK Flux 10.62) produced joints with an R_m value of 677 MPa [3]. Considering the tensile strength of the base material (R_m = 1434 MPa) [4], the mechanical property reduction in the welded region exceeds 50%. Similar observations were reported by Zuo et al. [5], where the tensile strength of Hardox 500 welded joints did not exceed 900 MPa, as well as by Teker et al. and Gupta et al. in studies [6,7]. The detrimental impact of microstructural alterations on mechanical properties can be effectively minimized only through laser welding technologies [8,9] or PWHT. The latter enables achieving tensile strengths of 1810 MPa for Hardox 600 and 1831 MPa for Hardox Extreme, corresponding to approximately 85% of the nominal base material strength [10,11]. Comparable conclusions were also drawn by other researchers [12–20], who consistently emphasized the necessity of implementing PWHT to restore desirable mechanical performance.

The pronounced reduction in mechanical properties within specific regions of a welded joint—resulting from adverse phase transformations induced by overheating and the consequent tempering of the base material, as well as the dendritic structure of the weld metal—also leads to a deterioration in the functional performance of these materials, including their resistance to abrasive wear. According to available literature data, within martensitic microstructures operating under dry (loose) abrasive conditions, hardness exerts the dominant influence on wear behavior [21]. However, this relationship must be interpreted with caution when selecting materials for structural components intended to operate in environments with higher frictional resistance [22–24]. Additional requirements imposed on martensitic steels to maintain a high level of resistance to abrasive wear include: (1) a fine-lath martensitic microstructure [25,26], (2) the ability to undergo surface work hardening during operation [27–30], and (3) a favorable distribution and morphology of secondary phase precipitates [31]. These factors may lead to distinct tribological behaviors even among materials with the same nominal hardness in the as-delivered condition [22,32,33]. Given the loss of key mechanical properties in martensitic steels as a consequence of welding processes, the present study aimed to assess the potential for

improving the abrasive wear resistance of welded joints of a selected armor steel grade with a nominal hardness of 500 HBW through the application of PWHT. This steel is classified as weldable and bendable, which significantly broadens its field of application [34]. In terms of performance, it may outperform Hardox Extreme steel, 38GSA steel (used for agricultural plowshares) [35], and carburized 20MnCr5 steel [36]. Beyond their use in defense and protective applications, materials of this type are also employed in cultivator coulters, crusher and feeder lining plates, as well as hammers used in recycling processes [34]. The combination of high abrasive wear resistance and good weldability makes the investigated steel a promising alternative to conventional materials used under conditions of severe abrasive wear.

Therefore, the aim of this study is to evaluate the abrasive wear resistance of welded joints in boron-alloyed martensitic armor steel and to identify possibilities for its improvement through the application of optimized PWHT parameters. The results obtained may provide a significant contribution to the advancement of welding technologies for armor steels, which are widely used in both military and civilian sectors.

2. Materials and Methods

The chemical composition was determined using a Leco GDS500A glow-discharge optical emission spectrometer (LECO Corporation, St. Joseph, MI, USA). The measurements were performed at a discharge voltage of 1250 V and a current of 45 mA, with high-purity argon (99.999%) supplied as the working gas. Each result represents the average of a minimum of five separate analyses to ensure measurement reliability. According to the obtained data (Tables 1 and 2), the examined armor-grade steel belongs to the group of medium-carbon alloys (C = 0.29%). Its hardenability is mainly influenced by the presence of manganese, chromium, nickel, and molybdenum. Nickel additionally contributes to lowering the ductile-to-brittle transition temperature, while molybdenum counteracts temper embrittlement. The very low levels of phosphorus and sulfur are beneficial, as they help maintain favorable mechanical performance. Aluminum and titanium act as grain refiners, supporting the formation of a fine lath-type microstructure, whereas the small boron addition (approximately 0.008%) markedly improves hardenability. The carbon equivalent value (CEV) of 0.69 and the equivalent carbon content (CET) of 0.47 indicate reduced weldability of the material, increasing the risk of cold cracking and typically implying the need for preheating prior to welding. The microstructure of the analyzed armor steel, shown in Figure 1, consists predominantly of tempered fine-lath martensite with a small fraction of fresh martensite regions.

Table 1. Chemical composition and carbon equivalent values of the analyzed armor steel. #—plate thickness; CEV—carbon equivalent according to IIW; CET—carbon equivalent according to SS-EN 1011-2 [37].

C	Mn	Cr	Ni	Mo	V	Cu	CEV	CET	#
Selected Chemical Element [wt.%]							[%]		[mm]
0.29	0.86	0.49	1.03	0.37	0.0230	0.23	0.69	0.47	6.0
CEV = C + Mn/6 + (Cr + Mo + V)/5 + (Cu + Ni)/15; CET = C + (Mn + Mo)/10 + (Cr + Cu)/20 + Ni/40									

Table 2. Chemical composition of the analyzed armor steel. #—plate thickness.

Si	P	S	Al	Ti	Nb	Co	B	#
Selected Chemical Element [wt.%]								[mm]
0.23	0.007	-	0.044	0.002	-	0.008	0.008	6.0

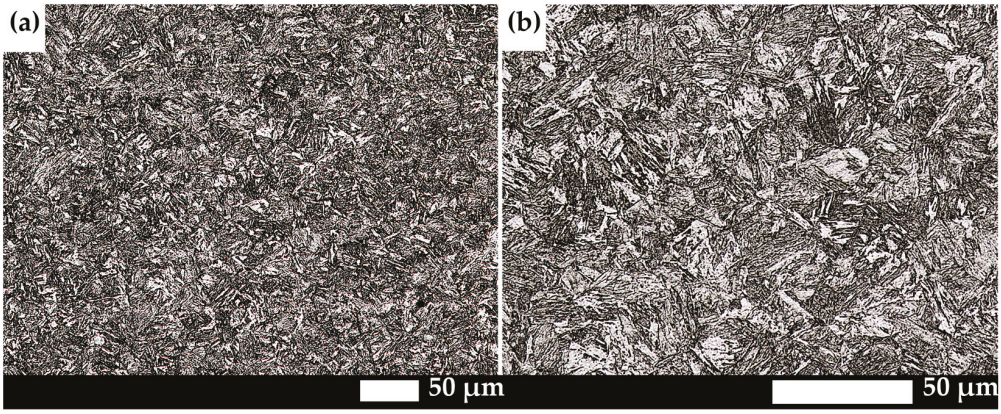

Figure 1. Microstructure of the investigated armor steel: (**a**) 200×, (**b**) 500×. Predominantly tempered fine-lath martensite with a few areas of fresh martensite. Light microscopy, etched with 3% HNO_3.

The welded joints were produced using the Metal Active Gas (MAG) process with filler materials intended for high-strength, low-alloy steels. Although several advanced welding technologies could potentially be considered for joining high-strength armor steels, the MAG/MIG process was selected in this study due to its dominant industrial relevance, high process efficiency, availability of consumables, and suitability for producing multi-pass welds in thick plates. These advantages make MAG/MIG welding the most practical and widely applicable technique for both experimental work and real manufacturing conditions. Based on our previous research experience, alternative methods were also tested; however, MAG/MIG and, to a lesser extent, SAW proved to offer the most reliable process stability and compatibility with the subsequent heat treatment route developed in this work. Welding was performed with an ESAB A2 Mini Trac system equipped with an ESAB LAE 800 power source. The steel plates were joined with a double-sided butt weld. The selected welding parameters ensured full penetration and proper fusion of the joint. The process was conducted in the PA (flat) position with a 1.0 mm electrode wire. The arc voltage and current settings for the first and second passes were 15 V/90 A and 28.2 V/170 A, respectively. Direct current with electrode positive polarity (DC+) was used, while the wire feed speed was maintained at 9 m/min. The consumable wire was OK AristoRod 89 (Mn4Ni2CrMo, [38]). The OK AristoRod™ 89 filler wire was selected based on technological, metallurgical, and application-oriented criteria relevant to the PWHT strategy adopted in this study. Unlike the majority of published approaches to welding low-alloy high-strength steels, the present work intentionally assumed that all welded joints would undergo PWHT. Consequently, the choice of filler material could not rely solely on manufacturer-provided mechanical data, which typically refer to the as-welded condition without subsequent thermal processing. The filler material was therefore chosen according to the following requirements: (1) the ability to produce defect-free welds with low susceptibility to cold or delayed cracking, (2) suitability for multi-pass welding without loss of structural integrity, (3) a high propensity for hardening during PWHT, enabling the formation of a fully martensitic microstructure, (4) a chemical composition closely matching that of the base material, ensuring microstructural compatibility and minimizing heterogeneity within the welded joint. These criteria considerably narrow the range of commercially available welding consumables suitable for the adopted PWHT approach. OK AristoRod™ 89 met all of the above requirements and has been previously used by the authors in related research. This provided an additional advantage, as prior experience with this filler material allowed for precise optimization of welding parameters and ensured the reproducibility and reliability of the welded joints produced in the present study. No preheating was applied, and the interpass temperature was kept below 80 °C.

The plates were welded without edge beveling. A schematic representation of the welded configuration is provided in Figure 2.

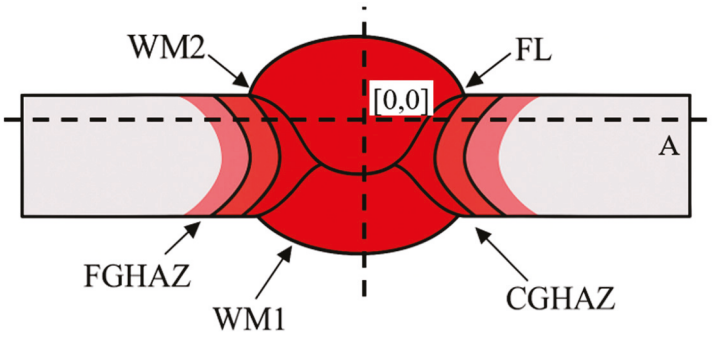

Figure 2. General schematic of the welded joints of analyzed steel. A—line of hardness distribution measurements, CGHAZ—coarse-grained heat-affected zone; FGHAZ—fine-grained heat-affected zone, FL—fusion line, WM1/WM2—individual weld layers in the order they were made.

Welding operations were carried out using OK AristoRod™ 89 welding wire (Table 3). This is a solid, copper-free wire designed for MAG welding of very high-strength steels (R_e < 900 MPa). OK AristoRod™ 89 is mainly used for welding structures such as lifting equipment, construction machinery, trucks, handling devices, and containers.

Table 3. Properties of the filler used to create the welded joint [39].

Filler Material	C	Mn	Si	Cr	Ni	Mo	$R_{p0.2}$	R_m	A	KV_{-40}
	Chemical Composition [% wt.]						[MPa]		[%]	[J]
OK AristoRod™ 89	0.10	1.90	0.80	0.30	2.10	0.65	920	960	18	55

All heat treatment operations were performed in gas-tight chamber furnaces (FCF 12SHM/R) manufactured by Czylok (Czylok, Jastrzębie-Zdrój, Poland), using a protective atmosphere of 99.95% argon. The quenching medium consisted of deoxidized water at a temperature not exceeding 30 °C. The heat treatment was performed according to the following parameters:

- Double normalization: 900 °C, 2 × 30 min, air cooling;
- Quenching: 930 °C, 20 min, water;
- Tempering: 100 °C, 5 h, air cooling.

The selection of heat treatment parameters was based on the chemical composition of both the base material and the weld metal, as well as on extensive preliminary experimental studies. Due to the significant microstructural alterations observed within HAZ of high-strength, low-alloy armor steels, a post-weld normalizing treatment was introduced as an essential step prior to quenching and tempering. The normalizing treatment was performed twice due to the substantial heat input generated during welding with the MAG process, which resulted in austenite grain growth, while a single-stage annealing treatment proved insufficient to eliminate the unfavorable microstructural changes. The normalizing temperature was selected experimentally to ensure the effective homogenization of the HAZ and weld metal. Austenitizing parameters were determined on the basis of the carbon content of the base steel and the weld metal, considering the need to achieve sufficient undercooling to obtain a fully martensitic microstructure across the entire joint. The selected quenching medium provided the required cooling rate to promote martensite formation through the full thickness of the welded plates. Tempering was carried out to relieve internal stresses generated during quenching. The selected parameters reflect

the authors' earlier experience with the heat treatment of high-strength armor steels and welded joints, confirming their suitability for the present investigation.

Hardness measurements on cross-sections of welded joints were performed using the Rockwell method (HRA) in accordance with [40], employing a universal hardness tester with a 60 kgf (588.399 N) load (ZwickRoell, Ulm, Geramny). The obtained hardness values were converted to the Vickers scale according to [41]. Measurements were carried out on cross-sections of specimens in the as-welded condition and after PWHT. Hardness profiles were measured using three independent traverses. The locations of the hardness profiles are schematically indicated by line A in Figure 2.

Microstructural observations were performed using a Nikon Eclipse MA200 light microscope (Nikon Corporation, Tokyo, Japan). Prior to imaging, the specimens were etched in a 3% nitric acid solution following the ASTM E407 standard [42]. Examinations of the worn surfaces after abrasive testing were carried out with a Phenom XL (Thermo Fisher Scientific, Waltham, MA, USA) scanning electron microscope SEM). The analyses were conducted using a secondary electron (SE) imaging, with the accelerating voltage set to 15 keV.

Abrasion resistance was evaluated using a T-07 tribological (Łukasiewicz—Institute for Sustainable Technologies, Radom, Poland) tester operating with loose abrasive (Figure 3), following the procedure specified in [43]. The tests were conducted under a constant load of F = 44 N (±0.25 N). The hardness of the rubber lining the wheel ranged between 78 and 85 ShA. Test specimens with dimensions 30 × 30 × 10 mm were used. Each test condition was evaluated on six independent specimens per condition, ensuring statistical repeatability of the results. Electrofused alumina grade No. 90, compliant with [44], served as the abrasive medium. The duration of each test was adjusted to the hardness of the examined steel and set at 1800 wheel revolutions (corresponding to 30 min). Mass loss was determined using a precision laboratory balance with a resolution of 0.0001 g. The purpose of the experiment was to calculate the relative abrasion resistance coefficient (k_b) with respect to a reference material—C45 steel in the normalized condition. The coefficient k_b was determined using Equation (1):

$$k_b = \frac{Z_w \cdot \rho_b \cdot N_b}{Z_b \cdot \rho_w \cdot N_w} \quad (1)$$

where

k_b—relative abrasion resistance coefficient;
Z_w—weight loss of reference samples in [g];
Z_b—weight loss of the tested material in [g];
N_w—number of roller revolutions during testing of the reference sample;
N_b—number of roller revolutions during testing of the sample;
ρ_w, ρ_b—density of the reference sample material and the tested material [g/cm^3].

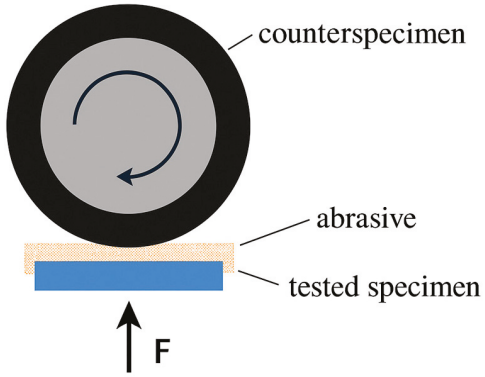

Figure 3. Layout of the T-07 tribotester.

Surface topography of the specimens was examined using a HITACHI TM-3000 scanning electron microscope (Hitachi, Ltd., Tokyo, Japan) equipped with dedicated 3D Viewer Version 2.1.0 software, which enabled visualization and quantitative assessment of height variations along the Z-axis. Prior to the measurements, each sample was cleaned with a dry stream of compressed air, visually inspected to exclude mechanically damaged regions, and marked at three predetermined locations selected for detailed surface characterization. All surface examinations were performed at a constant magnification and an accelerating voltage of 15 kV, with the evaluation length set to ten times the elementary segment lr = 198.03 μm, giving a total analyzed distance of approximately 1980 μm. Before commencing the measurements, the microscope was calibrated for working distance (WD) using a certified roughness reference specimen with a known profile.

3. Results

3.1. Metallographic Analysis

The chemical composition of the weld metal is characterized by a low carbon content of 0.12 wt.% (Tables 4 and 5). The presence of manganese (0.83 wt.%) and chromium (0.36 wt.%) contributes to increased hardenability. Notably high concentrations of nickel (2.02 wt.%) and molybdenum (0.56 wt.%) were recorded; these elements not only enhance the strength properties of the steel but also promote ductility, allowing tempering to be carried out with a reduced risk of temper embrittlement. Furthermore, the weld metal exhibits very low phosphorus and sulfur contents (0.008 wt.% and 0.002 wt.%, respectively) and contains a microaddition of boron (0.0014 wt.%), which significantly increases its hardenability.

Table 4. Chemical composition and carbon equivalent values of the weld metal. CEV—carbon equivalent according to IIW; CET—carbon equivalent according to [37].

C	Mn	Cr	Ni	Mo	V	Cu	CEV	CET
Selected Chemical Element [wt.%]							**[%]**	
0.12	0.83	0.36	2.02	0.56	0.007	0.088	0.59	0.33
CEV = C + Mn/6 + (Cr + Mo + V)/5 + (Cu + Ni)/15; CET = C + (Mn + Mo)/10 + (Cr + Cu)/20 + Ni/40								

Table 5. Chemical composition of the weld metal.

Si	P	S	Al	Ti	Nb	Co	B
Selected Chemical Element [wt.%]							
0.420	0.008	0.002	0.003	0.005	-	0.002	0.0014

The average hardness of the base material is 503 HV (measured at points −10.0 and 10.0 mm, highlighted by the green curve "AHT") (Figure 4). Welding processes lead to a reduction in hardness within the weld metal, reaching values between 210 and 240 HV, which corresponds to approximately 45% of the base material hardness (blue color, labeled "AW", range from −5.0 to +5.0 mm in Figure 4). It should be noted that, in all analyzed conditions, the hardness of the base material remains higher than that of the weld metal, even in specimens subjected to normalizing. Under this heat treatment condition, the weld metal hardness is approximately 217 HV, whereas the base material reaches around 410 HV, indicating increased hardenability due to higher carbon and chromium content.

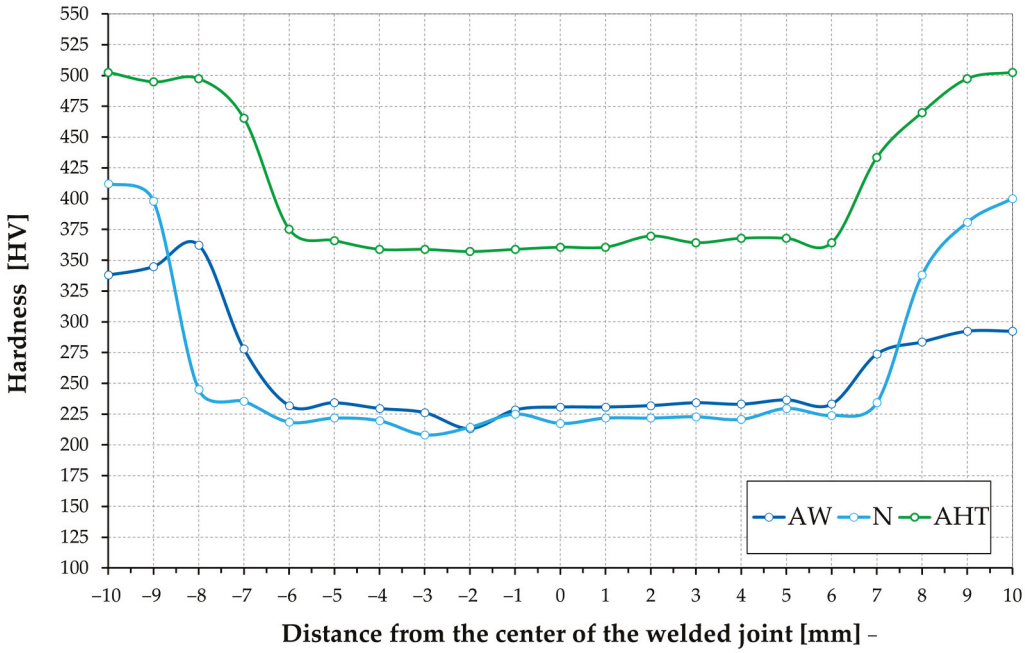

Figure 4. Hardness distribution of the analyzed welded joint along line A marked in Figure 2, AW—joint after welding, AHT—heat-treated, N—as-normalized.

The presence of adverse microstructural changes within the welded joint region is confirmed by the micrographs of all characteristic zones (Figure 5). Their morphology differs markedly from the initial condition due to heating of the material both above and below the austenitizing temperature. As a result, diffusion-controlled transformations occurred, leading to the formation of a tempered martensitic microstructure. As shown in Figure 5a, the microstructure of the weld metal consists predominantly of acicular (Widmanstätten) ferrite, where the growth of individual ferrite needles proceeds parallel to a limited number of habit planes of the matrix. Consequently, within a single prior austenite grain, the ferrite plates exhibit a parallel orientation with respect to each other. The presence of intragranular acicular ferrite is also observed; it nucleates independently within the grains on oxides, sulfides, or silicates, and its plates are randomly oriented. Additionally, allotriomorphic ferrite is found along the former austenite grain boundaries, while finely dispersed pearlite occurs in minor quantities. Along the fusion line, the microstructure remains characteristic of the weld metal; however, the ferrite exhibits an elongated morphology, resulting from its solidification in the direction of the maximum thermal gradient (Figure 5b). The coarse-grained heat-affected zone (CGHAZ) is composed mainly of upper bainite and lower bainite or tempered martensite (Figure 5c). Locally, the presence of Widmanstätten ferrite and finely dispersed pearlite is also observed, particularly in the region adjacent to the fusion line (Figure 5b). In the fine-grained heat-affected zone (FGHAZ), the microstructure consists primarily of tempered martensite, characterized by a distinct carbide network along the former austenite grain boundaries, with small fractions of upper bainite and/or Widmanstätten ferrite (Figure 5d).

The microstructure of the base material in the as-normalized condition consists mainly of martensite or lower bainite, confirming the high hardenability of the investigated steel (Figure 6a). At the same time, the presence of banding and distinct carbide precipitates along the former austenite grain boundaries can be observed, resulting from slower cooling rates after soaking. Locally, small amounts of ferrite are also present. A distinct change in microstructural morphology is evident in the fusion line region (Figure 6b). The weld metal exhibits heterogeneous microstructures, including globular bainite, upper bainite, and Widmanstätten ferrite (Figure 6c). Application of PWHT results in the formation of a

uniform martensitic microstructure across all characteristic zones of the welded joint. In the weld metal region, the presence of fresh martensite is observed, which arises from the lower carbon content of the filler material and the limited potential for carbide precipitation in the interblock regions of martensite (Figure 7).

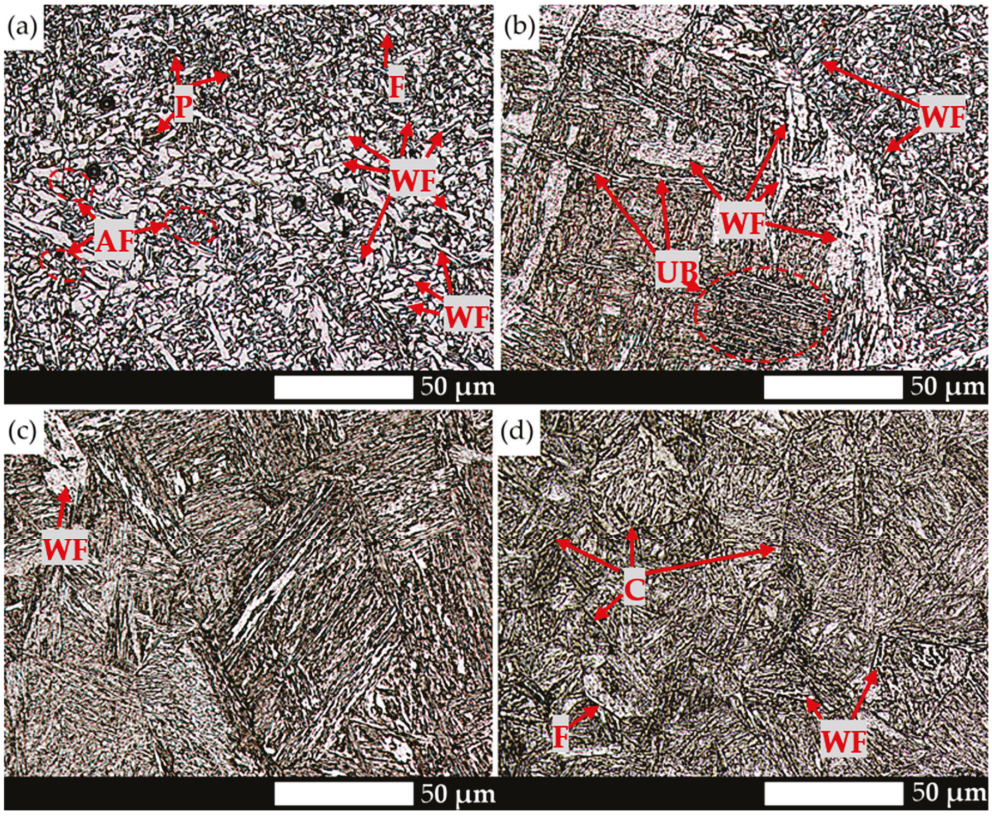

Figure 5. Microstructure of the analyzed welded joint; designation according to Figure 2: (**a**) weld material (WM), (**b**) fusion line (FL); (**c**) coarse-grained heat-affected zone (CGHAZ), (**d**) fine-grained heat-affected zone (FGHAZ). P—pearlite, AF—acicular ferrite, F—allotriomorphic ferrite, C—carbides, UB—upper bainite, WF—Widmanstätten ferrite, Light microscopy, etched with 3% HNO_3.

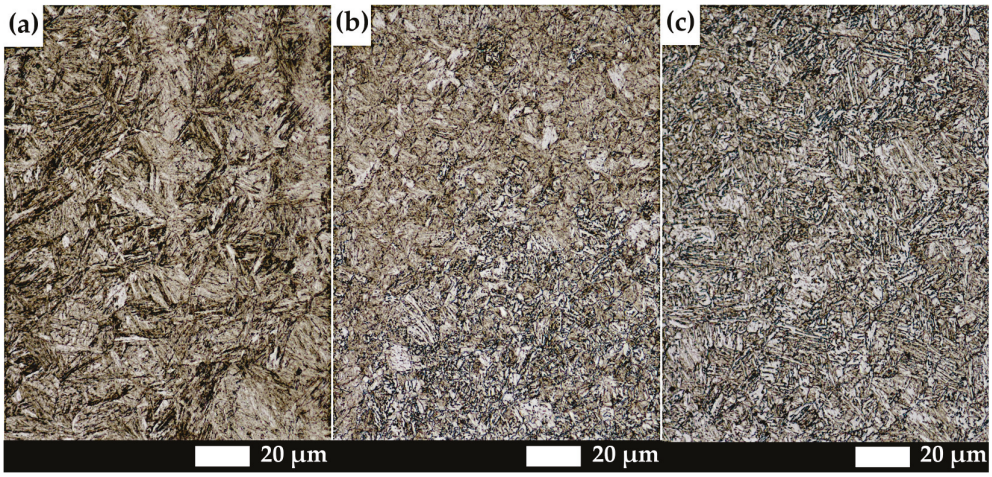

Figure 6. Microstructure of the analyzed material in the as-normalized condition; (**a**) base material; (**b**) fusion line; (**c**) weld material. Light microscopy, etched with 3% HNO_3.

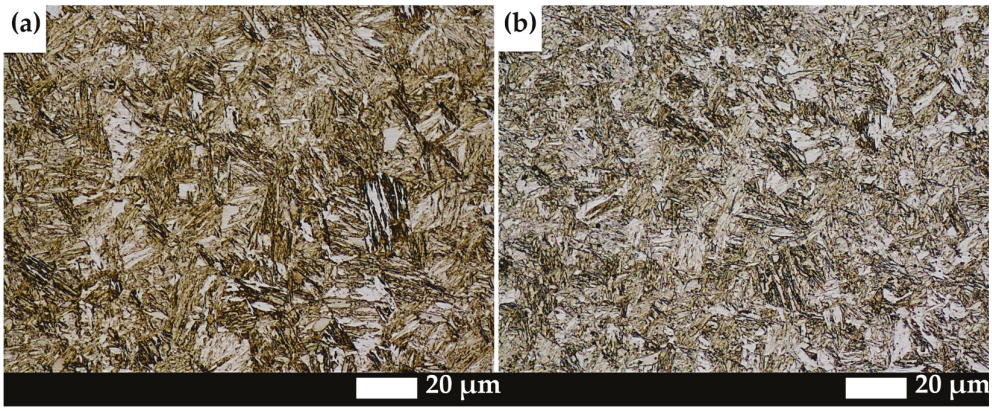

Figure 7. Microstructure of the analyzed welded joint after complex heat treatment: (**a**) fusion line; (**b**) weld material. Light microscopy, etched with 3% HNO_3.

3.2. Abrasive Wear Resistance Tests

Figure 8 presents the values of the relative abrasive wear resistance coefficient (k_b) of the welded joint in various heat treatment conditions, along with the corresponding hardness values (HV). The hardness of the weld metal was determined at a point located +3.00 mm from the weld axis, as indicated in Figure 4. The tribological tests revealed that the welded joint in the as-welded condition exhibited the lowest k_b value ($k_b = 0.98 \pm 0.01$), whereas the base material of the armor steel demonstrated the highest resistance, with $k_b = 1.18 \pm 0.02$. The application of post-weld heat treatment led to an increase in the abrasive wear resistance of the welded joint, reaching $k_b = 1.08 \pm 0.01$. For the normalized base material and normalized weld metal, the respective values were 1.10 ± 0.02 and 1.00 ± 0.02. It should be emphasized that hardness correlates strongly with the measured abrasive wear resistance indicators. The only deviation from this trend is observed in the normalized condition, where—despite a hardness decrease of 9 HV units—the welded joint exhibits a 0.02 higher k_b value compared to the as-welded state. This phenomenon can be attributed to the beneficial effect of normalization, which promotes microstructural refinement. Furthermore, the low standard deviations of the obtained results indicate their high reproducibility and uniformity.

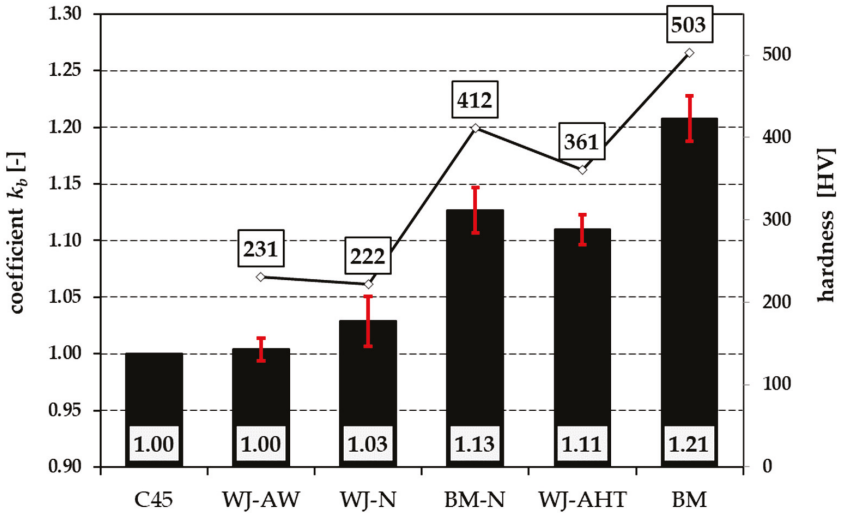

Figure 8. Relative abrasion resistance coefficients of analyzed armor steel and welded joint. C45—steel with a hardness of 220 HBW in the as-normalized condition; WJ-AW—welded joint in the as-welded condition, WJ-N—welded joint in the normalized condition, BM-N—base material in the normalized condition, WJ-AHT—welded joint in the post-heat-treated condition, BM—base material. Average values with standard deviation.

Figure 9 presents the surfaces of the specimens after abrasive wear testing. Examination of the microphotographic documentation indicates that the width of the grooves and pits formed is the greatest for the welded joint specimens in the as-welded condition. The wear tracks exhibit significant misalignment relative to the abrasive motion direction, and numerous chips are visible along their edges (Figure 9a–c). In the as-welded condition, in addition to deep pits resulting from the penetration of hard abrasive grains into the relatively soft matrix, the presence of cavities, wide grooves, and scratches arranged partially perpendicular to the abrasive movement direction is observed. Their proportion decreases markedly in the weld metal and base material after normalization, where the dominant wear mechanisms are microplowing and microscratching, accompanied by the formation of characteristic chips (Figure 9b). Distinct areas of abrasive particle penetration into the material are also visible, leading to the detachment of matrix fragments near the wider ends of the grooves. This phenomenon is associated with repeated local plastic deformation, followed by the removal of material fragments.

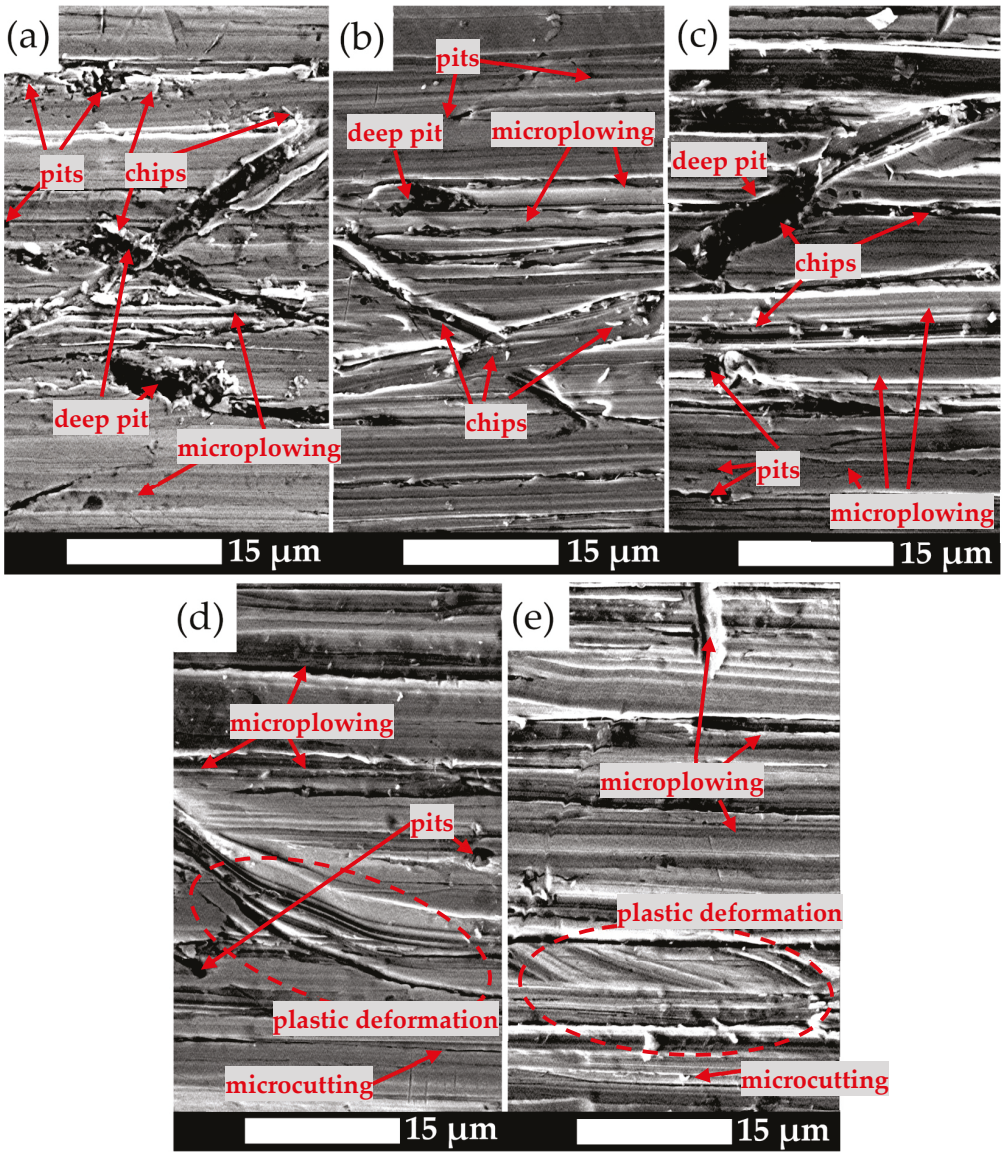

Figure 9. Worn surfaces of the analyzed welded joint; (**a**) WJ-AW—welded joint in the as-welded condition, (**b**) WJ-N—welded joint in the normalized condition, (**c**) BM-N—base material in the normalized condition, (**d**) WJ-AHT—welded joint in the post-heat-treated condition, (**e**) BM—base material. SEM, unetched.

The application of PWHT results in a noticeable improvement in the surface quality of the tested specimens. The scratches are mostly parallel to the abrasive motion direction, and their local misorientation occurs only sporadically. In both the weld metal and base material, plastic deformation, the presence of grooves, and a few chips are mainly observed. Wear mechanisms related to microcutting play a marginal role in this case, and the few pits that appear are relatively shallow. Therefore, it can be concluded that the dominant wear mechanisms in the analyzed material, regardless of the applied heat treatment variant, are primarily associated with microplowing and microscratching, while the contribution of microcutting wear remains minor in all analyzed cases.

On the cross-sections of the specimens after abrasive wear testing, distinct wear traces in the form of grooves, pits, and local cavities are visible (Figure 10). For the welded joint in the as-welded, normalized, and heat-treated conditions, the material elevations exhibit a smooth and elongated morphology. Local plastic deformation leads to the rounding of some asperities, giving the edges a gentle, wavy appearance. However, in the normalized base material, sharp asperity tips were observed, indicating non-uniform wear of the individual microstructural phases. In the as-delivered condition, more pronounced deformation of the martensitic microstructure is observed, which indicates relatively high ductility of the material and its ability to absorb the impact energy of the abrasive particles through local deformation rather than by intensive fragmentation.

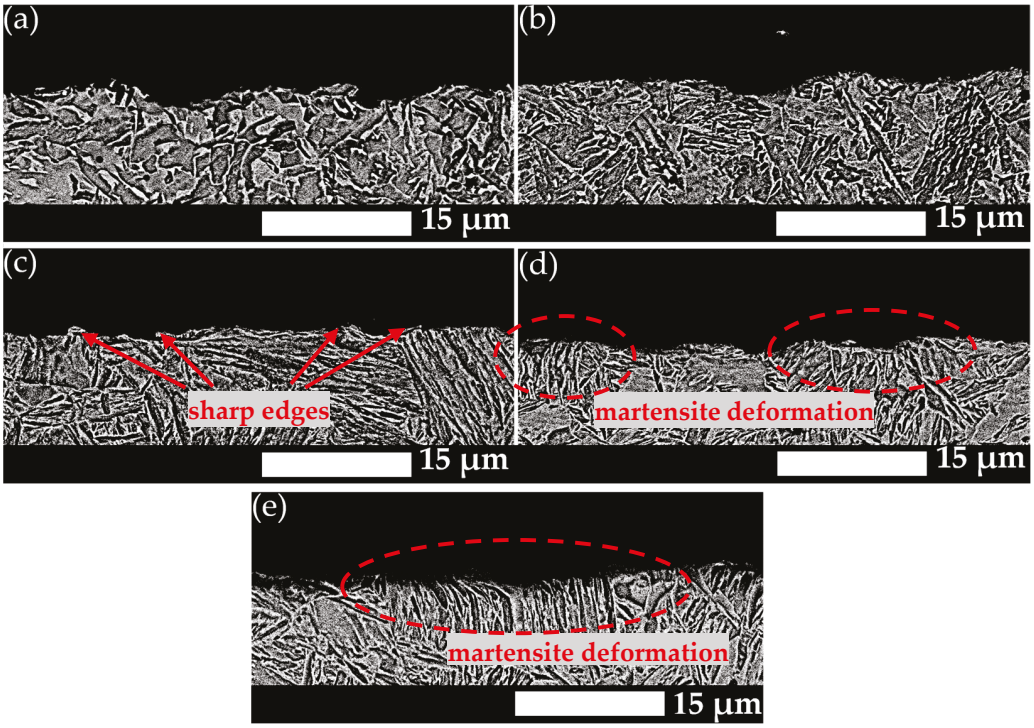

Figure 10. Microstructure of subsurface regions subjected to abrasive wear tests: (**a**) WJ-AW—welded joint in the as-welded condition, (**b**) WJ-N—welded joint in the normalized condition, (**c**) BM-N—base material in the normalized condition, (**d**) WJ-AHT—welded joint in the post-heat-treated condition, (**e**) BM—base material. SEM, etched with 3% HNO_3.

The surface topography reconstruction and roughness parameter evaluation after abrasive wear testing (Figures 11–13) complement the qualitative observations, enabling a precise characterization of the differentiated response of the investigated material conditions to abrasive interaction. For the welded joint in the as-welded condition (WJ-AW), the highest roughness parameter values were recorded (Ra = 0.46 µm, Rq = 0.59 µm, Rp = 1.75 µm, and Rv = 1.72 µm). Such high surface amplitude values result from the

formation of deep pits, grooves, and material detachments, which arise due to the intensive penetration of hard abrasive particles into the relatively soft microstructure of the weld metal. A similar character of microdamage was also observed in the normalized condition; however, the roughness parameters were lower in this case (Ra = 0.40 µm, Rq = 0.51 µm, Rp = 1.87 µm, and Rv = 1.42 µm). This behavior can be associated with microstructural refinement and homogenization, which reduced the intensity of local surface defects. After the application of comprehensive heat treatment, a slight increase in roughness parameter values was noted compared to the normalized condition (Ra = 0.42 µm, Rq = 0.55 µm, Rp = 1.73 µm, and Rv = 1.92 µm). Nevertheless, the surface topography reveals predominantly parallel, relatively shallow scratches and grooves, indicating a change in the dominant micromechanism of wear.

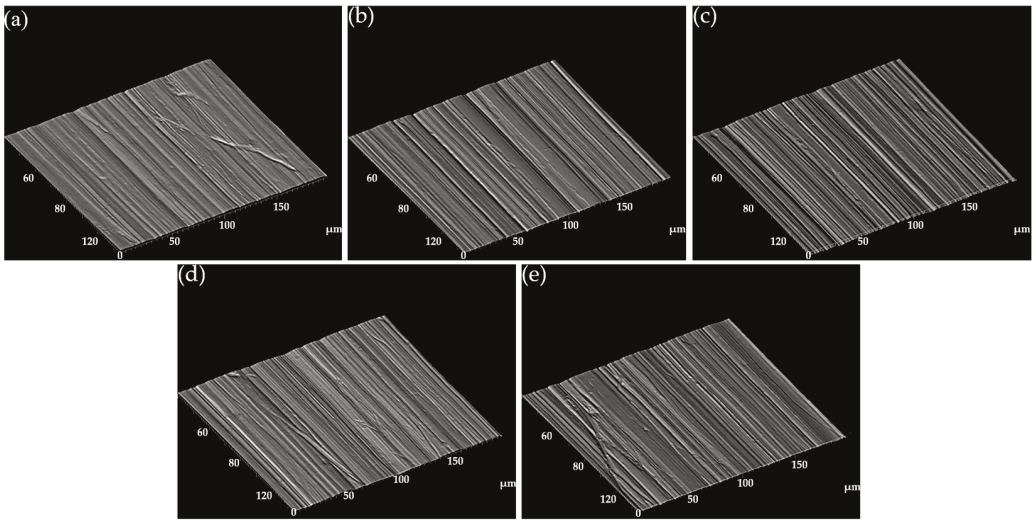

Figure 11. Three-dimensional images of sample surfaces subjected to wear testing along the longitudinal direction of abrasive movement; (**a**) WJ-AW—welded joint in the as-welded condition, (**b**) WJ-N—welded joint in the normalized condition, (**c**) BM-N—base material in the normalized condition, (**d**) WJ-AHT—welded joint in the post-heat-treated condition, (**e**) BM—base material.

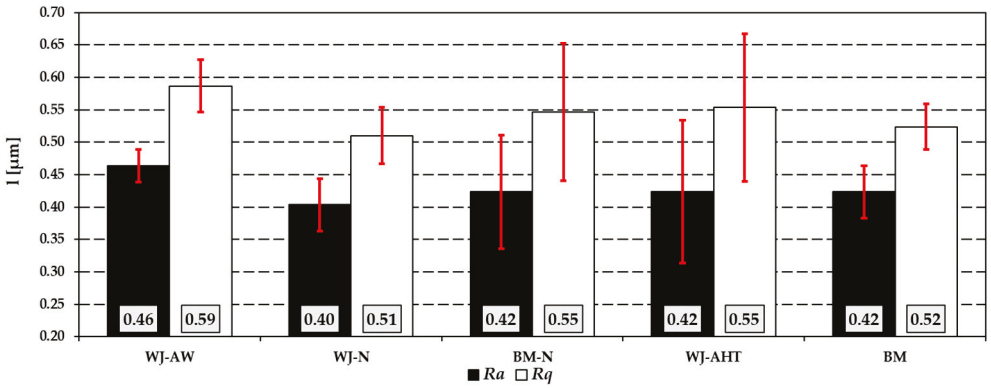

Figure 12. Roughness parameters Ra and Rq of the analyzed welded joint under different heat treatment conditions subjected to abrasive wear testing. Average values with standard deviation.

It should also be emphasized that depth-related parameters Rv and Rp are particularly significant in assessing wear resistance, as they reflect the presence of deep surface defects that constitute the primary factor reducing abrasive wear resistance based on mass loss. In the as-welded condition, the Rp and Rv values are similar (1.75 µm and 1.72 µm, respectively), yielding an Rv/Rp ratio of 0.98. This indicates that the depths of the valleys and the heights of the peaks are comparable, suggesting intense abrasive interaction that leads both

to the formation of grooves and pits and to the buildup of raised material around them. In the normalized condition, a distinct increase in the depth of valleys relative to peaks is observed (Rv = 1.87 µm, Rp = 1.42 µm, Rv/Rp = 1.32). This indicates the dominance of mechanisms associated with the formation of deep pits and scratches, with a limited contribution from elevations that arise either from plastic deformation of the material or from the detachment of previously raised fragments following rapid strain hardening. A similar relationship was observed for the normalized base material, where Rv and Rp values are close (1.96 µm and 1.86 µm, respectively), and the Rv/Rp ratio of 1.05 suggests a balance between valleys and peaks [45]. However, the higher absolute values of these parameters indicate a greater susceptibility of the material in this condition to microdamage induced by abrasive particles. Different results were obtained for samples subjected to comprehensive post-weld heat treatment. In this condition, the Rp value (1.92 µm) exceeds Rv (1.73 µm), and the Rv/Rp ratio decreases to 0.90. This relationship suggests a reduced intensity of deep pit formation and a predominance of microplowing and scratching mechanisms over material chipping. In contrast, the base material in the as-received condition (BM) is characterized by Rp = 1.48 µm and Rv = 1.65 µm (Rv/Rp = 1.11), indicating a slight predominance of depressions over elevations.

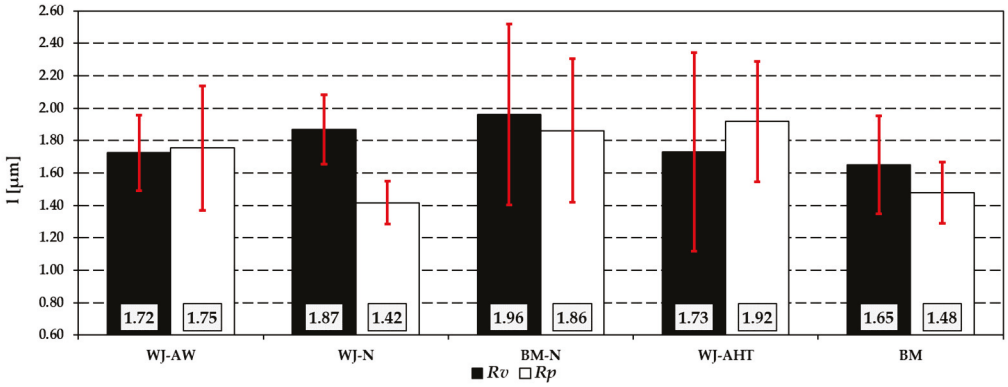

Figure 13. Roughness parameters Rv and Rp of the analyzed welded joint under different heat treatment conditions subjected to abrasive wear testing. Average values with standard deviation.

4. Discussion

The study presents the results of research on the abrasive wear resistance of welded joints of martensitic armor steel with a microaddition of boron. It was shown that the application of heat treatment allows for an improvement in the mechanical properties of the weld material, which, consequently, may contribute to increased durability of components operating under severe abrasive conditions.

The potential for improving the mechanical properties of the weld metal is primarily limited by the carbon content of commercially available welding consumables. Based on this, it can be stated that when welding steel with a hardness of 500 HBW, due to the carbon difference of 0.17% between the weld metal and the base material, achieving similar mechanical and tribological properties in the welded joint is significantly challenging. In the case analyzed, the mass loss of the heat-treated weld metal was greater than that of the base material. However, compared to the weld material in the as-welded condition, the obtained values are 55% more favorable. Similarly, for steel with a hardness of 466 HBW, it was shown that the weld made using the MAG method and subjected to heat treatment exhibits a k_b value lower by 0.03 compared to the base material. It should be emphasized, however, that such a small difference—three times smaller than in the present study—is due to the limited chemical composition of the base material, whose hardenability is primarily associated with the microaddition of boron. These observations are consistent with results

reported for welded joints of Hardox Extreme steel, which in all analyzed cases show lower abrasive wear resistance than the base material [46].

Figure 14 presents the results of abrasive wear resistance tests of welded joints of the analyzed armor steel, compared—based on available literature data—with the results obtained for Hardox 500 steel, as well as the base material and welded joints of Hardox 450 and Hardox Extreme steels [46]. To ensure the methodological consistency of the abrasion resistance comparison presented in Figure 14, all k_b values were referenced to the same measurement framework. Specifically, the data shown in the figure were obtained under identical testing conditions, i.e., using the GOST 23.208-79 standard [43], electrofused alumina No. 90 as the loose abrasive, and comparable loading and test duration parameters. All studies included in the comparison were conducted on the T-07 tester where the k_b coefficient is defined in an equivalent manner.

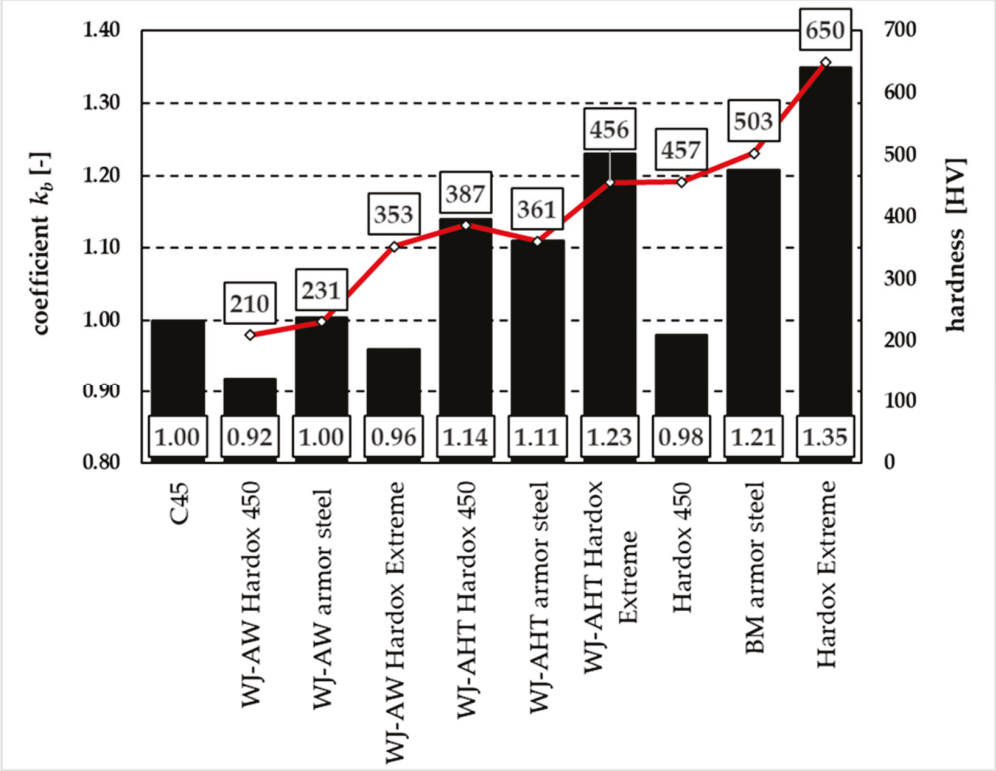

Figure 14. Relative abrasion resistance indices of the analyzed martensitic steels and welded joints. C45—normalized C45 steel (hardness 220 HBW); WJ-AW—welded joint in the as-welded condition; WJ-AHT—welded joint after heat treatment; BM—base material.

For this reason, the comparison was normalized with respect to the same reference material—normalized C45 steel—which serves as the baseline for calculating the abrasion resistance coefficient. The use of a common reference ensures that the k_b values reported in this work and in the cited literature are directly comparable. In all analyzed cases, the joints in the as-welded condition exhibited higher mass loss than C45 steel in the normalized state (hardness 220 HBW). It should be emphasized, however, that the application of heat treatment in all variants leads to a significant increase in abrasive wear resistance, providing performance exceeding that of steels with a declared hardness of 450 HBW. For welded joints produced using the submerged arc welding technique, the obtained abrasive wear resistance is comparable to that of steel with a declared hardness of 500 HBW—the k_b coefficient for the welded joint of Hardox 450 steel and the base material of Hardox 500 steel is 1.14.

It should also be noted that the tribological resistance of the analyzed armor steel differs from that of Hardox 500, indicating that despite similar properties, the wear mechanisms and interaction characteristics with the abrasive material are not identical. Hardox 500 steel exhibits a carbon content comparable to that of the analyzed armor steel (C = 0.29%), as well as similar levels of manganese and chromium. A significant difference, however, lies in the higher nickel and molybdenum content. The microstructure of both the analyzed armor steel and as-delivered Hardox steel consists of fine-lath tempered martensite with occasional regions of fresh martensite. The hardness of Hardox 500 steel is 512 HV, which is only 9 HV units higher than that of the tested armor steel [46]. In this case, however, the steel with a 0.97% higher nickel content exhibits a more favorable wear resistance—the k_b coefficient for Hardox 500 steel is lower by 0.04 compared to the analyzed armor steel. The presence of nickel promotes increased ductility and impact toughness, allowing for more effective dissipation of mechanical energy in the contact zone with abrasive particles. This facilitates initial wear through microplowing, followed—through repeated plastic deformation and resulting strain hardening—by wear via microfatigue or microcutting. Similar conclusions were presented in [47], where a heat-treated welded joint of Hardox 450 steel, produced by submerged arc welding, exhibited lower mass loss compared to the base material. The tests were conducted using both loose abrasive and soil mass presenting higher resistance. In this case, the nickel content in the weld material was 0.81% higher, while the carbon content was 0.04% lower than in the base material.

The proposed technology provides a significant improvement compared to the results reported in the available literature. In [48], the effect of welding processes on abrasive wear was analyzed for a low-carbon, manganese shipbuilding steel with a distinctly banded ferritic–pearlitic microstructure. Although the weld metal exhibited higher hardness, greater mass loss was observed compared to the base material. This phenomenon was attributed to the lower carbon content, the presence of residual stresses, and the differing microstructure. For Armox 500T steel—characterized by properties similar to high-strength martensitic steels—it was found that the wear processes within the welded joint occur with an intensity three to four times higher than in the base material [49]. In [49], it was shown that XAR 400 steel exhibits the highest wear rate in the heat-affected zone, which gradually decreases with increasing distance from the weld axis, i.e., towards regions of the material less affected by heat. It should be emphasized that within the weld metal itself, only slight differences in wear rate were observed between its lower and upper portions, approximately half of those recorded in the HAZ. Such minor variation within the weld indicates the homogeneity of its microstructure compared to the HAZ, where intensive thermal exposure promotes more pronounced microstructural heterogeneities and, consequently, greater variability in wear resistance. For welded joints made of low-alloy martensitic steel containing 0.28% carbon, abrasive wear intensifies as the measurement location approaches the weld centerline [50]. Preliminary observations for joints fabricated by laser welding—where the energy is highly concentrated and the resulting heat-affected zone remains very narrow—have also been published [51]. Despite the advantages associated with this welding technique, the abrasion-resistant steels examined (with tensile strengths of 1407 MPa and 1603 MPa) showed the highest friction coefficients within the weld metal region.

It should be highlighted that the previously referenced works did not investigate welded joints in a heat-treated state. Although the study presented in [52] yielded encouraging outcomes, the examined joint exhibited limited resistance under dynamic loading conditions. Moreover, the observations reported in [53] indicate that, for both rail welds and the parent rail material, the volume of impact wear increases with the number of impact cycles and the level of applied normal force. Despite this, the welded joint displays better

resistance to plastic deformation than the base material. As the number of impacts and load intensity rise, the dominant wear mechanisms evolve: in the rail steel from adhesive to fatigue wear, and in the welded joint from peeling to fatigue wear. Under more severe loading and higher impact frequencies, fatigue wear ultimately becomes the principal degradation mode in the weld joint.

In the normalized condition, the welded joint exhibits a k_b value comparable to that obtained in the as-welded state, despite its lower hardness. This effect results from the heat treatment, which promotes the formation of a fine-grained microstructure free of residual stresses. It is worth noting that the abrasive wear resistance of the base material in the normalized state also remains comparable to that of the heat-treated welded joint. Despite the base material exhibiting a hardness higher by 51 HV, the difference in the k_b coefficient between these two conditions is only 0.02. This behavior can be attributed to the elevated carbon content and the presence of alloying elements that enhance hardenability—such as boron, nickel, vanadium, manganese, and molybdenum (the latter exerting the strongest effect according to Grossman). As a result, the microstructure of the normalized base material is dominated by martensite, whose mechanical properties are superior to those of the martensite present in the weld metal. However, this phase is more susceptible to chipping and wear through micro-cutting. Moreover, the abrasion process progresses unevenly across the constituent phases. Hard carbide precipitates, located primarily along the prior austenite grain boundaries, exhibit significantly greater resistance to wear compared to the softer martensitic–bainitic–ferritic matrix. Consequently, phases containing coherent carbide precipitates play a particularly important role in enhancing local wear resistance. This phenomenon, when wear resistance is evaluated solely based on mass loss, results in a lower k_b value. The high plasticity of materials with increased nickel content has already been discussed in this paper in the context of differences between the wear behavior of the investigated armor steel and Hardox 500 steel. However, a similar relationship can also be observed when comparing the normalized base material of the analyzed boron steel with the more ductile weld metal.

An interesting issue is the relationship between surface roughness parameters and abrasive wear resistance, expressed by the k_b coefficient (Figure 15). Since the roughness measurements were carried out after the abrasive wear tests, the correlations reflect the combined effect of microstructural state, hardness distribution, and wear mechanisms on the resulting surface topography. Due to the limited number of experimental conditions, originating from the discrete PWHT variants, the polynomial fits should be interpreted as descriptive tools illustrating tendencies rather than as predictive statistical models. For small datasets of this type, low-order second-degree polynomial fitting is commonly used to visualize non-linear trends without introducing artificial overfitting. It should be emphasized that the objective of the fitting was not to produce a statistically model, but rather to support a qualitative interpretation of the observed relationships. The results revealed that, beyond a certain threshold, an increase in the roughness parameters *Ra* and *Rq* leads to a pronounced decrease in the k_b value. The obtained relationships were approximated by a second-degree polynomial, with a coefficient of determination R^2 ranging from 0.91 to 0.99. This indicates that, once a critical roughness level is exceeded, more pronounced surface irregularities after testing correspond to more intensive wear processes within the material. For the depth-related parameters (*Rv*, *Rp*), no such clear dependencies were observed. The relatively low determination coefficients (R^2 = 0.20 for *Rp* and R^2 = 0.54 for *Rv*) suggest that the occurrence of individual deep surface defects is not a sufficient quantitative criterion of tribological resistance. This result implies that the amplitude parameters *Ra* and *Rq*, which represent the averaged surface topography, provide a more reliable measure of wear behavior. These parameters better reflect the

overall effect of the abrasive medium, encompassing scratches, grooves, and small pits. This can be attributed to the fact that isolated pits or cavities may occur randomly and do not necessarily represent the general degree of surface degradation. It can therefore be concluded that *Ra* and *Rq* act as diagnostic indicators more closely correlated with macroscopic wear resistance, while *Rv* and *Rp* play an auxiliary role and do not determine the material's overall response under abrasive conditions. Nevertheless, minimizing local surface damage through appropriately selected heat treatment is important and can be achieved via microstructural modifications leading to increased hardness. A comparison between the armor steel in the as-delivered and normalized conditions and its welded joints showed that this material is characterized by relatively low roughness values, with microplowing and microscratching identified as the dominant wear mechanisms. This corresponds to favorable k_b values, confirming that a homogeneous and fine-grained microstructure contributes to minimizing material loss under abrasive conditions. The obtained results are consistent with previous observations indicating that PWHT reduces surface roughness and the number of deep surface defects, which directly translates into improved resistance to abrasive wear compared to the as-welded condition.

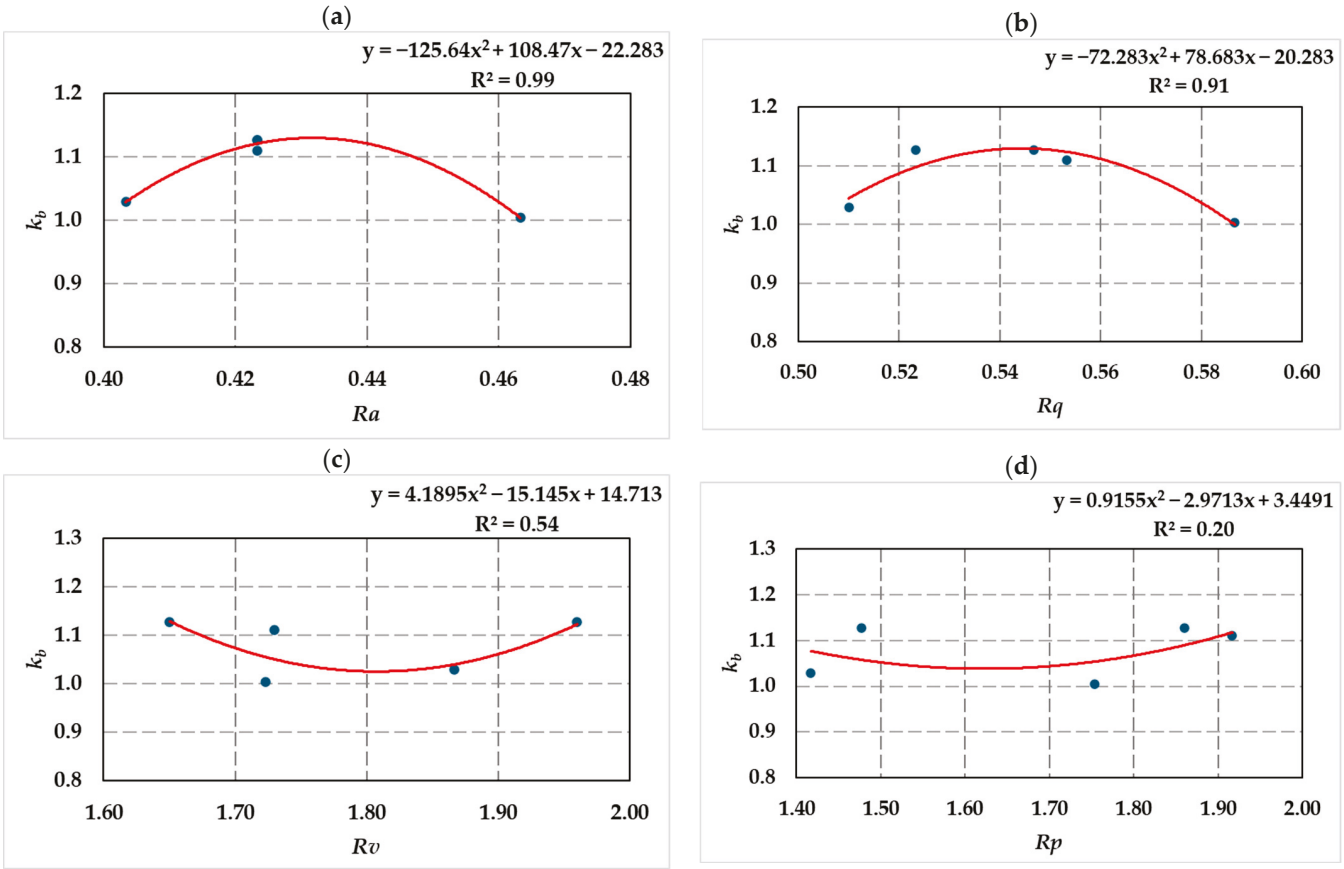

Figure 15. Relationship between the relative abrasion resistance coefficient (k_b) and selected surface roughness parameters: (**a**) $k_b(Ra)$, (**b**) $k_b(Rq)$, (**c**) $k_b(Rv)$, (**d**) $k_b(Rp)$.

5. Conclusions

Based on the presented results, the following conclusions can be drawn:

- The welded joint in the as-welded condition is characterized by a dendritic microstructure dominated by Widmanstätten ferrite, acicular ferrite, and allotriomorphic ferrite, with bainite and pearlite occurring only locally. The hardness of the weld metal ranges from 210 to 240 HV, corresponding to approximately 45% of the base material hardness (503 HV), which results in the lowest abrasive wear resistance ($k_b = 0.98 \pm 0.01$).

- In the normalized condition, the microstructure is refined and consists mainly of bainite and tempered martensite with carbide precipitates along the prior austenite grain boundaries. The hardness of the weld metal is approximately 217 HV, and that of the base material is about 410 HV. Despite the lower hardness compared to the as-welded state, the abrasive wear resistance increased (k_b = 1.00 ± 0.02 for the weld metal and 1.10 ± 0.02 for the base material), which can be attributed to the microstructural homogenization achieved through normalization.
- After the application of comprehensive post-weld heat treatment, a uniform martensitic microstructure was obtained throughout all zones of the joint, with fresh martensite observed in the weld metal. The hardness of the weld metal increased to 370–390 HV, while the base material retained its original hardness of 503 HV. The abrasive wear resistance coefficient reached k_b = 1.08 ± 0.01, representing an improvement of approximately 55% compared to the as-welded state.
- Surface examinations after abrasive wear testing revealed that, in the as-welded and normalized states, deep grooves, pits, and local material detachments predominated. Following the post-weld heat treatment, the surface was characterized by shallow, parallel scratches and traces of plastic deformation, indicating a shift in the dominant wear mechanisms towards microscratching and microplowing.
- The roughness parameter analysis confirmed a distinct differentiation of surface topography depending on the applied heat treatment condition. The highest values of all evaluated parameters were recorded for the as-welded joint, resulting from the presence of deep cavities and pits caused by the intensive penetration of abrasive particles. The application of post-weld heat treatment led to a clear surface smoothing effect, as reflected by the reduction in the ratio of depth-related parameters. Among the analyzed parameters, *Ra* and *Rq* demonstrated the strongest correlation with abrasive wear resistance, indicating their high prognostic relevance.
- Depth-related parameters, particularly their mutual relationship, can serve as sensitive indicators of the prevailing wear micromechanisms and the tribological response of materials. The analysis of the Rv/Rp ratio revealed that in the normalized state, wear processes are dominated by the formation of deep pits ($Rv/Rp > 1$), while after the post-weld heat treatment, their occurrence is significantly reduced, with wear mechanisms shifting towards microplowing and microscratching ($Rv/Rp < 1$).

Author Contributions: Conceptualization, M.Z. and B.B.; methodology, M.Z., B.B., M.S. and Ł.K.; validation, M.Z., B.B. and Ł.K.; formal analysis, M.Z. and B.B.; investigation, M.Z., B.B. and M.S.; resources, M.Z. and Ł.K.; data curation, M.Z. and B.B.; writing—original draft preparation, M.Z. and B.B.; writing—review and editing, M.Z., B.B. and Ł.K.; visualization, M.Z. and B.B.; supervision, Ł.K.; project administration, M.Z. and B.B.; funding acquisition, M.Z., B.B. and Ł.K. All authors have read and agreed to the published version of the manuscript.

Funding: This research received no external funding.

Institutional Review Board Statement: Not applicable.

Informed Consent Statement: Not applicable.

Data Availability Statement: The original contributions presented in the study are included in the article, further inquiries can be directed to the corresponding author.

Conflicts of Interest: The authors declare no conflicts of interest.

References

1. Frydman, S.; Konat, Ł.; Pękalski, G. Structure and Hardness Changes in Welded Joints of Hardox Steels. *Arch. Civ. Mech. Eng.* **2008**, *8*, 15–27. [CrossRef]
2. Baskutis, S.; Baskutiene, J.; Dragašius, E.; Kavaliauskiene, L.; Keršiene, N.; Kusyi, Y.; Stupnytskyy, V. Influence of Additives on the Mechanical Characteristics of Hardox 450 Steel Welds. *Materials* **2023**, *16*, 5593. [CrossRef] [PubMed]
3. Konat, Ł.; Zemlik, M.; Jasiński, R.; Grygier, D. Austenite Grain Growth Analysis in a Welded Joint of High-Strength Martensitic Abrasion-Resistant Steel Hardox 450. *Materials* **2021**, *14*, 2850. [CrossRef]
4. Białobrzeska, B.; Konat, Ł.; Jasiński, R. The Influence of Austenite Grain Size on the Mechanical Properties of Low-Alloy Steel with Boron. *Metals* **2017**, *7*, 26. [CrossRef]
5. Zuo, Z.; Haowei, M.; Yarigarravesh, M.; Assari, A.H.; Tayyebi, M.; Tayebi, M.; Hamawandi, B. Microstructure, Fractography, and Mechanical Properties of Hardox 500 Steel TIG-Welded Joints Using Different Filler Weld Wires. *Materials* **2022**, *15*, 8196. [CrossRef]
6. Teker, T.; Gencdogan, D. Heat Affected Zone and Weld Metal Analysis of HARDOX 450 and Ferritic Stainless Steel Double Sided TIG-Joints. *Mater. Test.* **2021**, *63*, 923–928. [CrossRef]
7. Gupta, A.; Sharma, V.; Kumar, P.; Thakur, A. Investigating the Effect of Ferritic Filler Materials on the Mechanical and Metallurgical Properties of Hardox 400 Steel Welded Joints. *Mater. Today Proc.* **2021**, *39*, 1640–1646. [CrossRef]
8. Prochenka, P.; Janiszewski, J.; Kucewicz, M. Crash Response of Laser-Welded Energy Absorbers Made of Docol 1000DP and Docol 1200M Steels. *Materials* **2021**, *14*, 2808. [CrossRef] [PubMed]
9. Turichin, G.; Kuznetsov, M.; Klimova-Korsmik, O.; Sklyar, M.; Zhitenev, A.; Kurakin, A.; Pozdnyakov, A. Laser-Arc Hybrid Welding of Ultra-High Strength Steels: Influence of Weld Metal Composition on Microstructure and Mechanical Properties. *Procedia CIRP* **2018**, *74*, 752–756. [CrossRef]
10. Konat, Ł. Structural Aspects of Execution and Thermal Treatment of Welded Joints of Hardox Extreme Steel. *Metals* **2019**, *9*, 915. [CrossRef]
11. Konat, Ł. Technological, Microstructural and Strength Aspects of Welding and Post-Weld Heat Treatment of Martensitic, Wear-Resistant Hardox 600 Steel. *Materials* **2021**, *14*, 4541. [CrossRef]
12. Valtonen, K.; Keltamäki, K.; Kuokkala, V.-T. High-Stress Abrasion of Wear Resistant Steels in the Cutting Edges of Loader Buckets. *Tribol. Int.* **2018**, *119*, 707–720. [CrossRef]
13. Barnes, N.; Joseph, T.; Mendez, P.F. Issues Associated with Welding and Surfacing of Large Mobile Mining Equipment for Use in Oil Sands Applications. *Sci. Technol. Weld. Join.* **2015**, *20*, 483–493. [CrossRef]
14. Gáspár, M. Effect of Welding Heat Input on Simulated HAZ Areas in S960QL High Strength Steel. *Metals* **2019**, *9*, 1226. [CrossRef]
15. Lee, H.W.; Yoo, K.J.; Tran, M.T.; Moon, I.Y.; Oh, Y.-S.; Kang, S.-H.; Kim, D.-K. Effect of Quenching-Tempering Post-Weld Heat Treatment on the Microstructure and Mechanical Properties of Laser-Arc Hybrid-Welded Boron Steel. *Materials* **2019**, *12*, 2862. [CrossRef] [PubMed]
16. Lu, Y.; Peer, A.; Abke, T.; Kimchi, M.; Zhang, W. Subcritical Heat Affected Zone Softening in Hot-Stamped Boron Steel during Resistance Spot Welding. *Mater. Des.* **2018**, *155*, 170–184. [CrossRef]
17. Bramowicz, M.; Kulesza, S.; Lewalski, P.; Szatkowski, J. Structural Studies of Welds in Wear-Resistant Steels. *Acta Phys. Pol. A* **2016**, *130*, 963–965. [CrossRef]
18. Krawczyk, R.; Słania, J.; Golański, G.; Zieliński, A. Evaluation of the Properties and Microstructure of Thick-Walled Welded Joint of Wear Resistant Materials. *Materials* **2022**, *15*, 7009. [CrossRef] [PubMed]
19. Uzunali, U.Y.; Cuvalcı, H.; Atmaca, B.; Demir, S.; Özkaya, S. Mechanical Properties of Quenched and Tempered Steel Welds. *Mater. Test.* **2022**, *64*, 1662–1674. [CrossRef]
20. Silva, A.P.; Węgrzyn, T.; Szymczak, T.; Szczucka-Lasota, B.; Łazarz, B. Hardox 450 Weld in Microstructural and Mechanical Approaches after Welding at Micro-Jet Cooling. *Materials* **2022**, *15*, 7118. [CrossRef]
21. Valtonen, K.; Ojala, N.; Haiko, O.; Kuokkala, V.-T. Comparison of Various High-Stress Wear Conditions and Wear Performance of Martensitic Steels. *Wear* **2019**, *426–427*, 3–13. [CrossRef]
22. Mondal, J.; Das, K.; Das, S. An Investigation of Mechanical Property and Sliding Wear Behaviour of 400 HV Grade Martensitic Steels. *Wear* **2020**, *458–459*, 203436. [CrossRef]
23. Jankauskas, V.; Žunda, A.; Katinas, A.; Tučkutė, S. Wear Study of Bulk Cargo Vehicle Body Materials Used to Transport Dolomite. *Coatings* **2025**, *15*, 227. [CrossRef]
24. Katinas, E.; Jankauskas, V.; Kazak, N.; Michailov, V. Improving Abrasive Wear Resistance for Steel Hardox 400 by Electro-Spark Deposition. *J. Frict. Wear* **2019**, *40*, 100–106. [CrossRef]
25. Haiko, O.; Javaheri, V.; Valtonen, K.; Kaijalainen, A.; Hannula, J.; Kömi, J. Effect of Prior Austenite Grain Size on the Abrasive Wear Resistance of Ultra-High Strength Martensitic Steels. *Wear* **2020**, *454–455*, 203336. [CrossRef]
26. Mukhamedov, A.A. Strength and Wear Resistance in Relation to the Austenite Grain Size and Fine Structure of the Steel. *Met. Sci. Heat Treat.* **1968**, *10*, 526–528. [CrossRef]

27. Rojacz, H.; Katsich, C.; Kirchgaßner, M.; Kirchmayer, R.; Badisch, E. Impact-Abrasive Wear of Martensitic Steels and Complex Iron-Based Hardfacing Alloys. *Wear* **2022**, *492–493*, 204183. [CrossRef]
28. Ratia, V.; Rojacz, H.; Terva, J.; Valtonen, K.; Badisch, E.; Kuokkala, V.-T. Effect of Multiple Impacts on the Deformation of Wear-Resistant Steels. *Tribol. Lett.* **2015**, *57*, 15. [CrossRef]
29. Lindroos, M.; Valtonen, K.; Kemppainen, A.; Laukkanen, A.; Holmberg, K.; Kuokkala, V.-T. Wear Behavior and Work Hardening of High Strength Steels in High Stress Abrasion. *Wear* **2015**, *322–323*, 32–40. [CrossRef]
30. Sundström, A.; Rendón, J.; Olsson, M. Wear Behaviour of Some Low Alloyed Steels under Combined Impact/Abrasion Conditions. *Wear* **2001**, *250*, 744–754. [CrossRef]
31. Gahr, K.-H.Z. Wear by Hard Particles. *Tribol. Int.* **1998**, *31*, 587–596. [CrossRef]
32. Jafari, A.; Dehghani, K.; Bahaaddini, K.; Abbasi Hataie, R. Experimental Comparison of Abrasive and Erosive Wear Characteristics of Four Wear-Resistant Steels. *Wear* **2018**, *416–417*, 14–26. [CrossRef]
33. Ojala, N.; Valtonen, K.; Heino, V.; Kallio, M.; Aaltonen, J.; Siitonen, P.; Kuokkala, V.-T. Effects of Composition and Microstructure on the Abrasive Wear Performance of Quenched Wear-Resistant Steels. *Wear* **2014**, *317*, 225–232. [CrossRef]
34. SSAB. *High-Strength Steel Sheet, Plate, Coil, Tube, Profile*; SSAB: Stockholm, Sweden, 2021.
35. Tarasiuk, W.; Napiórkowski, J.; Ligier, K. Impact of Slip Speed on the Wear Intensity of 38GSA and Hardox 500 Steels. *Q. Tribol.* **2018**, *280*, 121–125. [CrossRef]
36. Tarasiuk, W.; Napiórkowski, J.; Ligier, K.; Krupicz, B. Comparison of the Wear Resistance of Hardox 500 Steel and 20MnCr5. *Q. Tribol.* **2017**, *273*, 165–170. [CrossRef]
37. *EN 1011-2:2001*; Welding—Recommendations for Welding of Metallic Materials—Part 2: Arc Welding of Ferritic Steels. European Committee for Standardization: Brussels, Belgium, 2001.
38. *EN ISO 16834-A:2025*; Welding Consumables—Wire Electrodes, Wires, Rods and Deposits for Gas-Shielded Arc Welding of High-Strength Steels—Classification (System Based on Yield Strength + 47 J Impact Energy. ISO: Geneva, Switzerland, 2025.
39. ESAB. *Welding Consumables*; ESAB: North Bethesda, MD, USA, 2012.
40. *EN ISO 6508-1:2016*; Metallic Materials—Rockwell Hardness Test—Part 1: Test Method. ISO: Geneva, Switzerland, 2016.
41. *EN ISO 18265:2014*; Metallic Materials—Conversion of Hardness Values. ISO: Geneva, Switzerland, 2014.
42. *ASTM E407-07(2015)e1*; Standard Practice for Microetching Metals and Alloys. ASTM International: West Conshohocken, PA, USA, 2023.
43. *GOST 23.208-79*; Metallic Materials—Methods for Testing Wear Resistance Under Abrasive Conditions. Russian Technical Standard: Moscow, Russia, 1979.
44. *ISO 8486-2:1998*; Abrasive Grains—Testing—Part 2: Determination of Bulk Density. ISO: Geneva, Switzerland, 1998.
45. Hebda, M.; Wachal, M. *Tribology*; Scientific and Technical Publishing House: Warsaw, Poland, 1999.
46. Zemlik, M.; Konat, Ł.; Białobrzeska, B.; Stachowicz, M.; Hanszke, J. The Influence of Grain Size on the Abrasive Wear Resistance of Hardox 500 Steel. *Appl. Sci.* **2024**, *14*, 11490. [CrossRef]
47. Zemlik, M.; Konat, Ł.; Lemecha, M.; Ligier, K.; Napiórkowski, J. Tribological and Mechanical Aspects of the Welding and Post-Weld Heat Treatment of High Strength, Wear-Resistant Martensitic Boron Steel. *J. Tribol.* **2026**, *148*, 110271. [CrossRef]
48. Krishnan, S.N.; Toppo, V.; Basak, A.; Ray, K.K. Wear Behaviour of a Steel Weld-Joint. *Wear* **2006**, *260*, 1285–1294. [CrossRef]
49. Ligier, K.; Bramowicz, M.; Kulesza, S.; Lemecha, M.; Pszczółkowski, B. Use of the Ball-Cratering Method to Assess the Wear Resistance of a Welded Joint of XAR400 Steel. *Materials* **2023**, *16*, 4523. [CrossRef]
50. Ligier, K.; Napiórkowski, J.; Lemecha, M. Assessment of Changes in Abrasive Wear Resistance of a Welded Joint of Low-Alloy Martensitic Steel Using Microabrasion Test. *Materials* **2024**, *17*, 2101. [CrossRef]
51. Zhang, Y.; Liu, Z.; Wang, Y.; Chen, Z.; Liu, H.; Wang, X. Study on Microstructure and Sliding Wear Behavior of Similar and Dissimilar Welded Joints Produced by Laser-Arc Hybrid Welding of Wear-Resistant Steels. *Wear* **2025**, *562–563*, 205643. [CrossRef]
52. Roshanghias, A.; Barzegari, M.; Kokabi, A.H.; Mirazizi, M. The Effects of Functionally Graded Material Structure on Wear Resistance and Toughness of Repaired Weldments. *Mater. Des.* **2011**, *32*, 892–899. [CrossRef]
53. Jiang, W.J.; Liu, C.; He, C.G.; Guo, J.; Wang, W.J.; Liu, Q.Y. Investigation on Impact Wear and Damage Mechanism of Railway Rail Weld Joint and Rail Materials. *Wear* **2017**, *376–377*, 1938–1946. [CrossRef]

Disclaimer/Publisher's Note: The statements, opinions and data contained in all publications are solely those of the individual author(s) and contributor(s) and not of MDPI and/or the editor(s). MDPI and/or the editor(s) disclaim responsibility for any injury to people or property resulting from any ideas, methods, instructions or products referred to in the content.

applied sciences

MDPI

Article

Impact of Beam Shape and Frequency on Weld Seam Geometry and Penetration Depth Using a Coherent Beam Combining Laser

Karthik Ravi Krishna Murthy *, Reza Sanei, Abhay Sharma, Simon Olschok and Uwe Reisgen

Welding and Joining Institute, RWTH Aachen University, 52062 Aachen, Germany
* Correspondence: karthik.krishnamurthy@isf.rwth-aachen.de

Abstract

The geometry and quality of a weld seam are critical factors in laser beam welding, influencing mechanical performance and structural integrity. Dynamically modulated laser beams provide a precise means of tailoring energy input in high-power laser welding processes. This study investigates the influence of beam shape and modulated frequency on weld seam geometry, penetration depth, and capillary behaviour using a coherent beam combining (CBC) laser system from Civan Lasers. Three beam intensity distributions—single point, line–point–line (LPL), and boomerang—were applied across a modulation frequency range of 1, 10, and 100 kHz during the welding of duplex and austenitic stainless steels. High-speed imaging captured real-time capillary dynamics, and the data were analysed to assess capillary stability, measure capillary diameter, and determine the capillary front angle as a function of frequency and beam shape. Transverse cross-sections of the welds were prepared to evaluate seam geometry and microstructure. The results show that beam shape significantly affects energy distribution and weld profile, while modulation frequency critically influences capillary behaviour and penetration characteristics. These findings highlight the critical role of dynamic beam shaping and frequency modulation in optimizing laser welding processes for material-specific performance, offering a versatile platform for advancing precision manufacturing using CBC technology.

Keywords: coherent beam combining; beam shape; beam frequency; capillary behaviour; penetration characteristics; microstructure

1. Introduction

Laser beam welding is widely recognised as a high-precision joining technique that is particularly suited for applications demanding high mechanical strength and structural reliability. Its key advantages include confined fusion and heat-affected zones and minimal thermal distortion, which make it an ideal process for welding advanced and high-performance alloys [1,2]. Weld seam geometry and quality play a vital role in ensuring both the functionality and durability of safety-relevant components. Achieving consistent seam formation requires precise control of energy input, which depends on multiple factors including welding speed, laser wavelength, shielding conditions, and, most critically, the spatial intensity distribution of the laser beam on the workpiece. This intensity profile governs the local heat distribution, which significantly influences capillary formation and stability, and thus directly affects the weld quality [3,4]. While Marangoni convection is the dominant mechanism driving melt pool flow in conduction mode laser welding, the transition to the keyhole regime introduces additional influencing forces, including recoil pressure, vapour-induced shear stress, and capillary effects, resulting in significantly more

complex melt flow behaviour [5]. However, keyhole stability in the melt pool is widely recognised as a primary determinant of weld quality in deep penetration laser welding processes [6].

1.1. Research Background

High-energy welding processes benefit significantly from the ability to dynamically modulate the laser beam, which enables spatially and temporally resolved control of heat distribution in the workpiece. Dynamic beam shaping (DBS) has emerged as a promising technique in this context, offering innovative approaches to process control, particularly by modifying temperature gradients during the cooling phase, which, for example, can help in reducing hot-cracking in Al-alloys via beam shapes generated by laser beam oscillation [7]. Coherent beam combining (CBC) represents a more complex strategy in this category, enabling the customization of beam intensity profiles to achieve targeted melt pool dynamics and enhance overall welding quality. In order to form a CBC laser, the outputs of several single-mode fibre lasers (array) are combined while their light waves remain in phase. Using optical phase modulators, the electromagnetic waves reinforce each other constructively upon the target. The outputs are sorted in a two-dimensional array (optical phased array—OPA), and their beams are optically overlapped into one strong laser beam at a desirable focus point. This enables higher power, high beam quality, and—most importantly—dynamic control over the beam's phase, shape, and direction. What makes these types of lasers unique is their ability to create different types of intensity distributions (beam shapes), from classic spots, rings, and multiple spots to whole lines and complex shapes, and to change them practically in real time without relying on expensive and maintenance-intensive optics to generate mostly static, non-complex beam shapes, as is the case with conventional lasers. For instance, the maximum modulation frequency of OPA CBC lasers is 80 MHz, while the shortest possible lifetime of a single point is only 12.5 ns. For Civan CBC lasers in particular, a shape can consist of a maximum number of 1024 single points, while it is also possible to generate a sequence of up to 14 different shapes. For example, these shapes can be used for controlling the melt pool in the laser welding of copper, a material known for high thermal conductivity and difficult-to-weld melt pool viscosity [8,9]. It is also notable that this type of laser system does not need any mechanical mirrors or galvos to focus steering (unlike conventional lasers), since its phase control is electronic. This enables it to compete with welding strategies that were previously used mainly in electron beam welding (e.g., stirring the heat distribution in a weld pool in real time). Additionally, the used Civan laser system is capable of dynamically switching between beam patterns in real time, ranging from microseconds to several MHz. This gives the user an additional level of control over the laser welding process that goes beyond the capabilities of conventional lasers and other CBC systems, opening up a major research gap in the field of capillary, material, and weld seam geometry control. CBC lasers are capable of generating variable intensity distributions at high power levels. By combining tailored beam shapes with defined modulation frequencies, the beam–material interaction can be selectively adjusted to control melt pool dynamics and capillary behaviour [9–12]. This, in turn, has a direct impact on the resulting weld seam geometry. Troise et al. state that beam shapes such as the "boomerang" widen the weld seam and reduce the size of the upper bead, while there are significant differences when changing the frequency at which the shape is generated between 0.1 and 100 kHz. The higher frequency does lead to a coarser grain and a very wide heat-affected zone (HEZ) [13]. Active control of capillary behaviour is crucial, since the collapse of the keyhole may result in defects such as porosity and spatter-induced blow-outs [14]. Another capillary-related issue—although already problematic for conventional lasers— that can negatively influence welding results

with CBC lasers is the sensitivity of the projected beam shape to process plume during deep penetration welding. It can be controlled using a cross-jet placed directly above the workpiece, so that no welding fumes cross the beam path [15,16]. Table 1 summarizes a short selection of works relevant to this field.

Table 1. A selection of previous work in this field.

Reference	Beam Shaping Technology	Power [kW]	Material	Scope of Work/Influence on
[3]	FRM	4	Pure Nickel	Process dynamics
[7]	DBS Oscillated	5	Al-alloys	Hot crack sensitivity
[9]	DPS OPA	14	Stainless	Technology Benchmark
[8]	DBS OPA	14	Copper	Melt pool control
[13]	DBS OPA	14	Steel	Seam & melt pool geometry
[17]	FRM	2.4	Stainless	Capillary depth fluctuation
[18]	FRM	4	Stainless	Microstructure & mechanical prop.

1.2. Related Research

To date, efforts to specifically manipulate capillary behaviour by modulating intensity distributions have predominantly employed combinations of ring and core lasers as well as flexible ring mode lasers (FRMs) or classic oscillation [3,7]. For example, Xie et al. stated that for stainless steel, the ring part of an FRM laser is not only capable of reducing welding spatter but also has a notable impact on columnar grain size and ferrite density. This is explained by the lower temperature gradient in the melt pool, which is due to a diluted heat source that is achievable with an FRM laser [18]. An even simpler approach to adding a ring laser source to a central core laser can benefit the welding process, as shown by Zaiß et al., and therefore improve the welding results. This welding strategy can reduce capillary fluctuation through the production of a wider melt pool and a deceleration of melt velocities, which is beneficial for high–speed laser welding of stainless steel [17]. As previously mentioned, these strategies primarily aim to stabilize the capillary and prevent its collapse—a key mechanism underlying welding defects such as porosity and spatter in deep penetration laser welding [19]. It is worth noting that beam shaping influences not only capillary stability but also the spatial characteristics of the melt pool [20–22]. The complex process of scanning a dynamic beam shape can be compared to the simpler circular oscillation employed in conventional laser scanners. While the latter is generally considered a less sophisticated approach, it still enables effective control of capillary and melt pool behaviour, contributing to pore reduction and enhanced degassing [23]. Oscillating and stirring of the laser beam further contribute to a reduction in temperature gradients and melt pool flow velocities, which can in turn lead to improved weld quality [24]. As shown in many research articles—both experimental and simulated—a direct correlation between capillary and seam geometry can easily be drawn. The shape and depth of the capillary changes with the welding speed, which in turn affects the resulting weld penetration depth and seam shape, as well as the frequency of welding defects such as porosity [9,11,25,26]. This can also be influenced by the intensity distribution. Among other things, ray tracing of the laser radiation arriving on the surface also plays a role here, as it is absorbed and reflected back to varying degrees depending on the actual condition of the capillary. The influence of the metal vapour plume on the beam reflection in the keyhole should also not be neglected. Furthermore, different intensity distributions not only affect the weld seam

geometry but also lead to the development of distinct grain structures. This is attributed to variations in melt pool morphology and thermal gradients, which govern the direction and mode of grain growth during solidification [27–29]. The heat input—adjustable via laser intensity distribution in conjunction with power and travel speed or with varying oscillation diameters—plays a key role in determining the microstructure of stainless steels. In duplex stainless steels, the resulting phase balance is influenced not only by alloy composition but also by cooling conditions; elevated heat input promotes austenite formation by lowering the ferrite fraction through reduced cooling rates [30,31]. Ferrite in austenitic stainless steels exhibits a higher solubility for impurities such as sulfur and phosphorus. This helps to reduce their segregation into interdendritic regions, where the formation of low-melting-point phases can promote hot cracking and degrade mechanical properties. In duplex stainless steels, however, an excessive ferrite content can impair both corrosion resistance and toughness. Therefore, precise control of the ferrite fraction is essential. While the ferrite–austenite balance is primarily determined by the steel's chemical composition, in duplex steels it can also be influenced by cooling rates, particularly when the preceding heat input is relatively high [32].

1.3. Significance of the Work

Considering the state of the art regarding investigations of the impact of beam shape and frequency on weld seam geometry and penetration depth, to date, studies have mostly focused on simple beam shapes and slower oscillation frequencies or materials other than stainless steel (primarily copper and aluminium), which (by design) do not take into account the simultaneous influence of complex CBC-generated beam shapes and their high frequency oscillation on the steel's austenite–ferrite ratios. While the influence of conventional oscillation and non-CBC beam shaping strategies on cooling rates and the microstructure of stainless steels is fairly well investigated, there is an inescapable research gap regarding investigations of the behaviour of stainless steels in response to complex shape–sequence–frequency combinations that are only achievable with specialized CBC systems such as the Civan Laser System. Therefore, there is a clear need for more in-depth research regarding the contributions that Civan's significantly more complex CBC lasers can make to topics such as capillary control and dimensions, weld seam geometry, the resulting microstructure. Moreover, it is essential to identify and understand the novel challenges introduced by the increased number of adjustable parameters and the high dynamic behaviour inherent to the Civan CBC process, both from a research and application standpoint. Additionally, investigations are required to determine which specific combinations of beam shape, sequence, and oscillation—particularly those not applicable to conventional systems—can provide the greatest possible control of the most important weld pool properties, and which are fundamental for the subsequent welding result. In this context, the simultaneity of the available combinations and the ability to switch between them in near real time should also be considered a unique feature of this technology. The combination of near real-time adjustable, highly dynamic energy distribution and its influence on the weld pool behaviour in stainless steel is therefore a major research gap, building upon which, more in-depth investigations can be carried out considering individual aspects of the CBC laser system. This work is intended to lay the foundation for future work in this area. In contrast to previous work, novel evaluation methods will be used to demonstrate the influence of CBC lasers on capillary geometry—notably in real time—using high-speed imaging and complex measurement techniques. In summary, CBC represents a promising approach for reducing welding defects and enhancing weld seam quality. This study aims to systematically investigate the influence of various beam shapes and modulation frequencies on key process characteristics

of laser beam welding. Particular attention is paid to weld seam geometry, penetration depth, microstructural evolution, and the dynamic behaviour of the vapour capillary—all of which serve as indicators of process stability and energy input distribution.

2. Materials and Methods

The flowchart summarizes the overall methodology and structure of this work (Figure 1). In this study, high-alloy austenitic steel (1.4301) and Duplex steel measuring 100 × 50 × 4 mm were employed as the base materials for welding. Austenitic steel was chosen due to its known susceptibility to solidification cracking (hot cracking) during welding, primarily caused by its low thermal conductivity. Duplex steel, on the other hand, was selected for its thermally sensitive and complex dual-phase microstructure. Varying heat input during welding can alter the ferrite–austenite phase balance, directly affecting its corrosion resistance. These contrasting thermal and metallurgical characteristics make both steels ideal test materials for investigating the influence of beam shape and frequency on weld quality parameters such as hot cracking, grain structure, and weld pool dynamics.

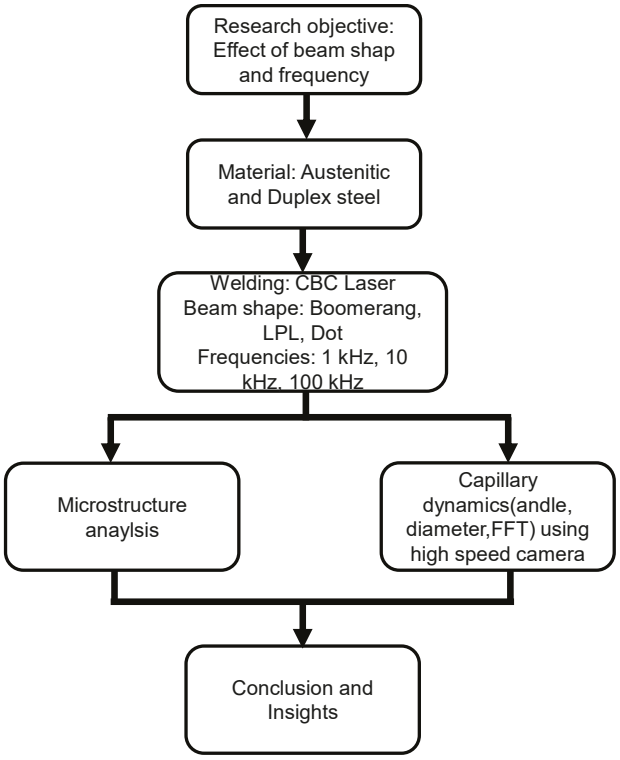

Figure 1. Research workflow overview.

The welding was performed with the help of a CIVAN High Power Single Mode CW Dynamic Beam Laser, which delivers laser radiation with a wavelength of 1064 nm in an optical phased array by combining multiple single mode fibre lasers. In this work, three beam shapes were generated—namely dot, boomerang and line-point-line (LPL). Where the dot is a continuous weld (CW) and the other two beam shapes are oscillated in the frequency range of 1, 10, and 100 kHz, as depicted in Figure 2. A laser power of 6 kW and a welding speed of 2 m/min were used for all the trials (Table 2).

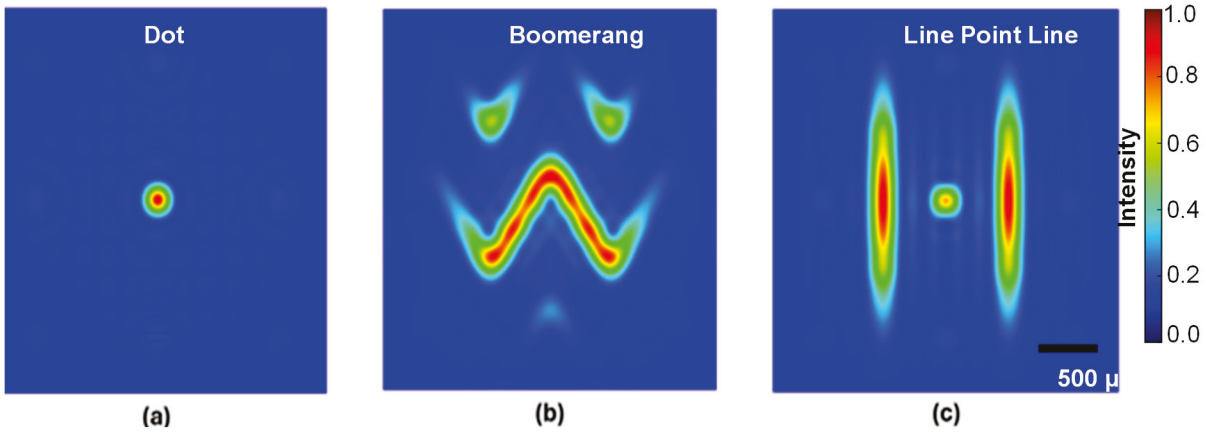

Figure 2. Dynamically generated laser beam with the shapes—(**a**) dot, (**b**) boomerang and (**c**) LPL.

Table 2. Welding parameters with beam shape and frequency.

Material	Beam Shape [-]	Frequency [kHz]	Power [kW]	Welding Speed [m/min]
Austenitic steel/Duplex steel	Dot	CW	6	2
	Boomerang	1, 10, 100	6	2
	LPL	1, 10, 100	6	2

To investigate the influence of beam shape and oscillation frequency on capillary dynamics during laser welding, a high-speed camera (Photron SA4, Photron Limited, Tokyo Japan) was employed to capture the weld process from multiple perspectives. All recordings were conducted at a frame rate of 10,000 to 100,000 frames per second (fps).

To analyse capillary fluctuations and the capillary diameter of the weld seam, bead-on-plate welds were performed at the centre of the specimen, and the camera was positioned at an inclined top-view angle relative to the welding axis (Figure 3a). This setup enabled visualization of the capillary opening and capillary diameter during beam oscillation. To examine the capillary front and its angular orientation, an edge-welding configuration was implemented. In this setup, welding was performed along the edge of the plate, which was optically coupled with a 5 mm thick quartz glass window. This allowed side-view imaging of the capillary front through the transparent medium (Figure 3b), ensuring unobstructed visualization of the capillary inclination and front-wall stability under varying beam conditions. These imaging configurations provided critical insights into the interaction between beam modulation parameters and capillary dynamics, which are directly correlated with weld stability and defect formation.

High-speed imaging data acquired using the Photron SA4 high-speed camera were post-processed using custom MATLAB 2024a scripts to extract quantitative information about capillary dynamics and capillary geometry.

a. Capillary Fluctuations:
To investigate the dynamic behaviour of the capillary, it was hypothesized that the capillary opening and closing would be influenced by the corresponding beam oscillation. Whenever the capillary opens, the laser radiation would enter it and be scattered by the vapour particles present. This scattering would result in a periodic change in the intensity of the pixels within the capillary. A MATLAB script was written to quantify this behaviour, calculating the cumulative intensity of all the pixels grayscale values within the region of interest where the vapour capillary was formed. The cumulative sum of the grayscale values was then plotted against

the frame number, depicting the time axis. Finally, a fast Fourier transform was performed on the intensity change data to identify the dominant frequencies.

b. Capillary front wall inclination:
It is known that the capillary front wall exhibits a change in its angle as the workpiece experiences a translative motion relative to the incident laser. To be able to quantify the same, a MATLAB code was written to reduce the noise in the video playback and binarize the frame data to highlight the vapour capillary. The code then identified the left boundary of the capillary and used the RANSAC algorithm to fit a line to the identified boundary points, as seen in Figure 4. The slope of the line was then plotted per frame. An angular constraint between 60°and 90° from the horizontal was set to avoid fluctuations arising due to noisy data.

c. Capillary dynamics:
The dynamics of the welding process are governed by the fluctuation of the capillary shape. So, avoiding the occurrence of defects in the seam by means of controlling the capillary stability is of significance. A MATLAB script was written to automatically track and analyse the capillary region from the high-speed videos. It processes grayscale frames, segments the capillary based on intensity characteristics as seen in Figure 5, tracks its area and thereby its diameters over time, and performs an FFT analysis on the change of diameter data. The underlying assumption here is that the capillary is circular, to meaningfully manipulate the diameter data to find its dependency on beam shape and oscillation frequency.

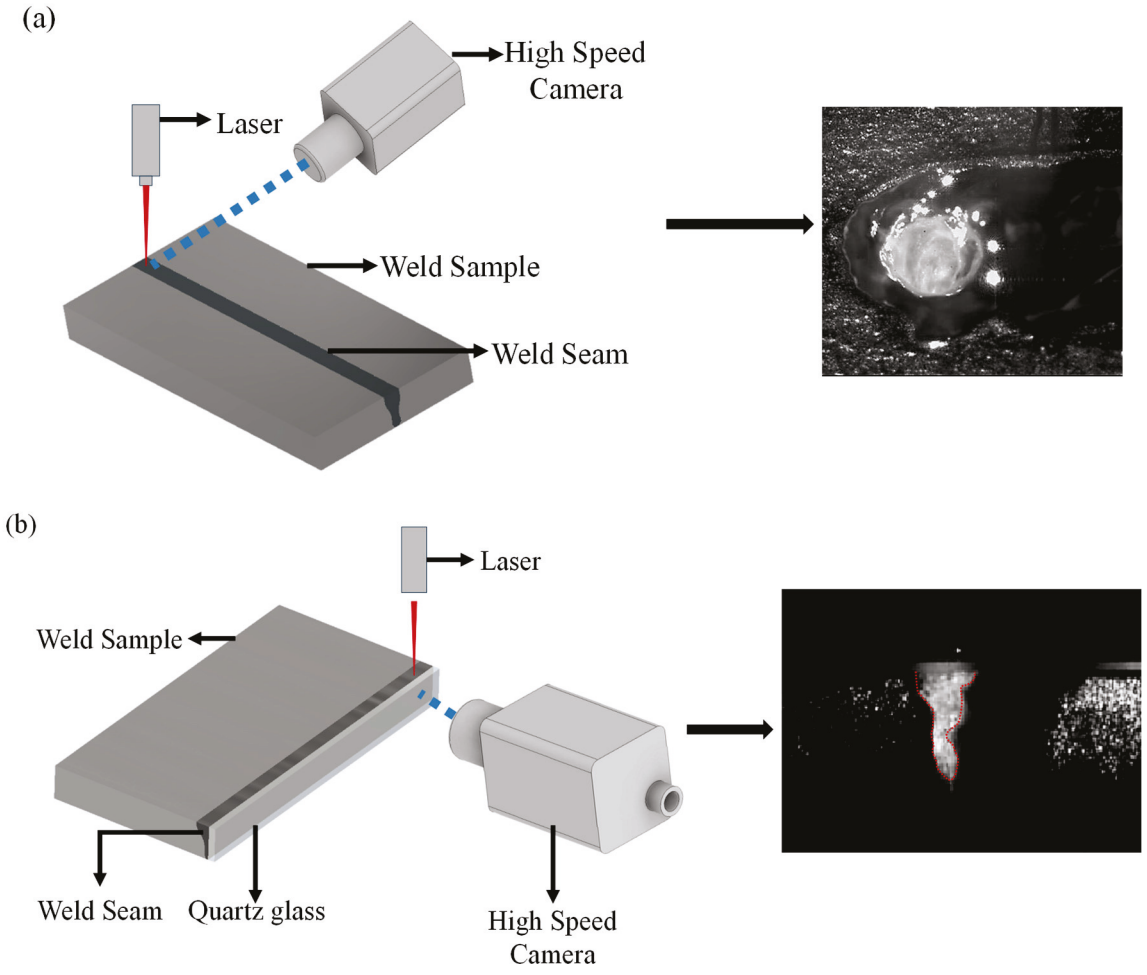

Figure 3. Experimental setup of the laser welding process with high-speed camera—(**a**) Camera positioned at an inclined top-view angle, (**b**) Camera positioned horizontal to the weld.

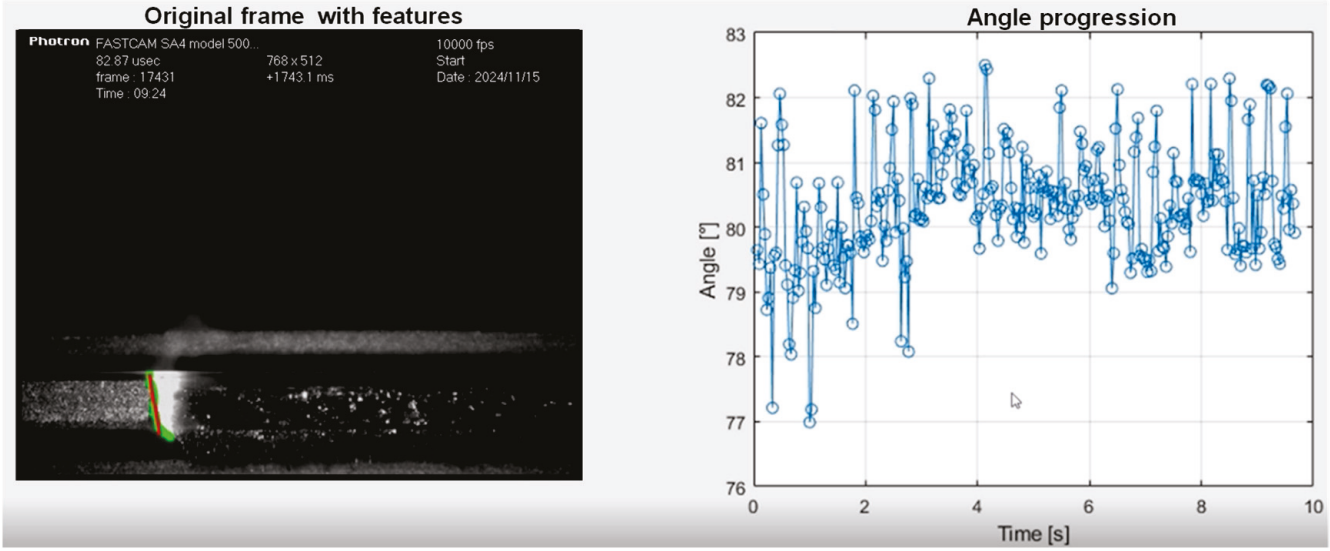

Figure 4. Identified points for the capillary front (green) and fitting line (red) (**left**) and the angle between the fitted line and the horizontal plotted over time (**right**).

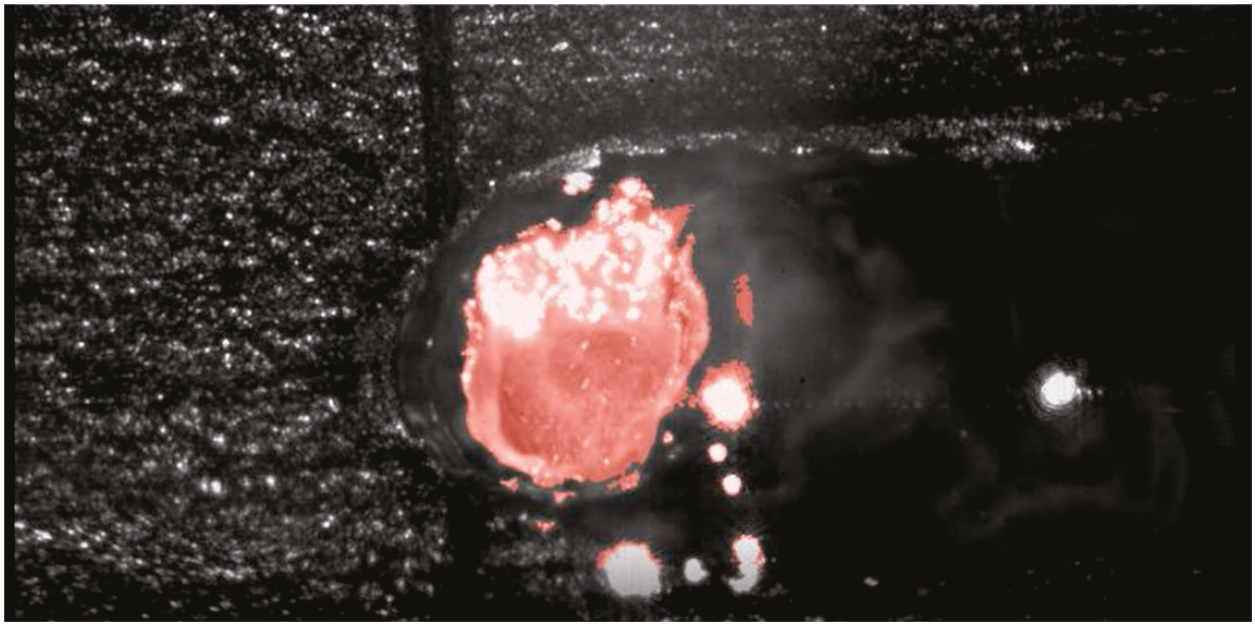

Figure 5. Capillary isolation using MATLAB script.

In addition, metallographic cross-sections were prepared to analyse the weld seam geometry and to establish correlations with the applied dynamic beam parameters. The cross sections are arranged in a matrix format, where the vertical column represents the steel and beam shape, and the horizontal row represents the frequency (Figure 6). As the frequency does not have any major implications for the dot beam shape, the cross section that represents the dot was welded with a 1 kHz beam frequency. The first image of the dot is austenitic steel, and the second is duplex steel.

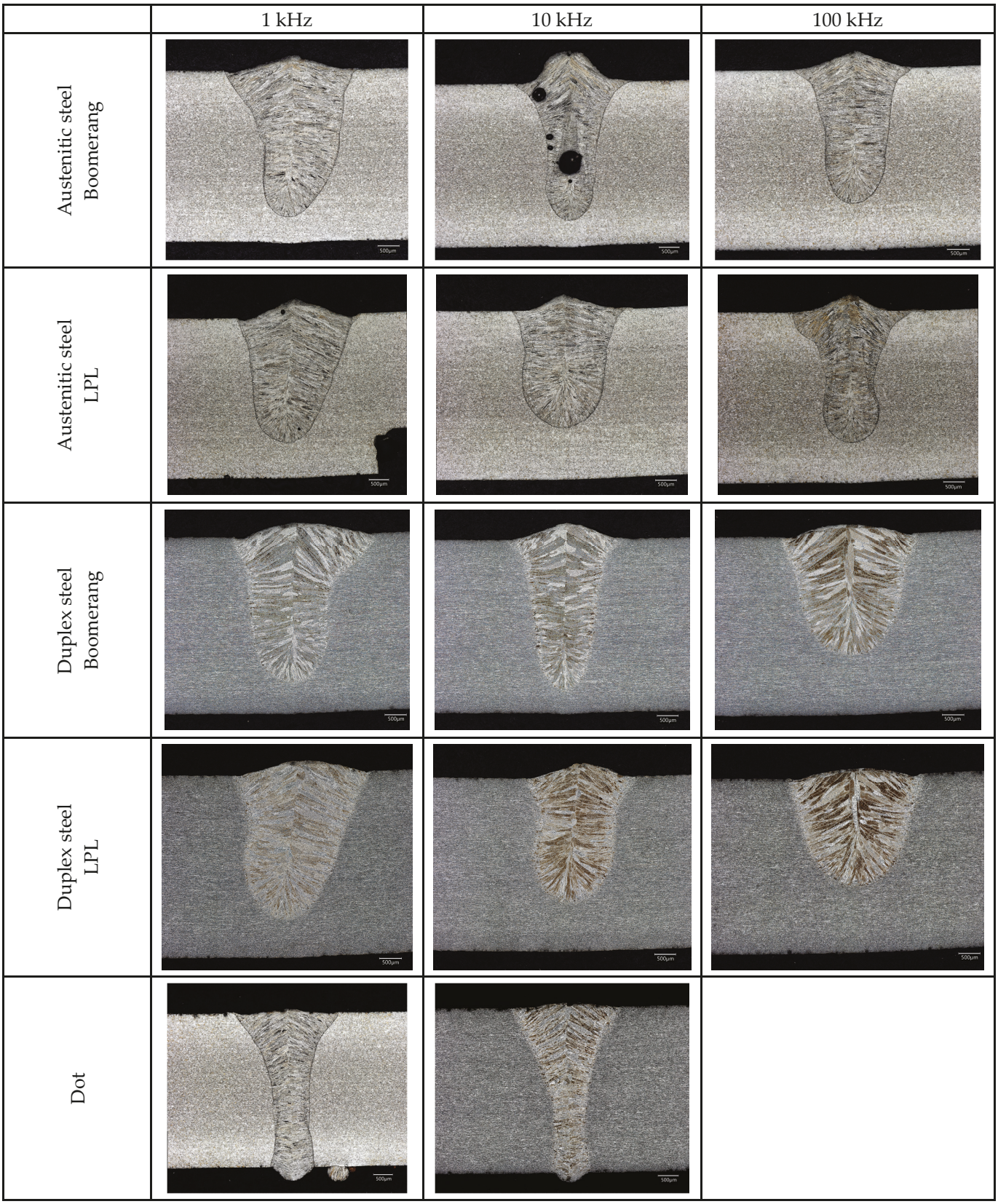

Figure 6. Weld seam cross-section for austenitic and duplex steel using a dynamically generated laser beam.

3. Results and Discussion

This section presents a comprehensive analysis of the effects of beam shape and frequency on weld seam geometry, microstructural evolution and capillary dynamics during laser welding of austenitic and duplex stainless steels using a CBC laser source. The findings are derived from a combination of metallographic cross-section analysis, high-speed imaging, and quantitative post-processing of the acquired data. Key parameters such as capillary fluctuations, capillary diameter, front wall inclination, and weld depth are examined in relation to the applied beam modulation conditions. Preliminary microstructural observations are also correlated with different beam configurations.

3.1. Effect of Beam Shape and Frequency on Weld Seam Geometry

The geometry of the weld seam is significantly influenced by both beam shape and oscillation frequency. To ensure a comparative study, the welding parameters were kept constant across all beam shapes, frequencies, and materials. As illustrated in Figure 6, for both austenitic and duplex steels, the dot beam shape results in a narrow and deep capillary, producing through-penetration welds. This is attributed to the localized energy concentration inherent to the dot shape. In contrast, the boomerang and LPL shapes distribute the energy over a wider area, leading to shallower and less penetrative welds under the same conditions.

As the oscillation frequency increases from 1 kHz to 10 kHz, the weld seam becomes more stable. Interestingly, despite the increased frequency, weld depth is maintained or even slightly increased, suggesting that dynamic beam shaping enhances melt pool control without sacrificing penetration. This behaviour is particularly evident in duplex steel, where more uniform heat distribution contributes to smoother weld profiles. However, in austenitic steel using the boomerang shape at 10 kHz, it is observed that the capillary is unstable, leading to the formation of porosity in the weld seam.

At 100 kHz, a significant broadening of the weld seam is observed, especially in duplex steel. This is likely due to the high thermal conductivity property and the reduced beam interaction time per unit area at high frequency, which causes the laser energy to be distributed more evenly across the oscillation path. Consequently, while weld depth slightly decreases, weld width increases, reflecting a shift from deep-penetration to conduction-mode welding.

Furthermore, for the same beam shapes (Boomerang (BR) and LPL) at 100 kHz, austenitic steel exhibits greater weld depth than duplex steel. This can be attributed to the lower thermal conductivity of austenitic steel, which reduces heat dissipation from the fusion zone, enabling higher peak temperatures and deeper penetration. It is also observed that the weld seams are not symmetric, and this is because the beam shape is rotated by 15° due to the mirror structure in the scanner.

A comprehensive overview of the weld seam depth across different beam shapes, frequencies, and materials is presented in Figure 7.

To further understand the mechanisms underlying the observed changes in weld seam geometry presented in Sections 3.1–3.3 explore the microstructural evolution and capillary dynamics, respectively, as a function of beam shape and modulation frequency. These aspects are intrinsically linked to weld formation, as they influence heat distribution, solidification behaviour, and energy absorption efficiency.

The microstructural analysis in Section 3.2 supports the macroscopic weld profile trends by revealing how thermal gradients and cooling rates, governed by beam dynamics, affect grain structure and phase balance. In parallel, the high-speed imaging results in Section 3.3 provide direct insights into capillary behaviour and stability. Together, these

sections provide an understanding of the overall impact of dynamic beam shaping and frequency modulation on the weld seam.

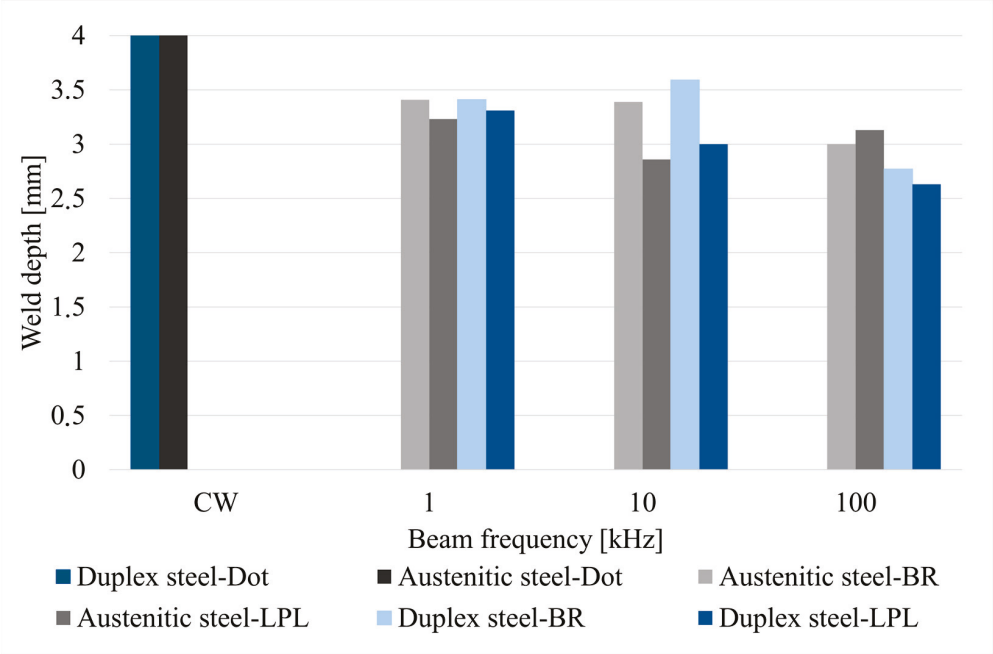

Figure 7. Weld depth comparison for different beam shapes and frequencies.

3.2. Weld Microstructure

Austenitic steel:

The weld zone predominantly consists of columnar austenite with interdendritic delta ferrite. At lower beam frequencies, rapid solidification favoured the formation of fine dendritic grains. As the beam frequency increased, grain size increased significantly due to a decrease in cooling rate. Higher frequencies caused the oscillating beam to broaden the molten pool, extending the solidification time and allowing grains to coarsen. This coarsening effect was most evident in the fusion zone near the weld centre. From Figure 8, the percentage area of the grain boundaries was calculated using ImageJ software (https://imagej.net/ij/, accessed on 18 June 2025). A comparative analysis between the dot and boomerang beam shapes revealed that, with increasing beam frequency, the percentage area of grain boundaries decreased, particularly in the boomerang configuration. This trend is attributed to asymmetric temperature gradients induced by the beam shape. As frequency increased, the molten pool became wider, reducing the local cooling rate at the weld centre. This, in turn, promoted the growth of larger, columnar or coarsened equiaxed grains.

Dot [CW]	Boomerang 1 kHz	Boomerang 10 kHz	Boomerang 100 kHz
	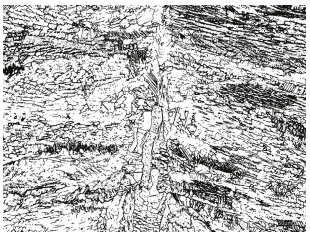	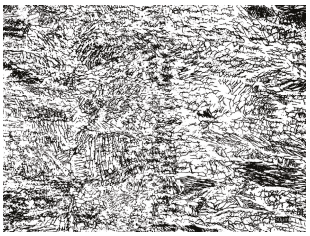	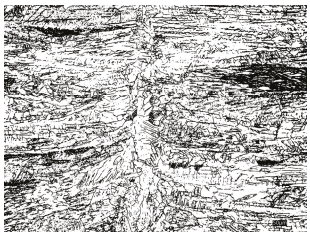
% of Area: 21.74	% of Area: 14.66	% of Area: 15.80	% of Area: 11.51

Figure 8. Microstructure at the centre of the weld seam for boomerang beam shape.

A similar trend was also noticed in the microstructure generated using the LPL beam shape in the case of 1 and 10 kHz. However, at 100 kHz, a finer equiaxed grain structure is developed as the weld seam geometry changes from a tapered weld seam to a nail head weld seam geometry as seen in Figure 6. This transformation is mainly due to the delivery of a symmetric concentrated energy by the combination of line-point-line, where the point is responsible for the generation of a deeper weld. This deep weld leads to fast cooling, resulting in a finer grain structure as seen in Figure 9. The percentage area of the grain boundary for the LPL beam shape at 100 kHz is found to be the highest (~17.3%) after the dot beam shape (~21.7%).

LPL 1 kHz	LPL 10 kHz	LPL 100 kHz
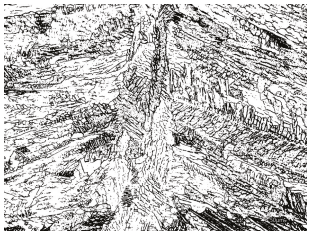	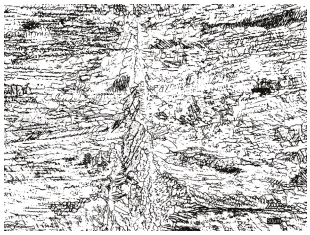	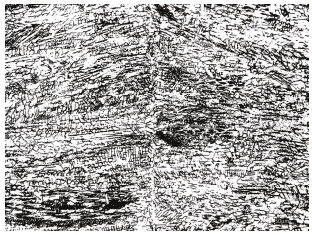
% of Area: 8.9	% of Area: 6.36	% of Area: 17.32

Figure 9. Microstructure at the centre of the weld seam for LPL beam shape.

Duplex steel: Duplex steel welds displayed a dual-phase microstructure of ferrite and austenite. At lower beam frequencies, the weld seam showed an acceptable balance between austenite and ferrite in the range of 24.90%–21.21%. However, at high frequencies (100 kHz), reduced cooling rates and altered thermal gradients promoted excessive ferrite at the weld centre. The austenitic phase fraction for both the beam shape and frequencies was calculated using ImageJ software. The highest austenitic phase fraction (28% in the weld seam) was observed using the dot beam shape. The calculated austenitic phase fractions for both beam shapes are illustrated in Figures 10 and 11. Improper phase balance in duplex steel can negatively affect corrosion resistance and mechanical properties. Therefore, it is important to select the beam shape and frequency based on the application.

Dot [CW]	Boomerang 1 kHz	Boomerang 10 kHz	Boomerang 100 kHz
		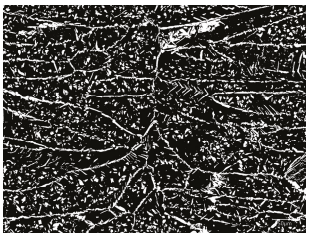	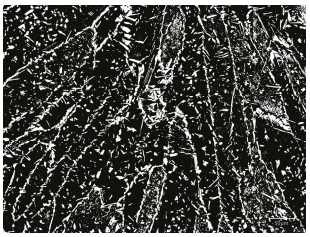
Austenite fraction: 28%	Austenite fraction: 23.5%	Austenite fraction: 21.5%	Austenite fraction: 20.6%

Figure 10. Microstructure at the centre of the weld seam for boomerang and dot beam shapes.

Overall, the analysis demonstrates that both the beam shape and oscillation frequency significantly influence the local energy density distribution, which in turn affects the seam morphology, microstructure, and penetration profile during welding.

LPL 1 kHz	LPL 10 kHz	LPL 100 kHz
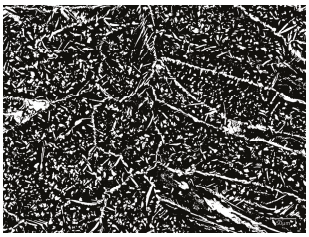	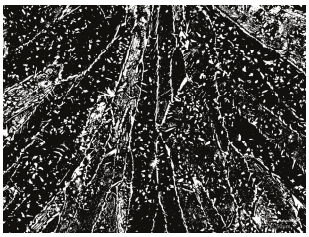	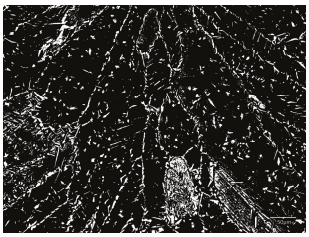
Austenite fraction: 24.9%	Austenite fraction: 21.2%	Austenite fraction: 11.9%

Figure 11. Microstructure at the centre of the weld seam for LPL beam shape.

3.3. Influence of Beam Oscillation on Capillary Dynamics and Stability

The dynamic interaction between beam oscillation frequency, beam shape, and capillary behaviour was analysed using high-speed imaging at 10,000 fps and 100,000 fps, enabling time-resolved studies at 1 kHz and 10 kHz modulation frequencies. This allowed for accurate characterisation of the capillary and capillary fluctuations across different material conditions.

Capillary Fluctuations:

For both austenitic and duplex stainless steels, fast Fourier transform (FFT) analysis of the cumulative grayscale intensity within the vapour capillary region revealed distinct frequency peaks at approximately 993 Hz (for 1 kHz oscillation) and 9886 Hz (for 10 kHz oscillation). These frequencies correspond to the periodic opening and closing of the capillary, modulated by the oscillation of the beam. This strongly supports the hypothesis that beam dynamics directly influence energy absorption efficiency by modulating capillary geometry and exposure time, thereby affecting laser–material interaction. Figure 12 shows the FFT of the change in cumulative pixel intensities of the capillary for both 1 kHz and 10 kHz.

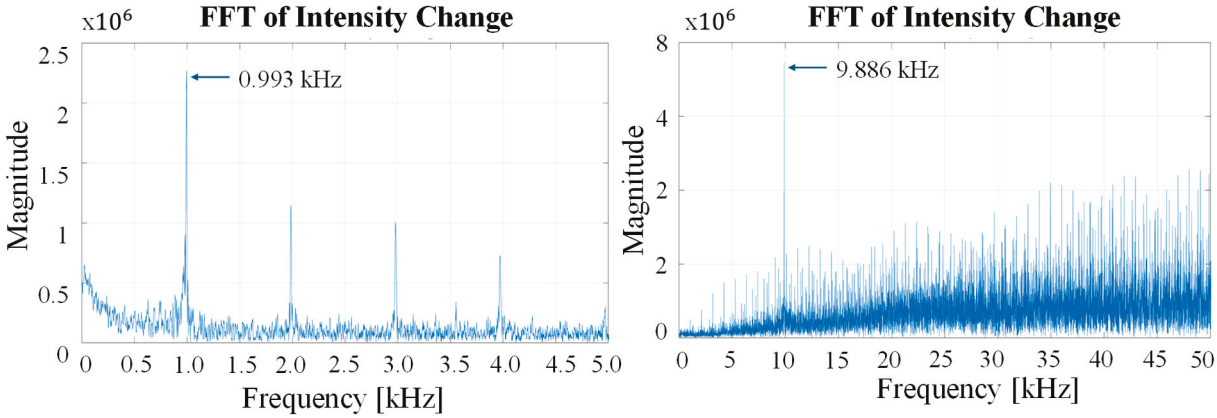

Figure 12. Graph depicting FFT of change in cumulative pixel intensities of the capillary for (**left**) 1 kHz boomerang beam oscillation and (**right**) 10 kHz boomerang beam oscillation.

The FFT-based analysis of grayscale intensity fluctuations is used here as an indirect indicator of capillary dynamics, based on the assumption that increased brightness corresponds to laser radiation entering the vapour capillary during its opening phases, enhanced by internal reflection and scattering within the keyhole. However, this interpretation has inherent limitations. Other dynamic phenomena, such as metal vapour formation, recoil pressure-induced melt pool motion, and thermal radiation, can also contribute to pixel intensity variations. Ideally, isolating these individual effects requires complementary

diagnostics, such as thermal imaging or Schlieren-based techniques, to distinguish between capillary behaviour and plume dynamics. Further work is focused on correlating intensity fluctuations with independent measurements of plume behaviour to refine this interpretation. Despite these limitations, the current approach offers a reasonable first-order approximation of capillary dynamics in response to beam modulation.

In parallel, the inclination angle of the capillary front wall was extracted frame-by-frame using MATLAB-based image analysis. The inclined wall geometry enhances absorption via repeated Fresnel reflections, which increases the effective path length of the laser inside the material. In this study, an increase in beam oscillation frequency for both the boomerang and line-point-line (LPL) beam shapes resulted in a positive capillary front angle, indicating a forward tilt of the capillary wall in the direction of welding. At lower frequencies (1 kHz), the capillary angle approached 0° (neutral), which was particularly evident in the dot beam configuration. This neutral orientation led to deeper penetration, attributed to the maximised recoil pressure acting directly downward into the material. In contrast, at higher frequencies, the positive capillary angle distributed energy over a wider area, promoting shallower penetration, greater capillary fluctuation, and wider melt pools. FFT analysis of the inclination angle also revealed the oscillation frequency as the dominant component, confirming that the beam motion also modulates the capillary front wall. This directly links beam oscillation to capillary shape evolution, further impacting melt pool dynamics and heat input localisation Figure 13.

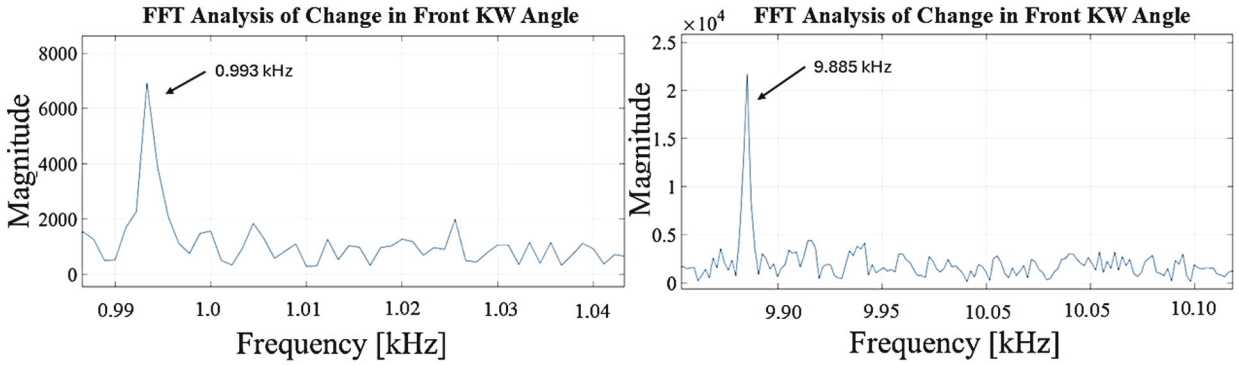

Figure 13. Angle of deflection of the capillary front as a function of frame number (**left**) and Fast Fourier Transform of the change in the angle (**right**).

Capillary diameter and beam shape dependence:

The capillary diameter was plotted as a function of beam shape and oscillation frequency. Among the tested shapes: dot, LPL, and boomerang, the LPL and dot configurations consistently exhibited larger capillary diameters, while the boomerang shape resulted in a smaller and more constricted capillary. This is attributed to the greater area coverage of the LPL shape, distributing energy over a broader region and producing a wider melt pool. Conversely, the dot shape focuses energy at a single point, increasing localised vaporisation and thereby creating a deep and wide capillary Figure 14.

Additionally, a clear inverse relationship was observed between capillary diameter and oscillation frequency. At lower frequencies, the beam dwells longer, allowing higher localised heat input and wider capillary formation. As the frequency increases, the energy input becomes more temporally distributed, leading to narrower and more stable capillaries. FFT analysis of the diameter variations over time further confirmed the presence of the beam oscillation frequency as a dominant spectral component, indicating a direct modulation of capillary stability and size by the laser dynamics Figure 15.

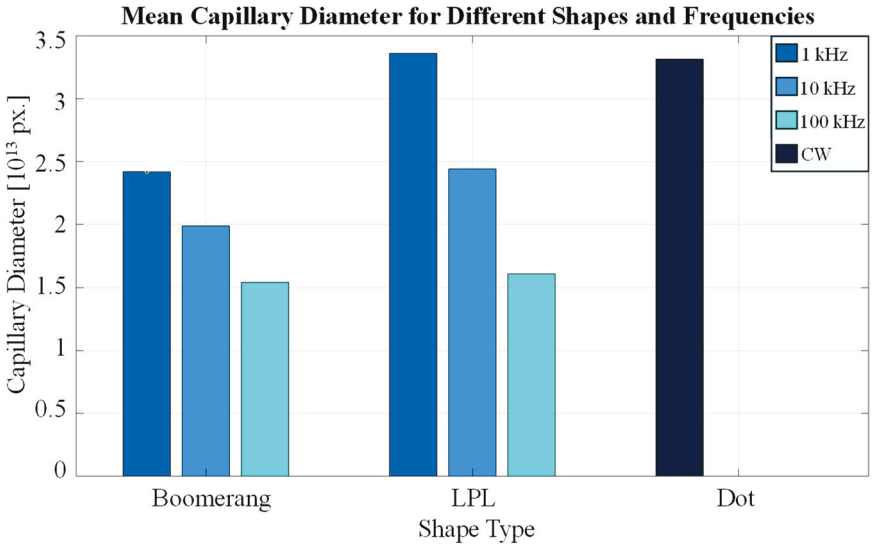

Figure 14. Capillary diameter as a function of beam shape and oscillation frequency.

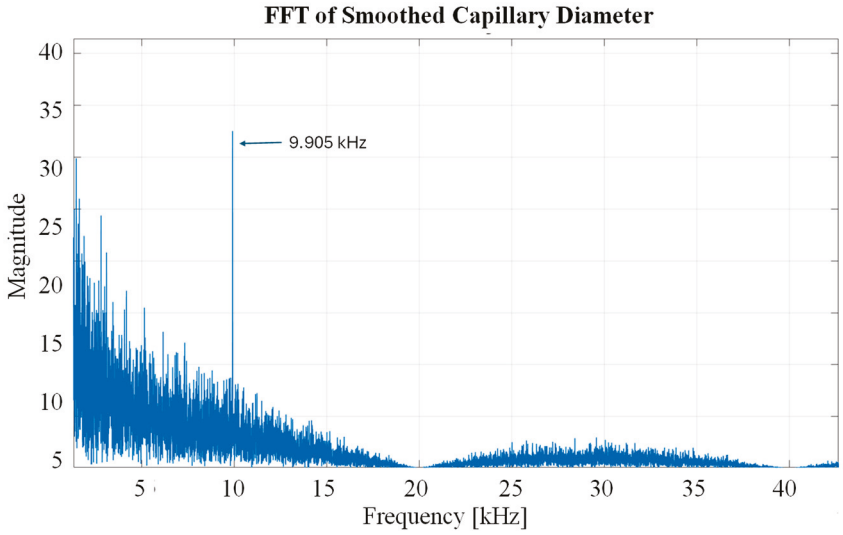

Figure 15. FFT of the capillary diameter for "LPL" beam shape with 10 kHz oscillation frequency.

These findings confirm that beam shape and frequency modulation significantly affect both capillary dynamics and capillary morphology, directly influencing the energy absorption characteristics, melt pool stability and, ultimately, weld quality.

Custom MATLAB-based tools were developed to analyse capillary dynamics from high-speed video data. Although not benchmarked against commercial software, internal validation was performed by manually tracking selected frames and comparing capillary diameter and centroid position. Edge detection and thresholding parameters were optimised based on known visual features, such as capillary contrast and beam reflection. Future work will include systematic benchmarking against independent methods to enhance reproducibility and comparability.

4. Summary and Outlook

This study investigates the effect of beam shape and oscillation frequency on weld quality, capillary dynamics, and microstructure during laser welding of austenitic (1.4301) and duplex stainless steels using a high-power Coherent Beam Combining (CBC) laser system. Advanced diagnostics, including high-speed imaging and metallographic analysis, were employed to understand how dynamic beam modulation influences material behaviour.

- Capillary Dynamics:
  High-speed imaging from top and side views revealed that capillary behaviour—such as opening, closure, and front wall inclination—varies significantly with oscillation frequency. Higher frequencies induced greater capillary fluctuations, especially in austenitic steel. FFT analysis confirmed that capillary oscillation matched the imposed modulation frequencies, indicating a dynamic material response.
- Capillary Diameter and Penetration Depth:
  Image analysis showed a reduction in capillary diameter with increasing frequency, due to more localised and transient energy input. However, penetration depth increased for specific beam shapes and frequencies, highlighting improved energy coupling under certain dynamic conditions.
- Microstructure and Weld Geometry:
  Metallographic cross-sections revealed beam shape and frequency-dependent changes in weld morphology and phase composition. In austenitic steel, higher frequencies promoted grain coarsening, while in duplex steel, increased frequency shifted the ferrite–austenite balance toward ferrite. Weld geometry transitioned from narrow–deep to wide–shallow in duplex steel with LPL beam shapes, whereas the opposite trend was observed in austenitic steel.

These results demonstrate that beam shape and frequency modulation can significantly influence energy delivery, melt pool behaviour, and final weld properties. Future work will explore correlations with residual stress, mechanical performance, and microstructural evolution using EBSD, TEM, and SPH-based numerical modelling to deepen the understanding of the process–structure–property relationships in dynamically modulated laser welding.

Author Contributions: K.R.K.M.: Writing—review & editing, Writing original draft preparation, Conceptualization, Methodology, Visualization, Investigation, Validation. R.S.: Writing introduction, Investigation. A.S.: Data curation, MATLAB scripts. S.O.: Project administration, U.R.: Project administration, funding acquisition. All authors have read and agreed to the published version of the manuscript.

Funding: This research was funded by the Deutsche Forschungsgemeinschaft e.V. (DFG, German Research Foundation). The sponsorship and support are gratefully acknowledged.

Institutional Review Board Statement: Not applicable.

Informed Consent Statement: Not applicable.

Data Availability Statement: The research data have been uploaded in the link below and will be made available upon request: http://hdl.handle.net/21.11102/1b9659b4-9392-4cbe-9a60-1096e6800816 (accessed on 18 June 2025).

Acknowledgments: The presented investigations were carried out at RWTH Aachen University Welding and Joining Institute ISF within the framework of the Collaborative Research Centre SFB1120-236616214 “Bauteilpräzision durch Beherrschung von Schmelze und Erstarrung in Produktionsprozessen”.

Conflicts of Interest: The Authors have no conflicts of interest to declare.

References

1. *Laser Welding MDPI*; Oliveira, J.P., Ed.; MDPI: Basel, Switzerland, 2020; ISBN 978-3-03928-862-5.
2. Klimpel, A. Review and Analysis of Modern Laser Beam Welding Processes. *Materials* **2024**, *17*, 4657. [CrossRef]
3. Möbus, M.; Pordzik, R.; Seefeld, T. Influence of intensity distributions on the process dynamics during laser deep penetration welding of pure nickel with a flexible ring mode laser source. *J. Laser Appl.* **2024**, *36*, 042073. [CrossRef]

4. Schiry, M.; Plapper, P. Influence of laser parameter on weld bead shape and process stability of laser welded steel sheets. In Proceedings of the 10th Conference on Photonic Technologies LANE 2018, Fürth, Germany, 3–6 September 2018.
5. Suder, W.; Chen, X.; Sierra, D.R.; Chen, G.; Wainwright, J.; Rajamudili, K.; Pardal, G.R.; Williams, S. Control of meltpool shape in laser welding. *Weld. World* **2024**, *68*, 1485–1495. [CrossRef]
6. Gong, S.; Pang, S.; Wang, H.; Zhang, L. (Eds.) *Weld Pool Dynamics in Deep Penetration Laser Welding*; Springer: Singapore, 2021; ISBN 978-981-16-0788-2.
7. Dittrich, D.; Keßler, B.; Strohbach, R.; Jahn, A. Laser beam welding of hot crack sensitive Al-alloys without filler wire by intensity controlled dynamic beam oscillation. *Procedia CIRP* **2022**, *111*, 435–438. [CrossRef]
8. Dittrich, D.; Börner, S.; Larrañaga, J.B.; Sahm, T.; Jahn, A.; Wetzig, A. Coherent beam combining—Beam characterization of a new 14 kW CBC laser source and first results on copper welding. *Procedia CIRP* **2024**, *124*, 724–729. [CrossRef]
9. Weber, R.; Wagner, J.; Peter, A.; Hagenlocher, C.; Spira, A.; Urbach, B.; Shekel, E.; Vidne, Y. Basic Properties of High-Dynamic Beam Shaping with Coherent Combining of High-Power Laser Beams for Materials Processing. *JMMP* **2025**, *9*, 85. [CrossRef]
10. Shekel, E.; Vidne, Y.; Urbach, B. 16kW single mode CW laser with dynamic beam for material processing. Fiber Lasers XVII: Technology and Systems. *SPIE* **2020**, *11260*, 267–272. [CrossRef]
11. Wagner, J.; Leis, A.; Armon, N.; Nissenbaum, A.; Hagenlocher, C.; Holland, J.; Weber, R.; Graf, T. Coherent beam combining—unlimited flexibility in laser material processing. *PhotonicsViews* **2022**, *19*, 60–63. [CrossRef]
12. Sawannia, M.; Wagner, J.; Stritt, P.; Ramsayer, R.; Hagenlocher, C.; Graf, T. Response of the melt pool and vapour capillary on dynamic beam shaping in the kHz regime during laser welding. *Procedia CIRP* **2024**, *124*, 430–433. [CrossRef]
13. Olschok, S.; Troise, M.; Reisgen, U. Laser beam welding of high thickness sheet metal with highly dynamic beam shaping. *Procedia CIRP* **2024**, *124*, 733–736. [CrossRef]
14. Berger, P.; Hügel, H.; Graf, T. Understanding Pore Formation in Laser Beam Welding. *Phys. Procedia* **2011**, *12*, 241–247. [CrossRef]
15. Brinkmeier, D.; Wagner, J.; Sawannia, M.; Wahl, J.; Menold, T.; Stritt, P.; Ramsayer, R.; Graf, T.; Michalowski, A. Influence of the laser-plume interaction on the beam profile during deep-penetration welding with coherent beam shaping. *Opt. Express* **2025**, *33*, 2702–2711. [CrossRef]
16. Wahl, J.; Frey, C.; Powell, J.; Zaiß, F.; Haas, M.; Olschok, S.; Reisgen, U.; Hagenlocher, C.; Graf, T. Laser-plume interactions in deep-penetration remote laser welding of stainless steel. *Opt. Laser Technol.* **2025**, *186*, 112678. [CrossRef]
17. Zaiß, F.; Haas, M.; Powell, J.; Wahl, J.; Diegel, C.; Schricker, K.; Bergmann, J.P.; Hummel, M.; Spurk, C.; Olowinsky, A.; et al. Reducing capillary depth fluctuations in high-speed laser welding of stainless steel using multi-core laser technology. *Procedia CIRP* **2024**, *124*, 413–417. [CrossRef]
18. Xie, W.; Tu, H.; Nian, K.; Zhang, D.; Zhang, X. Microstructure and mechanical properties of Flexible Ring Mode laser welded 304 stainless steel. *Opt. Laser Technol.* **2024**, *174*, 110563. [CrossRef]
19. Zaißa, F.; Haasa, M.; Wagnera, J.; Diegelb, C.; Schrickerb, K.; Bergmannb, J.P.; Hummel, M.; Olowinski, A.; Beckmann, F.; Moosmann, J.; et al. *Influence of Capillary SHAPE on spatter Formation During Welding with Ring-Core Fiber Systems*; Lasers in Manufcaturing Conference 2023; Helmholtz-Zentrum Hereon: Geesthacht, Germany, 2023.
20. Nahr, F.; Bartels, D.; Rothfelder, R.; Schmidt, M. Influence of Novel Beam Shapes on Laser-Based Processing of High-Strength Aluminium Alloys on the Basis of EN AW-5083 Single Weld Tracks. *JMMP* **2023**, *7*, 93. [CrossRef]
21. Wagner, J.; Heider, A.; Ramsayer, R.; Weber, R.; Faure, F.; Leis, A.; Armon, N.; Susid, R.; Tsiony, O.; Shekel, E.; et al. Influence of dynamic beam shaping on the geometry of the keyhole during laser beam welding. *Procedia CIRP* **2022**, *111*, 448–452. [CrossRef]
22. Kayahara, T.; Tanabe, T.; Sato, Y.; Takenaka, K.; Tsukamoto, M. Effects of beam shape formed by beam-splitting diffractive optical element on keyhole and molten pool behavior in high-power laser welding of stainless steel. *J. Laser Appl.* **2025**, *37*, 032014. [CrossRef]
23. Börner, S.; Dittrich, D.; Barrios Laranaga, J. Enhanced Process Understanding for Laser Welding of Copper and Aluminum Alloys with Dynamic Beam Oscillation. In Proceedings of the Lasers in Manufacturing Conference, Munich, Germany, 26–29 June 2023.
24. Ai, Y.; Yan, Y.; Han, S. Numerical Analysis of Molten Pool Dynamic Behaviors during High-Speed Oscillation Laser Welding with Aluminum Alloy. *Metals* **2024**, *14*, 192. [CrossRef]
25. Berger, P.; Heider, A.; Boley, M.; Förster, D. (Eds.) *Capillary Geometries During Welding of Metals Observed with X-Ray Technique and Calculated Using a Ray-Tracing Tool and a Finite Volume Program Treating Heat Diffusion and Fluid Flow*; Proceedings of the LiM; Institut für Strahlwerkzeuge: Stuttgart, Germany, 2015.
26. Börner, S.; Dittrich, D.; Sahm, T.; Ullmann, L.; Kamm, P.H.; Jahn, A. X-ray analysis of capillary and melt pool dynamics using laser beam oscillation welding for aluminum die-casts. *J. Laser Appl.* **2025**, *37*, 022019. [CrossRef]
27. Kang, S.; Joonghan, S. The effect of laser beam intensity distribution on weld characteristics in laser welded aluminum alloy (AA5052). *Opt. Laser Technol.* **2021**, *142*, 107239. [CrossRef]
28. Song, D.; Kim, R.; Choi, K.; Shin, D.; Lee, S. Effects of Beam Shape on the Microstructures and Mechanical Properties during Thin-Foil Laser Welding. *Metals* **2023**, *13*, 916. [CrossRef]

29. Zeng, X.; Lu, C.; Zhu, Q.; Cui, X.; Li, Z.; Shi, W.; Zhang, R.; Liu, X.; Di, T. Effect of Oscillating Amplitude on Microstructure and Mechanical Property of Laser Welding of Dissimilar Stainless Steel. *Coatings* **2024**, *14*, 1617. [CrossRef]
30. Pekkarinen, J.; Veli, K. The effects of laser welding parameters on the microstructure of ferritic and duplex stainless steels welds. *Phys. Procedia* **2010**, *5*, 517–523. [CrossRef]
31. Šimeková, B.; Dománková, M.; Kovaříková, I.; Kovačócy, P.; Martinkovič, M.; Šimek, M.; Ciuła, L. Microstructural and Mechanical Characterization of the Laser Beam Welded SAF 2507 Super-Duplex Stainless Steel. *Metals* **2024**, *14*, 1184. [CrossRef]
32. Lippold, J.C. (Ed.) *Welding Metallurgy and Weldability*; John Wiley & Sons: Hoboken, NJ, USA, 2014; ISBN 9780471473794.

Disclaimer/Publisher's Note: The statements, opinions and data contained in all publications are solely those of the individual author(s) and contributor(s) and not of MDPI and/or the editor(s). MDPI and/or the editor(s) disclaim responsibility for any injury to people or property resulting from any ideas, methods, instructions or products referred to in the content.

applied sciences

MDPI

Article

Mechanical Properties Analysis of WAAM Produced Wall Made from 6063 Alloy Using AC MIG Process

Ivica Garašić [1], Mislav Štefok [1], Maja Jurica [1], Davor Skejić [2] and Mato Perić [3,*]

[1] Faculty of Mechanical Engineering and Naval Architecture, University of Zagreb, Ivana Lučića 5, 10000 Zagreb, Croatia; ivica.garasic@fsb.hr (I.G.); mislav.stefok@fsb.hr (M.Š.); maja.remenar@fsb.hr (M.J.)
[2] Faculty of Civil Engineering, University of Zagreb, 10000 Zagreb, Croatia; davor.skejic@grad.unizg.hr
[3] Department of Mechatronics, University North, Trg dr. Žarka Dolinara 1, 48000 Koprivnica, Croatia
* Correspondence: mperic@unin.hr

Abstract: Wire and arc additive manufacturing (WAAM) is a promising method of producing medium- and large-sized aluminum alloy structures, though it faces challenges such as porosity, residual stresses and inconsistent mechanical properties. This study investigates the effect of current type (AC and DC MIG welding) and polarity balance (influencing the duration of the positive/negative period of the cycle) on the mechanical and microstructural properties of 6063 aluminum alloy walls produced by WAAM. A TiB_2-refined Al–Mg–Si (6063) filler wire, specifically developed for arc-based processing, was used. Tensile tests, Vickers hardness measurements (HV5), optical microscopy and X-ray diffraction based on cosα method were used to evaluate performance in terms of strength, ductility, hardness, grain structure, porosity and residual stress. The results showed that the balance of AC polarity significantly affects wall geometry, porosity and grain structure. Increasing the negative polarity period resulted in taller and narrower walls, while the widest walls were produced with increased positive polarity. Residual stress measurements revealed a tensile–compressive–tensile distribution, with the DC-MIG samples showing the highest surface stress values. The highest tensile strength (172 MPa) was measured in the lower region of the DC-MIG sample, suggesting that areas near the substrate benefit from faster cooling.

Keywords: AC MIG; WAAM process; 6063 alloy; residual stress; XRD method; mechanical properties

1. Introduction

Wire and arc additive manufacturing (WAAM) is a type of additive manufacturing that works according to the principle of wire arc direct energy deposition (WA-DED). In this process, a metal wire is used as feedstock and melted by an energy source, usually an electric arc, but possibly also a plasma arc, laser or electron beam, and then deposited layer by layer to build up a three-dimensional structure [1]. The additive manufacturing of large-volume components makes WAAM one of the most efficient direct energy deposition (DED) processes when it comes to achieving a low buy-to-fly (BTF) ratio, resulting in significant cost savings [2]. Therefore, WAAM is especially beneficial for producing expensive and high-performance materials such as titanium and nickel alloys, high-strength steels and aluminum alloys, which are normally difficult to machine [3].

This study deals with the limited existing research on WAAM of 6063 alloys, especially using AC MIG with different EN ratios. By evaluating mechanical and microstructural

behavior under controlled polarity balance, this research aims to identify process–property correlations and optimize manufacturing quality for potential structural applications.

Aluminum alloys have several desirable properties, including low density, high specific strength, good thermal and electrical conductivity and excellent corrosion resistance and formability. When processed using WAAM, aluminum alloys can exhibit mechanical properties that are comparable to or even better than their wrought counterparts [4,5]. However, despite these advantages, WAAM-produced aluminum components often suffer from process-related defects that limit their wider industrial application. These challenges are primarily related to process stability such as path planning, parameter optimization and melt pool shielding as well as alloy chemistry [6]. The most critical problems with aluminum WAAM are the formation of porosity, residual stress and deformation and solidification cracking [7].

Porosity in WAAM is caused by various factors such as the arc welding process, process parameters, interlayer temperature, wire quality and alloy composition and can be exacerbated in multilayer build-ups by the heat input from the subsequent layers, which promotes pore growth [8]. Pores can reduce mechanical properties such as yield strength, contribute to anisotropy and reduce tensile strength, while the choice of deposition strategy, the type of shielding gas and the gas flow rate have a direct influence on porosity growth [9].

The potential to reduce process-related defects in WAAM can be achieved by using modified GMAW techniques [10]. A significant advance is the development of the Cold Metal Transfer (CMT) process, which minimizes weld spatter by short-circuiting the arc through controlled dipping of the welding wire into the weld pool. This technique has been effectively applied to various aluminum alloys and has evolved into several improved variants, including CMT-P (pulsed), CMT-ADV (alternating polarity) and CMT-PADV (a combination of both), all of which contribute to providing better arc strike behavior and reliability, lower heat input and reduce the porosity and a refined microstructure [11].

An alternative solution that counteracts the cost and complexity of CMT is the implementation of the pulsed variable polarity GMAW (VP-GMAW) process, which provides comparable or better deposition efficiency at a lower process cost. This technique has demonstrated stable arc behavior, high deposition efficiency (up to 82.56%) and isotropic mechanical properties, making it a promising candidate for aluminum WAAM [12].

By comparing pulsed AC, pulsed, and CMT modes, it can be concluded that pulsed AC mode (with variable polarity) offers a significant improvement in porosity control, achieving porosity values up to ten times lower than conventional pulsed GMAW. Although the average grain size in pulsed AC mode was slightly higher, it maintained a favorable and uniform microstructure with a balanced distribution of equiaxed and columnar grains, contributing to improved material homogeneity and mechanical performance [13]. Furthermore, image-based symmetry analysis has demonstrated that pulsed AC deposition yields the best bead symmetry, further supporting its suitability for high-quality and consistent WAAM applications [14]. Grain size in WAAM is influenced by the applied power and polarity change frequency, with a higher EN pulse rate promoting a predominant equiaxed structure, reducing columnar growth, improving structural uniformity and increasing deposition weight [15].

Solidification cracks in aluminum alloys during the WAAM process occur within the liquid melt pool and is primarily caused by a wide solidification range, a columnar dendritic grain structure and the inability of the residual liquid to compensate for shrinkage-induced stresses near the solidus temperature [16]. An important prerequisite for the successful use of Al–Mg–Si alloys in WAAM is overcoming their susceptibility to such hot cracking. One of the most effective measures to prevent hot cracking is grain refinement. A promising approach to achieve this is the use of an advanced Al–Mg–Si alloy inoculated with a TiB_2-

containing structural refiner [17]. As a result, this modified alloy exhibits no macroscopic cracking in the deposited material. The resulting microstructure is characterized by fine, equiaxed grains smaller than 30 μm. These microstructural features are attributed to preferential heterogeneous nucleation, which reduces the tendency for epitaxial grain growth [18].

Due to its widespread use in structural applications and its favorable response to heat treatment and grain refinement, making it a promising and cost-effective candidate for WAAM technologies, 6063 is selected. To further enhance its processability for additive manufacturing, a TiB_2-refined Al–Mg–Si (6063) filler wire specifically developed for WAAM was used in this study, providing improved grain refinement, reduced cracking susceptibility and better microstructural control.

The high susceptibility of 6000 series aluminum alloys to cracking during solidification poses a challenge for additive manufacturing. However, the use of a TiB-alloyed AlMg0.7Si welding wire (S Al 6063-TiB) enabled the production of aluminum parts with fine, equiaxed grains and low porosity, effectively avoiding solidification cracks. A key advantage of the 6000 series alloys is their ability to undergo heat treatment, which significantly improves mechanical properties. After heat treatment, both the transverse and longitudinal specimens exhibited yield strength, tensile strength and ductility that matched or exceeded those of AW 6063-T6 in wrought form, demonstrating the alloy's great potential for high performance in WAAM applications [19].

Residual stresses in aluminum components produced by WAAM are primarily caused by uneven heating and cooling during solidification, resulting in forced thermal contraction [20]. These stresses are usually tensile stresses that reduce fatigue strength and potentially lead to deformation if they exceed the yield strength of the material [21,22]. Residual stress in WAAM components is strongly influenced by clamping conditions, the path planning strategy, welding parameters, the interlayer temperature and the component geometry, whereby longitudinal stresses (stresses in the welding direction) generally predominate along the build-up direction. These stresses are commonly measured using techniques such as neutron diffraction, X-ray diffraction (XRD) and hole-drilling [23]. During WAAM production of aluminum alloys, significant residual tensile stresses can occur, especially near the substrate and along the build direction, that approach the yield strength of the material, highlighting the need for stress reduction strategies such as process modifications or post-processing treatments [24].

Mechanical tensile tests, in particular the analysis of stress–strain behavior, provide crucial data for the evaluation of fatigue resistance and fracture performance—key aspects for the structural reliability of WAAM-manufactured parts.

Despite numerous studies on the WAAM process for aluminum alloys, the mechanical performance of 6000 series alloys produced by pulsed AC-MIG welding has been investigated only to a limited extent. This study investigates the mechanical properties of alloy 6063 produced by WAAM using pulsed AC-MIG with different electrode-negative (EN) ratios with the aim of evaluating its suitability for structural applications.

2. Materials and Methods

A Fronius FlexTrack 45 PRO Rail-guided welding carriage and OTC Daihen WB-W400 AC-MIG welding power supply were employed for wire and arc additive manufacturing (WAAM) of four samples. In this study, a 6063 aluminum alloy welding wire, an advanced Al–Mg–Si alloy (tailored to improve processability using a TiB_2-containing structural refiner) with a diameter of 1.0 mm, was selected as the deposition material (chemical composition is provided in Table 1). As the substrate material, a 5083 aluminum alloy with

dimensions of 300 mm × 70 mm × 8 mm was used, while the total length of the fabricated samples was approximately 250 mm.

Table 1. Chemical composition of the filler wire and base metal (wt.%).

Composition	Si	Fe	Cu	Mn	Mg	Cr	Zn	Be	Ti	B	Other	Al
6063	0.2–0.6	<0.35	<0.1	<0.1	0.45–0.9	<0.1	<0.1	<0.0003	0.2–0.3	0.04–0.06	<0.05	balance

Prior to welding, the substrate surface was cleaned with alcohol to remove any surface contamination that could compromise the integrity of the weld metal. The selected deposition parameters, along with the corresponding sample designations, are presented in Table 2. The interpass temperature was maintained at 100 °C. To ensure a constant interpass temperature, the time between individual layers was adjusted, with temperature measurements taken using an infrared thermometer (Fluke 568 Infrared Thermometer, Fluke Corporation, Everett, WA, USA). The contact tip-to-workpiece distance was fixed at 10 mm, and the welding speed was set to 76 cm/min. Argon (Ar ≥ 99.996%, Group I1 according to EN ISO 14175) was used as the shielding gas, with a constant flow rate of 19.5 L/min. All samples were fabricated with 50 overlapping layers using a zig-zag method, with the starting position for each subsequent layer placed at the opposite side of the previously deposited wall. To investigate the effects of polarity balance while maintaining process stability, the current was kept constant during all experiments. Accordingly, the wire feed rate and other parameters were adjusted to ensure arc stability.

Table 2. Welding parameters used for sample processing.

Sample	Current, A	Voltage, V	EN Ratio	Wire Feed Rate, m/min	Heat Input, kJ/mm
11	170	19.5	50	18	2.09
12	170	22.6	0	17.2	2.43
13	170	22.9	−50	15.2	2.46
14	170	21.8	DC	15.4	2.34

Sample 11 represents an aluminum wall fabricated using an alternating current (AC) with an electrode-negative (EN) ratio of 50. This indicates that, within a single cycle, the duration of the negative polarity is maximized, while the positive polarity is minimized. In contrast, Sample 13 was also fabricated using an AC, but with an EN ratio of −50, signifying a cycle in which the negative polarity duration is minimized, and the positive polarity is maximized. Sample 12 was produced using an EN ratio of 0, corresponding to a conventional AC waveform, where the durations of the positive and negative polarities are equal within each cycle.

Adjustments to the EN ratio inherently modify the welding voltage and wire feed speed, thereby contributing to improved process stability and weld quality. Sample 14 was fabricated using a direct current (DC). Based on the sample height data presented in Table 2, it may be concluded that an increased duration of the negative polarity within the pulse cycle correlates with reduced heat input and enhanced material deposition.

Upon completion of the welding process, residual stress measurements were conducted on both the upper and lateral surfaces of the samples using the cosα X-ray diffraction method [25,26]. The measurements were performed using the Pulstec μ-X360 system (Pulstec Industrial Co., Ltd., Hamamatsu, Japan).

Tensile test specimens were extracted from the additively manufactured thin-walled structures, as shown in Figure 1. All specimens had identical dimensions of 175 mm in length, 22 mm in width and 5 mm in thickness, with all geometrical parameters defined

and prepared in accordance with the EN ISO 6892-1 standard. All specimens were oriented horizontally. Specimens labeled "A" were obtained from the upper region of the aluminum walls, whereas those labeled "B" were extracted from the lower region. The start and end sections of the welding process were cut off and discarded and excluded from testing.

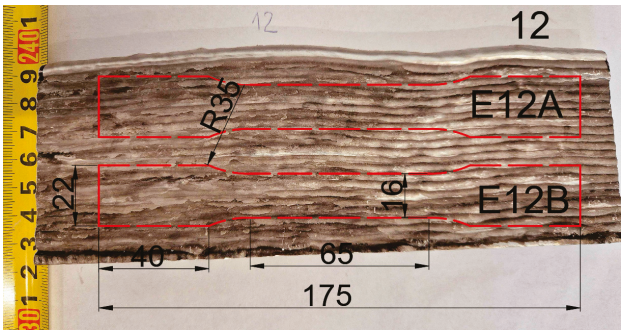

Figure 1. Dimensions and locations of samples for tensile testing.

Tensile testing was conducted using the Aramis optical measurement system, which enables high-precision displacement tracking and surface deformation analysis through the use of cameras, LED illumination and dedicated software (Figure 2). This system effectively replaces conventional devices such as extensometers and strain gauges and can be readily integrated with existing testing infrastructure.



Figure 2. Tensile testing setup with addition of Aramis system.

Metallographic specimens were prepared from the central section of the tensile samples for macrostructural analysis. The samples were mechanically polished and chemically etched using Keller's reagent. Vickers hardness measurements were performed across various layers of the deposited structure (from the bottom to the top), applying a test force of 49.03 N (HV 5) with indentation time of 10 s.

3. Results and Discussion

3.1. Macrostructure Characterization

The results of the basic macrostructural characterization of the as-built samples (11, 12, 13 and 14) are presented in Table 3, while images of the as-produced samples are shown in Figure 3. Analyzing the values obtained from measurements of the height and width of the samples produced with an AC, a linear correlation with the AC balance settings is evident. When the AC balance is set to 50 (the longest negative period), the highest and

narrowest walls are produced. Conversely, when the AC balance is set to −50 (the longest positive period), walls with the smallest height and the greatest width are produced.

Table 3. Macroscopic characterization.

Sample	Sample Width, mm	Sample Height, mm
11	9.1	92.3
12	10.6	71.6
13	12.1	57.1
14	12.5	64.5

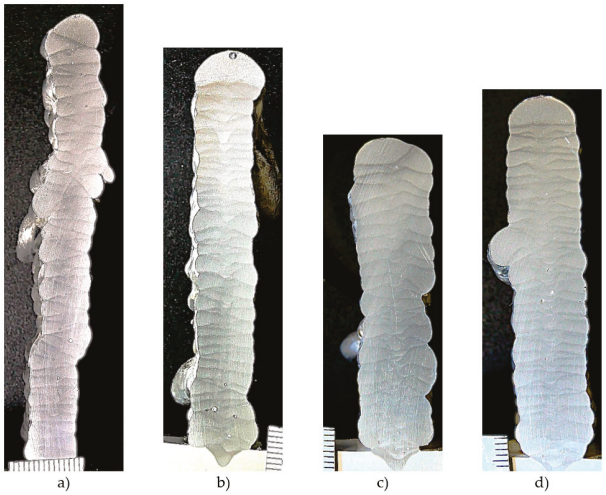

Figure 3. Macroscopic view of the samples (**a**) sample 11, (**b**) sample 12, (**c**) sample 13 and (**d**) sample 14.

These results are directly correlated with the heat distribution during the welding process. With the balance set to 50 and the longest negative period, heat is more directed toward the filler material, increasing the melting rate of the wire and resulting in a higher deposition rate. Consequently, in the same period of time, higher and narrower walls can be produced compared to those fabricated using an AC with a balance of 0 or −50.

Additionally, when comparing the sample produced using a DC to those produced with an AC, it can be observed that the width is greater, while the height falls between the values observed for the AC with balance set to −50 and 0. The width is largest when using a DC due to the heat distribution being concentrated on the wall, which increases the fluidity of the weld pool. As a result of the enhanced fluidity of the weld pool and the stability of the electric arc, the profile of the sample produced with a DC is significantly more uniform. When analyzing the homogeneity of the AC-produced samples, it is evident that the sample produced with the balance set to −50 has the fewest pores, and these pores are the smallest in diameter. This is also a direct consequence of the heat distribution; in this case, the heat is more concentrated on the wall, leading to a slower cooling rate. This allows gas bubbles to migrate through the molten pool more effectively.

These results are consistent with those of Lee et al. [15], who showed that an increased electrode-negative pulse ratio leads to higher and narrower deposits with lower porosity. The improved geometry was primarily attributed to a more stable metal transfer, which enables uniform and efficient material deposition.

3.2. Microstructure Characterization

The microstructural analysis of the samples was conducted using an Olympus GX51 light microscope with a depth of field of 0.2 µm. The microstructural observations were carried out on macrosections made from cross-sections of the walls produced with WAAM.

The observations were carried out at several points, particularly in the middle and upper areas of the walls, in order to determine representative microstructural features and the presence of specific defects. Figure 4a illustrates the microstructure of aluminum alloy 6063 in sample 11, which was produced using WAAM. The grains are predominantly regular in shape, polygonal, and uniform in size. Within the deposited layer, a uniform and homogeneous microstructure is observed, characterized by clearly defined aluminum grain boundaries along which intermetallic phases (precipitates) have formed. This suggests favorable and stable thermal conditions during solidification. Among the typical defects associated with WAAM processing of aluminum alloys, only gas pores of varying sizes were observed.

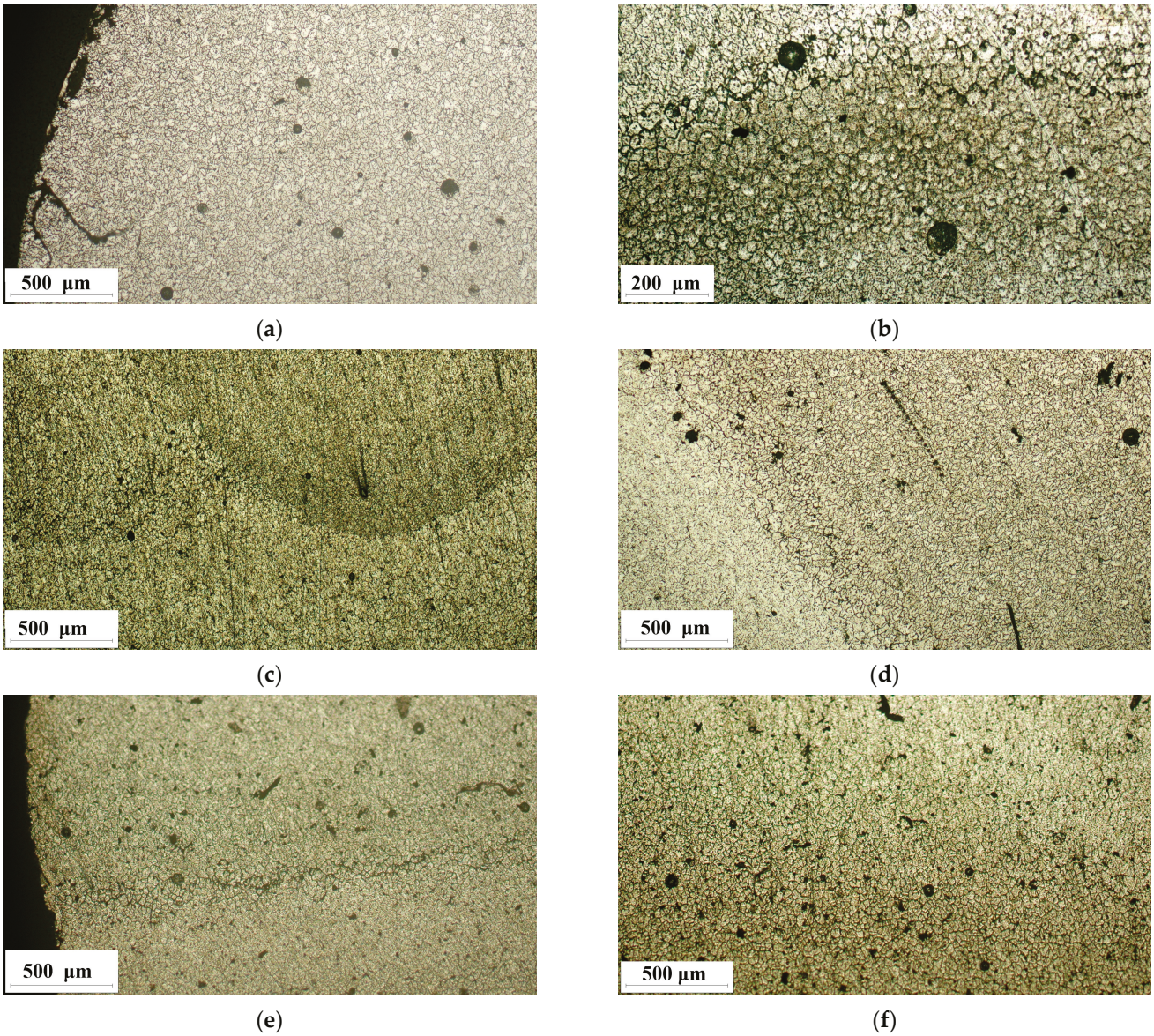

Figure 4. Microstructure of the aluminum alloy 6063 of produced with WAAM: (**a**) microstructure of sample 11, (**b**) three successive layers of sample 11, (**c**) microstructure of sample 12, (**d**) microstructure of sample 13, (**e**) microstructure of sample 14, and (**f**) intermetallic precipitates between two layers of sample 14.

Similar grain morphology and refinement trends were also observed in studies by Klein et al. [18] and Winterkorn et al. [19], who investigated WAAM processing using a structurally refined Al–Mg–Si filler wire and reported fine equiaxed grains with min-

imal columnar growth, supporting the effectiveness of TiB_2 additions in promoting a uniform microstructure.

Figure 4b shows three successive layers of sample 11, each exhibiting differences in grain size and morphology. These variations are attributed to the partial recrystallization of the previous layer, induced by repeated thermal cycling during deposition. The distinct separation between the layers indicates local thermal gradients and varying solidification conditions. Some porosity is also observed, likely caused by gas entrapment during solidification. This, along with the microstructural inhomogeneity, may influence the overall mechanical performance of the part.

Figure 4c presents the microstructure of sample 12, which shares similarities with the features observed in sample 11. The solidification patterns seen can be attributed to the heat dissipation trajectories resulting from subsequent thermal passes, suggesting directional solidification influenced by localized thermal gradients.

In the Al 6063 alloy, the central aluminum matrix has a higher melting point than the intermetallic precipitates, which normally form at the grain boundaries. During the WAAM process, additional segregation and precipitation of these phases occur at the boundaries of the individual deposition layers due to multi-layer welding (Figure 4d,f).

Figure 4e displays the microstructure of sample 14, produced via DC-MIG welding. A high density of medium-sized, rounded pores is clearly visible. The average pore diameter ranges from 30 to 50 μm, with some pores locally exceeding this range. The microstructure is characterized by a predominance of equiaxed grains, indicating relatively uniform solidification conditions. However, compared to the microstructures obtained during AC-MIG welding, this structure appears coarser, suggesting a different heat input and cooling behavior during DC-MIG deposition.

Figure 5 shows a comparative microstructural analysis of four different WAAM-fabricated samples (samples 11 to 14) at a higher magnification. All samples exhibit predominantly equiaxed grain structures with visible grain boundaries and varying densities of pores or inclusions. The samples produced with AC polarity show a clear trend: sample 11 has clean grain boundaries, fine equiaxed grains and minimal porosity. Sample 12 (balanced) has slightly coarser grains with occasional gas porosity. Sample 13 shows coarse grains, higher porosity and sometimes irregular grain boundaries. In contrast, sample 14, produced with DC MIG, displays the coarsest microstructure, with numerous gas pores the size of the grains, incomplete fusion and uneven solidification.

Higher EN polarity directs more heat into the filler wire rather than the base material, resulting in a higher melt rate but lower net heat input into the wall. This promotes faster cooling and solidification, which in turn favors grain refinement and the formation of equiaxed microstructures. The observed refinement of grains with increasing EN ratio is consistent with previously reported results [15], where higher negative polarity promoted directional solidification and favored the formation of equiaxed grains.

3.3. Hardness

Each sample was produced in 50 layers, with hardness measurements taken approximately every two layers. The hardness distribution of the samples under different processing parameters using AC welding current is shown in Figure 6. Testing was performed on the sample along the path represented by the dotted line, as indicated in the chart. The arrow above the sample represents the direction of testing. Along the mid-width line of the samples, the average hardness values are 48.9 HV5 for sample 11, 51.7 HV5 for sample 12 and 50.3 HV5 for sample 13.

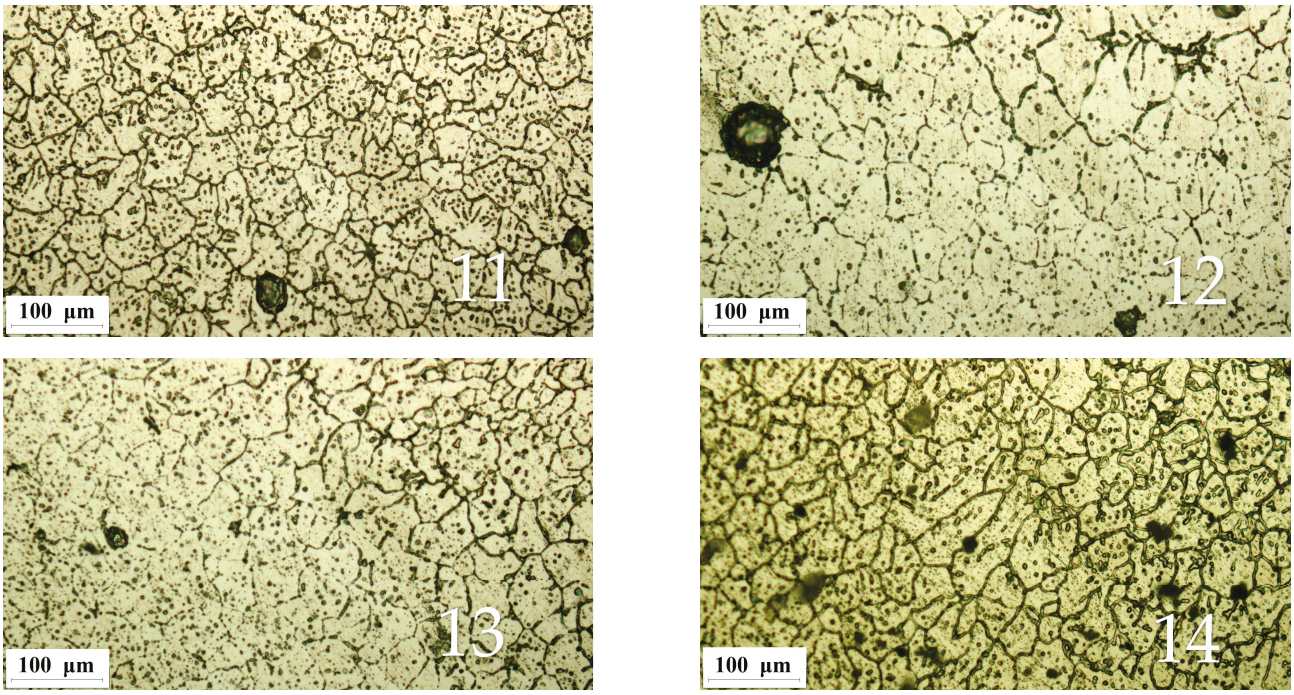

Figure 5. Comparison of microstructures of four WAAM samples at higher magnification.

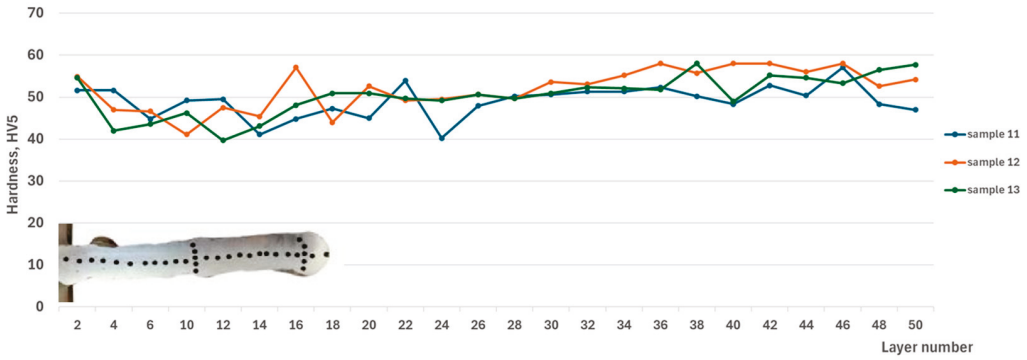

Figure 6. Hardness distribution of samples produced by AC welding current (samples 11, 12 and 13).

When comparing the extreme average hardness values, it is evident that the maximum hardness is achieved when using an AC with the balance set to 0 (equal duration of the positive and negative periods in one cycle), while the minimum hardness is observed when using an AC with the balance set to 50. The difference in these extreme values is 5.3%, suggesting that variations in the balance of polarity distribution during the cycle do not significantly influence the overall hardness of the WAAM-AC MIG-produced 6063 aluminum alloy walls. Due to the relatively high standard deviations (± 5.03 for sample 12, ±4.75 for sample 13 and ±3.83 for sample 11), the overlap in variability also means that the differences between the samples are not statistically significant. Therefore, although it can be assumed that sample 12 has the highest average hardness, this conclusion should be interpreted with caution. It can also be concluded that the maximum hardness values are achieved when using AC with a balance set to 0.

Along the mid-height line of the samples, the average hardness values are 47.8 HV5 at the middle and 50.6 HV5 at the top of sample 11, 50.7 HV5 at the middle and 58.5 HV5 at the top of sample 12 and 49.9 HV5 at the middle and 54.8 HV5 at the top of sample 13. As observed from all obtained values, a linear increase in hardness is evident from the bottom towards the top of all samples produced using an AC, with no significant influence of the polarity balance.

3.4. Tensile Properties

Tensile specimens were extracted from different samples, all oriented horizontally to the deposited build. Figure 7 presents the stress–strain curves for all samples, while Table 4 provides a comparison of the ultimate tensile strength (UTS), yield strength (YS) and elongation (ε) at room temperature for the different samples. The narrow ranges of UTS and YS (excluding the value for sample 11A) indicate stable strength properties of the deposited material. In contrast, the comparatively broader range of elongation suggests lower stability in ductility properties relative to strength. Overall, the maximum UTS values were obtained in samples extracted from the bottom part of the WAAM-produced wall (designated as "B" samples).

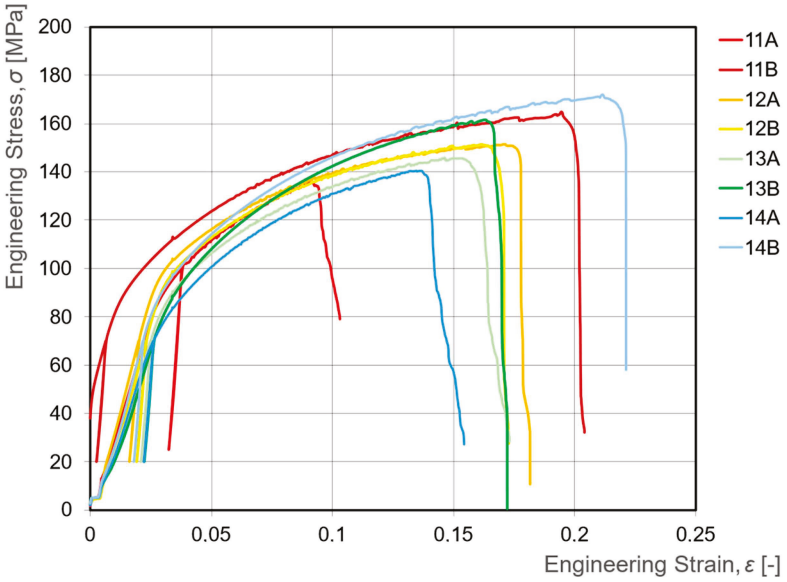

Figure 7. Comparison of stress strain curves.

Table 4. Comparison of tensile test results.

Sample	UTS, MPa	ε, /	YS, MPa	Sample	UTS, MPa	ε, /	YS, MPa
11A	135.72	0.103	99.93	**11B**	164.84	0.204	70.06
12A	151.42	0.182	70.03	**12B**	151.43	0.173	69.95
13A	145.83	0.173	69.98	**13B**	161.53	0.172	69.90
14A	140.42	0.154	69.90	**14B**	171.99	0.221	70.02

Due to slippage during gripping, sample 11B exhibited an unusually high initial stress of about 40 MPa, in contrast to the other specimens, which started near zero. This probably affected the accuracy of the yield strength. However, the ultimate tensile strength (UTS) is still considered reliable as the fracture occurred within the gauge length, indicating that the sample experienced proper deformation and failure despite the initial slippage.

In the WAAM production process, cooling and heating rates are not uniform along the build-up direction. Samples taken from the bottom region, near the substrate, experience rapid cooling (compared to samples extracted from the upper region of the wall) as layers are deposited onto the cooled substrate. This cooling effect promotes fine grain formation, leading to increased strength (up to 172 MPa) in the bottom region. Additionally, the subsequent "heat treatment" from the electric arc of the following deposited layers positively affects the mechanical properties.

The effect of heat input and distribution can also be observed when analyzing the UTS value of sample 14B. Although the heat input is almost the lowest, the distribution of heat

is primarily directed to the deposited layer, which acts as a heat treatment for the produced layers and ultimately plays a beneficial role in improving mechanical properties.

The mechanical properties achieved in this study—particularly the ultimate tensile strength (UTS) of up to 172 MPa—are in good agreement with the results of Winterkorn et al. [19], who also investigated WAAM-manufactured components using a TiB_2-modified Al–Mg–Si filler wire. Their study yielded comparable UTS and yield strength values, confirming that the use of structurally refined filler wire enables stable and competitive mechanical performance in WAAM-produced aluminum alloys.

Among the tested samples, those with higher porosity also tended to have lower UTS values. This can be explained by the fact that increased porosity leads to stress concentrations that act as crack initiation points under tensile loading. This reduces the effective load-bearing cross-section and thus leads to a measurable reduction in ultimate tensile strength. This correlation reinforces the importance of controlling the process parameters, not only for the geometry but also for the mechanical performance.

3.5. Residual Stresses

After the additive manufacturing of the samples was completed and cooled to ambient temperature, residual stresses were measured using X-ray diffraction based on the cosα method. The measurements were performed using the Pulstec μ-X360 device (Pulstec Industrial Co., Ltd.), as shown in Figure 8. The measurements of longitudinal residual stresses (i.e., in the direction of welding) were conducted on the last layer at the top of the samples, as well as along line A-B (Figure 8). The measurements on the last layer were taken immediately after sample preparation, while the measurements along line A-B were performed after cutting the substrate from the sample due to the geometrical limitations of the measurement equipment. For the last layer, the distance between measurement points was 20 mm, while on the centerline, the distance was 5 mm.

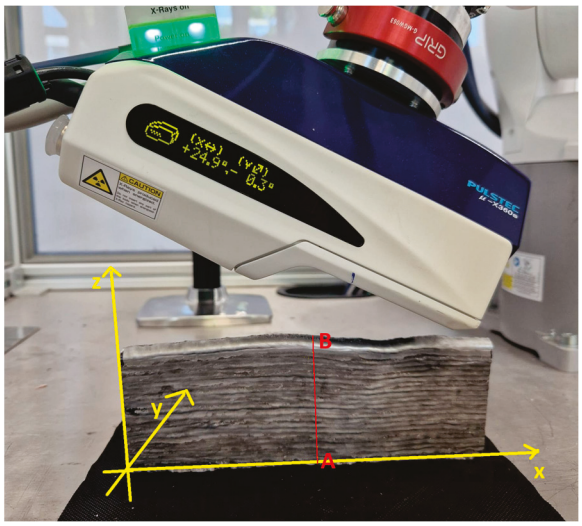

Figure 8. X-ray residual stress measurement.

For the last layer, the highest normal residual stresses were observed in sample 14, produced with DC-MIG, amounting to −110 MPa in compression and 80 MPa in tension. The residual stresses in the samples obtained with AC-MIG were slightly lower, with maximum tensile stresses of 55 MPa in sample 12 and compressive stresses of approximately −80 MPa in sample 13. The obtained results correlate with findings from the literature [27], showing slightly higher tensile stresses but significantly lower compressive stresses. This discrepancy is attributed to the fact that in the referenced literature, the stresses were measured after 20 layers, while in our study, they were measured after 50 layers.

The distribution of residual stress along line A-B, as presented in Figure 9, reveals a tensile–compressive–tensile pattern extending from the top layers of the deposit down to the substrate. This pattern results from the complex thermal cycling and mechanical constraints inherent in the WAAM process.

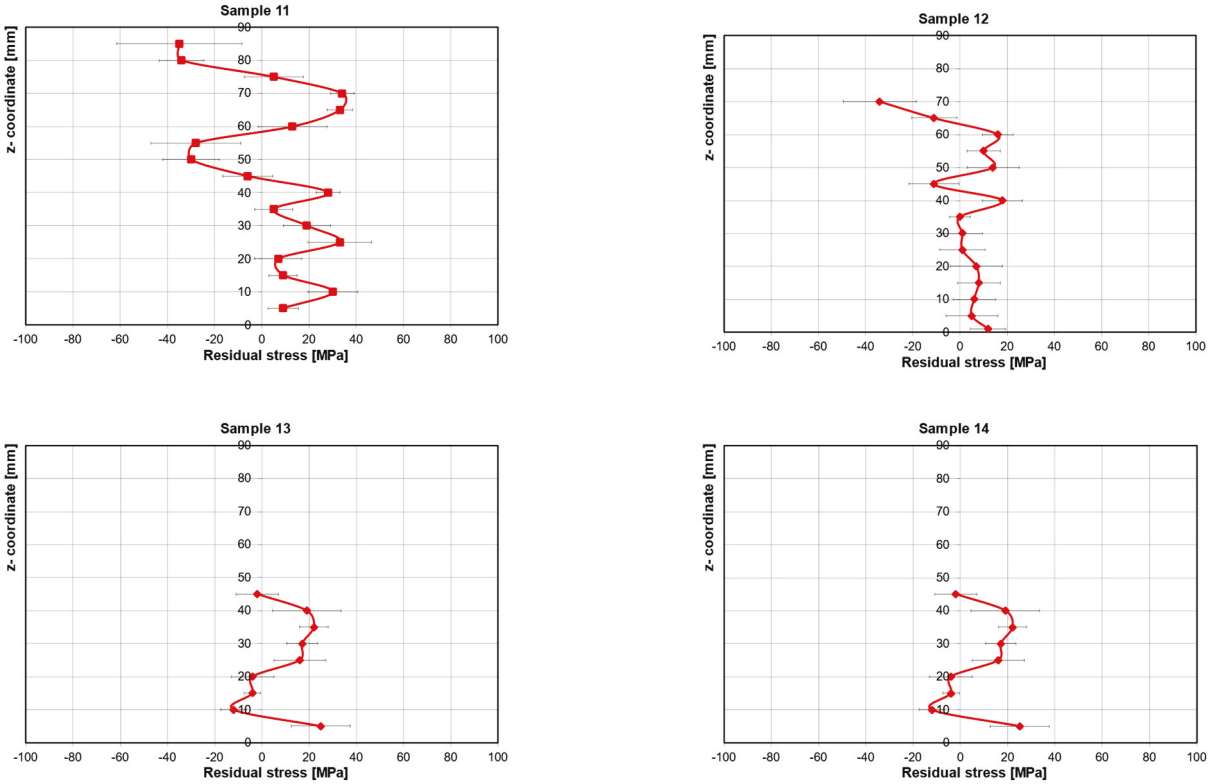

Figure 9. Distribution of longitudinal residual stress along the line A-B (Figure 6).

The overall distribution indicates that tensile residual stresses occur in the middle of the deposition layers and near the top, while compressive stresses are intermittently present in certain areas, particularly at the ends of the last deposition layer in samples 11 and 12. Notably, sample 11 exhibits the highest tensile residual stress of approximately 40 MPa, located several layers below the top surface.

Among the analyzed samples, sample 11 not only achieved the greatest height with the same number of layers but also exhibited the highest residual stress values among the samples produced by AC-MIG. Furthermore, the frequency of transitions between tensile and compressive stresses becomes more pronounced as the height of the structure increases. Sample 14, produced with DC-MIG, also exhibited tensile stresses of around 40 MPa.

Overall, the determined residual stress distributions and magnitudes are consistent with the results reported in the literature [28], confirming the expected stress distributions in WAAM-manufactured components of aluminum alloy 6063.

4. Conclusions

In the present work, the mechanical properties and microstructural characteristics of WAAM walls made of aluminum alloy 6063 using the AC-MIG process were investigated. The results show that polarity balance significantly influences wall geometry, porosity and grain structure. A higher electrode-negative (EN) ratio (AC balance 50) resulted in taller and narrower walls with reduced porosity, while a higher positive polarity (AC balance −50) resulted in wider walls. Microstructural analysis revealed predominantly equiaxed and polygonal grains with minimal defects, with gas pores being the only typical WAAM-

related defects. Although the DC-MIG samples exhibited slightly coarser grains, they also showed a higher density of gas pores. The highest average hardness was measured in samples produced with balanced polarity (EN = 0), but due to the relatively high standard deviations, the observed differences were not statistically significant. The tensile test showed stable mechanical performance for all samples, with the highest tensile strength (172 MPa) measured in the lower region of the DC-MIG sample, which is probably due to rapid cooling near the substrate. Residual stress analysis showed that the DC-MIG samples had the highest surface stress values, while the AC-MIG samples showed lower stresses with a characteristic tensile–compressive–tensile pattern. Among the AC-MIG samples, sample 11—which reached the highest build-up height—also exhibited the highest tensile residual stress, suggesting a correlation between structure height and residual stress accumulation.

Author Contributions: Conceptualization, I.G.; methodology, I.G., M.J. and M.Š.; validation, M.P., D.S. and I.G.; formal analysis, M.J.; investigation, M.P.; resources, I.G.; data curation, M.P. and D.S.; writing—original draft preparation, M.J. and M.Š.; writing—review and editing, M.J.; visualization, M.J. and M.P.; supervision, I.G. and D.S. All authors have read and agreed to the published version of the manuscript.

Funding: This work was partly supported by the Croatian Science Foundation under the project number HRZZ-IP-2022-10-9298 (REAL-fit: Reliable design methods for aluminium structures fit for the future requirements, project leader: Davor Skejić).

Institutional Review Board Statement: Not applicable.

Informed Consent Statement: Not applicable.

Data Availability Statement: No new data were created or analyzed in this study.

Conflicts of Interest: The authors declare no conflicts of interest. The funders had no role in the design of the study; in the collection, analyses, or interpretation of data; in the writing of the manuscript; or in the decision to publish the results.

Abbreviations

The following abbreviations are used in this manuscript:

WAAM	Wire And Arc Additive Manufacturing
DED	Direct Energy Deposition
DC-MIG	Direct Current Metal Inert Gas Welding
AC-MIG	Alternating Current Metal Inert Gas Welding
XRD	X-ray Diffraction
WA-DED	Wire Arc Direct Energy Deposition
BTF	Buy-To-Fly
GMAW	Gas Metal Arc Welding
CMT	Cold Metal Transfer
CMT-P	Cold Metal Transfer-Pulsed
CMT-ADV	Cold Metal Transfer- Alternating Polarity
CMT-PADV	Cold Metal Transfer-Pulsed Alternating Polarity
VP-GMAW	Pulsed Variable Polarity Gas Metal Arc Welding
EN	Electrode Negative
UTS	Ultimate Tensile Strength
YS	Yield Strength
HV5	Vickers Hardness (5 kg load)
TiB_2	Titanium Diboride

References

1. Kumar, N.; Bhavsar, H.; Mahesh, P.V.S.; Srivastava, A.K.; Bora, B.J.; Saxena, A.; Dixit, A.R. Wire arc additive manufacturing—A revolutionary method in additive manufacturing. *Mater. Chem. Phys.* **2022**, *285*, 126–144. [CrossRef]
2. Liu, J.; Xu, Y.; Ge, Y.; Hou, Z.; Chen, S. Wire and arc additive manufacturing of metal components: A review of recent research developments. *Int. J. Adv. Manuf. Technol.* **2020**, *111*, 149–198. [CrossRef]
3. Rodrigues, T.A.; Duarte, V.; Miranda, R.M.; Santos, T.G.; Oliveira, J.P. Current status and perspectives on wire and arc additive manufacturing (WAAM). *Materials* **2019**, *12*, 1121. [CrossRef]
4. Treutler, K.; Wesling, V. The current state of research of wire arc additive manufacturing (WAAM): A review. *Appl. Sci.* **2021**, *11*, 8619. [CrossRef]
5. Skejić, D.; Valčić, A.; Čudina, I.; Garašić, I.; Dokšanović, T. A Roadmap for the Reliable Design of Aluminium Structures Fit for Future Requirements—The REAL-Fit Project. *Buildings* **2025**, *15*, 1906. [CrossRef]
6. Langelandsvik, G.; Akselsen, O.M.; Furu, T.; Roven, H.J. Review of aluminum alloy development for wire arc additive manufacturing. *Materials* **2021**, *14*, 5370. [CrossRef]
7. Vimal, K.E.K.; Srinivas, M.N.; Rajak, S. Wire arc additive manufacturing of aluminium alloys: A review. *Mater. Today: Proc.* **2021**, *41*, 1139–1145. [CrossRef]
8. Arana, M.; Ukar, E.; Rodriguez, I.; Iturrioz, A.; Alvarez, P. Strategies to reduce porosity in Al-Mg WAAM parts and their impact on mechanical properties. *Metals* **2021**, *11*, 524. [CrossRef]
9. Gierth, M.; Henckell, P.; Ali, Y.; Scholl, J.; Bergmann, J.P. Wire arc additive manufacturing (WAAM) of aluminum alloy AlMg5Mn with energy-reduced gas metal arc welding (GMAW). *Materials* **2020**, *13*, 2671. [CrossRef]
10. Derekar, K.S.; Addison, A.; Joshi, S.S.; Zhang, X.; Lawrence, J.; Xu, L.; Melton, G.; Griffiths, D. Effect of pulsed metal inert gas (pulsed-MIG) and cold metal transfer (CMT) techniques on hydrogen dissolution in wire arc additive manufacturing (WAAM) of aluminium. *Int. J. Adv. Manuf. Technol.* **2020**, *107*, 311–331. [CrossRef]
11. Zhang, C.; Li, Y.; Gao, M.; Zeng, X. Wire arc additive manufacturing of Al-6Mg alloy using variable polarity cold metal transfer arc as power source. *Mater. Sci. Eng. A* **2018**, *711*, 415–423. [CrossRef]
12. Jeon, J.; Kim, H.; Lee, I.; Cho, J. Basic Research of Directed Energy Deposition for Aluminum 4043 Alloys Using Pulsed Variable Polarity Gas Metal Arc Welding. *Int. J. Precis. Eng. Manuf.* **2024**, *25*, 1475–1487. [CrossRef]
13. Aldalur, E.; Suárez, A.; Veiga, F. Metal transfer modes for Wire Arc Additive Manufacturing Al-Mg alloys: Influence of heat input in microstructure and porosity. *J. Mater. Process. Technol.* **2021**, *297*, 117271. [CrossRef]
14. Veiga, F.; Suárez, A.; Aldalur, E.; Bhujangrao, T. Effect of the metal transfer mode on the symmetry of bead geometry in WAAM aluminum. *Symmetry* **2021**, *13*, 1245. [CrossRef]
15. Lee, T.H.; Kim, C.; Kang, M. Effects of Electrode Negative Pulsing Ratio in Direct Energy Deposition via Variable-Polarity Cold Metal Transfer Process on the Deposition Behavior and Microstructural Characteristics. *Metals* **2022**, *12*, 475. [CrossRef]
16. NConiglio, C.E. Cross, Mechanisms for solidification crack initiation and growth in aluminum welding. *Int. Mater. Rev.* **2013**, *58*, 375–397. [CrossRef]
17. Li, T.; Chen, J.; Zeng, L.; Tuo, Z.; Ren, J.; Zheng, Z.; Wu, H. Microstructure and Mechanical Properties of TiB_2/TiC Particle Modified Al-Mg-Si Alloys Fabricated by Wire-Arc Additive Manufacturing. *Materials* **2025**, *18*, 1978. [CrossRef]
18. Klein, T.; Arnoldt, A.; Lahnsteiner, R.; Schnall, M. Microstructure and mechanical properties of a structurally refined Al–Mg–Si alloy for wire-arc additive manufacturing. *Mater. Sci. Eng. A* **2022**, *830*, 142318. [CrossRef]
19. Winterkorn, R.; Pittner, A.; Rethmeier, M. Wire arc additive manufacturing with novel Al-Mg-Si filler wire—Assessment of weld quality and mechanical properties. *Metals* **2021**, *11*, 1243. [CrossRef]
20. Sun, J.; Hensel, J.; Köhler, M.; Dilger, K. Residual stress in wire and arc additively manufactured aluminum components. *J. Manuf. Process.* **2021**, *65*, 97–111. [CrossRef]
21. Perić, M.; Garašić, I.; Štefok, M.; Osman, K.; Čikić, A.; Tonković, Z. Metal-Cored Arc Welding of I-Profile Structure: Numerical Calculation and Experimental Measurement of Residual Stresses. *Metals* **2023**, *13*, 1766. [CrossRef]
22. Kik, T.; Garašić, I.; Perić, M.; Landek, D.; Jurica, M.; Tonković, Z. Modifications of the heat source model in numerical analyses of the metal-cored arc welding process. *Energy* **2024**, *302*, 131811. [CrossRef]
23. Zhang, C.; Shen, C.; Hua, X.; Li, F.; Zhang, Y.; Zhu, Y. Influence of wire-arc additive manufacturing path planning strategy on the residual stress status in one single buildup layer. *Int. J. Adv. Manuf. Technol.* **2020**, *111*, 797–806. [CrossRef]
24. Klein, T.; Spörk-Erdely, P.; Schneider-Bröskamp, C.; Oliveira, J.P.; Abreu Faria, G. Residual Stresses in a Wire and Arc-Directed Energy-Deposited Al–6Cu–Mn (ER2319) Alloy Determined by Energy-Dispersive High-Energy X-ray Diffraction. *Metall. Mater. Trans. A* **2024**, *55*, 736–744. [CrossRef]
25. Lin, J.; Ma, N.; Lei, Y.; Murakawa, H. Measurement of residual stress in arc welded lap joints by cosα X-ray diffraction method. *J. Mater. Process. Technol.* **2017**, *243*, 387–394. [CrossRef]
26. Hensel, J.; Nitschke-Pagel, T.; Dilger, K. On the effects of austenite phase transformation on welding residual stresses in non-load carrying longitudinal welds. *Weld. World* **2015**, *59*, 179–190. [CrossRef]

27. Köhler, M.; Fiebig, S.; Hensel, J.; Dilger, K. Wire and arc additive manufacturing of aluminum components. *Metals* **2019**, *9*, 608. [CrossRef]
28. Huang, W.; Wang, Q.; Ma, N.; Kitano, H. Distribution characteristics of residual stresses in typical wall and pipe components built by wire arc additive manufacturing. *J. Manuf. Process.* **2022**, *82*, 434–447. [CrossRef]

Disclaimer/Publisher's Note: The statements, opinions and data contained in all publications are solely those of the individual author(s) and contributor(s) and not of MDPI and/or the editor(s). MDPI and/or the editor(s) disclaim responsibility for any injury to people or property resulting from any ideas, methods, instructions or products referred to in the content.

applied sciences

MDPI

Article

Multi-Objective Optimisation of Welding Parameters for AZ91D/AA6082 Rotary Friction Welded Joints

Radosław Winiczenko [1,*], Andrzej Skibicki [2] and Paweł Skoczylas [3]

[1] Institute of Mechanical Engineering, Warsaw University of Life Sciences, Nowoursynowska 166, 02-787 Warsaw, Poland
[2] Faculty of Mechanical Engineering, Bydgoszcz University of Science and Technology, Kaliskiego 7, 85-789 Bydgoszcz, Poland; askibic@utp.edu.pl
[3] Institute of Mechanics and Printing, Warsaw University of Technology, Narbutta 85, 02-524 Warsaw, Poland
* Correspondence: radoslaw_winiczenko@sggw.edu.pl; Tel.: +48-225-934-624

Abstract: Recently, rotary friction welding has been used to join magnesium alloys. FRW uses friction heat to bond magnesium alloys with aluminium alloys. Combining these light alloys can provide many promising applications in the industry. The welding parameters such as friction and upsetting force, rotational speed, and welding time play a significant role in determining the joint strength. The paper presents a new approach to multi-objective optimisation of friction welding process parameters for AZ91D/AA6082 alloy joints. Multi-objective optimisation is based on artificial neural networks and genetic algorithms as non-conventional AI techniques. The methods were used to determine the following optimal welding process parameters: friction force, upsetting force and friction time for simultaneously maximised tensile strength and minimised metal loss (shortening) during welding. The ultimate tensile strength and metal loss of the friction welding joints were studied numerically and experimentally. Moreover, the influence of welding parameters on the ultimate tensile strength and shortening of friction joints was also studied. A genetic algorithm successfully found a set of welding parameters for which the joint strength increases from 24 to 81 MPA and the joint shortening decreases from 8.25 to 0.23 mm. The results show that a low friction force and upsetting force give a high value of tensile strength and the lowest shortening of the bimetal joints.

Keywords: rotary friction welding; AZ91D magnesium alloy; tensile strength; MOGA

1. Introduction

Recently, much attention has been focused on magnesium and aluminium alloys in many industrial sectors because of their unique properties. For their practical applications, joining technologies should also be developed in addition to considering issues such as alloy design, microstructure control, plastic forming, casting, and surface treatment [1]. Combining aluminium alloys with magnesium alloys contributes to reducing the weight of components and increasing production efficiency by replacing aluminium alloys with magnesium alloys wherever possible. Joining the mentioned metals is very difficult using conventional welding methods [2]. During standard joining, due to the melting of materials and a large amount of heat supplied, significant grain growth occurs in the heat-affected zone (HAZ), and many brittle intermetallic metal compounds (IMCs) are formed [3]. The aluminium–magnesium equilibrium system has partial solubility of magnesium and aluminium. However, in the range of several percent by weight and the remaining compositions, the IMCs are made [4,5]. The magnesium alloy was efficiently

joined with the aluminium alloy by laser [6,7] and diffusion welding methods [8,9]. Various Mg/Al joints are made primarily by friction stir welding (FSW) to take advantage of the lower ability to form an intermetallic phase in the case of solid-state welding [10–12]. Authors in the following papers [10,13,14] observed the presence of precipitates of the intermetallic phase, which caused a substantial increase in hardness at the weld zone. The defect-free joints were observed for various rotational speeds in the study [15]. Moreover, no intermetallic phases or cracks were found in the joint area. The maximum value of 132 MPa tensile strength and extremely low elongation of 2% was achieved for a tool rotation speed of 1000 rpm in reference [16]. The literature results indicate the possibility of producing sound Mg/Al welded joints with different mechanical properties using solid-state friction welding methods [17,18].

Recently, a relatively common solid-state welding method is rotary friction welding (FRW) [19]. Friction welding of metals can be performed using an inertia friction welding (IFW) or direct-drive rotational friction welding (DD-FRW) process. In the IFW, the rotating part is connected to a flywheel, and energy is supplied to the joint through the loss of kinetic rotational energy. The DD-FRW method directly converts mechanical energy into thermal energy on mutually rubbing surfaces in the contact area [20]. The friction welding process can be divided into two periods: friction and upsetting. The key parameters of the FRW process are friction time (FT), friction force (FF), upsetting force (UF) and rotational speed (RS). The parameters determine the temperature in the contact area and the temperature gradient in the weld zone. Friction time is necessary to heat the elements to the required temperature. The key process parameter during the upsetting period is the upsetting force (UF). The UF parameter is applied to heated metals. The upsetting force brings the crystals of the rubbing surfaces closer to the distance of the spatial mesh [21]. Moreover, the upsetting parameter facilitates the diffusion process and leads to the consolidation of the joint. The optimisation of welding parameters is necessary for the proper course of thermal phenomena and its effects on the mechanical properties and microstructure of the joint [20].

Many works have presented the optimisation of welding parameters for dissimilar metals using statistical methods, neural networks, response surface methods, factorial design, genetic algorithms, or hybrid artificial intelligence methods. A factorial design for selecting the process parameters and predicting the bead width, height and penetration in the joint was investigated [22]. The optimal weld pool geometry in the tungsten insert gas (TIG) welding of the stainless steel was studied [23]. The authors [24] intensively explored the effect of process parameters on the weld pool geometry using the Taguchi method. A statistical response surface method for optimising welding parameters was developed [25,26]. Multi-regression methods and neural network models to predict optimal weld parameters were also analysed in [27–29]. The neural networks have been used to identify the welding parameters in real-time [30]. ANNs successfully predicted the desired weld beam geometry in gas metal arc welding. The optimal process parameters like feed rate, welding voltage and weld speed have been found to predict the beam height and depth of penetration of the weld beam [31]. Simulated annealing (SA) was also applied as an intelligent method for optimising welding parameters and weld pool in the TIG welding process [32]. The neural networks and genetic algorithm as the hybrid intelligent method were also studied to search optimal process parameters [33–35]. The evolutionary algorithms (EAs), particle swarm (PSO) and SA algorithms have been used to determine welding parameters to maximise tensile strength and minimise metal loss in friction welding steel [36]. A multi-objective optimisation for maximising the tensile strength and minimising the flash diameter and the HAZ width for the ductile iron with low-carbon steel joints was carried out in the study [37]. A genetic algorithm modeling temperature

distribution during heating and cooling AZ31B magnesium alloys with 7075 aluminium alloy friction welded joints was investigated [38].

Rotary friction welding is a suitable welding method for joining light (Mg and Al) alloys [39,40]. In addition, FRW between dissimilar materials has recently received much attention [41]. However, more research is needed to optimise dissimilar FRW between Mg and Al alloys with relatively high strength using the conventional friction welding method [42–45]. In addition, it is difficult to fully understand the effects of basic processing parameters such as friction force, upsetting force and friction time on the dissimilar FRW between magnesium and aluminium alloys.

In this study, the previous joining of AZ91D with 6xxx series alloy bars by the direct-drive friction welding method was conducted. Then, the influences of the welding parameters on tensile properties and metal loss of the joints were experimentally and numerically investigated.

2. Materials and Methods

2.1. Materials

The rotary friction welding was carried out on AZ91D magnesium alloy and 6082T6 aluminium alloy bars of 20 mm in diameter and 100 mm in length. Bars were obtained by the extrusion process. The chemical composition and mechanical properties of the base metals are shown in Tables 1 and 2.

Table 1. Alloying elements (wt.%) of parent materials.

Material	Chemical Composition					
	Mg	Al	Zn	Cu	Si	Mn
AZ91D	Rest	8.5–9.5	0.45–0.9	0.02	0.08	0.17–0.4
AA6082	0.60–1.20	Rest	0.20	0.10	0.70–1.30	0.40–1.0

Table 2. The mechanical properties of base materials.

Material	Mechanical Properties			
	Tensile Strength (MPa)	Yield Strength (MPa)	Elongation A_5 (%)	Hardness (HB)
AZ91D	280	160	7	49
AA6082	310	260	8	95

Before welding, the surfaces were prepared on the abrasive cut-off machine. After that, all contacting surfaces of samples were polished using grit silicon carbide papers to reduce the effect of oxide films and surface roughness. The specimens were cleaned in acetone to remove dirt and grease.

2.2. Sample Preparation

Figure 1a shows the friction welding process on a continuous drive friction machine (ZT4-13 type). The aluminium alloy bar is rotated with the spindle during welding, and the magnesium bar is moved axially under the axial pressure. A detailed diagram of the welding process cycle is shown in Figure 1b. The samples are pressed under an axial force after reaching the desired rotational speed (RS). The heated contact surfaces rub against each other, and the metal slowly squeezes out as a flash (see Figure 1a). The rotation of the sample stops, and upsetting force (UF) is applied to consolidate the welding joint, as shown in Figure 1a. A set of reducers and compressed air valves performs the welding

machine's work cycle. The air pressure during the friction and welding phases was set according to the graph shown in Figure 1c.

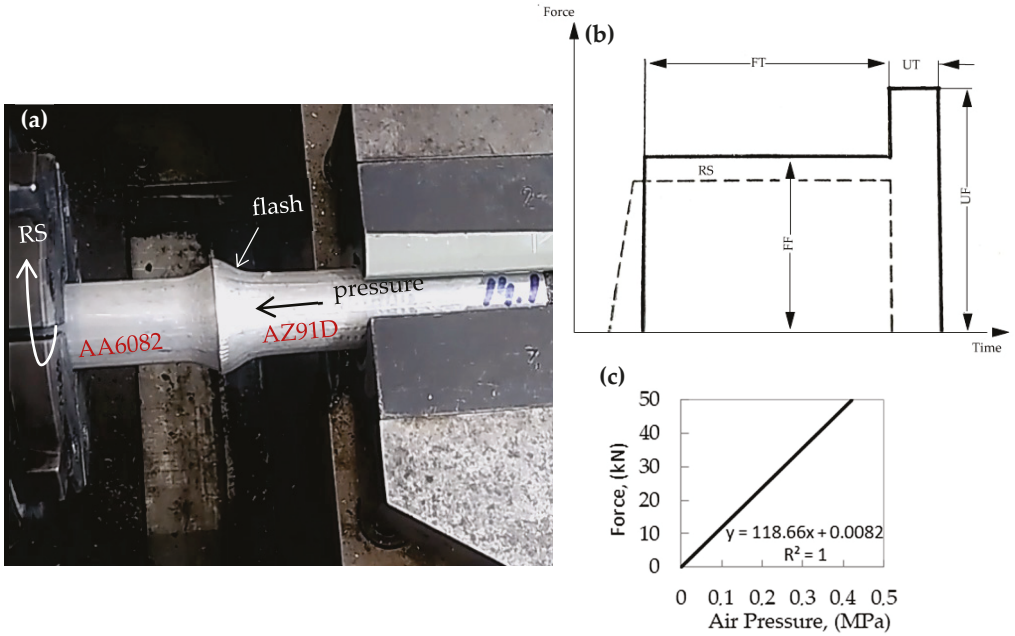

Figure 1. (**a**) FRW of Mg alloy to Al alloy (FF = 40 kN, UF = 45 kN and FT = 12 s); (**b**) friction welding process cycle; (**c**) air pressure during the friction and welding phases.

The process parameters used in the welding process are shown in Table 3. The choice of parameters for welding was based on the previous reports [43–46]. In the experiment, the rotational speed (RS) and upsetting time were constant and equal to 1450 rpm and 6 s, respectively.

Table 3. The welding parameters.

No.	Friction Force (kN)	Friction Time (s)	Upsetting Force (kN)
S1	35	6	40
S2	45	6	40
S3	35	12	40
S4	45	12	40
S5	35	6	50
S6	45	6	50
S7	35	12	50
S8	45	12	50
S9	35	9	45
S10	45	9	45
S11	40	6	45
S12	40	12	45
S13	40	9	40
S14	40	9	50
S15	40	9	45

2.3. Macrographs

The joining of the magnesium to aluminium alloy was conducted successively using a conventional friction welding process. Macrographs of the welded samples with various welding conditions (see Table 3) are shown in Figure 2.

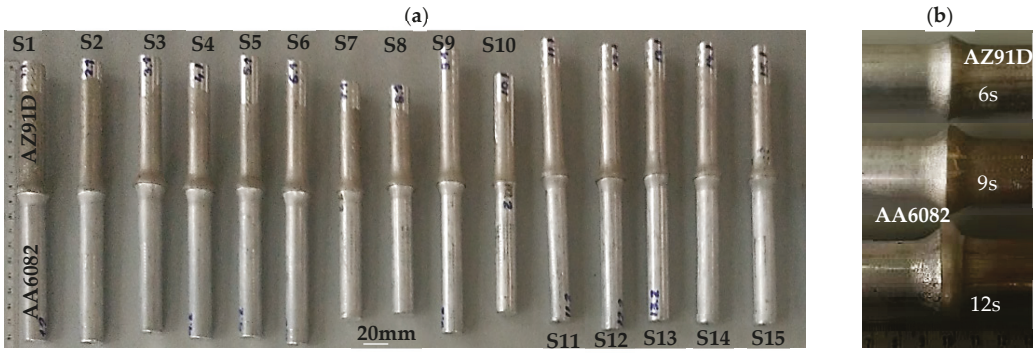

Figure 2. Macrographs of the welded samples: (**a**) various welding conditions; (**b**) flash diameter vs. friction time.

Before and after FRW, the length of the samples was measured to calculate the amount of material loss (shortening) during welding. Material loss (ML) is the difference between the total lengths (TLs) of both materials and the length of the friction weld (WL) after welding. The flashes in Figure 2 were symmetrically formed around the weld interface on magnesium and aluminium alloy sides. Flash formation increased with metal loss. During welding, the accumulated friction heat is enough to soften the base metal. The heated metal reaches a plastic state and is removed outwards due to the action of an axial force. Also, plastic deformation increased with increasing friction welding time, as shown in Figure 2b.

2.4. Testing

A tensile test was conducted on universal testing Instron, a servo-controlled machine (100 kN) at a constant movement rate of 1 mm/min (Figure 3). Room temperature tensile tests were carried out as per the ASTM:E8/E8M-13a standard specimen pattern [19].

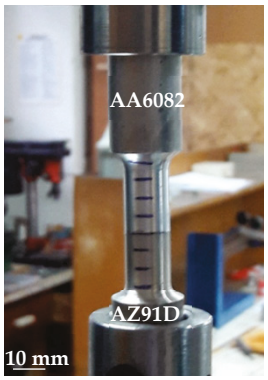

Figure 3. A universal tensile test machine with the AZ91D/AA6082 joint.

Three specimens were tested for each group of welding parameters. From each Mg/Al joint, the average of three tests was recorded.

3. The Basic Experimental Results

The basic experimental results of the tensile strength and shortening measurements of the materials after the tensile test are presented in Table 4.

Table 4 shows the welding parameters (FF, UF and FT) and experimental results matching TS and ML. The experimental results range from 24 to 81 MPa for TS and from 4.12 to 40.8 mm for ML. The basic results establish a dataset for modelling the relationship between welding parameters and the strength and shortening of materials using artificial neural networks.

Table 4. Experimental results of tensile strength and metal loss.

No.	Inputs			Outputs	
	FF (kN)	UF (kN)	FT (s)	TS (MPa)	ML (mm)
1	35	40	6	25	10.82
2	35	40	6	26	10.83
3	35	40	6	24	10.81
4	45	40	6	30	6.76
5	45	40	6	31	6.77
6	45	40	6	29	6.75
7	35	50	6	80	8.01
8	35	50	6	81	8.02
9	35	50	6	79	8.00
10	45	50	6	64	4.13
11	45	50	6	65	4.15
12	45	50	6	63	4.12
13	35	40	12	72	11.4
14	35	40	12	73	11.6
15	35	40	12	71	11.2
16	45	40	12	64	9.78
17	45	40	12	65	9.80
18	45	40	12	63	9.72
19	35	50	12	56	40.6
20	35	50	12	57	40.8
21	35	50	12	55	40.4
22	45	50	12	59	40.33
23	45	50	12	60	40.36
24	45	50	12	58	40.30
25	35	45	9	65	6.80
26	35	45	9	66	7.00
27	35	45	9	64	6.60
28	45	45	9	45	34.95
29	45	45	9	46	35.00
30	45	45	9	44	34.85
31	40	40	9	61	6.00
32	40	40	9	62	6.50
33	40	40	9	60	5.50
34	40	50	9	71	7.35
35	40	50	9	72	7.45
36	40	50	9	70	7.25
37	40	45	6	75	8.98
38	40	45	6	76	9.00
39	40	45	6	74	8.96
40	40	45	12	51	7.90
41	40	45	12	52	7.95
42	40	45	12	50	7.85
43	40	45	9	62	9.51
44	40	45	9	61	12.53
45	40	45	9	60	14.40
46	40	45	9	63	15.46
47	40	45	9	59	14.12
48	40	45	9	60	14.8

4. Modeling and Optimisation

ANNs are an artificial intelligence method with excellent approximation properties. Additionally, ANNs have a high accuracy in mapping nonlinear functions. In our example, the neural networks were used to find the objective function for the genetic algorithm. The

neural networks have found relationships between the process parameters and the tensile strength and shortening of the joint. In our study, the 48 cases (see Table 4) were normalised between 0 and 1, dividing them by their maximum values: 45, 50, 12 for the input parameters and 81, 40.8 for the TS and ML as output parameters, respectively. The input data were randomly divided into training (75%), testing (15%) and validation (15%) cases.

The input and output variables, the symbols used for each, the minimum and maximum values, and the mean and standard deviations of each variable are shown in Table 5.

Table 5. The range of input and output variables.

	Unit	Symbols	Min	Max	Mean	St. Dev.
Friction force	(kN)	FF	35	45	40	7.1
Upsetting force	(kN)	UF	40	50	45	7.1
Friction time	(s)	FT	6	12	9	4.2
Tensile strength	(MPa)	TS	24	81	52.5	40.3
Metal loss	(mm)	ML	4.12	40.8	22.5	25.9

4.1. Network Architecture

The neural network architecture was studied for twelve different cases based on previous literature. To find the best relations between the inputs (friction force, friction time and upsetting force) and outputs (tensile strength and metal loss), different activation functions and different numbers of neurons in the hidden layer were tested (see Table 6). The number of hidden nodes in a network is especially critical to network performance [27]. The effectiveness of the model was measured using the mean square error of validation samples (MSE *valid*.) and the correlation coefficient (*R*-value).

Table 6. Statistical analysis of ANN architecture.

No.	Activate Function in the Hidden Layer	Number of Neurons in the Hidden Layer	Activate Function in the Output Layer	Statistical Analysis	
				MSE *Valid.*	*R*-Value
1		6		0.0051899	0.98335
2		9	*log-sigmoid*	0.00019381	0.99932
3	*log-sigmoid*	12		0.00025457	0.99898
4		8		0.0307550	0.82024
5		9	*pure-line*	0.00027127	0.99827
6		12		0.0002623	0.9984
7		6		0.0013337	0.99288
8		9	*pure-line*	0.000234	0.9981
9	*tan-sigmoid*	12		0.0019702	0.99359
10		6		0.00081242	0.99662
11		9	*log-sigmoid*	0.00039503	0.99769
12		12		0.00042046	0.99803

The typical architecture of an ANN includes an input layer, one or more hidden layers, and an output layer. The layers consist of one or more neurons linked together by weights and biases. In this study, a multilayer perceptron of ANN architecture is shown in Figure 4. The optimum architecture is taken as 3-9-2: three neurons in the input layer FF (x_1), UF (x_2), and FT (x_3), nine neurons in the hidden layer and two neurons in the output layer UTS (y_1) and ML (y_2). Logarithmic–sigmoidal activation functions for the hidden and output layers were selected for the study.

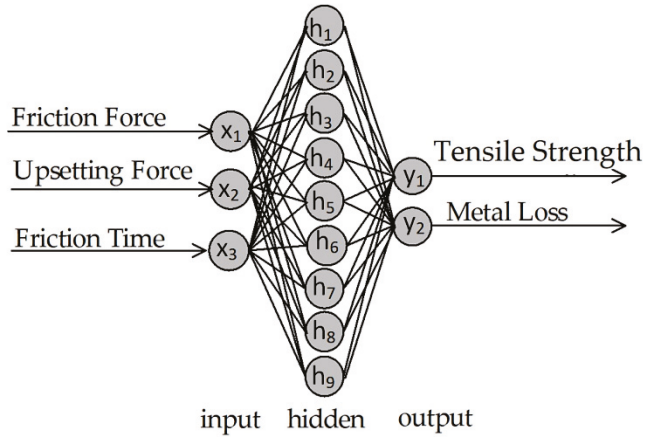

Figure 4. Architecture of the neural networks.

4.2. Validation and Learning Process

The relationship between process parameters and the tensile strength of the joint and the shortening of materials were modelled using artificial neural networks (ANNs) in Matlab. In this case study, a multilayer neural network with a backpropagation algorithm used the *Lavenberg Marquart* method for learning data [47]. The best MSE for the validation test is shown in Figure 5.

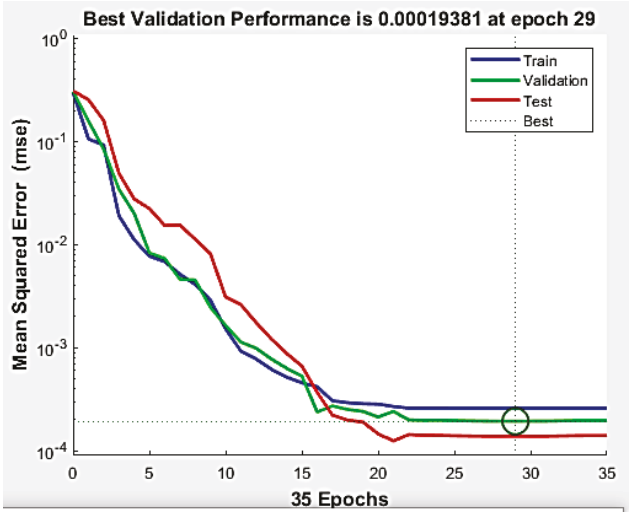

Figure 5. The course of the neural network training process.

The best fit was obtained after 29 epochs, for which the smallest MSE error was 0.00019381. The low value of the mean squared error indicates that the neural network model developed will provide good predictions.

Figure 6 shows the performance plot for training, validation, testing and overall data. A correlation coefficient (*R*-value) close to 1 implies a close relationship between definite output and forecast output.

Figure 6 shows the results of the correlation coefficient *R* for the training, test, validation and total sets. The values for these sets are 0.9986, 0.9993, 0.9992 and 0.998, respectively. These values are close to 1; hence, it can be concluded that the neural network has been well-modelled and can be used to optimise the process parameters [47].

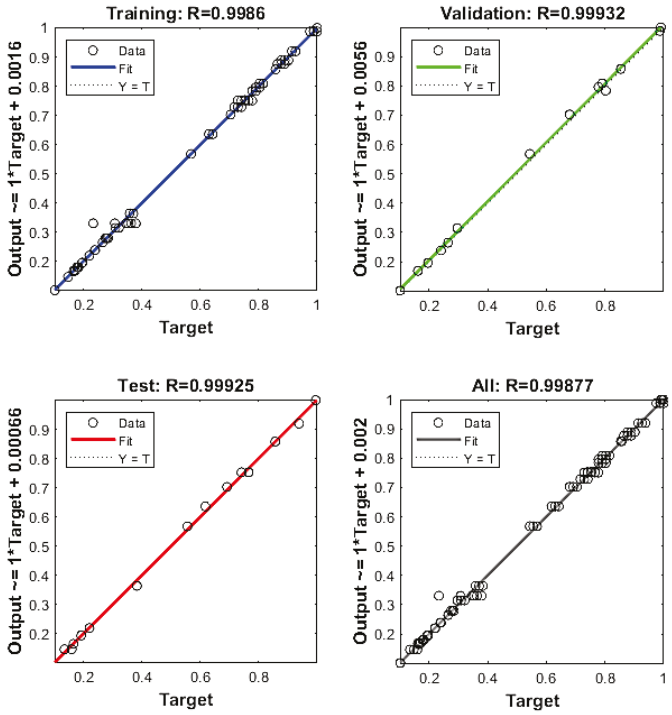

Figure 6. Performance plot (*R*-value) of the ANN for ultimate tensile strength vs. metal loss.

4.3. Formulation of Objective Function

The objective functions for ultimate tensile strength (UTS) and metal loss (ML) are calculated as follows:

$$\text{Maximise TS} = \left(\frac{1}{1+e^{-(-2.48\times F1+3.49\times F2-3.97\times F3-4.41\times F4+3.57\times F5-1.46\times F6+2.59\times F7+1.19\times F8+1.05\times F9+3.30)}}\right) \quad (1)$$

$$\text{Minimise ML} = \left(\frac{1}{1+e^{-(-0.82\times F1+1.72\times F2-0.80\times F3-6.62\times F4+0.04\times F5-1.18\times F6-2.62\times F7-6.37\times F8+15.97\times F9+6.90)}}\right) \quad (2)$$

The mathematical formulations (1) and (2) can be derived from resulting weights and activation function (3).

The activation function was given as

$$E_i = \left(\frac{1}{1+e^{-T_i}}\right), \quad (3)$$

Function (3) determines the value of the state of the neurons, which will be transmitted to the downstream neurons.

where

$$T_i = w_1 \times x_1 + w_2 \times x_2 + w_3 \times x_3 + b \quad (4)$$

The constants used to estimate the T_i are given in Table 7.

In this study, functions (1)–(4) are simultaneously optimised according to the lower and upper bounds, as shown below:

$$35 \leq x_1 \leq 45 \quad (5)$$

$$40 \leq x_2 \leq 50 \quad (6)$$

$$6 \leq x_3 \leq 12 \quad (7)$$

The constraints in Equations (5)–(7) are the constraints for the friction force x_1, the upsetting force x_2 and the friction time x_3, respectively.

Table 7. Weights (w_i) and biases (bi) derived from input and hidden layer of neural network.

i	w_1	w_2	w_3	b
1	32.06	43.76	9.00	−75.68
2	−11.04	1.27	−22.02	28.69
3	−30.41	41.24	−9.48	4.66
4	−23.66	19.73	−27.44	25.19
5	−28.80	46.06	3.44	−17.64
6	−22.36	−33.61	22.25	33.11
7	−8.82	44.44	−18.80	−20.31
8	6.98	−37.82	16.70	14.74
9	−12.07	41.93	16.38	−47.43

4.4. Genetic Algorithms

Recently, many works have been devoted to multi-criteria optimisation using genetic algorithms. The most popular are the multi-criteria genetic algorithms MOGA and NSGA. Both methods provide solutions in the form of a Pareto chart. These algorithms are an optimisation method based on the natural evolution of populations of living organisms. The algorithms conduct searches on populations built of chromosomes. These, in turn, are built of genes. Genetic algorithms search for the best solutions from a population and not from a single point. Genetic algorithms use random methods of chromosome selection in which crossover and mutation operators play an important role. Crossover is the exchange in a sequence of genes between two chromosomes. A mutation parameter involves changing the value of a gene in a single chromosome [48]. Genetic algorithms optimise tasks in a big search space for nonlinear functions of complex problems.

A multi-objective genetic algorithm (MOGA) is employed to optimise engineering tasks where multiple criteria impact the quality of the solutions. MOGA identifies a set of decision variables that meet specific constraints to provide satisfactory values for all objective functions. The algorithm minimises or maximises several objective functions [46,48]. MOGA produces a set of optimal solutions known as Pareto optimal solutions. The Pareto front represents all of these non-dominated solutions within the objectives space. This study used the Non-Sorting Genetic Algorithm II (NSGA-II) for the multi-objective optimisation of process parameters. The main steps of the NSGA-II have been demonstrated in previous papers [49,50].

Multi-objective optimisation was performed using the *Gamultiobj* procedure in the Optimisation Tool of Matlab R2018a software. *Gamultiobj* uses the NSGA II for multi-objective optimisation [47,51]. The main parameters of the multi-objective genetic algorithm are presented in Table 8.

Table 8. *NSGA-2* main parameters.

GA Parameter	Symbol	Value
Number of generations	N_g	500
Population size	$Pop._{size}$	80
Crossover function	C_f	heuristic
Crossover probability	C_{prob}	0.9
Mutation function	M_f	uniform
Mutation probability	M_{prob}	0.2

5. Results and Discussion

Table 9 shows the thirty-two solutions (No. 1–32) of the optimal set in the *Pareto* sense.

Table 9. The predicted *Pareto* results of tensile strength and metal loss.

No.	FF (kN)	UF (kN)	FT (s)	TS (MPa)	ML (mm)
1	35	40	9	30.06	0.23
2	35	48	6	80.13	8.25
3	35	48	8	79.76	7.84
4	35	41	9	44.23	0.30
5	35	42	11	78.81	5.34
6	35	40	9	33.37	0.24
7	35	42	10	78.62	4.81
8	35	42	10	78.18	3.94
9	35	42	10	77.41	2.93
10	35	42	10	76.72	2.30
11	35	40	9	40.44	0.29
12	35	48	8	79.39	7.60
13	35	42	10	72.92	1.19
14	35	42	10	75.98	1.94
15	35	42	10	75.36	1.86
16	35	41	9	54.99	0.40
17	35	41	9	52.85	0.38
18	35	42	10	77.04	2.76
19	35	42	11	79.17	7.03
20	35	42	11	78.89	5.77
21	35	40	9	40.44	0.29
22	35	42	10	73.98	1.35
23	35	42	10	77.72	3.28
24	35	42	10	74.25	1.54
25	35	41	9	49.89	0.34
26	35	42	10	78.42	4.42
27	35	48	7	80.07	8.18
28	35	42	10	71.42	0.94
29	35	42	11	78.81	5.34
30	35	41	9	58.62	0.43
31	35	42	11	78.93	6.06
32	35	42	11	79.10	6.63

Table 9 shows that the best solutions were obtained for a low friction force of 35 kN and a friction welding time of 10 s. According to the results (see Table 9, No. 7–10), the tensile strength was about 80 MPa, and the average joint shortening was only 3.5 mm. For these solutions, the upsetting force was also low. Increasing the upsetting force to almost the maximum value (48 kN) caused more significant material losses of up to 8 mm. It is worth noting that in the optimisation case, a lower material loss of about 50% was achieved, comparing Table 4, No. 7, 8 with Table 9, No. 7, 8.

The Pareto curve of UTS and ML using genetic algorithms is presented in Figure 7.

The set of solutions consists of 32 points, forming a *Pareto* curve, with limits defined by the extreme points ID1 and ID2 (see No. 1 and 2, Table 9). Point ID2 in Figure 7 is the highest point on the *Pareto* curve with the highest UTS = 80.13 MPa and the highest metal loss ML = 8.25 in mm (see Table 9, point No. 2). For point ID2, the welding parameters are as follows: friction force is 35 kN, friction time is 6 s, and upsetting force is 48 kN. The lowest point on the *Pareto* curve is ID1 (see Figure 7). For point ID = 1, the lowest metal loss is 0.23 mm, while the lowest UTS = 30 MPa is received (see No. 1 in Table 9). For point ID1, the following welding parameters (FF = 35 kN, FT = 9 s and UF = 40 kN) were found.

When the *Pareto* solutions are analysed further, more information regarding the variation in the process parameters is exposed. All the Pareto solutions are numbered and sorted in order to increase the tensile strength of the joint and decrease metal loss for all cases.

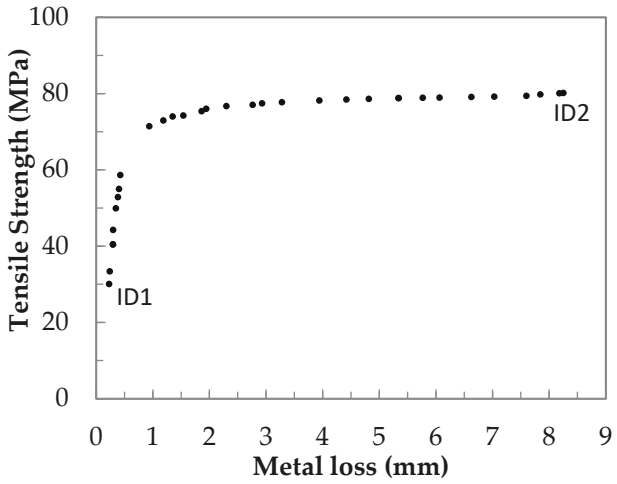

Figure 7. *Pareto* front solutions of tensile strength and metal loss for AZ91D/6082 joint.

Figure 8 shows the variation in UTS and ML values of the *Pareto* solutions for the AZ91D/6061 joint (arranged in ascending order and plotted as the population size (Pop_{size}).

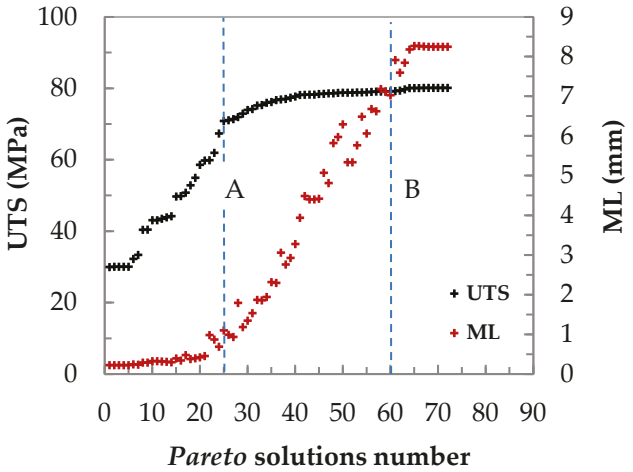

Figure 8. The ultimate tensile strength and metal loss in the *Pareto* solution number for AZ91D/6082 joints.

Conflicting relations between the objective functions (UTS and ML) of welding process quality have been observed. The *Pareto* solution number of UTS vs. ML was optimised using a combination of *Ngen* and population size. In this optimisation task, the N_{gen} and Pop_{size} values were 80. The probability crossover of 0.9 and mutation of 0.2 are kept constant in all optimisation procedures. In this problem, the UTS and ML were optimised simultaneously. However, finding a solution that simultaneously optimises UTS and ML is not possible. From Figure 8, it can be observed that the range of region (A–B) of higher UTS (68–80 MPA) with metal loss that changed in the range (0.7–7 mm) was selected for further analysis of the *Pareto* results. The solution numbers corresponding to the region (A–B) are 25 to 60, which could be used to determine the ranges of best FF, FT, and UF welding parameters.

The process parameter solutions FF (a), UF (b) and FT (c) in all 80 *Pareto* solutions with increasing tensile strength are shown in Figure 9.

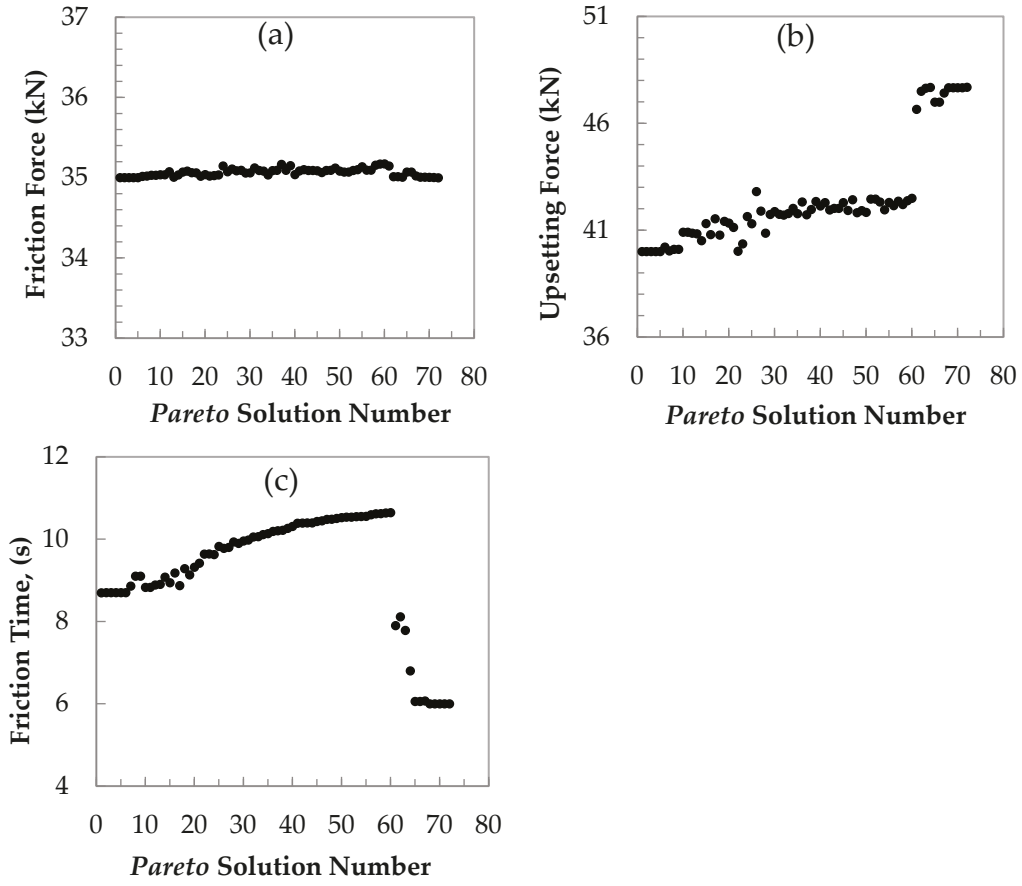

Figure 9. Variation in friction force (**a**), upsetting force (**b**), and (**c**) friction time in the Pareto solution in order according to increasing the tensile strength of the AZ91/6082 joints.

The optimisation results in Figure 9 show many variants of *Pareto* solutions for welding parameters. Figure 9a indicates the average value of 35 kN for FF, whereas UF increases linearly from 67 to 80 MPa (Figure 9b). Figure 9b,c show the increasing UF and UT values in the A–B range. Moreover, the constant values outside the range are visible. The UF and UF values are 48 kN and 6 s, respectively.

Figure 10 shows the variation in the FF, UF and FT parameters in all 80 *Pareto* solutions with decreasing metal loss.

Figure 10 shows the predicted effects of friction force, upsetting force and friction time on the metal loss in the *Pareto* solution number. As expected, with increasing upsetting force and more shortening of metal in the considered area (A–B), UF decreases linearly from 42 to 40 kN, or logarithmically from 27 to 46%. After reaching 60 generations, the shortening value stabilises at an 8 mm level. The predicted pattern shows linearly decreasing metal loss with decreasing upsetting force and friction time [52,53].

The new experimental runs for FF = 35 kN, UF = 48 kN, and FT = 6 s were used to confirm the developed model. The validation UTS and ML results are presented in Table 10.

Table 10. Validation results.

	UTS	**ML**
Experimental values (y_{ei})	82	8.50
Predicted values (y_{pi})	80	8.25
Errors $= \frac{y_{ei}-y_{pi}}{y_{pi}} \cdot 100\%$	2.4	3.0

Table 10 shows that the experimental values are close to those obtained by the genetic algorithm. So, the absolute relative error between them was only 3%.

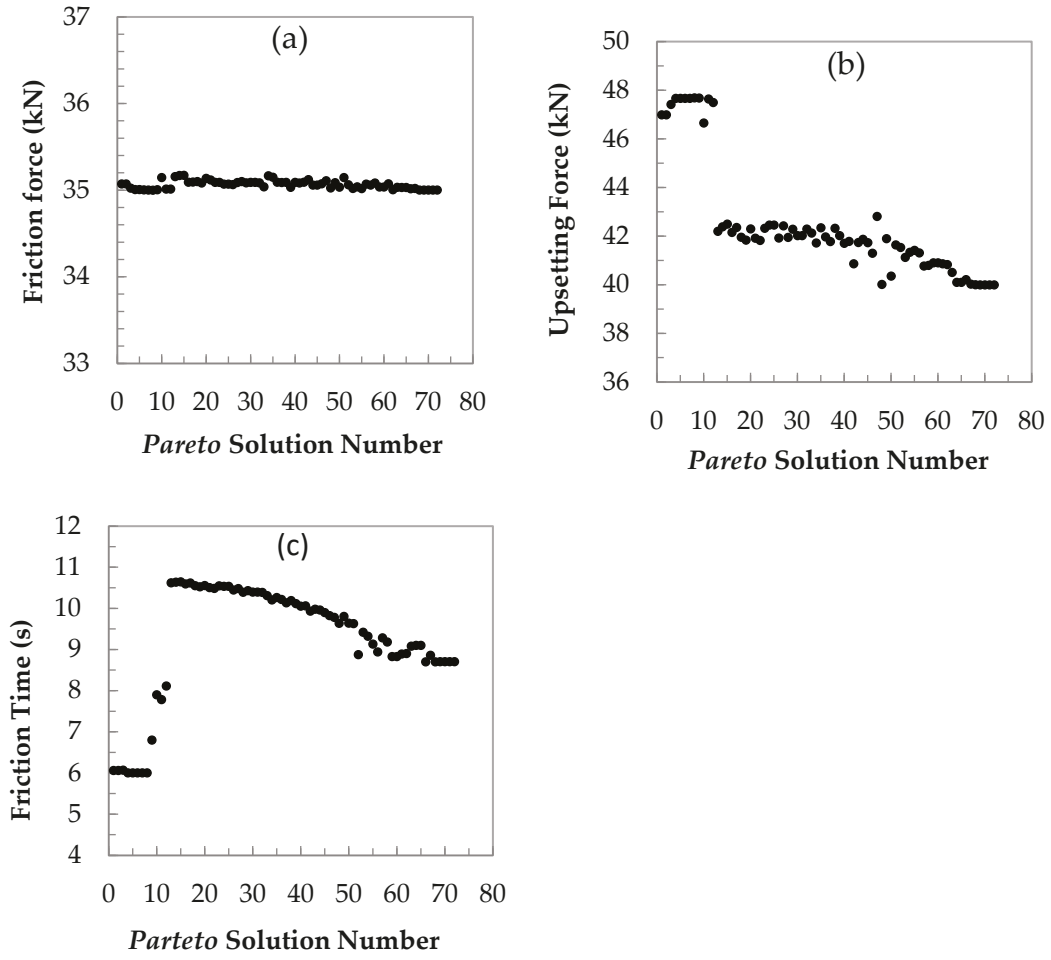

Figure 10. Variation in friction force (**a**), upsetting force (**b**), and (**c**) friction time in the Pareto solution (in order according to decreasing metal loss) of the AZ91/6082 joints.

6. Conclusions

In the present study, the first sound joint was attained between the AZ91D magnesium alloy and AA6082 aluminium alloy using a conventional friction welding method. Additionally, a new approach in multi-criteria optimisation of welding parameters was presented to obtain maximum joint strength and minimum shortening of joints. The following conclusions can be drawn from the research:

1. A neural network with nine neurons in the hidden layer and a log-sigmoidal activation function were the best approximators in formulating a multi-objective function for the genetic algorithm.
2. The *NSGA-2 genetic* algorithm found a set of welding parameters for which the joint strength increases from 24 to 81 MPA, and the joint shortening decreases from 8.25 to 0.23 mm. These solutions are in constant conflict with each other.
3. The increase in welding time and upsetting force has a positive effect on the increase in the tensile strength of the welded joint and a negative effect on material losses.
4. The results show that a low friction force (35 kN) and upsetting force (42 kN) give a high value of tensile strength (78 MPa) and the lowest shortening (3.5 mm) of the bimetal joints.
5. During the verification of the model for the new welding parameters, its error did not exceed 3%.

This study can be extended to the microstructure and crack behaviour at the joint interface. The influence of welding parameters on the formation of intermetallic compound (IMC) layers and microcracks, reported in the references [42–44] for this pair of joined materials, should be investigated.

Author Contributions: R.W.: Proposal of the research topic; formal analysis; experiments; optimisation; writing of the manuscript; review and editing. A.S.: Formal analysis; experiments. P.S.: Formal analysis: experiments. All authors have read and agreed to the published version of the manuscript.

Funding: This research received no external funding.

Institutional Review Board Statement: Not applicable.

Informed Consent Statement: Not applicable.

Data Availability Statement: Data are contained within the article.

Conflicts of Interest: The authors declare no conflicts of interest.

References

1. Liu, L. *Welding and Joining of Magnesium Alloys*; Woodhead Publishing Limited: Cambridge, UK, 2010.
2. Lathabai, S. *Fundamentals of Aluminium Metallurgy*; Fundamentals of Aluminium Metallurgy Production, Processing and Applications A volume in Woodhead Publishing Series in Metals and Surface Engineering; Woodhead Publishing: Cambridge, UK, 2011; pp. 607–654.
3. Guo, J. Solid State Welding Processes in Manufacturing. In *Handbook of Manufacturing Engineering and Technology*; Nee, A.Y.C., Ed.; Springer: London, UK, 2015.
4. Liu, L.; Ren, D.; Liu, F. A review of dissimilar welding techniques for magnesium alloys to aluminum alloys. *Materials* **2014**, *7*, 3735–3757. [CrossRef] [PubMed]
5. Liu, P.; Li, Y.; Geng, H.; Wang, J. Microstructure characteristics in TIG welded joint of Mg/Al dissimilar materials. *Mater. Lett.* **2007**, *61*, 1288–1291. [CrossRef]
6. Borrisutthekul, R.; Miyashita, Y.; Mutoh, Y. Dissimilar material laser welding between magnesium alloy AZ31B and aluminum alloy A5052-O. *Sci. Technol. Adv. Mater.* **2005**, *6*, 199–204. [CrossRef]
7. Liu, L.M.; Zhao, X. Study on the weld joint of Mg alloy and steel by laser-GTA hybrid welding. *Mater. Charact.* **2008**, *59*, 1279–1284. [CrossRef]
8. Liu, P.; Li, Y.; Wang, J.; Haijun, M.A.; Guo, G.; Geng, H. Microstructure and phase constituents in the interface zone of Mg/Al diffusion bonding. *Met. Mater. Trans. B* **2006**, *37*, 649–654. [CrossRef]
9. Zhao, L.M.; Zhang, Z.D. Effect of Zn alloy interlayer on interface microstructure and strength of diffusion-bonded Mg–Al joints. *Scr. Mater.* **2008**, *58*, 283–286. [CrossRef]
10. Mclean, A.A.; Powell, G.L.F.; Brown, I.H.; Linton, V.M. Friction stir welding of magnesium alloy AZ31B to aluminium alloy 5083. *Sci. Technol. Weld. Join.* **2003**, *8*, 462–464. [CrossRef]
11. Firouzdor, V.; Kou, S. Al-to-Mg friction stir welding: Effect of material position, travel speed, and rotation speed. *Met. Mater. Trans. A* **2010**, *41*, 2914–2935. [CrossRef]
12. Fu, B.; Qin, G.; Li, F.; Meng, X.; Zhang, J.; Wu, C. Friction stir welding process of dissimilar metals of 6061-T6 aluminum alloy to AZ31B magnesium alloy. *J. Mater. Process. Technol.* **2015**, *218*, 38–47. [CrossRef]
13. Zhao, Y.; Jiang, S.; Yang, S.; Lu, Z.; Yan, K. Influence of cooling conditions on joint properties and microstructures of aluminum and magnesium dissimilar alloys by friction stir welding. *Int. J. Adv. Manuf. Technol.* **2016**, *83*, 673–679. [CrossRef]
14. Somasekharan, A.; Murr, L. Characterization of complex, solid-state flow and mixing in the friction-stir welding (FSW) of aluminum alloy 6061-T6 to magnesium alloy AZ91D using color metallography. *J. Mater. Sci.* **2006**, *41*, 5365–5370. [CrossRef]
15. Tan, M.; Wu, C.; Shi, L. Formation Mechanism of Thicker Intermetallic Compounds in Friction Stir Weld Joints of Dissimilar AA2024/AZ31B Alloys. *Materials* **2023**, *16*, 51. [CrossRef] [PubMed]
16. Prasad, B.L.; Neelaiah, G.; Krishna, M.G.; Ramana, S.V.; Prakash, K.S.; Sarika, G.; Reddy, G.P.; Dumpala, R.; Sunil, B.R. Joining of AZ91 Mg alloy and Al6063 alloy sheets by friction stir welding. *J. Magnes. Alloy.* **2018**, *6*, 71–76. [CrossRef]
17. Kato, K.; Tokisue, H. Dissimilar friction welding of aluminium alloys to other materials. *Weld. Int.* **2004**, *18*, 861–867. [CrossRef]
18. Kimura, M.; Fuji, A.; Shibata, S. Joint properties of friction welded joint between pure magnesium and pure aluminium with post-weld heat treatment. *Mater. Des.* **2015**, *85*, 169–179. [CrossRef]
19. American Welding Society. *Recommended Practice for Friction Welding*; AWS: Miami, FL, USA, 1989.
20. Vill, V.I. *Friction Welding of Metals*; American Welding Society: New York, NY, USA, 1962.

21. Crossland, B. Friction welding. *Contemp. Phys.* **1971**, *12*, 559–574. [CrossRef]
22. Kim, I.S.; Son, K.J.; Yang, Y.S.; Yaragada, P.K.D.V. Sensitivity analysis for process parameters in GMA welding processes using a factorial design method. *Int. J. Mach. Tools Manuf.* **2003**, *43*, 763–769. [CrossRef]
23. Murti, K.G.K.; Sundaresan, S. Parameter optimization in friction welding dissimilar materials. *Metal. Constr.* **1983**, *15*, 331–335.
24. Juang, S.C.; Tarang, Y.S. Process Parameter selection for optimizing the weld pool geometry in the tungsten inert gas welding of stainless steel. *J. Mater. Process. Technol.* **2002**, *122*, 33–37. [CrossRef]
25. Paventhan, R.; Lakshminarayanan, P.R.; Balasubramanian, V. Prediction and optimization of friction welding parameters for joining aluminium alloy and stainless steel. *Trans. Nonferrous Met. Soc. China* **2011**, *21*, 1480–1485. [CrossRef]
26. Srichok, T.; Pitakaso, R.; Sethanan, K.; Sirirak, W.; Kwangmuang, P. Combined Response Surface Method and Modified Differential Evolution for Parameter Optimization of Friction Stir Welding. *Processes* **2020**, *8*, 1080. [CrossRef]
27. Padmanaban, G.; Balasubramanian, V. Prediction of tensile strength and optimization of process parameters for friction stir welded AZ31B magnesium. *Proc. Inst. Mech. Eng. B J. Eng. Manuf.* **2010**, *224*, 1519–1528. [CrossRef]
28. Shojaeefard, M.H.; Behnagh, R.A.; Akbari, M.; Givi, M.K.B.; Farhani, F. Modelling and Pareto optimization of mechanical properties of friction stir welded AA7075/AA5083 butt joints using neural network and particle swarm algorithm. *Mater. Des.* **2013**, *44*, 190–198. [CrossRef]
29. Okuyucu, H.; Kurt, A.; Arcaklioglu, E. Artificial neural network application to the friction stir welding of aluminum plates. *Mater. Des.* **2007**, *28*, 78–84. [CrossRef]
30. Zhang, Y.M.; Kovacevic, R.; Li, L. Characterization and real-time measurement of geometrical appearance of the weld pool. *Int. J. Mach. Tools Manuf.* **1996**, *36*, 799–816. [CrossRef]
31. Kim, D.; Rhee, S. Optimization of arc welding process parameters using a genetic algorithm. *Weld. J.* **2001**, *80*, 184–189.
32. Kumaran, S.S.; Muthukumaran, S.; Vinodh, S. Optimization of friction welding of tube to tube plate using an external tool by hybrid approach. *J. Alloy Compd.* **2011**, *509*, 2758–2769. [CrossRef]
33. Winiczenko, R.; Salat, R.; Awtoniuk, M. Estimation of tensile strength of ductile iron friction welded joints using hybrid intelligent methods. *Trans. Nonferrous Met. Soc. China* **2013**, *23*, 385–391. [CrossRef]
34. Canyurt, O. Estimation of welded joint strength using genetic algorithm approach. *Int. J. Mech. Sci.* **2005**, *47*, 1249–1261. [CrossRef]
35. Canyurt, O. Fatigue strength estimation of adhesively bonded tubular joint using genetic algorithm approach. *Int. J. Mech. Sci.* **2004**, *46*, 359–370. [CrossRef]
36. Sathiya, P. Optimization of friction welding parameters using evolutionary computational techniques. *J. Mater. Process. Technol.* **2009**, *209*, 2576–2584. [CrossRef]
37. Chen, H.; Zhu, Z.; Zhu, Y.; Sun, L.; Guo, Y. Solid-State Welding of Aluminum to Magnesium Alloys: A Review. *Metals* **2023**, *13*, 1410. [CrossRef]
38. Winiczenko, R.; Skibicki, A.; Skoczylas, P.; Trajer, J. Multi-objective optimization of the process parameters for friction welding of dissimilar metals. *E3S Web Conf.* **2019**, *132*, 01028. [CrossRef]
39. Winiczenko, R.; Skibicki, A.; Skoczylas, P.; Trajer, J. A genetic algorithm modelling of temperature distributions in the AZ31B magnesium alloys with 7075 aluminium alloy friction welded joints. *E3S Web Conf.* **2019**, *132*, 01029. [CrossRef]
40. Singh, K.; Singh, G.; Singh, H. Review on friction stir welding of magnesium alloys. *J. Magnes. Alloy.* **2018**, *6*, 399–416. [CrossRef]
41. Gaurav, S.; Mishra, R.S.; Zunaid, M. A critical review on mechanical and microstructural properties of dissimilar aluminum (Al)-magnesium (Mg) alloys. *Adhes. Sci. Technol.* **2022**, *37*, 1117–1149. [CrossRef]
42. Liang, Z.; Qin, G.; Wang, L.; Meng, X.; Li, F. Microstructural characterization and mechanical properties of dissimilar friction welding of 1060 aluminum to AZ31B magnesium alloy. *Mater. Sci. Eng. A* **2015**, *645*, 170–180. [CrossRef]
43. Liang, Z.; Qin, G.; Geng, P.; Yang, F.; Meng, X. Continuous drive friction welding of 5A33 Al alloy to AZ31B Mg alloy. *J. Manuf. Process.* **2017**, *25*, 153–162. [CrossRef]
44. Guo, W.; You, G.; Yuan, G.; Zhang, X. Microstructure and mechanical properties of dissimilar inertia friction welding of 7A04 aluminum alloy to AZ31 magnesium alloy. *J. Alloys Compd.* **2017**, *695*, 3267–3277. [CrossRef]
45. Meran, C. Prediction of the optimized welding parameters for the joined brass plates using genetic algorithm. *Mater. Des.* **2006**, *27*, 356–363. [CrossRef]
46. Rutkowski, L. *Computational Intelligence, Methods and Techniques*; Springer: Berlin/Heidelberg, Germany, 2008.
47. Deb, K. *Optimization for Engineering Design*; Prentice-Hall: New Delhi, India, 1998.
48. Gen, M.; Cheng, R. *Genetic Algorithms and Engineering Design*; Wiley: New York, NY, USA, 1997.
49. *MATLAB 7.6 R2008a. Documentation R*; MathWorks, Inc.: Natick, MA, USA, 2008.
50. Winiczenko, R.; Górnicki, K.; Kaleta, A.; Martynenko, A.; Janaszek-Mańkowska, M.; Trajer, J. Multi-objective optimization of convective drying of apple cubes. *Comput. Electron. Agric.* **2018**, *145*, 341–348. [CrossRef]
51. Winiczenko, R. Effect of friction welding parameters on the tensile strength and microstructural properties of dissimilar AISI 1020-ASTM A536 joints. *Int. J. Adv. Manuf. Technol.* **2016**, *84*, 941–955. [CrossRef]

52. Winiczenko, R.; Skibicki, A.; Skoczylas, P. Optimization of friction welding parameters to maximize the tensile strength of magnesium alloy with aluminum alloy dissimilar joints using genetic algorithm. *Processes* **2021**, *23*, 1550. [CrossRef]
53. Srinivasan, M.; Loganathan, C.; Balasubramanian, V.; Nguyen, Q.B.; Gupta, M.; Narayanasamy, R. Feasibility of joining AZ31B magnesium metal matrix composite by friction welding. *Mater. Des.* **2011**, *32*, 1672–1676. [CrossRef]

Disclaimer/Publisher's Note: The statements, opinions and data contained in all publications are solely those of the individual author(s) and contributor(s) and not of MDPI and/or the editor(s). MDPI and/or the editor(s) disclaim responsibility for any injury to people or property resulting from any ideas, methods, instructions or products referred to in the content.

applied sciences

MDPI

Article

Development of an Artificial Neural Network Model to Predict the Tensile Strength of Friction Stir Welding of Dissimilar Materials Using Cryogenic Processes

Mingoo Cho [1], Jinsu Gim [2], Ji Hoon Kim [1,*] and Sungwook Kang [3,*]

[1] Department of Mechanical Engineering, Pusan National University, Busan 46241, Republic of Korea; cmg0142@pusan.ac.kr
[2] Extreme Process Control R&D Group, Korea Institute of Industrial Technology, Jinju 52845, Republic of Korea; jgim@kitech.re.kr
[3] Department of Smart Ocean Mobility Engineering, Changwon National University, Changwon 51140, Republic of Korea
* Correspondence: kimjh@pusan.ac.kr (J.H.K.); swkang@changwon.ac.kr (S.K.); Tel.: +82-51-510-3031 (J.H.K.); +82-55-213-3681 (S.K.)

Abstract: The objective of this study was to develop an artificial neural network (ANN) model for predicting the tensile strength of friction stir welding (FSW) joints between dissimilar materials, with a particular focus on aluminum and copper, using cryogenic processes. The research addresses the challenges posed by differences in material properties and the complex nature of FSW, where traditional experimental methods are time-consuming and costly. FSW experiments were conducted under a variety of conditions, and the resulting temperature data were utilized as input for a heat transfer analysis. The maximum temperature and temperature gradient obtained from the analysis were employed as input variables for training the ANN. The ANN was optimized using the Hyperband tuner and validated against experimental results. The model successfully predicted tensile strength with an average error of 5.4%, demonstrating its potential for predicting mechanical properties under different welding conditions. This approach offers a more efficient and accurate method for optimizing FSW processes.

Keywords: friction stir welding; dissimilar materials; aluminum alloy; copper alloy; finite element method; tensile strength; artificial neural networks; cryogenic process

1. Introduction

Friction stir welding (FSW) is a welding method developed by TWI (The Welding Institute) in the UK in 1991, in which a high-speed rotating non-consumable tool is inserted into the base material to be joined, and the softened base material is subjected to a forcible stirring action by the rotating tool, which is caused by the generation of frictional heat between the tool and the base material [1–4]. It is a solid-phase welding rather than fusion welding such as arc welding, gas welding, electron beam welding, etc., and has the advantages of small deformation, excellent mechanical strength of the welded part, and almost no defects such as pores and cracks [5–7]. FSW is suitable for joining lightweight alloys and casting parts, such as aluminum, copper, magnesium, and titanium, which is difficult to achieve with conventional welding technologies, so its application fields are expanding in the automotive, aviation, aerospace, shipbuilding, and electronics industries [8,9]. In recent years, there has been a growing need to manufacture parts by joining different materials in order to improve their strength, lightness, electrical properties, and other characteristics. This has led to a significant amount of research and development activity, driven by the economic and technological advantages associated with this approach [10–12]. In particular, the joining of copper and aluminum alloys is employed in a variety of applications due

to their excellent thermal and electrical conductivity. In the automotive industry, copper and aluminum are utilized in automotive batteries due to the implementation of electric drive systems [13–15]. The inverter of an electric vehicle is a device that converts DC power from the battery into AC power to control the speed of the motor, and coolant circulates through the inverter housing to perform thermal management. Conventional inverter housing covers are made of aluminum, but they are being replaced with copper materials to increase efficiency. The joining of copper and aluminum is prone to defects due to differences in melting temperature, fluidity, and material properties, as well as the chemical composition of the materials [16–18]. In friction stir welding, the maximum temperature reached and the temperature gradient encountered during welding depend on the welding process conditions such as tool rotation speed, feed rate, tool geometry (shoulder diameter, pin pattern, pin length, pin diameter), and other factors. Consequently, the mechanical properties of the weld are also affected, including tensile strength and elongation [19–22]. Experimental methods to determine the mechanical properties of welds by parameters are time-consuming and expensive. To solve this problem, many studies have been conducted to predict mechanical properties using machine learning, a type of artificial intelligence [23,24]. Artificial neural network (ANN), a type of machine learning, is an algorithm that mimics the function of the human brain. Researchers who applied ANN to predict the mechanical properties of FSW built a neural network by setting various parameters as input variables and material properties such as elongation, tensile strength, and hardness as output variables. Jayaraman et al. [25] used tool rotation speed, welding speed, and axial force as input variables, and used RSM (Response Surface Model) and ANN to predict and compare the tensile strength of A356 Alloy. Vignesh et al. [26] used tool rotation speed, welding speed, pin diameter, and shoulder diameter as input variables and applied the LM (Language Model) algorithm and ANN trained with the BFGS (Broyden–Fletcher–Goldfarb–Shanno) quasi-Newton algorithm to predict the tensile strength of AA1100 aluminum alloy. Okuyucu et al. [27] used rotation speed and welding speed as input variables, and built a feed forward ANN to predict tensile strength, yield strength, elongation, and hardness, and compared the actual experimental data and simulation results with the predicted results. Maleki [28] used rotation speed, welding speed, downward force, tool hardness, shoulder diameter, and pin diameter as input variables, and tensile strength, yield strength, hardness, and tensile strength of notch as output variables to estimate FSW parameters for Al7075-T6 aluminum alloy using a neural network model with the back propagation algorithm. Previous studies using machine learning to predict the mechanical properties of FSW mainly used rotation speed, welding speed, shoulder diameter, etc., as input data. In this case, there was a limitation that various parameters such as pin diameter, pin height, plunge depth, pin thread, shoulder pattern, tilting angle, etc., were not considered. Accordingly, the temperature gradient and maximum temperature during the FSW process, which are representative of the FSW process parameters, were selected as new input data for the present study. First, in order to obtain the input variables required for ANN training, specimens were fabricated using copper and aluminum to perform FSW experiments under various process conditions. The temperature data for each process condition were then collected using thermocouples. The maximum temperature and temperature gradient were determined by correlating the collected temperature data with the results of the heat transfer analysis of the finite element analysis. The data were subsequently quantified and employed as input variables for the ANN. In order to train the ANN, the tensile strength obtained from the tensile test subsequent to FSW was employed as the output variable. The artificial neural network (ANN) model was constructed using the Python programming language, and the Hyperband tuner was employed to optimize the ANN's hyperparameters. The overall process flow of this study is shown in Figure 1. Finally, to assess the efficacy of the constructed ANN model, the validation data were applied to the trained ANN model and the predicted tensile strength was compared with the actual tensile strength of the validation data.

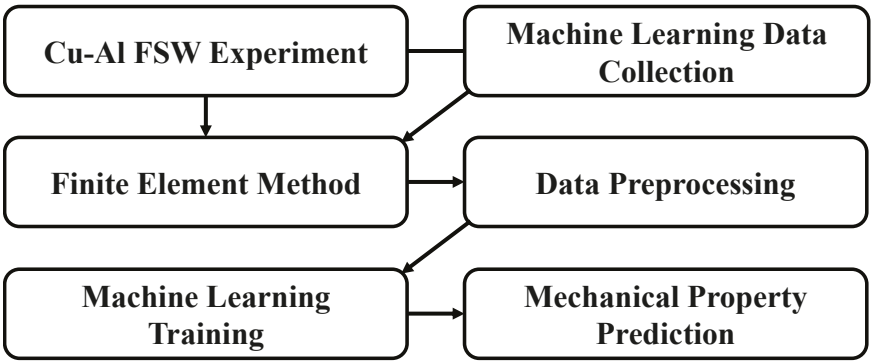

Figure 1. Flow diagram of the process.

2. Dissimilar FSW Experiments

Copper and aluminum specimens were used for the FSW experiments. To simulate the FSW applied to the inverter housing of a real electric vehicle, a specimen with a mixture of butt and lap joints was used. A copper plate was FSWed to an aluminum casting, and 10 holes with a diameter of 1 mm were created to insert thermocouples at intervals of 5 to 10 mm from the weld centerline for temperature data measurement during FSW.

To collect temperature data, K-type thermocouples were inserted into the hole and heat-resistant tape was used to securely fix the thermocouple. The welding tool is made of tungsten carbide material. When welding hard and soft materials in FSW, the position in which the materials are clamped affects the quality of the weld [5,29–31]. In general, good weld quality is obtained when the hard material is clamped on the advancing side and the soft material is clamped on the retreating side [5,29]. In addition, in the Al/Cu joint, the weld quality depends on the offset of the tool pin, and a high-quality weld face is obtained when it is offset to the Al side [32,33]. Al-Roubaiyet et al. conducted a FSW study by fixing pure copper on the advancing side and Al 5086-H116 on the retracting side, and offsetting the tool pin to the Al side. The offset to the Al side was 0 to 0.4 mm, and the maximum weld strength was obtained at 0.2 mm offset [17]. Xue et al. reported that in the FSW of pure copper and Al 1060, a good weld surface without defects could be obtained when the copper plate was fixed on the advancing side and the tool pin was offset by more than 2 mm towards the aluminum side [32]. Bakkiyaraj et al. conducted FSW experiments on the joining of pure aluminum and copper by fixing the copper plate on the advancing side and the aluminum plate on the retracting side [33]. They reported that a sound weld surface was obtained when the tool pin was offset by 2 mm in the direction of the aluminum, and tunnel defects occurred when the tool pin was fixed in the center. Therefore, in this study, the copper plate was fixed on the advancing side and the aluminum plate was fixed on the retracting side. The welding tool was rotated clockwise and offset by 1.1 mm toward the aluminum plate so that the tip edge of the probe was located on the line where the dissimilar materials meet. Figure 2 shows a schematic and real of the overall FSW experiment.

After performing the dissimilar material FSW, the cross-section was observed as shown in Figure 3. The cross-section after FSW shows a good joint at line ① section, which is closest to the beginning of the weld. However, as the FSW progressed, internal tunneling defects were observed at ② section, and unfilled areas on the weld surface appeared at lines ③ and ④ section.

This was due to the different melting points and fluidity of the two materials, as well as the high temperature of the FSW tool, which caused the base material to stick to the tool as shown in Figure 4. The defects observed in Figure 3 are a result of the FSW tool probe no longer fulfilling its function as a stirrer and passing over the weld line.

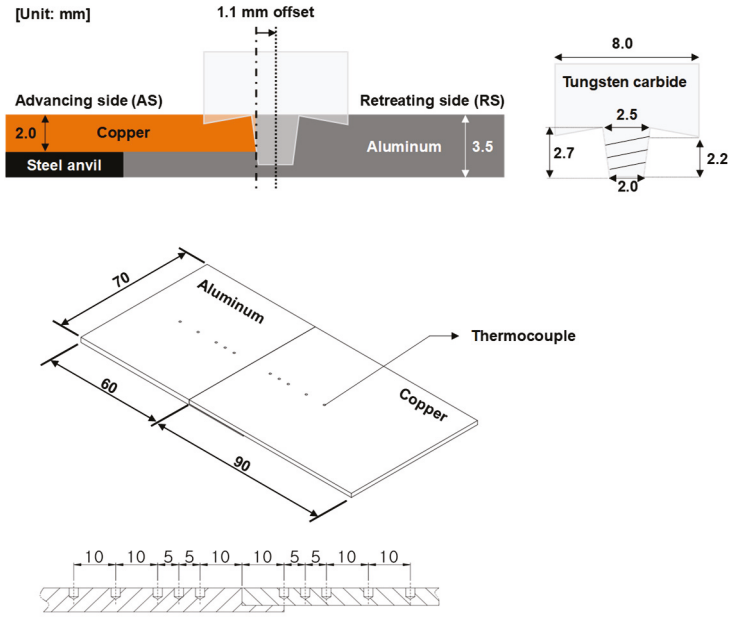

(**a**)

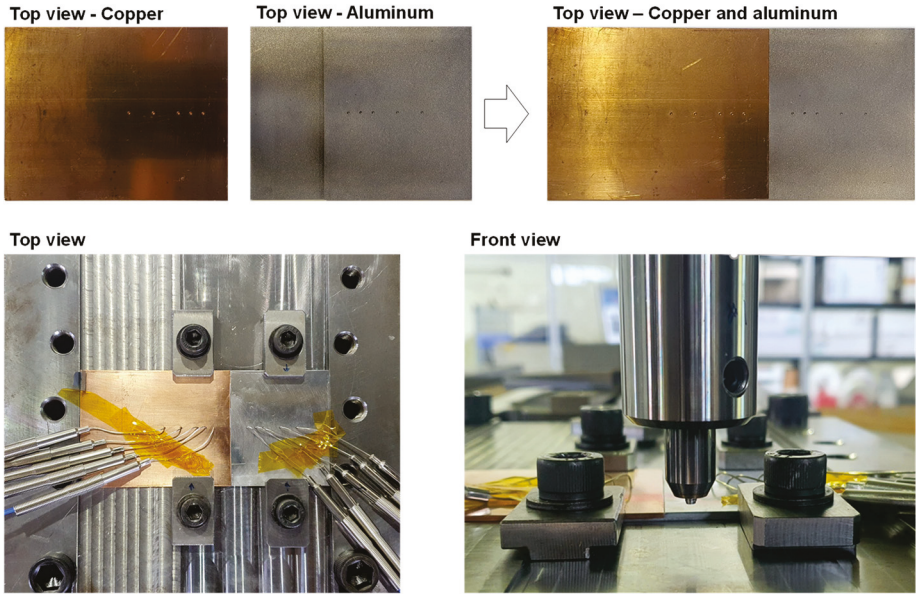

(**b**)

Figure 2. Schematic (**a**) and real (**b**) of the overall FSW experiment.

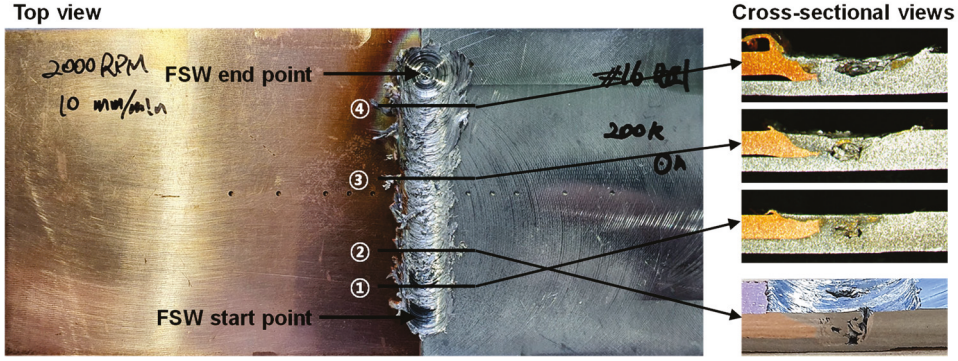

Figure 3. Specimen and cross-section results after FSW.

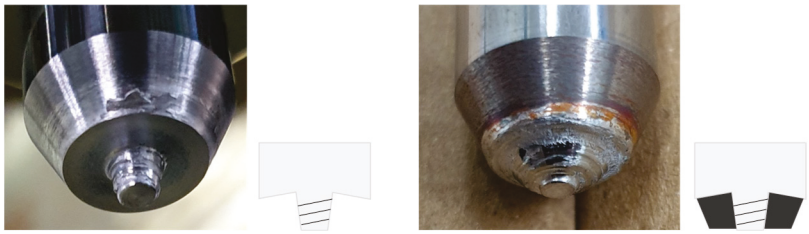

(**a**) (**b**)

Figure 4. Base material sticks to the tool probe: (**a**) before FSW; (**b**) after FSW.

To overcome the issue of the workpiece adhering to the FSW tool probe, a solution was devised whereby liquid nitrogen (LN_2) at a temperature of −196 °C was sprayed onto the side of the FSW tool. This was an effective method of reducing the temperature of the tool. As a result, the quality of the weld joint was visibly improved, as shown in Figure 5. Experiments were conducted under different rotational speeds and feed rates to obtain data for the construction and training of the ANN. The experimental conditions are shown in Table 1 and were performed in the order shown.

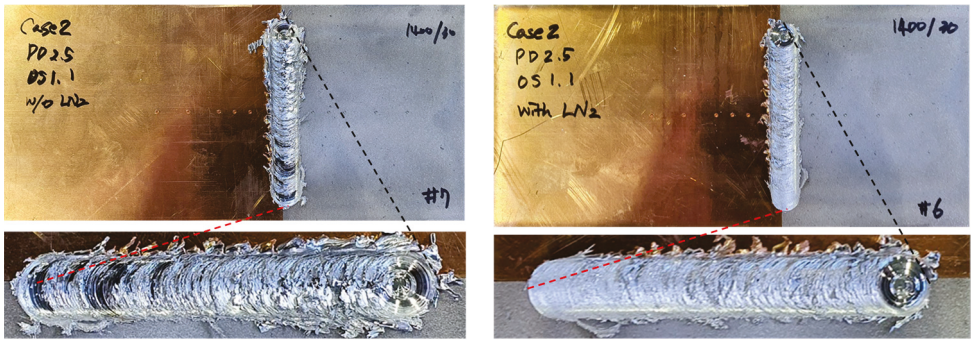

(**a**) (**b**)

Figure 5. Dissimilar FSWed joint results: (**a**) FSW process without LN_2; (**b**) FSW process with LN_2.

Table 1. FSW experiment condition for training set.

Rotation Speed (RPM)	Feed Rate (mm/min)					
	1000	**500**	**300**	**100**	**50**	**25**
1000	#1	#5	#9	#13	#17	#21
1200	#2	#6	#10	#14	#18	#22
1400	#3	#7	#11	#15	#19	#23
1600	#4	#8	#12	#16	#20	#24

The experimental conditions to obtain data for training the ANN were set with rotational speeds ranging from 1000 to 1600 rpm and feed rates from 25 to 1000 mm/min, and the experiments were conducted under a total of 24 cases. As mentioned before, the temperature was measured in 10 channels during the FSW process. Since the FSW tool was offset by 1.1 mm from the aluminum specimen during welding, the highest temperature values were measured in the channel closest to the weld line of the aluminum specimen. Table 2 shows the maximum temperature values measured using thermocouples for each process condition. The results for the 1200 RPM-25 mm/min and 1600 RPM-300 mm/min conditions were excluded because the temperature values were not measured properly during the experiment.

Table 2. Maximum temperature data of FSW experiment condition.

Rotation Speed (RPM)	Feed Rate (mm/min)					
	1000	**500**	**300**	**100**	**50**	**25**
1000	367.77	264.9	219.45	248.04	145.43	147.3
1200	321.66	251.07	262.96	216.37	176.81	X
1400	362.51	245.92	210.7	202.24	188.74	190.52
1600	284.9	261.07	X	168.72	199.82	157.44

In previous studies, the temperature trend according to rotation speed and feed rate showed that when the rotation speed is constant, the temperature tends to increase as the speed of the feed rate decreases [34–36]. However, in this study, the temperature measured here shows that the lower the feed rate of the tool, the lower the temperature. Based on this result, it is believed that the lower temperature gradient as the tool feed rate decreased was caused by the increased time the FSW tool was exposed to LN_2 as the feed rate decreased. In addition, as shown in Figure 6, the actual FSW experiment showed that the weld surface cracked as the feed rate decreased, which is believed to be caused by heat loss due to cracking of the weld during FSW. The experimentally measured temperature data were used as heat source values in the heat transfer analysis of the finite element analysis.

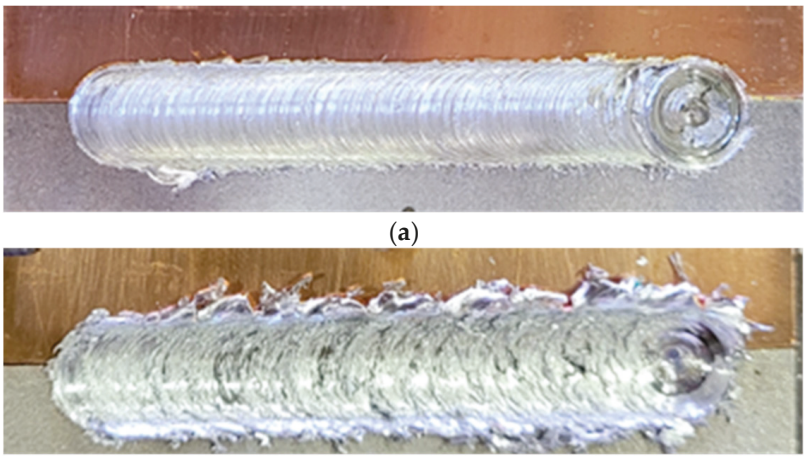

(**a**)

(**b**)

Figure 6. Surface results after FSW experiment with LN_2: (**a**) 1000 RPM-1000 mm/min; (**b**) 1000 RPM-25 mm/min.

The tensile test was conducted using an Instron-type tensile tester (SHIMADZU, AG-IS, 5 Ton, Kyoto, Japan) at a crosshead speed of 1 mm/min at room temperature. The test specimens, which adhered to ASTM-E8 specifications, were machined using electric discharge perpendicular to the welding line, as illustrated in Figure 7. For each FSW condition, three tensile specimens were made and the tensile strength was measured as shown in Figure 7. The average value of the three tensile strengths was used as output data for machine learning in Section 4.

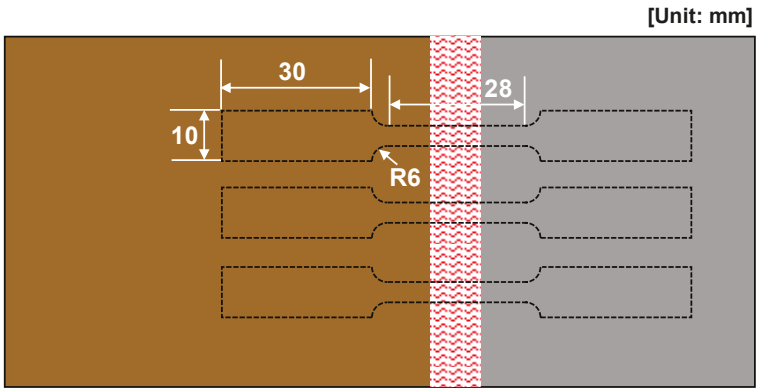

Figure 7. Uniaxial tensile test specimens.

3. Heat Transfer Analysis Using Finite Element Method

As previously stated, the input data for the machine learning model are the temperature gradient and the maximum temperature value, which depend on the specific welding process conditions. To obtain these data, the temperature data measured in the experiment was correlated with the heat transfer analysis results. Then, the temperature gradient perpendicular to the weld line and the maximum temperature during the process were calculated. For this purpose, a heat transfer analysis using the finite element method was performed.

3.1. Finite Element Model and Mesh

To calculate the temperature gradient and maximum temperature of the FSW process, heat transfer analysis was performed using the commercial software ANSYS Workbench 2022 R2. The finite element model used in the heat transfer analysis was the same size as the specimens used in the FSW experiment, as shown in Figure 8. To create an environment similar to the actual experiment, a backing plate was created under the specimen model. In addition, the area of the specimen was divided to reflect the location where temperature measurements were taken and the direction and length of tool travel.

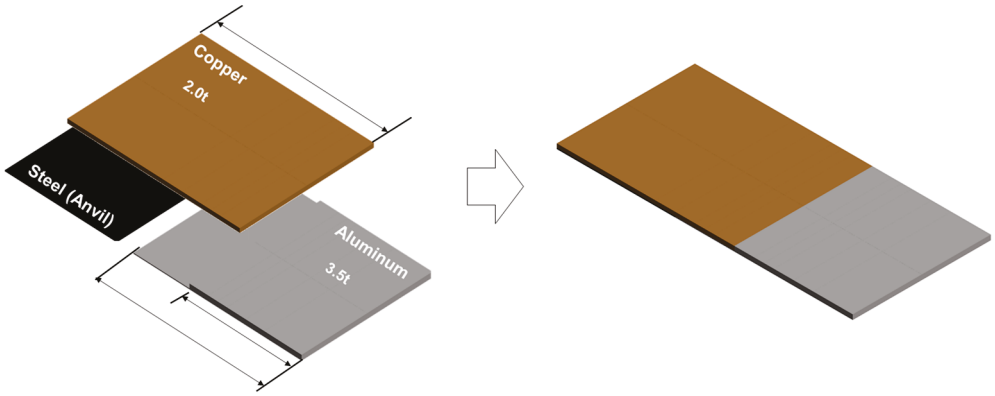

Figure 8. Three-dimensional finite element model for heat transfer analysis.

The elements in the analysis model were tetrahedral elements with 1.0 mm near the FSW tool path and 2.0 mm elsewhere. The number of nodes was 25,051 and the number of elements was 103,663. Figure 9 shows the mesh for heat transfer analysis.

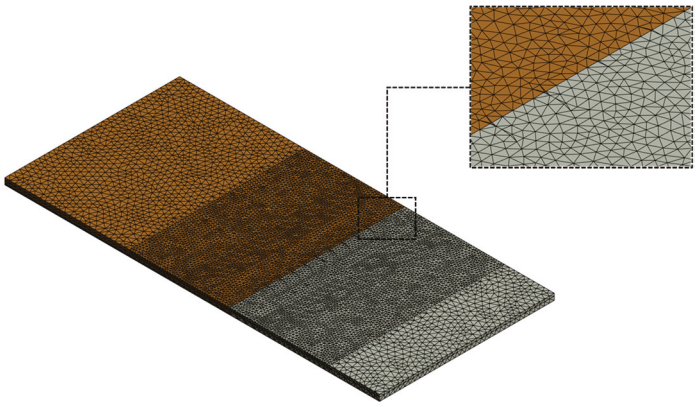

Figure 9. Finite element mesh model for heat transfer analysis.

3.2. Material Properties and Boundary Conditions

The temperature-dependent material properties such as density, specific heat, and thermal conductivity of aluminum and copper used in the dissimilar FSW transient heat transfer analysis are shown in Tables 3 and 4 [37,38].

Table 3. Temperature-dependent material properties of aluminum [37].

Temperature [°C]	Density [kg/m^3]	Specific Heat [J/kg°C]	Thermal Conductivity [W/m°C]
25	2700	900	198.33
100	2690	940	203.54
150	2680	960	205.17
200	2670	990	205.82
260	2650	1010	205.66
320	2640	1040	204.72
370	2630	1060	194.91
420	2620	1080	194.14
570	2580	1170	191.81

Table 4. Temperature-dependent material properties of copper [38].

Temperature [°C]	Density [kg/m^3]	Thermal Conductivity [W/m°C]	Temperature [°C]	Specific Heat [J/kg°C]
26.85	8910	398	24.85	385
126.85		392	599.85	442
526.85		371	799.85	462
726.85		357	999.85	482

The heat source value was calculated by correlation analysis with the temperature results measured in the experiment. The transient heat transfer analysis was used to consider the moving heat source. To consider convective heat transfer, 20 W/m^2°C was applied to the surface exposed to the air, and 200 W/m^2°C was applied to the bottom surface [39]. By correlating the temperature distribution results measured in Section 2 with the heat transfer analysis results using the finite element method, the temperature distribution along the vertical direction of the weld line during FSW was calculated and is presented in Figure 10.

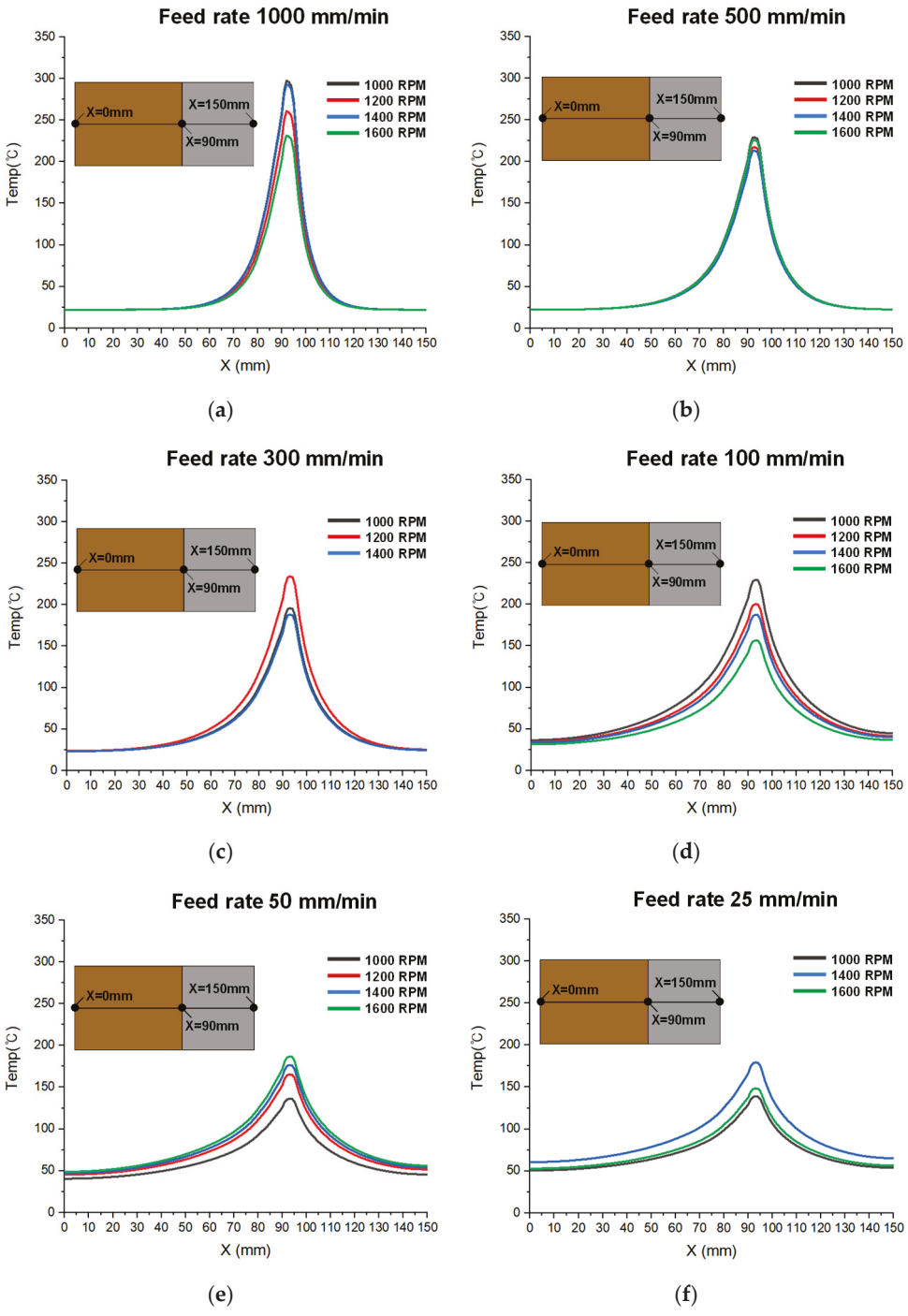

Figure 10. Temperature distribution results along the perpendicular direction of the weld line using heat transfer analysis: (**a**) Feed rate 1000 mm/min; (**b**) Feed rate 500 mm/min; (**c**) Feed rate 300 mm/min; (**d**) Feed rate 100 mm/min; (**e**) Feed rate 50 mm/min; (**f**) Feed rate 25 mm/min.

4. Artificial Neural Network

An artificial neural network is a machine learning algorithm that mimics the principles and structure of neural networks in the human brain or animal brains and is used to solve a variety of problems in many applications. An artificial neural network is a network structure of interconnected nodes that mimic neurons and consists of nodes, an input layer, a hidden layer, and an output layer, as shown in Figure 11.

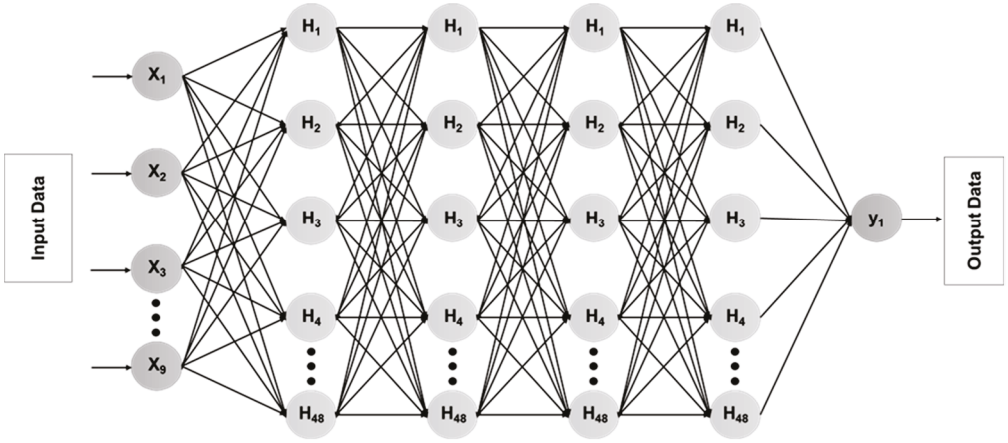

Figure 11. Artificial neural network structure.

The nodes in an ANN play an important role in processing and transmitting information, connecting the layers. When data enter the input layer, they are propagated to the hidden layer with a given weight and activation function, and the data trained in the hidden layer are propagated to the output layer in the same way to produce the output result. The activation function is a function that converts the sum of the input signals into an output signal and determines whether the input signal is output or not, allowing nonlinearity to be represented. Activation functions include Sigmoid, Tanh, and ReLU. The Sigmoid function outputs values between 0 and 1, but when the input is very large or small, the output becomes nearly zero, leading to the vanishing gradient problem. The Tanh function outputs values between -1 and 1 and is slightly better than Sigmoid, but it can still suffer from the vanishing gradient problem. The vanishing gradient problem refers to a phenomenon where the gradient becomes too small, preventing the weights from being updated. In contrast, the ReLU function is effective in addressing this issue. The ReLU function (Rectified Linear Unit function) is expressed as shown in Equation (1):

$$x = \max(0, x) \tag{1}$$

If the value of x is negative, it outputs 0, and if it is positive, it outputs x as it is. It is the most popular activation function because it is simple to compute and fast to learn. Weights control the importance of each input signal to the output signal, and biases determine the conditions under which neurons are activated. Weights and biases are the key parameters of an artificial neural network and are adjusted through the learning process. Gradient descent is an optimization algorithm that adjusts the neural network model to minimize the loss function by adjusting the weights and biases. During the initial training stage, the model calculates the loss error between the predicted and actual values and then derives the gradient for each variable through differentiation. This process is repeated until the gradients reach a minimum value. If the temperature gradient has a significant impact on the predictive model, the weight for this variable will be adjusted more substantially to reduce the loss. Conversely, if the maximum temperature has a smaller impact on the loss, the adjustment to this variable's weight will be smaller.

4.1. Artificial Neural Network for Friction Stir Welding

In this study, the ReLU function was used as the activation function of the neural network model, and the gradient descent method was used to minimize the loss function. TensorFlow (2.7.0) is an open-source software library developed by Google, offering various features that make it easy to use machine learning and deep learning in a Python environment. It is specifically designed to simplify the construction and execution of complex computations, such as neural networks. Therefore, in this study, the neural network was built and trained using TensorFlow in a Python environment. The input variables for train-

ing were the temperature gradient and maximum temperature values derived from FSW experiments and heat transfer analysis. The temperature gradient values were separated into copper plate side temperature gradient values and aluminum plate side temperature gradient values to reduce the error, and then the natural logarithm was taken to reduce the slope of the graph as shown in Figure 12. The slope-reduced temperature gradient values were represented by a third-order polynomial using a trend line. The input variables for the ANN were four third-order polynomial coefficients of the temperature gradient on the copper plate side, four third-order polynomial coefficients on the aluminum plate side, and one maximum temperature. The output data were the tensile strength values obtained from the tensile test, and the final data used in the ANN are shown in Table 5.

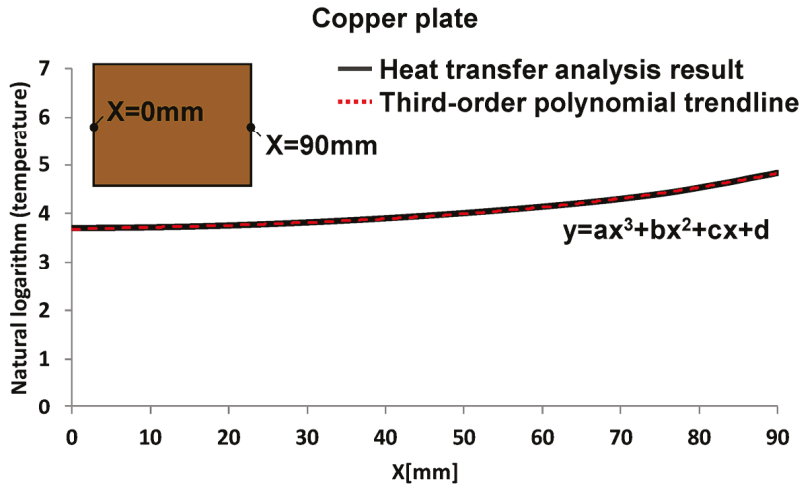

(a)

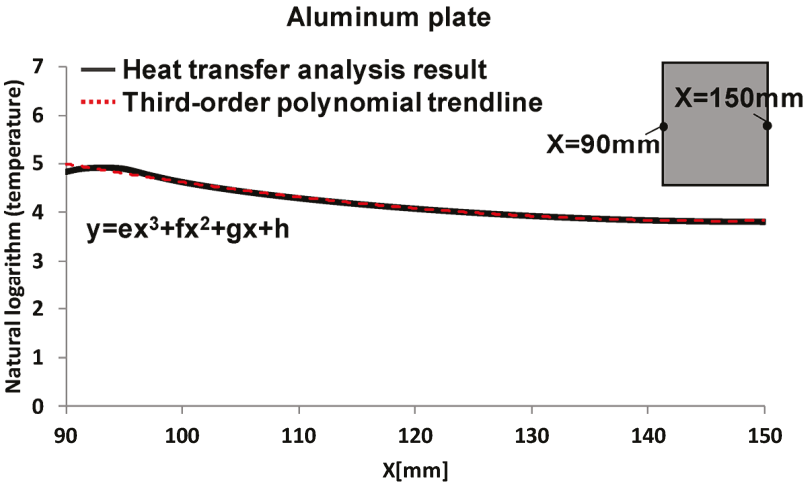

(b)

Figure 12. Temperature data and trend line for input data of artificial neural networks.

Table 5. Artificial neural networks data for dissimilar FSW.

	Input Data									Output Data
No.	**a**	**b**	**c**	**d**	**e**	**f**	**g**	**h**	**Max. Temp.**	**Tensile Strength**
#1	1.0×10^{-5}	-7.0×10^{-4}	0.0136	3.0419	-1.0×10^{-5}	0.0062	−0.9558	51.55	367.77	185.5
#2	1.0×10^{-5}	-7.0×10^{-4}	0.0148	3.0337	-1.0×10^{-5}	0.0067	−1.0026	52.845	321.66	176.1
#3	1.0×10^{-5}	-7.0×10^{-4}	0.0137	3.041	-1.0×10^{-5}	0.0062	−0.9613	51.71	362.51	199

Table 5. *Cont.*

Input Data										Output Data
No.	**a**	**b**	**c**	**d**	**e**	**f**	**g**	**h**	**Max. Temp.**	**Tensile Strength**
#4	1.0×10^{-5}	-7.0×10^{-4}	0.0158	3.0273	-1.0×10^{-5}	0.007	−1.0364	53.674	284.9	233.4
#5	4.0×10^{-6}	-1.0×10^{-4}	0.0019	3.0996	-2.0×10^{-5}	0.0008	−0.2581	22.02	264.9	194.9
#6	4.0×10^{-6}	-2.0×10^{-4}	0.0024	3.0963	6.0×10^{-7}	0.001	−0.2815	22.777	251.07	189.4
#7	4.0×10^{-6}	-2.0×10^{-4}	0.0026	3.0951	-3.0×10^{-8}	0.0011	−0.2903	23.058	245.92	182.1
#8	4.0×10^{-6}	-1.0×10^{-4}	0.002	3.0987	-3.0×10^{-7}	0.0009	−0.2646	22.229	261.07	194.1
#9	2.0×10^{-6}	2.0×10^{-5}	0.0013	3.1378	4.0×10^{-7}	−0.0004	−0.0776	13.425	219.45	143.1
#10	2.0×10^{-6}	9.0×10^{-5}	0.0005	3.1527	3.0×10^{-6}	−0.001	−0.0162	11.427	262.96	226.2
#11	2.0×10^{-6}	1.0×10^{-5}	0.0015	3.1347	5.0×10^{-6}	−0.0003	−0.0911	13.859	210.7	161.6
#13	8.0×10^{-7}	9.0×10^{-5}	0.0047	3.5734	3.0×10^{-6}	−0.0007	0.002	8.8281	248.04	200.6
#14	9.0×10^{-7}	7.0×10^{-5}	0.0045	3.5167	3.0×10^{-6}	−0.0006	−0.0137	9.2287	216.37	224.6
#15	1.0×10^{-6}	7.0×10^{-5}	0.0044	3.4903	3.0×10^{-6}	−0.0005	−0.0218	9.3438	202.24	210.7
#16	1.0×10^{-6}	4.0×10^{-5}	0.0041	3.4247	3.0×10^{-6}	−0.0003	−0.0444	10.012	168.72	241.5
#17	1.0×10^{-6}	-1.0×10^{-5}	0.0039	3.682	2.0×10^{-6}	0.0003	−0.1019	11.468	145.43	254.8
#18	1.0×10^{-6}	-1.0×10^{-6}	0.004	3.7925	1.0×10^{-7}	0.0002	−0.0911	11.362	176.81	210.6
#19	1.0×10^{-6}	3.0×10^{-6}	0.0041	3.8315	5.0×10^{-7}	0.0002	−0.0875	11.322	188.74	234.4
#20	1.0×10^{-6}	6.0×10^{-6}	0.0041	3.8665	6.0×10^{-7}	0.0001	−0.0844	11.286	199.82	246.6
#21	1.0×10^{-6}	-4.0×10^{-5}	0.0036	3.9051	7.0×10^{-7}	0.0005	−0.1178	11.804	147.3	198.8
#23	1.0×10^{-6}	-3.0×10^{-5}	0.0038	4.0842	-5.0×10^{-7}	0.0004	−0.1107	11.909	190.52	218.8
#24	1.0×10^{-6}	-4.0×10^{-5}	0.0037	3.95	-2.0×10^{-7}	0.0005	−0.1162	11.841	157.44	239

In neural network models, hyperparameters such as the number of neurons in each layer, batch size, learning rate, and weight reduction depending on parameters are important for the performance of the model. To optimize the performance of the model through these hyperparameters, we used TensorFlow's Keras Tuner library, which is used to automate hyperparameter tuning and find the optimal model configuration. Keras Tuner has several built-in tuners, of which we used Hyperband Tuner in this paper. Hyperband progressively increases the amount of resources allocated to each hyperparameter configuration during testing. Initially, a small amount of resources is assigned to each hyperparameter to quickly evaluate performance. Then, configurations with lower performance are terminated early to save resources, allowing more resources to be allocated to other configurations. This approach enables Hyperband to focus more resources on configurations with superior performance, ultimately deriving the optimal hyperparameters. The optimization results showed that the best results were obtained using forty-eight nodes and four hidden layers. Therefore, the neural network architecture used in the study consisted of an input layer with five nodes, four hidden layers with forty-eight nodes, and an output layer with one node. The accuracy of an ANN model depends on the quality and quantity of training data. In our experiments, we used 22 input and output datasets, 90% of which were used for training and 10% for testing. Mean squared error (MSE) was used as a loss function to evaluate the difference between the predicted values of the neural network and the values of the actual data. MSE calculates the mean squared error between the predicted and actual values and serves as an intuitive metric for evaluating model performance. Additionally, since MSE is mathematically differentiable, it is often used when applying optimization algorithms such as gradient descent. The MSE is expressed as in Equation (2), where the number of epochs used was 5000.

$$E = \frac{1}{n} \sum_{i-1}^{n} (\hat{y}_i - y_i)^2 \quad (2)$$

Figure 13 shows the evolution of the loss function as the number of epochs increases. We observe that the loss function decreases and then remains constant as the number of epochs increases.

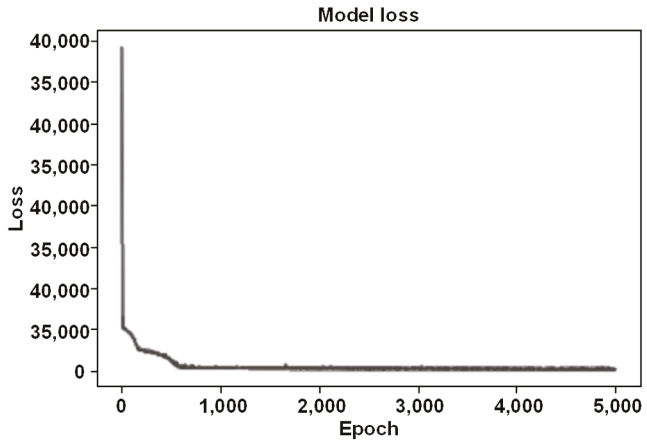

Figure 13. Loss function with respect to number of epochs.

4.2. Artificial Neural Network Verification for Friction Stir Welding

Further experiments were conducted to verify the prediction accuracy of the trained ANN model on new input data. The experimental conditions were the same as the previous experimental method, and the experiments were conducted under the conditions of five FSW cases, with the welding conditions set to 800–1400 rpm and the feed rate set to 20–200 mm/min, as shown in Table 6. The temperature data measured by the experiment were used as the heat source value for the heat transfer analysis of the finite element analysis. The maximum temperatures obtained through heat transfer analysis and the temperature gradient values were taken as natural logarithms to reduce the slope of the graph and represented as third-order polynomials using trend lines. As before, the coefficients of the third-order polynomial and the maximum temperature were set as input data, and the data used for verification are shown in Table 7. Here, the output data are the tensile strength values from the actual experiment. The error was calculated by comparing the tensile strength predicted by inputting the validation data to the trained ANN model with the actual tensile strength of the validation data, and is shown in Table 8. The error between the tensile strength predicted by the verification data and the actual tensile strength is 5.4% on average and 7.4% on the maximum, which shows that it is possible to predict the tensile strength according to the new process conditions.

Table 6. FSW experiment condition for verification set.

Rotation Speed (RPM)	Feed Rate (mm/min)		
	200	**40**	**20**
800		#3	
1000	#4		
1400		#2	#1
1600	#5		

Table 7. Verification dataset for artificial neural networks.

	Input Data								Output Data	
No.	**a**	**b**	**c**	**d**	**e**	**f**	**g**	**h**	**Max. Temp.**	**Tensile Strength**
#1	1.0×10^{-6}	-4.0×10^{-5}	0.0037	4.0346	-5.0×10^{-7}	0.0005	−0.1165	11.89	167.42	234.7
#2	1.0×10^{-6}	-2.0×10^{-5}	0.0038	3.7764	-1.0×10^{-7}	0.0004	−0.1091	11.653	148.04	259.9
#3	1.0×10^{-6}	-1.0×10^{-5}	0.0039	3.8878	1.0×10^{-7}	0.0003	−0.1014	11.636	177.24	233.6
#4	2.0×10^{-6}	6.0×10^{-5}	0.0022	3.1735	4.0×10^{-6}	−0.0008	−0.0089	9.5664	176.57	199.4
#5	2.0×10^{-6}	-3.0×10^{-5}	0.003	3.1377	1.0×10^{-6}	8.0×10^{-5}	−0.0999	12.261	120.99	200.1

Table 8. Verification of artificial neural networks results.

No.	Feed Rate (mm/min)	Rotation Speed (RPM)	Tensile Strength (MPa)	Predict Tensile Strength (MPa)	Error (%)
#1	20	1300	234.7	252.1	7.4
#2	40	800	259.9	246.8	5.0
#3	40	1300	233.	239.9	2.7
#4	200	1000	199.4	211.9	6.3
#5	200	1400	200.1	211.7	5.6

5. Conclusions

In this study, an artificial neural network was used to predict the mechanical properties of FSW of dissimilar materials using a cryogenic process (LN_2). In order to accurately predict the mechanical properties after FSW, new input data different from previous studies were considered. The temperature gradient and data obtained through experiments and finite element analysis were used as input data for machine learning by setting the coefficients of a third-order polynomial using trend lines, and the tensile strength derived from tensile test results was used as output data for the artificial neural network. By applying the validation data obtained from the experiment to the neural network model trained with the new input data, the error between the predicted results and the experimental results was within 10%. It is expected that this neural network structure can be utilized to predict mechanical properties under new welding conditions.

Author Contributions: Conceptualization, M.C. and S.K.; methodology, J.H.K.; software, M.C.; validation, M.C. and S.K.; formal analysis, M.C.; investigation, J.G.; resources, S.K.; data curation, J.G.; writing—original draft preparation, M.C.; writing—review and editing, S.K.; visualization, J.G.; supervision, J.H.K.; project administration, S.K.; funding acquisition, S.K. All authors have read and agreed to the published version of the manuscript.

Funding: This study has been conducted with the support of the Korea Institute of Industrial Technology as "Predicting the quality of friction stir weld joint on curved lines XAI (JE240016)". And The APC was funded by Changwon National University.

Data Availability Statement: The original contributions presented in the study are included in the article, further inquiries can be directed to the corresponding author.

Conflicts of Interest: The authors declare no conflicts of interest.

References

1. Thaiping, C. Process parameters study on FSW joint of dissimilar metals for aluminum-steel. *J. Mater. Sci.* **2009**, *44*, 2573–2580.
2. Morishige, T.; Kawaguchi, A.; Tsujikawa, M.; Higashi, K. Dissimilar Welding of Al and Mg Alloys by FSW. *Mater. Trans.* **2008**, *49*, 1129–1131. [CrossRef]
3. Pietras, A.; Zadroga, L.; Lomozik, M. Characteristics of welds formed by pressure welding incorporating stirring of the weld material (FSW). *Weld. Int.* **2010**, *18*, 5–10. [CrossRef]
4. Bruce, H.; John, F.H. Friction Stir Welding (FSW) of Littoral Combat Ship Deckhouse Structure. *J. Ship Prod. Des.* **2007**, *23*, 161–163.
5. Tanaka, T.; Morishige, T.; Hirata, T. Comprehensive analysis of joint strength for dissimilar friction stir welds of mild steel to aluminum alloy. *Scr. Mater.* **2009**, *61*, 756–759. [CrossRef]
6. Wang, G.; Zhao, Y.; Hao, Y. Friction stir welding of high-strength aerospace aluminum alloy and application in rocket tank manufacturing. *J. Mater. Sci. Technol.* **2018**, *34*, 73–91. [CrossRef]
7. Li, B.; Shen, Y.; Hu, W. The study on defects in aluminum 2219-T6 thick butt friction stir welds with the application of multiple non-destructive testing methods. *Mater. Des.* **2011**, *32*, 2073–2084. [CrossRef]
8. Prakash, K.S.; Sukhomay, P.; Surjya, K.P.; Rahul, J. Influence of plate position, tool offset and tool rotational speed on mechanical properties and microstructures of dissimilar Al/Cu friction stir welding joints. *J. Mater. Process. Technol.* **2016**, *235*, 55–67.
9. Tan, C.W.; Jiang, Z.G.; Chen, Y.B.; Chen, X.Y. Microstructure evolution mechanical properties of dissimilar Al-Cu joints produced by friction stir welding. *Mater. Des.* **2013**, *51*, 466–473. [CrossRef]
10. Mononen, J.; Siren, M.; Hanninen, H. Cost Comparison of FSW and MIG Welded Aluminium Panels. *Weld. World* **2003**, *47*, 32–35. [CrossRef]

11. Kallee, S.W. 5-Industrial applications of Friction stir welding. In *Friction Stir Welding*; Woodhead Publishing Series in Welding and other Joining Technologies; Woodhead Publishing: Sawston, UK, 2010; pp. 118–163.
12. Pedemonte, M.; Gambaro, C.; Lertora, E.; Mandolfino, C. Fatigue assessment of AA 8090 friction stir butt welds after surface finishing treatment. *Aerosp. Sci. Technol.* **2013**, *27*, 188–192. [CrossRef]
13. Isa, M.S.M.; Moghadasi, K.; Ariffin, M.A.; Raja, S.; bin Muhamad, M.R.; Yusof, F.; Jamaludin, M.F.; bin Yusoff, N.; bin Ab Karim, M.S. Recent research progress in friction stir welding of aluminum and copper dissimilar joint: A review. *J. Mater. Res. Technol.* **2021**, *15*, 2735–2780.
14. Vivek, P.; Jeroen, D.B.; Henrik, H.; Mattias, I.; Saeed, A.; Joel, A.; Jorgen, S. High-speed friction stir welding in light weight battery trays for the EV industry. *Sci. Technol. Weld. Join.* **2022**, *27*, 250–255.
15. Omkar, M.; Tarig, A.; Desham, M.; Surjya, K.P.; Prakash, S. Characterization and modelling of Al and Cu busbar during charging and discharging of Li-ion battery for electric vehicles. *Appl. Therm. Eng.* **2023**, *218*, 119239.
16. Beygi, R.; Kazeminezhad, M.; Kokabi, A.H. Butt joining Al-Cu bilayer sheet through friction stir welding. *Trans. Nonferrous Met. Soc. China* **2012**, *22*, 2925–2929. [CrossRef]
17. Al-Roubaiy, A.O.; Nabat, S.M.; Batako, A.D.L. Experimental and theoretical analysis of friction stir welding of Al-Cu joints. *Int. J. Adv. Manuf. Technol.* **2014**, *71*, 1631–1642. [CrossRef]
18. Liu, P.; Shi, Q.; Wang, W.; Wang, X.; Zhang, Z. Microstructure and XRD analysis of FSW joints for copper T2/aluminum 5A06 dissimilar materials. *Mater. Lett.* **2008**, *62*, 4106–4108. [CrossRef]
19. Arun, K.K.; Pankaj, B. The study of material flow behaviour in dissimilar material FSW of AA6061 and Cu-B370 alloys plates. *J. Manuf. Process.* **2018**, *34*, 96–105.
20. Khodaverdizadeh, H.; Mahmoudi, A.; Heidarzadeh, A.; Nazari, E. Effect of friction stir welding(FSW) Parameters on strain hardening nehavior of pure copper joints. *Mater. Des.* **2012**, *35*, 330–334. [CrossRef]
21. Yang, J.; Wang, D.; Xiao, B.L.; Ni, D.R.; Ma, Z.Y. Effects of Rotation Rates on Microstructure, Mechanical Properties, and Fracture Behavior of Friction stir-Welded (FSW) AZ31 Magnesium Alloy. *Metall. Mater. Trans. A* **2013**, *44*, 517–530. [CrossRef]
22. Elmetwally, H.T.; SaadAllah, H.N.; AbdElhady, M.S.; AbdelMagied, R.K. Optimum combination of rotational and wlding speeds for welding of Al/Cu-butt joint by friction stir welding. *Int. J. Adv. Manuf. Technol.* **2020**, *110*, 163–175. [CrossRef]
23. Tauqir, N.; Mohammed, A.; Qasim, Z.; Davut, S. Applications of Machine Learning to Friction Stir Welding Process Optimization. *J. Kejuruter.* **2020**, *32*, 171–186.
24. Abdelhakim, D.; Fouzi, H.; Ying, S. Exploring Deep Learning Methods to Forecast Mechanical Behavior of FSW Aluminum Sheets. *J. Mater. Eng. Perform.* **2023**, *32*, 4047–4063.
25. Jayaraman, M.; Sivasubramanian, R.; Balasubramanian, V.; Lakshminarayanan, A.K. Application of RSM and ANN to predict the tensile strength of Friction Stir Welded A319 cast aluminium alloy. *Int. J. Manuf. Res.* **2009**, *4*, 306–323. [CrossRef]
26. Vignesh, R.V.; Padmanaban, R. Comparison of ANN Training Algorithms for Predicting the Tensile Strength of Friction Stir Welded Aluminium Alloy AA1100. *Int. J. Veh. Struct. Syst.* **2018**, *10*, 98–102. [CrossRef]
27. Okuyucu, H.; Kurt, A.; Arcaklioglu, E. Artificial neural network application to the friction stir welding of aluminum plate. *Mater. Des.* **2007**, *28*, 78–84. [CrossRef]
28. Maleki, E. Artificial neural network application for modeling of friction stir welding effects on mechanical properties of 7075-T6 aluminum alloy. In *IOP Conference Series: Materials Science and Engineering*; IOP Publishing: Bristol, UK, 2015; Volume 103.
29. Watanabe, T.; Takayama, T.; Yanagisawa, A. Joining of aluminum alloy to steel by friction stir welding. *J. Mater. Process. Technol.* **2006**, *178*, 342–349. [CrossRef]
30. DebRoy, T.; Bhadeshia, H.K.D.H. Friction stir welding of dissimilar alloys—A perspective. *Sci. Technol. Weld. Join.* **2010**, *15*, 266–270. [CrossRef]
31. Choi, D.H.; Lee, C.Y.; Ahn, B.W.; Yeng, Y.M.; Park, S.H.C.; Sato, Y.S.; Kokawa, H.; Jung, S.B. Effect of fixed location variation in friction stir welding of steel with different carbon contents. *Sci. Technol. Weld. Join.* **2010**, *15*, 266–336. [CrossRef]
32. Xue, P.; Ni, D.R.; Wang, D.; Xiao, B.L.; Ma, Z.Y. Effect of friction stir welding parameters on the microstructure and mechanical properties of the dissimilar Al-Cu joints. *Mater. Sci. Eng. A* **2011**, *528*, 4683–4689. [CrossRef]
33. Bakkiyaraj, M.; Stephen Bernard, S.; Saikrishnan, G.; Guruyogesh, S.; Guruprasanna, T.G.; Dineshkumar, K. Effect of tool offset condition on mechanical and metallurgical properties of FSW dissimilar Al-Cu joint. *Mater. Today Proc.* **2021**, *43*, 824–827. [CrossRef]
34. Chetkin, E.; Kilickap, E.; Celik, Y.H. Investigation of the Effects of Welding Force, Vibration and Temperature on Mechanical Properties and Microstructure in FSW Welding. *J. Polytech.* **2023**, *26*, 445–455.
35. Sakthivel, T.; Sengar, G.S.; Mukhopadhyay, J. Effect of welding speed on microstructure and mechanical properties of friction-stir-welding aluminum. *Int. J. Adv. Manuf. Technol.* **2009**, *43*, 468–473. [CrossRef]
36. El-Rayes, M.M.; Soliman, M.S.; Abbas, A.T.; Pimenov, D.Y.; Erdakov, I.N.; Abdel-mawla, M.M. Effect of Feed Rate in FSW on the Mechanical and Microstructural Properties of AA5754 Joint. *Adv. Mater. Sci. Eng.* **2019**, *12*, 4156176. [CrossRef]
37. Kang, S.W.; Kim, J.W.; Jang, Y.J.; Lee, K.J. Welding Deformation Analysis, Using an Inherent Strain Method for Friction Stir Welded Electric Vehicle Aluminum Battery Housing, Considering Productivity. *Appl. Sci.* **2019**, *9*, 3848. [CrossRef]

38. Mughal, M.P.; Fawad, H.; Mufti, R. Parametric thermal analysis of a single molten metal droplet as applied to layered manufacturing. *Heat Mass Transf.* **2006**, *42*, 226–237. [CrossRef]
39. Kang, S.W.; Jang, B.S. Comparisons with friction stir welding heat transfer analysis methods and parametric study on unspecified input variables. *J. Mech. Sci. Technol.* **2014**, *28*, 4233–4246. [CrossRef]

Disclaimer/Publisher's Note: The statements, opinions and data contained in all publications are solely those of the individual author(s) and contributor(s) and not of MDPI and/or the editor(s). MDPI and/or the editor(s) disclaim responsibility for any injury to people or property resulting from any ideas, methods, instructions or products referred to in the content.

applied sciences

MDPI

Review

State of Knowledge in the Field of Regenerative Hardfacing Methods in the Context of the Circular Economy

Wiesław Czapiewski, Stanisław Pałubicki, Jarosław Plichta and Krzysztof Nadolny *

Faculty of Mechanical and Energy Engineering, Department of Production Engineering, Koszalin University of Technology, Śniadeckich 2, 75-453 Koszalin, Poland; wieslaw.czapiewski@op.pl (W.C.); stanislaw.palubicki@tu.koszalin.pl (S.P.); jaroslaw.plichta@tu.koszalin.pl (J.P.)
* Correspondence: krzysztof.nadolny@tu.koszalin.pl

Abstract

Regenerative hardfacing of steel substrates is an important technology for restoring the surface layer of components operating under wear conditions, supporting the goals of the circular economy (CE) by extending the service life of components, reducing material and energy consumption throughout their life cycle, and shortening downtime during machine repairs. The article provides a synthetic analysis of the literature on the production of functional layers exclusively on steels and systematizes process → structure → properties (PSP) relationships in the context of technological quality and the prediction of the functional properties of welds. The review covers methods used and developed in steel hardfacing (including arc processes and variants with increased energy concentration), analyzed on the basis of measurable process indicators: energy parameters (arc energy/heat input/volume energy), dilution, bead geometry, heat-affected zone characteristics, and the risk of welding defects. It has been shown that these factors determine the structural effects in the weld and the area at the fusion boundary (including phase composition and morphology, hardness gradient, and susceptibility to cracking), which translates into functional properties (hardness, wear resistance, adhesion, and fatigue life) and durability after regeneration. The main result of the work is the development of a PSP table dedicated to hardfacing on steel substrates, mapping the key "levers" of the process to structural consequences and trends in functional properties. This facilitates the identification of optimization directions (minimization of energy input and dilution while ensuring fusion continuity), which translates into longer durability after regeneration and a lower risk of defects—key, measurable effects of CE. Research gaps have also been identified regarding the comparability of results (standardization of energy metrics) and the need to determine and verify "technology windows" within the WPS/WPQR (welding procedure specification/welding procedure qualification record) for layers deposited on steels.

Keywords: hardfacing; hardfacing-based remanufacturing; circular economy; heat input; arc energy; wire arc additive manufacturing; directed energy deposition

1. Introduction

Hardfacing is one of the key technologies for shaping and restoring the surface layer of machine parts [1–3]. Today, it is one of the main techniques to reduce the life cycle costs of machines and shorten downtime. In industrial practice, it is used in two ways [4]:

- For the regeneration of machine parts—wear in the form of geometric defects within the surface layer is more intense than contact fatigue wear, which is the basis for the

possibility of multiple regeneration by surfacing (shafts, journals, rollers, sockets) [5–9];
- For the manufacture of functional layers with predetermined properties (resistance to wear, corrosion, erosion) [1,10–13].

These solutions fit well into the circular economy (CE) action plan and are supported by the development of high-efficiency arc welding processes and their robotization [7,14,15]. CE is based on maximizing the "useful life" of a product and minimizing primary waste streams. Hardfacing fits in with the CE principles because it allows products to be kept "in circulation for as long as possible" through repair and regeneration, which is one of the pillars of the EU's circular economy strategy and EU policies aimed at designing durable, repairable products and extending their life cycle. This is explicitly emphasized by the European Commission and the European Parliament, which point to "repair, renew, and regenerate" activities as key measures for extending the life of products and reducing waste streams and consumption of primary materials. Regenerative hardfacing allows the surface layer to be selectively restored and/or functionality (e.g., tribological resistance, corrosion resistance) to be added without replacing the entire component. For maintenance organizations, this means shorter restoration times and lower logistical risks, and for designers, it means the need to define "technological windows" that stabilize technological and functional quality with acceptable process variability [16–18].

From a product life cycle assessment perspective, studies show that regeneration/repair—including the restoration of the functional layer by hardfacing methods—can significantly reduce the environmental footprint compared to the manufacture of a new component; significant reductions in energy and material consumption and a decrease in environmental impacts have been demonstrated in comparative analyses of various product groups (e.g., turbochargers, mining machinery, electrical equipment). The literature emphasizes that the selection of process parameters determines the geometry and fusion of the weld, dilution, arc stability, and, consequently, the functional properties of the welds and their adhesion to the substrate. The type and flow rate of the shielding gas are also important [2,19,20]. It is therefore necessary to determine "technological windows", i.e., recommendations for the welding procedure specification (WPS) and welding procedure qualification record (WPQR) for specific material–process combinations.

According to a study by the *American Welding Society* [21], surfacing processes may be grouped as surface cladding, buildup, buttering, and hardfacing. In a study entitled *The Practical Reference Guide for Hardfacing*, these processes are defined as follows:

- Cladding—a surfacing variation that deposits or applies surfacing material, usually to improve corrosion or heat resistance;
- Buildup—a surfacing variation in which surfacing material is deposited to achieve the required dimensions;
- Buttering—a surfacing variation that deposits the surfacing metal on one or more surfaces to provide metallurgically compatible weld metal for the subsequent completion of the weld;
- Hardfacing—a surfacing variation in which surfacing material is deposited to reduce wear.

A strong reason for undertaking research on regenerative hardfacing is the growing demand from the steel, energy, mining, metallurgical, and automotive industries for stable and repeatable hardfacing technologies using gas metal arc welding (GMAW)—a widely used, easily robotized, and highly efficient process. Reviews and case studies show that conscious shaping of thermal history (e.g., by controlling linear energy, interpass temperature, interpass cooling) translates into the quality and predictability of the properties of the deposited layers and the economy of the process [7,22,23].

https://doi.org/10.3390/app16020792

In recent years, there has also been an evolution from classic hardfacing towards wire arc additive manufacturing (WAAM) technology, which belongs to the additive manufacturing processes of directed energy deposition (DED). This applies to the reduction in dilution and control of microstructure, stresses, and surface quality through interpass strategies (e.g., forced cooling between passes/layers, interpass rolling, local shielding) [24–27]. The same concepts are successfully transferred to functional layers made using the GMAW method, which reinforces the need for research on process maps and dependency models: parameters → technological quality → functional properties.

From the operational perspective of industrial companies, correctly validated "technological windows" for GMAW hardfacing enable the following:

- Reduction in downtime and scrapping costs due to effective regeneration of high-value parts.
- Increased reliability due to predictable properties of the hardfaced layer (hardness, adhesion, wear resistance).
- Increased productivity through conscious management of bead geometry, blending, and dilution without excessive increase in heat input.
- The possibility of robotization and standardization (WPS/WPQR), based on methodical experiment planning and statistical analysis.

The application and scientific context of regenerative hardfacing on steel substrates, defined above, indicates its importance both for surface engineering (recreation and modification of the surface layer, increased wear resistance) and for the circular economy (extending the service life of components, reducing material and energy consumption during the life cycle). At the same time, it has been shown that despite the wide range of research and the maturity of the technology's implementation, the literature in the field of hardfacing on steels is characterized by limited comparability of results, due to inconsistent definitions of thermal parameters, differences in reporting technological quality, and fragmentary descriptions of the relationships between process parameters, microstructure, and performance properties. This allowed us to establish a problem framework and clearly formulate the objective of the work, which is to organize the process → structure → properties (PSP) relationship for hardfaced layers on steels and prepare methodological foundations for developing a PSP table as the main result of the article.

2. The Amount of Heat Introduced and Its Significance for the Hardfacing Process

Hardfacing is a welding process that involves the controlled deposition of additional metal onto a substrate to restore the dimensions of worn surfaces or give them specific operational functions (tribological, corrosion, and erosion resistance). Hardfacing is used in repairs to restore the serviceability of machine or equipment parts (regenerative hardfacing), or it can be used in the production process of new products (technological hardfacing). A feature that distinguishes the surfacing process from other methods of applying metallic coatings is the melting of the substrate material onto which the surfacing material is applied. Meeting this condition is essential to achieve the appropriate depth of fusion, which guarantees the adhesion of the surfaced layer to the substrate material [1–4].

The properties of the fusion zone, which is a transition layer between the weld and the base material, have a significant impact on the welding result. The technological quality of welds is determined by the bead geometry (b—width, h—height, p—fusion), dilution D (proportion of base metal in the weld), the presence of dissimilarities, and the corresponding functional properties (microstructure, (micro)hardness, adhesion, and wear resistance). It is crucial to manage the amount of heat input and the thermal history (pre- and interlayer temperature and cooling rate).

https://doi.org/10.3390/app16020792

Heat input in welding/hardfacing is a commonly used technological parameter for selecting welding conditions and a quantity that serves as the basis for other indicators that are calculated and used in welding [2,10].

The heat input of welding/hardfacing is a measure of the amount of heat per unit length of the weld [28]. It cannot be measured directly—it is calculated based on the measured values of the arc voltage, welding current, and welding speed, using the following Equation (1):

$$Q = k \times \frac{U \cdot I}{v} \times 10^{-3}, \text{kJ/mm}, \quad (1)$$

where Q—heat input of welding/hardfacing, kJ/mm; k—thermal efficiency coefficient of the welding/hardfacing process; U—arc voltage, V; I—welding/hardfacing current, A; and v—welding/hardfacing speed, mm/s.

The heat transfer coefficient k values for different welding/hardfacing methods are shown in Table 1.

Table 1. Thermal efficiency coefficient k for different welding/hardfacing methods [29].

Method No.	Welding/Hardfacing Method	Coefficient k
121	Submerged arc welding with wire electrode (SAW)	1.0
111	Manual-arc welding with a covered electrode (MMA)	0.8
131	Metal inert gas (MIG) welding	0.8
135	Metal active gas (MAG) welding	0.8
114	Flux-cored wire metal-arc welding without gas shield	0.8
136	Flux-cored wire metal-arc welding with active gas shield	0.8
137	Flux-cored wire metal-arc welding with inert gas shield	0.8
138	Metal-cored wire metal-arc welding with active gas shield	0.8
139	Metal-cored wire metal-arc welding with inert gas shield	0.8
141	Tungsten inert gas (TIG) welding	0.6
15	Plasma arc welding (PAW)	0.6

During welding/hardfacing, significant fluctuations in electrical parameters (in particular, current intensity and arc voltage) are observed, resulting from the high dynamics of the process and the complexity of the phenomena occurring in the glowing welding arc. In practice, however, this variability is usually ignored when calculating linear energy, as the calculations are based on time-averaged values, rather than instantaneous parameter values [30].

When using a pulsed current in the welding/hardfacing process, the average current value is calculated using Equation (2) [31]:

$$I_{av} = \frac{I_i \times t_i + I_b \times t_b}{t_i + t_b}, \text{ A}, \quad (2)$$

where I_{av}—average current intensity, A; I_i—pulse current intensity, A; I_b—base current intensity, A; t_i—pulse current duration, ms; and t_b—base current duration, ms.

Heat input in welding and hardfacing processes is a quantitative technological parameter describing the amount of heat introduced into the joint/layer, thus allowing the process conditions to be numerically related to changes in the properties of the base material and weld metal. At the same time, this parameter is commonly used as a comparative measure for comparing the effects of different welding processes, including pulsed variants, on the weldability of the base material [32].

To enable a proper comparison of heat input in various welding/hardfacing processes on different types/generations of welding equipment (including devices that allow current waveforms to be shaped), the concept of heat input of the welding arc—*arc energy*—was

https://doi.org/10.3390/app16020792

introduced in the Technical Report [33]. The dimensionless thermal efficiency coefficient was omitted from the calculation of arc energy. Depending on the measuring systems with which welding power sources are equipped, various relationships giving equivalent results, (3), (4) and (5), are used to calculate the arc energy:

- Formula (3) determines arc energy based on the welding/hardfacing current and arc voltage values:

$$E = \frac{U \cdot I}{v} \times 10^{-3}\,\text{, kJ/mm}, \tag{3}$$

where E—welding/hardfacing arc energy, kJ/mm; U—arc voltage, V; I—welding/hardfacing current, A; and v—welding/hardfacing speed, mm/s;

- Equation (4) defines arc energy using instantaneous energy:

$$E = \frac{IE}{L} \times 10^{-3}\,\text{, kJ/mm}, \tag{4}$$

where IE—instantaneous energy, J and L—weld length, mm;

- Equation (5) defines arc energy using instantaneous power:

$$E = \frac{IP}{v} \times 10^{-3}\,\text{, kJ/mm}, \tag{5}$$

where IP—instantaneous power, J/s and v—welding/hardfacing speed, mm/s.

Any of the above relationships can be used to calculate the heat input of the welding arc during standard welding/hardfacing. During welding/hardfacing using controlled pulse waveforms, it is permissible to use relationship (4) or (5). Work [33] recommends the use of a data acquisition system that is capable of capturing arc voltage and welding current samples at a sampling frequency of at least 10 times the pulse frequency.

Instantaneous energy (*IE*), used in Equation (4), is a measure of the total energy of the welding/hardfacing process, which is determined based on the recording of instantaneous current and voltage waveforms. In practice, it is calculated by the discrete sum of the products $I(t)$, $U(t)$, and the time step Δt between successive measurement samples, recorded at high frequency, which allows us to capture rapid changes that are characteristic of the dynamic course of the process. Consequently, *IE* represents the energy supplied to the system for a given weld/joint throughout its execution time.

Instantaneous power (*IP*), used in Equation (5), is a measure of the welding/hardfacing process power, determined based on arc current and voltage values sampled at short intervals. In practice, it is calculated as the time-averaged value of the product $U_i \times I_i$ recorded at high frequency, which allows for rapid fluctuations in process parameters to be considered. Thus, *IP* corresponds to the average instantaneous power (i.e., average power in the sense of time) over the time interval under consideration.

The amendment to EN ISO 15614-1 in 2017 [34] allows the heat input of welding/hardfacing to be replaced in welding/hardfacing technology testing, with the heat input of the welding arc calculated according to the ISO/TR 18491:2015 standard [33]. When calculating heat input, the k factor according to [29] must be considered. The WPQR welding/hardfacing technology qualification protocol must specify the method used to calculate heat input or arc energy.

Wojsyk et al. [35,36] demonstrated that a clear measure of heat input in welding/hardfacing can be the volume of material melted by it, or its representation, assuming a constant process speed—the cross-sectional area of the weld within the joined or hardfaced elements. The method of assessing the amount of heat input by measuring the cross-sectional areas of welds allows for a comparison of the actual thermal efficiency of

https://doi.org/10.3390/app16020792

different welding/hardfacing methods and is particularly useful in the assessment of pulse and hybrid methods.

Winczek and Wojsyk [37] proposed an alternative method for determining the amount of heat supplied to a welded/hardfaced joint. Instead of the classic measure referring to a unit of stitch length, they introduced an indicator normalized to a unit of volume, i.e., the volumetric energy of welding/hardfacing. The presented concept and the general expression of the relationship (6) are based on the basic technological parameters of the process (in particular, the energy generated by the electric arc and the welding/surfacing speed) and on the cross-sectional area of the weld/surfacing joint, which is the reference value for the volume of the deposited material:

$$E_{vw} = \frac{U \times I}{v \times A}, \text{ J/mm}^3, \tag{6}$$

where E_{vw}—welding/hardfacing volumetric energy, J/mm^3; U—arc voltage, V; I—welding/hardfacing current, A; A—cross-sectional area of the weld, mm^2; and v—welding/hardfacing speed, mm/s.

Lowering the Q value (while maintaining process stability) helps to reduce D and the width of the heat-affected zone, which is of paramount importance in material systems with increased sensitivity to the heat cycle. In practice, the relationships between the current, voltage, deposition speed, wire diameter and feed rate, and electrode stick-out determine both arc stability (and metal transfer mechanism) and bead shape and penetration depth.

In the weld, especially in its upper part, there is almost pure molten material of the filler metal used, while in the lower part, the molten material partially mixes with the base material, forming a fusion zone, as in welding. The transition line is a conventional boundary between the base material and the weld metal of the filler material [2,3,38].

The change in the concentration of the base material components in the weld metal decreases from 100% at the transition line to 0% outside the fusion zone, as the distance from the transition line and the base material (BM) increases. The course of this change depends on the dimensions (thickness) of the deposited layer. The BM area adjacent to the weld, heated by the heat supplied during the deposition process, is the heat-affected zone, where structures depend on the temperature reached by individual weld layers and the cooling rate. These structures change as they move away from the transition line, until they reach the intact BM structure [38].

The degree of mixing is determined by the coefficient of substrate metal content in the weld. The substrate metal content in the weld U_p (7) is the ratio of the cross-sectional area of the melted substrate metal F_w to the sum of the cross-sectional areas of the weld F_n and the substrate metal F_w [3,39]:

$$U_p = \frac{F_w}{F_n + F_w} \times 100\% \tag{7}$$

where U_p—substrate metal content in weld, %; F_w—cross-sectional area of melted substrate metal, mm^2; and F_n—surface area of the weld overlap, mm^2.

Other indicators characterizing the hardfacing process are as follows [39]:

- *Hardfacing efficiency*—This is the mass of the hardfacing layer per unit of time, most often given in kg/h;
- *Surface hardfacing efficiency*—This is the surface area hardfaced per unit of time, m^2/h;
- *Width of the deposited layer* in a single pass, mm;
- *Thickness of the deposited layer* in a single pass, mm.

The quantitative description of energy input into the process as the primary factor determining the thermal cycle was supplemented with characteristics of dilution, stitch geometry, heat-affected zone features, and an analysis of the risk of hardfacing nonconfor-

https://doi.org/10.3390/app16020792

mities in steels. It has been shown that heat input alone, even when corrected by a thermal efficiency factor, does not automatically ensure the comparability of results between different methods and technological conditions if it is not supplemented by unambiguous definitions, consistent units, and a minimum set of data enabling the reconstruction of the heat balance and deposition efficiency. Therefore, the method of defining and applying energy input measures in further analysis has been standardized, and the conditions for their correct application and reporting have been indicated. Thus, this Section creates a methodological bridge between the description of the process and the analysis of structural and property effects, enabling the consistent use of energy metrics as an organizing axis in the PSP table.

3. Hardfacing Methods in Regeneration

Hardfacing can be performed using various methods. The most-used methods of regenerative hardfacing are described below.

3.1. Gas Hardfacing (Acetylene–Oxygen)

Gas hardfacing (acetylene–oxygen) involves applying a layer of additional metal—melted by the heat of a gas flame—to the surface of an object, onto a previously melted substrate, to form a durable weld.

The quality of the resulting layer is determined by flame stability and composition, burner operation, additional material supply kinetics, and heat balance control in the hardfacing zone [1,3,10,39–42]. Solid wires, powder wires, cast rods (sticks), or metal powders are used as binders.

A variation in this process is gas–powder hardfacing, in which the filler material is in the form of a metallic or cermet powder with a grain size of approx. 0.03–0.10 mm. The powder is sucked from the container by a stream of combustible gas, transported through the burner nozzle, melted in the flame, and then transferred by the kinetic energy of the gases, settling on the molten substrate to form a weld [1,3,10,39–42].

In industrial practice, acetylene (flame temperature $\approx 3100\ ^{\circ}C$) is almost exclusively used as a combustible gas, due to its clearly defined flame zones and the possibility of adjusting the nature of the flame from oxidizing to carburizing. Other gases are used sporadically, due to their lower flame temperature, higher oxygen consumption, and limited adjustment possibilities compared to acetylene [1,3].

The process requires precise flame control, as its composition and enthalpy determine the chemical interaction with the metal pool and the overmelt zone. The quality of the welds is largely a function of the accuracy of the torch guidance and the thermal stability of the substrate. Depending on the material combination (substrate/binder), the following are often necessary: preheating, temperature control during surfacing, slow cooling after the process, and, in some cases, heat treatment to stabilize the microstructure and reduce residual stresses [1,39].

Gas hardfacing allows coatings of virtually any chemical composition to be applied to steel, cast steel, cast iron, and other metal and alloy substrates. It can be performed manually (most often), as well as semi-automatically or automatically, which facilitates the treatment of geometrically complex surfaces—both small and large and flat and rotary, including in hard-to-reach places [1,3,42].

The process enables the production of welds with a smooth, even surface, with minimal melting of the substrate and a low proportion of substrate material in the coating (typically 2–10%). In a single pass layer, thicknesses of 0.02–3.5 mm are achieved, which often allows the required chemical composition and target performance properties to be achieved after the first layer [1,3,10,39,41,42].

https://doi.org/10.3390/app16020792

The main advantages include low equipment costs, the possibility of hardfacing elements with complex shapes and very small surfaces, and conducting the process in various welding positions. The limitations include the need for very careful surface preparation, the frequent requirement for preheating and heat treatment after hardfacing, an increased risk of deformation and welding stresses, and possible adverse structural changes in the substrate material. The relatively low deposition rate (approx. 0.5–5 kg/h), depending on the technique and equipment used, should also be considered [1–3,10,39–42].

Gas hardfacing is a technology with high application flexibility and low implementation barriers. It ensures high-quality welds with a properly selected thermal regime and torch parameters but requires technological discipline due to its sensitivity to surface preparation conditions and limited efficiency compared to methods with higher energy density [1,3].

3.2. Manual Arc Hardfacing with Coated Electrode (Shielded Metal Arc Welding)

Manual arc hardfacing with a coated electrode, also known as shielded metal arc welding (SMAW), involves melting the end of a coated electrode and the molten layer of the substrate with the heat of an electric arc, creating a metallic coating with specified performance characteristics. Due to the manual nature of the process, heat input is difficult to determine unambiguously and varies significantly, depending on the operator's technique (hardfacing speed, arc length, downtime), which limits the repeatability of the thermal parameters and makes it difficult to strictly control the heat-affected zone [1–3].

Compared to methods with higher energy density, the SMAW process usually causes greater dilution of the weld metal with the base metal and a wider heat-affected zone. This results in a modification of the composition and microstructure of the hardfaced layer (including a reduction in the effective content of alloying elements in Fe-Cr-C welds, reduction/dispersion of hard phases, and grain growth in the heat-affected zone) as well as a different cooling curve, which promotes the formation of heterogeneous phase structures. As a consequence, internal stresses and deformations increase (greater thermal shrinkage), which can lead to a deterioration of selected operational properties: a decrease in hardness and wear resistance (due to dilution and change in phase proportions), a reduction in impact strength (due to grain growth and microstructural gradient), and (in some alloy systems) a deterioration in corrosion resistance (e.g., due to local Cr depletion). For these reasons, SMAW is sometimes used as a reference or complementary option in local repairs and smaller-scale applications, while for tasks requiring low dilution, a narrow heat-affected zone, and high repeatability, it is more advantageous to use processes with a higher energy density [1,3].

Hardfacing electrodes are most often made as medium- or thick-coated (rutile, basic) with a solid core (Ø 2.5–6 mm) or powder core (Ø 4–11 mm). The use of a powder core expands the possibilities for shaping the chemical composition of welds and, due to the higher electrical resistance of the core, allows for more than 100% increase in efficiency compared to solid core electrodes, reducing melting time [1–3]. The process can be carried out with an alternating current (AC) or direct current (DC) with positive or negative polarity, depending on the application requirements and the type of electrode [1–3].

The high temperature of the arc (up to approx. 6000 °C) promotes significant melting of the substrate. The proportion of substrate material in the weld typically reaches 10–40%, depending on the technique and process settings. As a result, only the third layer achieves a chemical composition that is consistent with that of the electrode. A layer thickness of 1–5 mm is achieved in a single pass, and the deposition rate is in the range of 1–5 kg/h [1,3,42]. The method allows for the application of materials with a composition

https://doi.org/10.3390/app16020792

identical to that of the substrate or with different properties (e.g., hardened, wear-resistant layers) [42].

The quality of welds manufactured using the SMAW method is highly dependent on the welder's manual skills, the stability of the arc length, the speed of movement, and consistency in cleaning the slag from the weld pool [3,39]. The advantages include low equipment costs, the ability to work in various positions (including forced ones) and the possibility of hardfacing elements with complex geometry and limited access. The disadvantages include, above all, low productivity resulting from the manual nature of the process (breaks for electrode replacement, slag cleaning), increased risk of non-conformities (pores, blisters), and greater susceptibility to deformation and adverse structural changes associated with a wide heat-affected zone [2,39,41].

SMAW remains a valuable hardfacing method for repair and field tasks, but when high repeatability, heat input control, and dilution size are required, mechanized processes with greater thermal control are more advantageous. When selecting a technology, a compromise must be made between mobility and cost on the one hand, and the quality and metallurgical requirements of the material system on the other.

3.3. Arc Hardfacing with a Non-Consumable Electrode in an Inert Gas Shield (Gas Tungsten Arc Welding/Tungsten Inert Gas)

Arc hardfacing with a non-consumable electrode in an inert gas shield, using the gas tungsten arc welding (GTAW) or tungsten inert gas (TIG) method, involves depositing filler material in the arc zone between a non-consumable tungsten electrode and the hardfacing substrate in an inert gas shield. The filler material (wire, solid or powder rod, tape, or possibly powder melted directly onto the substrate) melts in the metal pool and forms a weld on the previously melted surface [1,3,10,39]. The non-consumable electrode is made of tungsten. To increase durability and glow stability, oxide additives (ThO_2, La_2O_3, CeO_2, ZrO_2, Y_2O_3) are used to improve the ignition and current-carrying capacity. The filler material is usually supplied from the outside (wire/rod), and in variants with tape or powder, wider beads with precisely controlled geometry are formed [1,3,10]. Argon and helium are standard gases. Helium increases the enthalpy of the arc and the depth of penetration, while argon promotes stability and easy ignition. To increase the temperature of the arc, hydrogen or nitrogen additives (approx. 5–10% in the mixture) are sometimes used. However, the addition of hydrogen is not acceptable when welding aluminum, copper, and their alloys, and it is not recommended for steels that are susceptible to hydrogen cracking (the need to assess the risk of hydrogen-induced cracking—HIC, and dewatering conditions) [2,3,10].

The process is usually carried out using DC with negative polarity on the electrode, which ensures high arc stability, precise heat input control, and low dilution. In the case of aluminum and magnesium (or their alloys), positive polarity on the electrode or AC is used, which is beneficial due to the cleaning effect of the oxide layer [3,10]. Heat input can be kept low without losing weld pool stability, which limits the proportion of base metal in the weld and the width of the heat-affected zone [19,26].

For manual hardfacing, typical productivity is 0.5–2 kg/h and the proportion of substrate material in the weld is around 5–15%. The use of the hot wire technique (resistive heating of the wire from a separate source) allows the productivity to be increased to 5–8 kg/h, while reducing the melting of the substrate (lower dilution). A layer with a thickness of 1.5–5.0 mm is usually deposited in a single pass [2,3,10,39].

GTAW hardfacing is generally performed in a downward position or at an angle of less than 30°. The process can be manual, semi-automatic, or automatic, including robotic systems. The method is used on steels, cast irons, cast steels, and copper and aluminum

https://doi.org/10.3390/app16020792

alloys. High-alloy steels, nickel, cobalt, copper, and aluminum alloys, as well as selected cermets, are applied as welds [1–3,10,39].

GTAW is characterized by the highest precision and purity of the weld pool. The absence of spatter and slag reduces post-hardfacing processing. In practice, a narrow heat-affected zone and low dilution are achieved, which helps us to reach the target chemical composition that is already in the initial layers. The texture and microstructure are strongly dependent on the heat history, which can be consciously programmed (e.g., by controlling the cooling rate, the maximum allowable temperature of the previous weld layer before starting the next layer, and cooling breaks), due to the precise regulation of the arc current/voltage and hardfacing speed [19,26].

In functional applications and hybrids (e.g., GTAW + hot wire, GTAW + interlayer rolling), as well as WAAM/DED, it is possible to additionally modulate the heat input and control the height and width of the deposit, which improves the homogeneity of the layer and reduces properties' gradients. Such solutions increase repeatability and reduce residual stresses, as well as structural anisotropy [19,26].

The key advantages of GTAW hardfacing include metallurgical inertness (Ar/He shielding), narrow heat-affected zone, low mixing ratio, and high surface quality. Limitations include lower productivity (especially in manual mode), the requirement for stable gas-shielding conditions (usually in enclosed spaces), and greater sensitivity to gas flow disturbances. When selecting gas application, limitations must be considered, e.g., no H_2 addition for Al and Cu and caution with steels that are susceptible to hydrogen embrittlement [2,39].

When hardfacing on steel substrates with difficult weldability, the priority is to maintain a low heat input while maintaining arc stability, controlling preheat and interpass temperatures, and avoiding factors that increase the risk of cold cracks (including hydrogen in the shielding gas). GTAW, due to its precise thermal control and low dilution, promotes the safe formation of functional layers on such substrates, albeit at the expense of a lower deposition rate compared to GMAW/SAW [3,10,19,26].

3.4. Arc Hardfacing with a Consumable Electrode in a Gas Shield (Gas Metal Arc Welding)

Arc hardfacing with a consumable electrode in a gas shield using the gas metal arc welding (GMAW) method involves depositing additional metal from a consumable electrode in the arc area between the end of the wire and the hardfaced substrate in a gas shield. The heat of the arc melts the end of the electrode and overheats the substrate. After mixing and crystallization, a weld with the specified properties is formed [19,43–46]. Depending on the type of shielding gas used, the GMAW hardfacing process is classified into two basic technological variants (MIG and MAG) [2,3]:

- MIG (metal inert gas)—Hardfacing in a chemically inert gas shield, i.e., argon (Ar), helium (He), or mixtures thereof.
- MAG (metal active gas)—Hardfacing in a shield of chemically active gases, such as CO_2, H_2, O_2, N_2, and NO, used alone or as additives to Ar or He.

The effectiveness and quality of the GMAW hardfacing process are determined by the following parameters: hardfacing current, arc voltage, hardfacing speed, free wire length, wire diameter, grade and shielding gas composition, and flow rate, while heat input is used to measure the heat load. The appropriate selection of these parameters allows for control of penetration, dilution, weld geometry, arc stability, and spatter level [2,3,19,45].

The form of liquid metal transfer from the end of the wire to the weld pool depends on the current and voltage parameters, wire diameter, shielding atmosphere, and length of the electrode's free outlet. The transfer of liquid metal in the arc during GMAW hardfacing

can take place in various ways. Each mode affects arc stability, spatter, penetration depth and hardfacing process efficiency differently [10,45,46]:

- *Short-circuit metal transfer mechanism*—Low heat input, low penetration and dilution; beneficial for thin layers and constrained positions;
- *Globular metal transfer mechanism*—Larger droplets, moderate stability, increased splatter;
- *Spray metal transfer mechanism*—High stability and efficiency, high fusion;
- *Pulsed-spray mechanism*—Controlled droplet detachment in an electrical pulse; compromise: stable spraying with reduced heat input;
- *Rotational metal transfer mechanism*—Droplet separation due to the rotational momentum of the liquid column; used in special configurations.

In the GMAW hardfacing process, solid wires (metal) with a diameter of approx. 0.5–2.4 mm and flux-cored wires with a diameter of approx. 1.2–4.8 mm are used. Hardfacing is performed semi-automatically or automatically (including robotically), typically with a direct current, with positive polarity on the wire (DC+) [3,10].

With DC+ and spray transfer, a yield of 4–10 kg/h is achieved, but the proportion of substrate metal in the weld is high (20–40%) due to high penetration. For short-circuit arcs and thin wires of 0.5–1.2 mm, dilution can be limited to less than 5%, and stresses and deformations can be significantly reduced. Typical productivity is 2–3.5 kg/h [1,3,42]. The thickness of the layers in a single pass is usually in the range of 0.5–6 mm [1] and in some applications, it is up to 10 mm [3].

GMAW hardfacing can be performed with numerous process modifications and strategies to limit the amount of heat input:

- Pulsed GMAW—Precise heat input and droplet control; less base metal melting, easier work in forced positions [3,42];
- Electro-vibration (vibrostic) GMAW—Wire vibration along the axis (50–100 Hz, amplitude~wire diameter), limits substrate heating; useful for thin coatings of 0.5–3 mm on rotating parts; currently used sporadically [1,39,42];
- Hot wire—an additional, resistance-heated wire introduced into the arc zone; the efficiency increases up to 20–30 kg/h [1–3,39];
- Varieties with reduced heat, e.g., cold metal transfer (CMT)—an advanced welding/hardfacing method, a development of the MIG/MAG process, which uses the forward and backward movement of the welding wire to precisely control the metal transfer process)—combine stable spraying with a low heat input, which helps to reduce dilution and improve geometry [47–49];
- WAAM/DED—Conscious control of the heat history (interpass rolling) reduces dilution (the proportion of base metal in the weld), improves layer homogeneity and operational properties [24–27].

The GMAW method enables hardfacing of elements of almost any shape and size: carbon and alloy steels, cast steel, alloy cast iron and nickel, titanium, copper, and aluminum alloys. Low- and high-alloy steels (Cr, Cr-Ni), nickel, cobalt, copper and aluminum alloys are used as welds [1,3,42].

The advantages include high efficiency, easy robotization, operation in all positions, no slag, and a wide range of parameter adjustment (*I*-*U*-*v*, free wire outlet length, shielding gas). Limitations include susceptibility to pores/gas bubbles and spatter at suboptimal settings and the need to protect the work area from drafts due to the stability of the gas shield [39].

GMAW (MIG/MAG) is the process of choice for hardfacing, due to its combination of high productivity and high controllability. Low dilution and limited heat input requirements are met by selecting the transfer mode (short circuit/pulse), thin wires, conscious

heat input control, and interpass strategies. When maximum productivity is a priority, spray transfer is preferred, accompanied by measures to limit the effects of increased penetration (e.g., interpass rolling).

3.5. Submerged Arc Hardfacing Under Flux (Submerged Arc Welding)

Submerged arc welding (SAW) involves creating an electric arc between a consumable electrode and a hardfaced substrate, with the arc zone and molten metal pool completely covered by a layer of flux. The heat of the arc melts the end of the electrode and the surface layer of the substrate. After crystallization, a weld layer with specific geometry and properties is formed. Thermal and metallurgical phenomena occur in an environment shielded from atmospheric air, which promotes high metallurgical purity of the weld metal [1,3,10,42].

The process is carried out, mechanized or automatically, mostly in a downward position (exceptionally in a wall-mounted position, with safeguards against flux spillage). The electrode is fed continuously at a constant speed and can be in the form of solid or powder wire, as well as tape (solid or powder). The use of tape increases the width of the seam and improves the uniformity of the face while maintaining high deposition efficiency [1,3,10,42].

The selection of the type and granulation of the flux is an important tool for controlling the quality and geometry of welds. The flux performs the following functions [1,3,10,42]:

- *Shielding*—This completely isolates the arc and weld pool from the atmosphere.
- *Metallurgical*—This refines liquid metal, affecting oxygen/nitrogen content and modifying the chemical composition of welds (e.g., by transferring Si, Mn).
- *Technological*—This stabilizes the arc, shapes the face, and reduces the rate of heat dissipation, which affects bead formation and temperature distribution.

SAW is characterized by very high efficiency and uniformity of beads, which makes the method ideal for large surfaces and thick layers (rollers, skids, shafts). Due to the possibility of using high current intensities, efficiencies of up to >40 kg/h can be achieved. However, the high thermal load usually results in increased heat input, and with it, greater penetration depth, a higher proportion of base metal in the weld (often 30–40%), and a wider heat-affected zone. In practice, this means that to ensure the target chemical composition of the weld, it may be necessary to deposit at least two or three layers [1,3,10,42].

Significant heat input values can cause deformation of components with insufficient cross-sectional rigidity. For this reason, SAW is mainly used for the regeneration of large components (according to [42]—thicknesses > 30 mm or diameters of rotating components >100 mm; according to [1,3]—also plates with a thickness of 10–30 mm and rotating parts with a diameter of 50–60 mm). In each case, thermal history management is required: preheating, control of the maximum interlayer temperature, and cooling rate [1,3,10,42].

To improve efficiency and/or reduce melting, the following are used, among others:

- Oscillation (pendulum motion) of the head, transversely to the direction of hardfacing, allows us to reduce the depth of penetration, reduce flux consumption, and at the same time increase productivity;
- SAW with filler (additional powder/chips fed into the weld pool) increases the deposition rate;
- Additional wire (cold or hot-wire) increases productivity without a proportional increase in arc energy;
- Multi-electrode systems (tandem, twin, multi-wire) increase efficiency and bead width with profile and fusion control.

These treatments allow a compromise to be achieved between efficiency and thermal impact to meet the requirements of specific hardfaced layers [1,3,10,42].

https://doi.org/10.3390/app16020792

The typical layer thickness after one pass is 2–8 mm. The literature also states that it is possible to obtain layers > 100 mm (in multi-track/multi-layer configurations, with tape and high-performance systems) [1,3,42].

SAW is used for applying layers of low-carbon and low-alloy steels, high-alloy and special steels, nickel, cobalt and chromium alloys, high-chromium cast irons, and selected copper and aluminum alloys. The method is suitable for the regeneration and production of functional layers on large machine and equipment components [1,3,39].

Advantages and limitations of the method [39,41]:

- Advantages: Very high efficiency and homogeneity of beads, high metallurgical purity of welds, safe working conditions (invisible arc), and extensive possibilities for mechanization/automation;
- Limitations: The need to work in a downward position (or wall-mounted position with flux protection), increased substrate metal content in the weld and a wide heat-affected zone, lack of direct observation of the weld pool during the process, and higher costs of specialized equipment and accessories.

SAW is the method of choice for hardfacing large surfaces and thick layers when efficiency and repeatability are priorities. In material systems that are sensitive to the thermal cycle, it is necessary to precisely control the heat input and thermal history, as well as to consciously select process strategies to limit melting, dilution, and adverse metallurgical effects [1,3,42].

3.6. Plasma Hardfacing

Plasma hardfacing involves melting filler material in a very high temperature plasma arc (around 15,000–20,000 K) and then depositing it on a slightly molten substrate to produce a weld layer with specified properties [3,10]. In industrial practice, a plasma transferred arc (PTA) is the most common method, in which granulated metallic or cermet powder with a grain size of 60–300 μm is introduced into the arc zone. The grains melt in the plasma stream and are kinetically deposited on the molten substrate. After solidification, they form a weld with minimal dilution—typically <5%. The powder melting efficiency is usually 90–95%, depending on the composition and fraction of the powder. As the current intensity increases, so does the deposition efficiency, but also the melting of the substrate (and the proportion of native material in the weld), which requires conscious management of heat input (*I*-*U*-*v*) and torch spacing. The plasma-forming gases are argon, helium, or mixtures thereof. The outer shield is usually argon or mixtures of Ar/H_2 or He/H_2 (the addition of H_2 increases the enthalpy of the arc and the fluidity of the weld pool). In the powder configuration, there is also a carrier gas for the powder. Alternatively, wire feeding (PTA with wire) is used when higher deposition rates or dust reduction are desired [1,3,10,42].

Balancing the plasma, shielding and carrier gas flows is critical for arc column stability, penetration depth, and temperature distribution in the heat-affected zone. The process can be performed manually, semi-automatically, or automatically. Due to the mobility of the weld pool and powder feed, powder PTA is performed in practice in a downward position. Wire variants allow for a wider range of positions, including forced ones, with appropriate parameter restrictions [3,10].

Typical outputs range from 0.5 to 15 kg/h (up to 22 kg/h for high-power burners) and the layer thickness after a single pass range from 0.25 to 7 mm [1,3,10,42]. Due to low heat input and a concentrated plasma column, a narrow heat-affected zone, low penetration depth, and low substrate material content are achieved, which facilitates the formation of the weld composition in the first layer. A smooth, even surface (typically $Sa < 0.5$ mm) often allows for a reduction in machining allowances [39,41]. At the same time, the relatively

https://doi.org/10.3390/app16020792

low heat input allows for the hardfacing of small elements (thickness of 3–5 mm, diameter of 20–50 mm) with limited deformation [1].

PTA allows for welding of a wide range of alloys: based on Co, Ni, Fe, Cr, Mo, Zr, Cu, and Sn, with the addition of refractory metals, ceramic phases, and cermet composite layers. Steel elements (carbon, alloy, stainless), cast steel, selected cast irons, copper, and aluminum alloys are hardfaced, both on flat and rotating surfaces [1,3,10,42].

The key advantages of the PTA hardfacing process include high metallurgical purity of welds, very low dilution, narrow heat-affected zone, and a wide range of thicknesses that are achievable in a single pass and smooth surface finish, which together translate into low thermal interference and high repeatability. The limitations are the high costs of PTA sources and equipment, expensive powder materials, the requirement for precise surface preparation, and a stable power supply. In addition, powder PTA is usually performed in a downward position. For some applications, the efficiency is lower than in GMAW/SAW, which requires balancing quality and economic criteria [39,41].

The high energy density plasma arc and powder/tape feed enable the formation of narrow, repeatable beads with low dilution and a narrow heat-affected zone (parameters that are difficult to achieve in processes with a higher heat input). Compared to GMAW/SAW, the plasma transferred arc offers better controllability of heat input at the expense of lower productivity. As a result, it is the process of choice for layers with high quality requirements (wear/erosion resistance, composition stability) and on substrates that are sensitive to thermal cycling [1,3,42].

3.7. Laser Beam Hardfacing (Laser Cladding/Laser Metal Deposition)

Laser beam hardfacing, also known as laser cladding (LC) or laser metal deposition (LMD), involves the localized melting of a thin layer of substrate and filler material (powder fed coaxially/laterally or wire), using laser beam energy to produce a controlled weld layer with specified functional properties.

Compared to arc processes, LC/LMD is characterized by a high power density, a narrow heat-affected zone, low dilution, and high cooling rates, which promotes the formation of a fine-grained microstructure and precise bead geometry [50].

The key controllable parameters and conditions for LC/LMD hardfacing are beam power, travel speed, spot diameter, filler material, feed method, flow rate, focusing distance, and gas shield parameters. These settings determine the heat balance of the weld pool, bead height/width, penetration depth, and dilution. Process stability is ensured by coaxial powder feeding and atmosphere control (Ar/He, local chambers), supplemented by vision/pyrometric sensors for monitoring and feedback controllers [50]. Coaxial powder feeding refers to a head arrangement in which the powder stream is axially coaxial with the laser beam axis. The particles, carried by the carrier gas, are focused into a "powder cone," in which the powder focus converges near the beam focus on the substrate surface. As a result, the powder penetrates directly into the metal weld pool, regardless of the direction of the head movement, forming a weld layer with controlled geometry and low dilution.

LC/LMD is being intensively developed in three interrelated areas [51,52]:

- *Material and metallurgical*—A wide range of welds, including Ni/Co/Fe-based alloys (including stellites and Inconel), stainless and tool steels, and metal matrix composite (MMC), i.e., composite weld metals (Ni/Co/Fe matrix) containing dispersed particles of tungsten carbide (WC) or WC cermet with cobalt binder (WC-Co), which are designed for use in conditions of severe abrasion/erosion. The appropriate selection of the hardfacing process and parameters is aimed at minimizing particle dilution and degradation (dissolution/decarburization), ensuring high tribological resistance with stable adhesion to the substrate;

https://doi.org/10.3390/app16020792

- *Process and quality*—Process maps and "technological windows" limiting the following typical non-conformities: porosity (powder quality/atmosphere, deposition speed), cracks (residual stresses, hot brittleness), spatter/powder loss (jet aerodynamics), and excessive melting (power/focus selection). This indicates the effectiveness of the following strategies: substrate heating, interpass temperature control, remelting, trajectory and overlap shaping, and modification involving the feeding of two powders;
- *Modeling and control*—Hybrid models predicting geometry and temperature fields, i.e., analytical models using the finite element method (FEM) or computational fluid dynamics (CFD), machine learning correlations (data-driven) for parameter selection, and surveillance systems (coaxial camera, color pyrometry) coupled with quality control algorithms during the hardfacing process.

Due to low dilution, a narrow heat-affected zone and the ability to precisely manage the energy supplied, LC/LMD is a technology that is particularly suited to forming functional layers on difficult-to-weld steels. With the right choice of parameters and thermal strategy, the method allows the target composition and geometry to be achieved in the initial layers, limiting the risk of adverse metallurgical phenomena in the heat-affected zone and at the weld–substrate interface [50–52].

3.8. Other Methods of Regenerative Hardfacing

Complementing classic arc methods and processes with increased energy density, e.g., PTA (plasma transferred arc) and LC (laser cladding), are technologies in which the energy flow or deposition mechanism leads to a significantly different heat balance and degree of fusion and dilution, and thus to different characteristics of the process → structure → properties (PSP) relationship. This group includes, among others, hardfacing/deposition using an electron beam in vacuum conditions, as well as spraying processes, including cold spray (solid deposition) and detonation gun spraying (DGS).

Hardfacing/electron beam cladding/electron beam surfacing is a process in which a small area of the substrate surface and additional material (usually wire, less often powder) are locally melted, and the resulting pool of liquid metal solidifies as a hardfaced layer. The process is usually carried out in a vacuum, which limits the influence of the atmosphere, reduces the risk of oxidation and contamination, and promotes stable bead/layer formation [53,54]. Compared to arc methods, the electron beam allows for very high energy concentration and precise control of heat input and weld geometry, which is advantageous for local hardfacing, precision repairs, and when heat-affected zones need to be limited. Vacuum conditions and high energy density promote the production of layers with increased metallurgical quality, but the process requires specialized infrastructure (vacuum chamber) and is limited by the size of the components [54]. From the PSP perspective, the key factors are dilution at the fusion boundary, the nature of the heat-affected zone, and the microstructure of the hardfaced zone. Due to the local, intense energy input and rapid solidification, it is possible to obtain fine-grained microstructures, but the triad that is typical of remelting processes still occurs—weld metal–fusion line–heat-affected zone—with consequences for gradient hardness, susceptibility to cracking, and internal stresses. The literature also describes variants of electron beam hardfacing with powder (multi-pass), indicating the possibility of forming tool layers on steel substrates [55]. EB-cladding can serve both as hardfacing (wear layers) and cladding (protective layers), depending on the choice of filler material and working environment. In the context of steel components, an important advantage is the possibility of precise "dosing" of energy and material in critical areas without excessive heating of the entire part [53,54].

Cold spray (CS) is a deposition technique in which powder particles are accelerated to very high speeds in a gas stream (de Laval nozzle), and their adhesion to the substrate

https://doi.org/10.3390/app16020792

results from intense plastic deformation during impact, at temperatures remaining below the melting point of the particles. For this reason, CS is classified as a solid deposition process with minimal thermal impact on the substrate [56,57]. Unlike remelting processes, CS does not involve a classic heat-affected zone and dilution in the metallurgical sense, and thermal deformation is severely limited. This means that metrics such as heat input have less organizing power here than in arc/laser processes; in practice, the role of "process leverage" is taken over by the kinetic parameters of the jet (gas type and pressure, gas temperature, nozzle design, spray distance, powder granulation, and morphology), which determine the critical adhesion velocity [58,59]. The microstructure of CS coatings is usually characterized by a low degree of oxidation (compared to classic thermal spraying) and strong deformation strengthening in the particle–particle and particle–substrate contact zones. The literature emphasizes that solid deposition allows the characteristics of the powder material to be largely preserved, while at the same time obtaining favorable mechanical and tribological properties that are suitable for regenerative applications. The limitation is the difficulty of depositing brittle and very hard materials without the use of a matrix/binding metal (composite systems are often used) [56,57,59].

Detonation gun spraying (DGS) is a thermal spraying process in which cyclic detonations of a gas mixture in the barrel of a detonation device simultaneously heat and accelerate powder particles, directing them onto a prepared substrate surface at very high speed. As a result, it is possible to produce coatings with high density, high hardness, and good adhesion, which makes this technology useful in anti-wear applications [60,61]. The structure of DGS coatings is typical for spray coatings: lamellar (splat-based), with the possible presence of oxides, inter-lamellar discontinuities, and porosity, with detonation parameters and surface preparation significantly determining the degree of compaction and adhesion. In practice, DGS is sometimes used to produce carbide-based layers and metal–ceramic systems, where the key factors are resistance to abrasion/erosion, stability at elevated temperatures, and resistance to contact forms of degradation [60–62]. The limitations of the DSG process include safety and noise emission requirements, difficulties with complex geometry (line-of-sight), the need for rigorous substrate preparation (roughness, degreasing), and the sensitivity of properties to detonation cycle stability [60,61].

3.9. Critical Assessment of the State of Research: Trends, Contradictions, and Limitations of Data Comparability

An analysis of the literature on hardfacing functional layers on steel substrates indicates a clear trend away from qualitative descriptions toward attempts to quantitatively link the "leverage" of the process with structural effects and functional properties, in terms of process → structure → properties (PSP). At the same time, the comparability of results between publications remains limited due to the heterogeneous definitions of the metrics used, variability in process boundary conditions, and fragmentary reporting of input data. As a result, some of the interpretative discrepancies in the literature may not be due to actual contradictions in the phenomena, but to methodological incompatibility and a lack of consistent reporting standards.

In recent years, three dominant directions in the development of hardfacing process research have been observed:

1. Energetization of process description—The growing role of energy input metrics (linear, mass, and volumetric) as organizing parameters and as a basis for transferring results between processes and workstations.
2. Reduction in dilution and control of the transition zone—Increased interest in strategies that minimize the proportion of substrate metal in the weld and stabilize the geometry/fusion, as these parameters strongly determine the microstructure and

https://doi.org/10.3390/app16020792

functional properties (especially the wear resistance and corrosion behavior of protective layers).

3. Shift in emphasis from set parameters to achieved (actual) parameters—increased importance of resultant and intermediate parameters (e.g., dilution, weld cross-sectional area, process stability indicators, non-conformities), which are a more direct link to PSP than current and voltage settings alone.

The literature reports conflicting conclusions regarding the influence of thermal metrics on microstructure and properties. For example, for seemingly similar heat input conditions, there are reports of both an increase in hardness/wear resistance (associated with a finer microstructure and limited dilution) and a decrease (associated with a higher proportion of Fe from the substrate, longer exposure to high temperatures, or an increase in the proportion of defects). Such contradictions most often result from the overlap of at least four effects:

- Incompatibility of energy metrics (different definitions and methods of calculating heat input, different assumptions regarding source efficiency);
- Lack of control or reporting of boundary conditions (preheating, inter-stitch temperature, thickness/thermal mass of the element, heat dissipation);
- Variability of dilution and stitch geometry (the same settings do not necessarily lead to the same melt volume and the same D);
- Differences in filler material and its form (solid wire vs. powder vs. powder) and in the multi-layer strategy.

Consequently, without parallel reporting of the parameters achieved (D, geometry, heat-affected zone, defects), interpreting PSP trends based solely on U, I, v, and heat input carries a significant risk.

The literature review identified recurring reporting deficiencies that directly limit the possibility of replication and inter-center comparisons:

1. Energy metrics and their definitions—Part of the publication does not specify whether heat input was calculated from average values or instantaneous values, does not provide sampling frequencies, and does not indicate assumptions regarding thermal efficiency/effectiveness. This results in a situation where the same numerical value in kJ/mm may refer to different metric designs, and thus to incomparable energy states of the process.
2. The boundary conditions of the heat cycle are often overlooked—Interpass temperature, preheating, cooling method, workpiece clamping, and the geometric characteristics of the sample (thickness/thermal mass). The lack of this data makes it impossible to interpret differences in the heat-affected zone, microstructure, and deformations as a function of the energy supplied alone.
3. Dilution and geometry of the weld—In many studies, dilution is reported without indicating the method of determination (field definition, number of cross-sections, location of cross-sections, uncertainty), and weld geometry parameters are presented selectively. Meanwhile, D and geometry are critical PSP links for steel substrates.
4. Microstructure description and quantitative structural measures—The description is often limited to qualitative images without quantitative characteristics (phase fraction, particle/column size distribution, hardness as a function of distance from the fusion line). This makes it difficult to establish reliable structure–property relationships.
5. Methodology for testing functional properties—Comparisons of wear or corrosion resistance are often hampered by inconsistent test conditions (tribological configuration, load, friction path, counter sample, environment and corrosion exposure time,

https://doi.org/10.3390/app16020792

surface preparation). There is also a lack of consistent reporting of result dispersion (number of repetitions, deviations, confidence intervals).

To increase data comparability and enable critical synthesis in terms of PSP, it is recommended that publications on hardfacing on steels report the following, at least:

- Energy metrics with definitions (calculation variant, instantaneous vs. average values, efficiency/assumptions);
- Full thermal context (preheat, interpass, component geometry, cooling/clamping conditions);
- Parameters achieved: dilution (with determination method), weld geometry, heat-affected zone, defects;
- Quantitative characteristics of the structure (hardness profile, phase/carbide content, transition zone features);
- Explicit functional test conditions and statistical evaluation of the repeatability of results.

4. From Process Parameters to Technological Quality and Performance Characteristics

Based on the literature review, the technological quality of the hardfaced layer is characterized by a set of features that are directly resulting from the hardfacing process and assessable without operational testing. These include bead geometry (weld width, weld height, penetration depth), dilution (proportion of substrate metal in the weld), weld continuity and lack of continuity of the metallurgical bond between the weld and the substrate or between adjacent beads/layers (LOF, lack of fusion), porosity, wave face, heat-affected zone, and residual stresses. In turn, the service quality of the hardfaced layer refers to the fulfillment of functional service criteria: hardness/micro-hardness, wear resistance (abrasive/erosive/adhesive), corrosion resistance (passivation, pitting corrosion), fatigue resistance, and adhesion of the layer to the substrate. In the literature, both concepts are combined in the Process → Structure → Properties (PSP) relationship. The distribution of heat fields and metal flow (resulting from *I-U-v*, the type of shielding gas, the length of the free electrode outlet, and the mode of metal transfer in the welding arc) shapes the geometry, inconsistencies, and microstructure that determine the performance characteristics [63–65].

4.1. Benefits and Drawbacks of the Feedstock Materials for Hardfacing

Feedstock is one of the key factors determining the outcome of the hardfacing process, as it influences the following:

- The chemical composition and dilution of the hardfacing.
- Solidification mechanisms and phase transformations (and thus, microstructure).
- Susceptibility to defects (e.g., cracks, porosity, lack of fusion).
- Functional properties (wear resistance, corrosion resistance, fatigue life, adhesion).

From the perspective of the process → structure → properties (PSP) relationship, the selection of the type of filler material is equivalent to the selection of the energy source and thermal parameters, as it determines both *what* is deposited (chemistry and phases) and *how* it is deposited (process stability, productivity, deposition efficiency).

In practical terms, hardfacing consumables should be evaluated simultaneously in four dimensions:

- Design possibilities (including composites and phase additives).
- Process compatibility (arc/jet stability, susceptibility to automation).
- Metallurgical and technological quality (dilution, heat-affected zone, defects, repeatability).
- Economics and logistics (cost, availability, storage, health and safety requirements).

https://doi.org/10.3390/app16020792

Tables 2–6 summarize the main groups of feedstock materials used in regeneration/hardfacing: solid electrodes/wires/rods (Table 2), flux-cored/metal-cored and powder-cored electrodes (Table 3), powders (Table 4), strip electrodes and strips (Table 5), and pre-applied powders and mixtures (Table 6) [1–3,10,19,26,39–42,45].

Table 2. Characteristics of solid electrodes/wires/rods used as the feedstock materials for hardfacing.

General description	Solid electrodes/wires/rods—this group of feedstock includes shielded metal arc welding (SMAW) electrodes, solid wires for GMAW/MAG and GTAW (mechanically fed), and rods for gas metal arc welding/GTAW. Their chemical composition is achieved by using a homogeneous metal without a "powder charge" in the core.
Advantages	High repeatability of composition and homogeneity of feedstock (lower risk of segregation of components in feedstock).
	Good feeding stability (in the case of solid wires) and high reliability in robotic applications.
	Relatively simple logistics (storage, batch traceability, lower risk of material degradation due to improper storage than with some powders).
	Predictable behavior in the process (especially in GMAW/MAG), which promotes WPS/WPQR qualification and standardization.
Limitations	Limited freedom in designing microstructure compared to powder feedstock (it is more difficult to introduce high proportions of hard phases/composites, e.g., carbides, in a technologically stable manner).
	Less flexibility in shaping the chemical composition (especially for high-alloy brazing), where non-standard alloy systems or mixtures of components with different melting points are required.
	Depending on the method, greater sensitivity to dilution and thermal effects (wider heat-affected zone, greater deformation) is possible, which results not so much from the form of the additional material as from the typical energy of arc processes used with solid wires.

Table 3. Characteristics of flux-cored/metal-cored and powder-cored electrodes used as the feedstock materials for hardfacing.

General description	Flux-cored/metal-cored and powder-cored electrodes consist of a metal casing (mantle) filled with powder(s). In practice, there are powder wires for GMAW/MAG/FCAW (including rutile/basic/metallic varieties) and coated electrodes of a "powder" nature (similar functions: process stabilization, composition shaping, and weld pool protection).
Advantages	High flexibility in composition design: possibility of introducing alloying additives, hard phases, and metallurgical modifiers in a manner that is difficult to achieve with solid wire.
	High deposition efficiency (often higher than for solid wires under comparable conditions), which facilitates the regeneration of large-size components.
	Possibility of improving performance properties (e.g., abrasion/erosion resistance) by controlling the proportion and morphology of reinforcing particles and the composition of the matrix.
	Additional process stabilization mechanisms (depending on the type of core and coating), which can reduce spatter and facilitate face shaping.
Limitations	Risk of variability related to filling quality (homogeneity, moisture, powder bulk density, mantle tightness), which may affect the repeatability of composition and susceptibility to porosity.
	Sensitivity to operating parameters (electrode extension, feed stability, synergistic settings)—critical for repeatability of dilution and weld geometry.
	In slag-containing variants, the need to remove slag and the risk of interpass inconsistencies in multi-layer welds if the procedure is not strictly followed.

Table 4. Characteristics of powders used as the feedstock materials for hardfacing.

General description	Powders are used in processes such as PTA, LC/LMD, electron beam deposition, thermal spraying, and cold spray. The powder can be a single-component alloy, mixed, or composite (e.g., metallic matrix + hard phase).
Advantages	Maximum freedom in material design: possibility to compose multi-component systems (e.g., matrix + carbides, borides), control grain size and particle morphology, and thus the microstructure and properties of the coating/weld.
	Possibility of supplying components with different properties and particle sizes, which is particularly important for composite layers and for coatings with an exceptionally high wear resistance.
	In many powder processes, it is possible to limit dilution (especially in LC) and precisely control the heat-affected zone.
Limitations	Powder quality requirements—particle size distribution, sphericity, flowability, bulk density, purity, and degree of oxidation—directly affect feeding stability and layer quality.
	Sensitivity to storage conditions (moisture, oxidation) and risk of segregation in mixtures of powders with different densities and granulations.
	Greater complexity of equipment (dispensers, powder flow calibration, process gas system), which increases qualification costs and repeatability requirements.
	For spray and cold spray processes: no classic metallurgical fusion (depending on the method), which shifts the quality criteria from heat-affected zone/dilution to adhesion, porosity, oxidation, and lamellar cohesion.

Table 5. Characteristics of strip electrodes and strips used as the feedstock materials for hardfacing.

General description	Strip electrodes and strips are mainly used in high-performance hardfacing processes (e.g., SAW strip cladding) to produce wide layers, often in protective applications (cladding) and surface restoration of large components.
Advantages	Very high deposition rate and surface coverage efficiency with large weld widths, which significantly reduces regeneration time.
	Good repeatability of geometry under stable operating and automation conditions.
	Possibility of achieving layers of uniform thickness on large surfaces.
Limitations	Limited geometric flexibility (less suitable for local repairs with complex geometry).
	Typically, higher "thermal inertia" of the process (depending on parameters) and the need to control deformation on slender elements.
	Less freedom in shaping complex composite systems than in the case of powders and powder wire parts.

Table 6. Characteristics of pre-applied powders and mixtures used as the feedstock materials for hardfacing.

General description	Pre-applied powders and mixtures—powder or mixture is pre-applied to the substrate (e.g., as a powder layer, paste with binder, powder tape) and then melted or consolidated by an energy source (flame, arc in special variants, laser, electron beam). This solution is sometimes used when it is important to control the location of the material and limit losses.
Advantages	Very high composition flexibility (like powders) and the ability to create gradient or multi-component layers.
	Good material utilization in local applications (less waste than in some powder feed solutions).
	Easier implementation in selected spot repairs and hard-to-reach areas.

Table 6. *Cont.*

Limitations	Risk of heterogeneity in the thickness and composition of the initial layer (segregation, uneven distribution, variability in binder content), which may translate into porosity and variability in properties.
	Sensitivity to the remelting process (overheating, excessive dilution, loss of volatile components/oxidation) requiring a careful procedure.
	An additional technological stage (preparation and consolidation of the layer), which increases time and operating costs.

From the point of view of steel component regeneration, there is no universally best form of feedstock material. The choice of feedstock is a compromise between functional requirements (wear/corrosion/temperature), substrate thermal limitations, required performance, and the ability to ensure technological quality. Solid wires and electrodes ensure high repeatability and simplicity of implementation and powder wires/electrodes significantly expand the scope for designing composition and microstructure, while powders (including mixed and pre-placed systems) offer the greatest material flexibility at the expense of higher equipment and quality requirements. Strips remain a highly efficient solution for large areas. This classification of additional materials allows for a clear link between the material (composition, form) and possible "process levers" and predicted structural and property consequences.

4.2. Key Indicators of Technological Quality

Dilution (D) is an indicator of the metallurgical purity of the weld, increasing with heat input and the susceptibility of the process to deeper penetration into the hardfaced material. Dilution directly modifies the chemical composition of the weld and the nature of the passive layer and co-determines the microstructure (proportion of strengthening/eutectic phases), microhardness, and modes of degradation in tribocorrosion [66]. For nickel welds (e.g., Inconel 625), Xue et al. [67] demonstrated that reducing the Fe content in the weld (extremely low $D < 0.5\%$ obtained during hardfacing with the CMT variant of the GMAW method) reduces susceptibility to intergranular corrosion by changing the composition and stability of the passive film. This relationship is threshold-like and is strongly evident in the near-surface zone. Hanif et al. [68] showed that in high-temperature environments (KCl, 600 °C), the effect of D on the composition of oxides and the rate of metal loss on FeCrAl layers is unambiguous: an increase in D worsens high-temperature corrosion resistance.

Bead geometry and imperfections—The response surface methodology (RSM) for the GMAW method shows that *I*-*U*-*v*, wire diameter, and electrode free exit length determine the width and height of the weld deposit and thus the risk of overlaps, discontinuities in the metallurgical bond between the weld and the substrate, or between adjacent beads/layers and local stress concentrators. Optimization of the "parameter windows" allows us to both reduce D and stabilize the face profile (which reduces technological notches and improves fatigue/tribological properties) [69]. In welds with Inconel 625, due to D of 30–40% in the first layer, $\geq$2 layers are often required to achieve the target composition and properties, which additionally links technological quality (geometry and overlap control) with functional quality (corrosiveness, hardness) [70].

Another group of technological quality indicators are *residual stresses* (RS) and *heat-affected zone width*. RS during hardfacing arise because of the following [22,45]:

- Uneven heating and cooling (hot weld + cool substrate $\rightarrow$ during cooling, the weld shrinks but is "held" by the substrate $\Rightarrow$ tensile stresses in the layer and/or heat-affected zone, compressive stresses in other areas, the system balances itself);

https://doi.org/10.3390/app16020792

- Phase transformations (e.g., austenite → martensite/bainite) accompanied by a change in volume;
- Sequence of bead/layer deposition and interpass cooling cycles.

In hardfacing on steels, the RS value and its sign result mainly from Q, thermal history, and path sequence. High heat input widens the heat-affected zone and promotes tensile stresses, which can be critical for difficult-to-weld steels, degrading fatigue life. In arc-based additive manufacturing (WAAM) processes, it is recommended to control the heat history by reducing the temperature gradients, controlling the preheating and interpass temperatures, and using interpass/interlayer rolling to reduce RS as well as improve grain uniformity [63,71]. Studies on AM/DED have shown that controlling the thermal history and mechanical treatments shifts RS towards compressive, which directly increases resistance to fatigue crack initiation [72].

4.3. Performance Indicators and Their Dependence on Technological Quality

This section describes the *corrosion resistance* of protective coatings (corrosion-resistant overlays/cladding) applied to steel substrates, as in the practice of steel component regeneration, resistance to the environment (general and local corrosion) alone or in conditions of corrosion-wear synergy is a frequent requirement. Unlike hardfacing in the strict sense, where the primary goal is to reduce wear, in protective coatings, it is critical to maintain the composition and ability to form a stable passive layer. For this reason, the key technological parameter is dilution D, which controls the proportion of Fe from the substrate in the weld volume and the local chemical composition of the top layer, and consequently, the composition and stability of the passive layer.

For Ni-based welds on carbon steels, dilution D directly affects the Fe content in the coating and the ratio of passivating elements in the surface layer. The literature indicates that local fluctuations in D (and thus, local fluctuations in composition) can be as important as the average value, which justifies controlling the geometry of the weld, the stability of the arc glow, and the repeatability of the process. Wang et al. [73] showed that dilution heterogeneity is a factor initiating local corrosion heterogeneity. In nickel welds on carbon steels, the interaction between D, microstructure, and passive layer determines the course of pitting and intergranular corrosion. At very low D (<1%) and in welds of varying thickness [67], more stable passivation and lower susceptibility to damage penetration are observed. Additionally, the technological parameters shaping the application of welds (pitch, degree of coverage) affect local corrosion by modulating the microstructure and roughness. It has been shown that the optimum application of ~80% welds in multi-welds hardfacing can reduce surface porosity and electrochemical activity [74].

The mechanism D → chemical composition of the layer → passive/discontinuous state → local corrosion is not specific to Ni alloys but is a general rule for protective layers on steels for the following groups of materials [75–80].

1. Austenitic stainless steels (e.g., 304L/316L) and duplex steels: An increase in D reduces the effective Cr/Mo/N content in the weld (especially in the first layer), which impairs local corrosion resistance. In this group, PREN (pitting resistance equivalent number) indices are often cited, which approximately rank the influence of passivating elements on susceptibility to pitting corrosion. A decrease in the Cr/Mo/N content due to dilution translates into a decrease in the passivation potential of the layer. At the same time, thermal cycling and dilution can disturb the phase equilibrium (important for duplex) and generate zones of increased corrosion susceptibility near the fusion line.
2. Co-based alloys (e.g., stellite): In many applications, they combine wear resistance with good stability in corrosive environments and/or at elevated temperatures, but

https://doi.org/10.3390/app16020792

their protective effectiveness also depends on maintaining the composition in the layer and limiting local discontinuities (porosity, micro-shrinkage), and material costs often force the optimization of thickness and number of layers.

3. Fe-Cr alloys and Fe-Cr-(Mo, Ni) systems: Corrosion resistance is strongly related to the minimum Cr content in the layer. Dilution can locally reduce the Cr content below the effective passivation threshold, while uneven stitch geometry and surface roughness can create sites for crevice/pitting corrosion initiation.
4. Composite systems (metallic matrix + hard phase): The presence of hard phases increases wear resistance but may introduce micro-pores/discontinuities and local galvanic cells. In such layers, corrosion behavior is determined by matrix continuity, tightness, and chemical homogeneity on a local scale, which remain sensitive to *D* and the stitching strategy.

From the perspective of the PSP relationship, the corrosion resistance of hardfacing layers on steels should be interpreted because of the chain: process parameters and application strategy → dilution (average and local) and metallurgical quality of the clad zone → microstructure and chemical homogeneity of the surface zone → stability of the passive layer and susceptibility to local corrosion. Consequently, in addition to alloy selection, it is critical to control *D*, limit discontinuities, and stabilize the geometry and roughness of the face, as these factors determine the initiation and development of pitting/crevice corrosion on a local scale.

Tribological wear—Fine-grained microstructure and low substrate content (e.g., in LC/PTA) increase hardness and abrasion resistance. Additionally, MMCs (e.g., Ni/Fe-based with WC/WC-Co) increase layer durability if particle dissolution/decarburization is limited (energy and powder flow control). Studies by Chen et al. [81] and Xu et al. [82] confirm the effectiveness of WC gradient architectures in achieving high wear resistance with acceptable ductility. In Ni- and Fe-based welds, a reduction in *D* and a fine-grained microstructure (LC/PTA) increase the hardness and wear resistance. Further improvement is provided by MMC (e.g., Ni/WC, Ni/WC-Co) if particle dissolution/decarburization is limited by controlling energy and powder flow. Studies by Xiang et al. [83] and Gain et al. [84] for LC combine high technological quality (low *D*, fine grain, few defects) with low wear rates under abrasive/erosive conditions [83,84].

Fatigue—Residual stresses and surface condition (smoothness, technological notches) influence crack initiation. Energy reduction, smoothing (material-free passage of a heat source over a previously laid weld to remelt only the upper part of the layer, followed by recrystallization, known as remelting) and post-process treatments (e.g., interpass rolling, hammering) reduce tensile RS and improve fatigue life [27].

Based on the analyzed literature, a PSP relationship for the hardfacing process on a steel substrate was developed. It organizes the relationship between the controllable process variables (P), the resulting weld structure and heat-affected zone (S), and the final functional properties (P), Table 7.

Table 7. PSP characteristics for the hardfacing process on a steel substrate: P—controllable process parameters (source, *I*-*U*-*v*, filler material, gas, temperature, trajectory); S—macro-/microstructure of the weld and heat-affected zone (geometry, *D*, defects, RS, phases); and P—functional properties (HV, wear, corrosion, adhesion, fatigue). Optimization direction: min. *Q* and *D* while maintaining arc/weld pool stability and joint continuity.

Process Parameters and Conditions (P)	→	Structural Effect (S)	→	Consequence in Functional Properties (P)
↓ *Q* (pulse/short circuit, ↑ *v*, thinner wire, proper gas)		↓ *p*, ↓ *D*, narrower heat-affected zone, less segregation		↑ corrosion resistance (less Fe in the weld), ↑ hardness (finer grain), lower risk of cracking in the heat-affected zone
Stable transfer (pulse/CMT), correct *U*		Smooth surface, no pores/possible lack of fusion		↓ notches, ↑ fatigue, ↓ adhesive wear
Interpass temperature control, cooling breaks		Uniformity of the layer microstructure and heat-affected zone		Repeatable HV, smaller property gradients, ↓ deformations
Interpass rolling/remelting (material-less passage of the heat source over the previously laid weld, aimed at re-melting only the upper part of the layer and its recrystallization and then re-solidification)		Grain refining, profile alignment (height and waviness)		↓ tensile RS, ↑ fatigue; more stable geometry of subsequent paths
Coaxial powder feed (LC)/PTA		Low *D*, narrow heat-affected zone, few pores		High adhesion and tribological resistance with small allowances
Increasing *U* (at constant *I*)		↑ *b*, ↓ *p*, risk of spatter/pores if *U* is too high		Possible reduced adhesion and corrosivity (surface defects)
Excessive *Q*/spray metal transfer mechanism in welding arc (SAW/GMAW)		↑ *p*, ↑ *D*, wide heat-affected zone		≥2–3 layers required for final composition; ↑ risk of cracks/deformation

↑—high, ↓—low.

5. Conclusions

The analysis of the subject literature confirms that regenerative hardfacing is a technology that is of significant importance for the implementation of circular economy (CE) principles, as it enables repeated extension of the service life of machine components, reduction in primary material and energy consumption, and reduction in waste streams throughout the entire product life cycle. In the case of functional layers on steel substrates, it is crucial to control the process → structure → properties (PSP) relationship, which allows layers to be designed for operational requirements (wear, corrosion, fatigue) while maintaining high reliability of the cladding–substrate bond.

The literature review covers both traditional hardfacing methods (gas, SMAW, GTAW/TIG, GMAW/MAG, SAW) and processes with increased energy density and/or limited dilution (PTA, LC/LMD), as well as the developing WAAM/DED technologies that utilize the phenomena characteristic of additive manufacturing. An important result of the work is the PSP table, which synthesizes the literature data between controllable process variables (P), the resulting weld and heat-affected zone structure (S), and the final functional properties (P) in the form of directional relationships and is a tool that enables a comparable interpretation of results and identification of critical "technological levers".

It has been demonstrated that a prerequisite for the comparability of process results and technology transfer between research centers and industry is the consistent use of

energy metrics (energy input/arc energy, linear energy, and, where justified, volumetric energy) calculated based on actual process parameters, depositing speed, and bead geometry. At the same time, it has been confirmed that energy metrics are only useful for classification when analyzed in parallel with "achieved" parameters, i.e., dilution D, weld geometry (fusion, height, width), heat-affected zone width, and the occurrence of non-conformities (especially lack of fusion—LOF). Consequently, the PSP table deliberately combines energy metrics with technological quality parameters to reduce the risk of misleading comparisons resulting from heterogeneous definitions of heat input and incomplete reporting of input data.

Significant research gaps have been identified, including the lack of verified "technology windows" for GMAW cladding on steel substrates with difficult weldability, limited quantitative data on the influence of shielding gas composition and metal transfer mode on dilution and face topography, and a lack of models that coherently combine process parameters, technological quality indicators, and service properties (including tribocorrosion and fatigue life). Comparisons of hardfacing technology variants, i.e., the influence of electrode wire type, path-laying strategy, and different thermal conditions while maintaining the same heat input value, also need to be supplemented, which is necessary for a reliable assessment of quality–economic trade-offs under CE conditions.

Based on the analysis of source materials, several detailed conclusions were formulated, which are presented below.

1. **Technological windows for the process of hardfacing on steel substrates with difficult weldability using the GMAW method.** The current state of research does not provide complete, experimentally verified ranges of settings I, U, v, contact tip to work distance (CTWD), and shielding gas composition/flow for surfacing steel with difficult weldability. This results in large fluctuations in D, heat-affected zone width, and surface smoothness. In PSP logic, this means that there is no stable transition from process descriptors $\rightarrow$ process effects, which makes it impossible to predict the performance properties. The priority is to develop process maps and practical setting cards based on WPS/WPQR, with clear acceptance criteria: target D range, no LOF, and repeatable geometry.
2. **Composition of shielding mixtures—no quantitative thresholds.** The effect of Ar-CO_2 mixtures with added O_2 on edge wetting, surface smoothness, and dilution is described mainly in qualitative terms in the literature. To generalize the PSP, it is necessary to determine the threshold content of components (CO_2, O_2), ensuring a simultaneous reduction in LOF and the required face topography when surfacing steel with increased hardenability.
3. **Limits of metal transfer modes for difficult-to-weld steels.** The location of the boundaries between short-circuit, globular metal, and spray transfer as a function of U, v, wire diameter, and CTWD is not clearly defined for difficult-to-weld steels. The lack of this data limits the possibility of reducing the energy input without increasing the risk of LOF and porosity, thus hindering the simultaneous control of two key PSP nodes: Q-D-LOF.
4. **CTWD and current intensity as variables controlling short-circuit dynamics and dilution.** The contact tip to work distance and the current intensity determine the dynamics of short circuits, droplet size, splashing, penetration depth, and, indirectly, dilution. A methodology for selecting CTWD for a specific wire diameter and source characteristics is required, formulated as a technological compromise: minimization of LOF $\leftrightarrow$ minimization of D.
5. **Deficit of multi-response models of technological quality.** Statistical models simultaneously covering D, weld geometry, porosity, and surface roughness are rare. In

https://doi.org/10.3390/app16020792

terms of CE, local process models (material–wire–gas–source) are desirable, which will enable the selection of settings that ensure the reduction in energy input while meeting quality criteria (no LOF, porosity control, acceptable face topography).

6. **Preheat and interpass—compromise between heat-affected zone ↔ D ↔ deformation.** Increasing the preheat and interpass temperatures reduces the tendency for hardening structures and cracks in the heat-affected zone but may increase D and deformation. It is necessary to determine the functional relationships linking these temperatures with the base metal content and deformations as a function of the geometry of the component and the cooling conditions, which has a direct impact on the reliability of the regeneration of high-value components.
7. **Welds layout strategy, stresses, and fatigue life.** Coverage, oscillation, welds layout sequence, and cooling intervals determine the distribution of residual stresses and deformation and consequently, fatigue life. For steels with difficult weldability, there is a lack of quantitative data linking the welds strategy to stresses and durability, which limits the informed design of regeneration in critical nodes.
8. **Feedstock material form—no comparisons at the same heat input.** Solid wires, metal powders, and flux-cored wires differ in heat balance, face cleanliness, slag presence, melting efficiency, and dilution, which affects the finishing costs. There is a lack of systematic comparisons conducted at the same linear energy value and controlled conditions that would allow for an unambiguous assessment of quality–economic trade-offs under CE conditions.
9. **No consistent correlations: D and geometry → hardness/wear/corrosion resistance.** In the literature, dilution and stitch geometry are not consistently linked to hardness, abrasion resistance, and pitting corrosion resistance within a single model. Quantitative correlations are needed, including tribocorrosion conditions, to enable the design of coatings based on operational criteria, rather than solely on geometric correctness.
10. **LOF as a critical criterion for joint reliability.** The reliability of welded joints and connections between welds requires the elimination of lack of fusion (LOF), while maintaining a minimum penetration depth and the lowest possible D. This regime promotes welds' composition stability and reduces heat-affected zone hardening and cracking, which is reflected in the PSP table by the dominant coupling between the metallurgical quality of the joint and its functional durability.
11. **Preferred technologies for high-hardenability substrates.** For high-hardenability steels, technologies that reduce the heat input and D (e.g., pulsed GMAW, PTA, LC/LMD) with strict interpass temperature control and, if necessary, interpass rolling, are advantageous. These approaches reduce the risk of unfavorable structures in the heat-affected zone, promote homogeneity of welds, and can improve the corrosion and fatigue resistance of refurbished components.
12. **Definition and function of "technological windows" in CE.** The limits of acceptance of process parameters ("technological windows") should be defined using multiple criteria: ensuring that minimum performance requirements are met (tribological resistance, corrosion resistance, adhesion, fatigue life) while maintaining high technological quality (low D, repeatable geometry, no LOF, and limited porosity) and acceptable deformations. In practice, this means that the technological window is determined not only by the heat input range, but also by a set of criteria indicated in the PSP table, which is a prerequisite for the implementation of regeneration as a CE tool on an industrial scale.

https://doi.org/10.3390/app16020792

Author Contributions: Conceptualization, W.C. and J.P.; formal analysis, W.C. and S.P.; investigation, W.C. and S.P.; resources, K.N. and J.P.; data curation, W.C. and S.P.; writing—original draft preparation, W.C. and S.P.; writing—review and editing, J.P. and K.N.; supervision, J.P. and K.N.; project administration, J.P. All authors have read and agreed to the published version of the manuscript.

Funding: This research received no external funding.

Institutional Review Board Statement: Not applicable.

Informed Consent Statement: Not applicable.

Data Availability Statement: No new data were created or analyzed in this study. Data sharing is not applicable to this article.

Conflicts of Interest: The authors declare no conflicts of interest.

References

1. Davis, J.R. *Hardfacing, Weld Cladding, and Dissimilar Metal Joining*; ASM Handbook, Vol. 6: Welding, Brazing, and Soldering; ASM International: Almere, The Netherlands, 1993; pp. 789–829.
2. Weman, K. *Welding Processes Handbook*, 2nd ed.; Woodhead Publishing Limited: Cambridge, UK, 2012.
3. Czupryński, A.; Adamiak, M.; Kříž, A.; Kovács, T.A. (Eds.) *Advanced Technologies of Welding, Surfacing, and Thermal Spraying of Modern Materials*; MDPI: Basel, Switzerland; Birkhäuser: Basel, Switzerland, 2024.
4. ESAB. *Repair and Maintenance Welding Handbook*, 2nd ed.; ESAB: North Bethesda, MD, USA, 2006.
5. Szczucka-Lasota, B.; Węgrzyn, T.; Lukaszkowicz, K. Low alloy steel shaft surface regenerative welding with micro-jet cooling. *Sci. J. Silesian Univ. Technol. Ser. Transp.* **2019**, *102*, 205–215. [CrossRef]
6. Chmielewski, T.; Golański, D. The role of welding in the remanufacturing process. *Weld. Int.* **2015**, *29*, 861–864. [CrossRef]
7. Kolasa, A.; Sarnowski, T.; Cegielski, P. Regeneration of Worn out Machine Parts Surfaces by Automatic Welding. *Weld. Technol. Rev.* **2015**, *87*, 50–57. [CrossRef]
8. Pytel, S.; Turek, J.; Okoński, S.; Zarębski, K. The properties and microstructure of padding welds built up on the surface of forging dies. *Arch. Foundry Eng.* **2010**, *10*, 5–10.
9. Kaszuba, M.D.; Widomski, P.; Kiełczawa, T.; Gronostajski, Z. The use of a measuring arm with a laser scanner for analysis and support of regenerative surfacing processes of forging dies. *Weld. Technol. Rev.* **2020**, *92*, 23–32. [CrossRef]
10. Pawlowski, L. *The Science and Engineering of Thermal Spray Coatings*, 2nd ed.; Wiley: Hoboken, NJ, USA, 2008.
11. Dobrzański, L.A.; Piec, M.; Klimpel, A. Improvement of the hot work tool steel surface layers properties using a high power diode laser. *J. Achiev. Mater. Manuf. Eng.* **2007**, *21*, 13–22.
12. Żuk, M.; Dojka, R. Repair welding of cast steel G20Mn5. *Weld. Technol. Rev.* **2018**, *90*, 112–116. [CrossRef]
13. Ambroziak, A.; Lange, A.; Białucki, P.; Kaczmarek, M. Properties of weld overlays on regenerated wheel hub of a mining vehicle. *Weld. Technol. Rev.* **2019**, *91*, 69–77. [CrossRef]
14. Broadbent, C. Steel's recyclability: Demonstrating the benefits of recycling steel to achieve a circular economy. *Int. J. Life Cycle Assess.* **2016**, *21*, 1658–1665. [CrossRef]
15. Gajdzik, B.; Wolniak, R.; Grebski, W.; Szymszal, J.; Grebski, M.E. *Sustainability and Smart Manufacturing: The Transformation of the Steelwork Industry*, 1st ed.; Routledge: London, UK, 2024. [CrossRef]
16. Available online: https://www.europarl.europa.eu/topics/en/article/20151201STO05603/circular-economy-definition-importance-and-benefits?utm_source=chatgpt.com (accessed on 15 October 2025).
17. Available online: https://eur-lex.europa.eu/legal-content/EN/TXT/HTML/?uri=CELEX:52020DC0098&utm_source=chatgpt.com (accessed on 15 October 2025).
18. Available online: https://www.europarl.europa.eu/topics/en/article/20210128STO96607/how-the-eu-wants-to-achieve-a-circular-economy-by-2050 (accessed on 15 October 2025).
19. Radaj, D. *Heat Effects of Welding–Temperature Field, Residual Stress, Distortion*; Springer: Berlin/Heidelberg, Germany, 1992.
20. Tukahirwa, G.; Wandera, C. Influence of process parameters in gas-metal arc welding (GMAW) of carbon steels. In *Welding-Materials, Fabrication Processes, and Industry 5.0*; IntechOpen: Rijeka, Croatia, 2023. [CrossRef]
21. Kvidahl, L.G. (Ed.) *The Practical Reference Guide for Hardfacing*; American Welding Society: Miami, FL, USA, 2002; Available online: https://pubs.aws.org/Download_PDFS/PRGHF-PV.pdf (accessed on 16 December 2025).
22. Stout, R.D. *Weldability of Steels*, 4th ed.; Welding Research Council: New York, NY, USA, 1987.
23. Grigorenko, G.M.; Kostin, W.A. Weldability of steel and criterion of its estimation. *Weld. Technol. Rev.* **2013**, *85*, 11–17. (In Polish)
24. Cegielski, P.; Skublewska, A.; Gawroński, P.; Ostrysz, M.; Dylewski, M.; Gajowniczek, M. Robotized 3D printing of the machines parts with welding methods. *Weld. Technol. Rev.* **2017**, *89*, 35–42. [CrossRef]

25. Panas, M.; Kowalski, P.; Ostrysz, M.; Łacisz, W.; Skublewska, A.; Dylewski, M.; Cegielski, P. Robotic Arc Surfacing in the Additive Technique-Aided Creation of Models. *Biul. Inst. Spaw. W Gliwicach* **2017**, *61*, 59–64. [CrossRef]
26. Prado-Cerqueira, J.L.; Diéguez, J.L.; Camacho, A.M. Preliminary development of a Wire and Arc Additive Manufacturing system (WAAM). *Procedia Manuf.* **2017**, *13*, 895–902. [CrossRef]
27. Cunningham, C.R.; Flynn, J.M.; Shokrani, A.; Dhokia, V.; Newman, S.T. Invited review article: Strategies and processes for high quality wire arc additive manufacturing. *Addit. Manuf.* **2018**, *22*, 672–686. [CrossRef]
28. *EN 1011-1: 2009*; Welding–Recommendations for Welding of Metallic Materials–Part 1: General Guidance for Arc Welding. iTeh, Inc.: Newark, DE, USA, 2009.
29. *ISO/TR 17671-1: 2002*; Welding–Recommendations for Welding of Metallic Materials–Part 1: General Guidance for Arc Welding. ISO: Geneva, Switzerland, 2002.
30. Pałubicki, S.; Plichta, J.; Nadolny, K. Effect of Heat Supplied to the Joint in the MAG Welding Process of Ferritic–Austenitic Stainless Steel 1.4462 on the Size of the Cross-Sectional Area of the Joints. *Materials* **2024**, *17*, 6192. [CrossRef]
31. Yousefieh, M.; Shamanian, M.; Saatchi, A. Optimization of the pulsed current gas tungsten arc welding (PCGTAW) parameters for corrosion Resistance of super duplex stainless steel (UNS S32760) welds using the Taguchi method. *J. Alloys Compd.* **2011**, *509*, 782–788. [CrossRef]
32. Melfi, T. New Code Requirements for Calculating Heat Input. *Weld. J.* **2010**, *89*, 61–63.
33. *ISO/TR 18491: 2015*; Welding and Allied Processes. Guidelines for Measurement of Welding Energies. ISO: Geneva, Switzerland, 2015.
34. *ENISO15614-1: 2017*; Specification and Qualification of Welding Procedures for Metallic Materials—Welding Procedure Test—Part 1: Arc and Gas Welding of Steels and Arc Welding of Nickel and Nickel Alloys. International Organization for Standardization: Geneva, Switzerland, 2017.
35. Wojsyk, K.; Macherzyński, M.; Lis, R. Evaluation of the amount of heat introduced into the welds and padding welds by means of their transverse fields measurement in conventional and hybrid welding processes. *Weld. Technol. Rev.* **2017**, *89*, 67–82. [CrossRef]
36. Macherzyński, M.; Słania, J.; Wojsyk, K. A new methodology for the determination of linear welding energy. *Biul. Inst. Spaw. W Gliwicach* **2023**, *67*, 50–56. [CrossRef]
37. Winczek, J.; Wojsyk, K. New method of calculating the amount of heat input to the weld. *Biul. Inst. Spaw. W Gliwicach* **2020**, *64*, 23–27. [CrossRef]
38. Arsić, D.; Lazić, V.; Nikolić, R.R.; Sczygiol, N.; Krstić, B.; Ivković, D.; Hadzima, B.; Pastorek, F.; Ulewicz, R. Weldability Assessment of Various Steels by Hard-Facing. *Materials* **2022**, *15*, 3082. [CrossRef] [PubMed]
39. Budinski, K.G. *Surface Engineering for Wear Resistance*; Prentice Hall: Englewood Cliffs, NJ, USA, 1988.
40. Ryabtsev, I.; Fomichov, S.; Kuznetsov, V.; Chvertko, Y.; Banin, A. *Surfacing and Additive Technologies in Welded Fabrication*; International Welding Engineers Textbook Series Under the Editorship of Borys Paton; Springer: Berlin/Heidelberg, Germany, 2023.
41. Burakowski, T.; Wierzchon, T. *Surface Engineering of Metals: Principles, Equipment, Technologies*, 1st ed.; CRC Press: Boca Raton, FL, USA, 1998.
42. Parmar, R.S. *Welding Engineering and Technology*, 3rd ed.; Khanna Publishers: New Delhi, India, 2022.
43. Lancaster, J.F. *The Physics of Welding*; International Institute of Welding: Genoa, Italy; Pergamon Press: Okford, UK, 1984; ISBN 0080305547.
44. Messler, R.W., Jr. *Principles of Welding*; John Wiley & Sons: Hoboken, NJ, USA, 1999; ISBN 978-0-471-25376-1.
45. Kou, S. *Welding Metallurgy*, 2nd ed.; John Wiley & Sons: Hoboken, NJ, USA, 2002; ISBN 0-471-43491-4.
46. Scotti, A.; Ponomarev, V.; Lucas, W. A scientific application oriented classification for metal transfer modes in GMA Welding. *J. Mater. Process. Technol.* **2012**, *212*, 1406–1413. [CrossRef]
47. Matusiak, J.; Pfeifer, T. Low-energy arc welding with gas shielding–the effect of material and technological conditions on joint quality and the emission of impurities in the workplace. *Weld. Int.* **2011**, *25*, 24–31. [CrossRef]
48. Zhang, H.T.; Feng, J.C.; He, P.; Zhang, B.B.; Chen, J.M.; Wang, L. The arc characteristics and metal transfer behaviour of cold metal transfer and its use in joining aluminium to zinc-coated steel. *Mater. Sci. Eng. A* **2009**, *499*, 111–113. [CrossRef]
49. Available online: https://www.fronius.com/en-gb/uk/welding-technology/info-centre/magazine/2019/cmt-cycle-step (accessed on 8 September 2024).
50. Toyserkani, E.; Khajepour, A.; Corbin, S.F. *Laser Cladding*, 1st ed.; CRC Press: Boca Raton, FL, USA, 2004. [CrossRef]
51. Zhu, L.; Xue, P.; Lan, Q.; Meng, G.; Ren, Y.; Yang, Z.; Xu, P.; Liu, Z. Recent research and development status of laser cladding: A review. *Opt. Laser Technol.* **2021**, *138*, 106915. [CrossRef]
52. Liu, Y.; Ding, Y.; Yang, L.; Sun, R.; Zhang, T.; Yang, X. Research and progress of laser cladding on engineering alloys: A review. *J. Manuf. Process.* **2021**, *66*, 341–363. [CrossRef]
53. Buchwalder, A.; Thronicke, J.; Jung, A.; Hengst, P.; Hunger, R.; Hartwig, S.; Zenker, R. Influence of different electron beam surface pre-treatments on the results of subsequent boriding-part I. *Mater. Und Werkst.* **2021**, *52*, 815–830. [CrossRef]

54. Osipovich, K.; Kalashnikov, K.; Chumaevskii, A.; Gurianov, D.; Kalashnikova, T.; Vorontsov, A.; Kolubaev, E. Wire-feed electron beam additive manufacturing: A review. *Metals* **2023**, *13*, 279. [CrossRef]
55. Panin, V.E.; Belyuk, S.I.; Durakov, V.G.; Pribytkov, G.A.; Rempe, N.G. Electron beam vacuum surfacing: Equipment, technology and properties of coatings. *Weld. Int.* **2000**, *14*, 580–584. [CrossRef]
56. Poza, P.; Garrido-Maneiro, M.Á. Cold-sprayed coatings: Microstructure, mechanical properties, and wear behaviour. *Prog. Mater. Sci.* **2022**, *123*, 100839. [CrossRef]
57. Moridi, A.; Hassani-Gangaraj, S.M.; Guagliano, M.; Dao, M. Cold spray coating: Review of material systems and future perspectives. *Surf. Eng.* **2014**, *30*, 369–395. [CrossRef]
58. Santos Da Silva, F.; Cinca I Luis, N.; Dosta Parras, S.; García Cano, I.; Guilemany, J.M.; Benedetti, A.V. Cold gas spray coatings: Basic principles, corrosion protection and applications. *Eclética Química J.* **2017**, *42*, 9–32. [CrossRef]
59. Zou, Y. Cold spray additive manufacturing: Microstructure evolution and bonding features. *Acc. Mater. Res.* **2021**, *2*, 1071–1081. [CrossRef]
60. Borowiecka-Jamrozek, J. Detonation-Sprayed Wc-12% Co and Wc-17% Co Diamond-Impregnated Segments/Natryskiwanie Detonacyjne Powłok Wc-12% Co I Wc-17% Co Na Spieki Metaliczno-Diamentowe. *Arch. Metall. Mater.* **2014**, *59*, 1227–1330. [CrossRef]
61. ASM Thermal Spray Society. Thermal Spray Processes and Application Examples. In *Thermal Spray Technology: Accepted Practices*; ASM International: Almere, The Netherlands, 2022; pp. 10–19. [CrossRef]
62. Azarmi, F.; Tangpong, X.W. Microstructural and Tribological Characteristics of Composites Obtained by Detonation Spraying of Iron-Based Alloy—Carbide Powder Mixtures. *Materials* **2023**, *16*, 6422. [CrossRef]
63. Hönnige, J.R.; Colegrove, P.A.; Ganguly, S.; Eimer, E.; Kabra, S.; Williams, S. Control of residual stress and distortion in aluminium wire + arc additive manufacture with rolling. *Addit. Manuf.* **2018**, *22*, 775–783. [CrossRef]
64. Hönnige, J.; Seow, C.E.; Ganguly, S.; Xu, X.; Cabeza, S.; Coules, H.; Williams, S. Study of residual stress and microstructural evolution in as-deposited and inter-pass rolled wire plus arc additively manufactured Inconel 718 alloy after ageing treatment. *Mater. Sci. Eng. A* **2021**, *801*, 140368. [CrossRef]
65. Dekis, M.; Tawfik, M.; Egiza, M.; Dewidar, M. Challenges and developments in wire arc additive manufacturing of steel: A review. *Results Eng.* **2025**, *26*, 104657. [CrossRef]
66. Ranjan, R.; Das, A.K. Protection from corrosion and wear by different weld cladding techniques: A review. *Mater. Today Proc.* **2022**, *57*, 1687–1693. [CrossRef]
67. Xue, Z.; Wang, H.; He, N.; Sun, Y.; Li, H.; Wang, Z.; Zhang, C.H.; Fang, Y.; Li, D.; Bao, K.; et al. Study on intergranular corrosion mechanism of low dilution rate Inconel 625 weld overlay. *Corros. Sci.* **2025**, *244*, 112659. [CrossRef]
68. Hanif, I.; Ssenteza, V.; Eklund, J.; Olovsjö, J.N.; Jonsson, T. High-temperature corrosion of weld overlay coating/bulk FeCrAl exposed in O_2 + H_2O + KCl(s) at 600 °C–A microstructural investigation. *J. Mater. Res. Technol.* **2023**, *25*, 7008–7023. [CrossRef]
69. Kannan, T.; Yoganandh, J. Effect of process parameters on clad bead geometry and its shape relationships of stainless steel claddings deposited by GMAW. *Int. J. Adv. Manuf. Technol.* **2010**, *47*, 1083–1095. [CrossRef]
70. Costa, J.F.M.; Jorge, J.C.F.; de Souza, L.F.G.; Mendes, M.C.; Farneze, H.N.; Magalhães, H.A.Y. Microstructural evaluation of Inconel 625 weld cladding deposited by the GMAW and GMAW with rotating electrode processes. *Tecnol. Em Metal. Mater. E Mineração* **2024**, *21*, e2848. [CrossRef]
71. Wang, L.; Qian, X.; Feng, L. Effect of welding residual stresses on the fatigue life assessment of welded connections. *Int. J. Fatigue* **2024**, *189*, 108570. [CrossRef]
72. Bastola, N.; Jahan, M.P.; Rangasamy, N.; Rakurty, C.S. A review of the residual stress generation in metal additive manufacturing: Analysis of cause, measurement, effects, and prevention. *Micromachines* **2023**, *14*, 1480. [CrossRef]
73. Wang, W.; Zhao, Z.; Zheng, W.; Wang, Y.; Shen, Z.; Ma, B.; Yang, J. Dilution induced variation in corrosion resistance properties on Co-Cr-Fe-Ni high-entropy alloy coatings prepared by laser cladding. *J. Mater. Res. Technol.* **2025**, *38*, 2506–2519. [CrossRef]
74. Bu, X.; Xu, X.; Lu, H.; Liang, Y.; Bian, H.; Luo, K.; Lu, J. Effect of overlap rate on the microstructure and properties of Cr-rich stainless steel coatings prepared by extreme high-speed laser cladding. *Surf. Coat. Technol.* **2024**, *487*, 131025. [CrossRef]
75. Matias, J.V.; Lourenco, M.J.; Jorge, J.C.; De Souza, L.F.G.; Farneze, H.N.; Mendes, M.C.; Araújo, L.S. Behavior of a superaustenitic stainless steel weld cladding deposited by the gas metal arc welding process. *Mater. Today Commun.* **2023**, *34*, 104978. [CrossRef]
76. Hemmati, I.; Ocelík, V.; De Hosson, J.T.M. Dilution effects in laser cladding of Ni-Cr-B-Si-C hardfacing alloys. *Mater. Lett.* **2012**, *84*, 69–72. [CrossRef]
77. Crook, P. The effects of dilution upon the corrosion and wear properties of cobalt-based weld overlays. *Corros. Sci.* **1993**, *35*, 647–653. [CrossRef]
78. Cunha, A.B.; Vatavuk, J.; Lima, C.R.C. Investigating the Effects of Iron Dilution on the Corrosion Resistance of Inconel 625 Welding Overlay on Carbon Steel. *Materials* **2025**, *18*, 5574. [CrossRef] [PubMed]
79. Kim, J.S.; Park, Y.I.; Lee, H.W. Effects of heat input on the pitting resistance of Inconel 625 welds by overlay welding. *Met. Mater. Int.* **2015**, *21*, 350–355. [CrossRef]

80. Bozeman, S.C.; Tucker, J.D.; Isgor, O.B. Corrosion resistance of 309L stainless steel claddings on carbon steel produced with wire-fed directed energy deposition. *Corrosion* **2023**, *79*, 771–781. [CrossRef] [PubMed]
81. Chen, S.; Ni, L.; Zhang, Y.; Wang, Y.; Cui, T.; Liang, J.; Wang, M. Laser cladding of a novel Fe-based coating with high wear resistance, corrosion resistance and self-lubricating properties. *Surf. Coat. Technol.* **2024**, *478*, 130468. [CrossRef]
82. Xu, Y.; Fu, S.; Lu, H.; Li, W. Process optimization, microstructure characterization, and tribological performance of Y_2O_3 modified Ti_6Al_4V-WC gradient coating produced by laser cladding. *Surf. Coat. Technol.* **2024**, *478*, 130496. [CrossRef]
83. Xiang, D.; Liu, Y.; Yu, T.; Wang, D.; Leng, X.; Wang, K.; Chen, Z. Review on wear resistance of laser cladding high-entropy alloy coatings. *J. Mater. Res. Technol.* **2024**, *28*, 911–934. [CrossRef]
84. Gain, S.; Veeman, D. A review on advances and challenges in wire arc additive manufacturing: Process parameters, microstructural evolution and material performance across alloys. *J. Alloys Compd.* **2025**, *1029*, 180735. [CrossRef]

Disclaimer/Publisher's Note: The statements, opinions and data contained in all publications are solely those of the individual author(s) and contributor(s) and not of MDPI and/or the editor(s). MDPI and/or the editor(s) disclaim responsibility for any injury to people or property resulting from any ideas, methods, instructions or products referred to in the content.

applied sciences

MDPI

Review

Research Status and Progress of All-Position Narrow-Gap GMAW for Pipelines

Wenji Liu *, Qing Li, Jianfeng Yue, Peng Zhu and Bing Li

School of Mechanical Engineering, Tiangong University, Tianjin 300387, China; lq2802426958@163.com (Q.L.); billyue@163.com (J.Y.); 15135065471@163.com (P.Z.); 15933823138@163.com (B.L.)
* Correspondence: liuwenji1981@126.com

Abstract: During the all-position narrow-gap welding process of pipelines, welding defects tend to occur in non-flat welding positions, constraining the quality and efficiency of pipeline construction. This paper addresses the sidewall and interlayer lack of fusion defects that commonly arise in all-position pipeline welding. Based on the research achievements of scholars and engineering technicians at home and abroad in recent years, the paper summarizes the influence laws of droplet transfer characteristics, arc morphology, and molten pool behavior on weld seam formation under different welding positions during gas metal arc welding. Additionally, the paper explores strategies for optimizing weld bead formation, including optimizing welding process parameters, controlling the molten pool flow with an external magnetic field, and using laser–arc hybrid welding. The paper points out the development trends of all-position pipeline welding technology, providing technical guidance and problem-solving ideas for alleviating the flow of the molten pool and optimizing the formation of all-position weld seams in engineering practice. Furthermore, it offers direction for scientific research for relevant researchers.

Keywords: all-position welding; narrow-gap gas metal arc welding; droplet transition; pipeline construction

1. Introduction

Oil and gas pipelines bear the responsibility of transporting oil and gas resources, serving as a bridge that connects supply and demand. Accelerating the construction of oil and gas pipelines is critical support for the high-quality development of the industry but also an effective aid to steady economic growth. Due to the constraints of on-site construction conditions, all-position welding methods are predominantly used in pipeline construction at present [1,2], involving manual or semi-automatic welding, which has relatively low efficiency. Compared with the traditional welding methods, narrow-gap welding reduces the bevel cross-sectional area, transforming the previously required large-angle, multi-layer, multi-pass welding process into multi-layer, single-pass welding process. This not only reduces the material consumption and improves the welding efficiency but also decreases heat input and thermal deformation, making it suitable for all-position welding. As a result, this method has been widely used in the on-site construction of long-distance oil and gas pipelines.

All-position narrow-gap gas metal arc welding (GMAW) is prone to the following defects during the construction process: (1) Due to the small bevel angle, the arc does not sufficiently heat the side wall, which is prone to side wall unfused defects; (2) In non-flat welding positions, the influence of gravity can cause the middle of the weld seam to bulge,

making it difficult for the arc to heat the concave areas where the groove side walls meet the previous weld pass during subsequent layer welding. This can easily generating porosity and interlayer lack of fusion defects.

In response to the aforementioned issues, summarizing the droplet transition behavior, arc morphology, and molten pool behavior under different positions in narrow-gap GMAW, analyzing strategies such as optimizing welding process parameters and improving welding methods, as well as the future technological development trends, holds significant guiding implications for the technical development of all-position welding in pipelines.

2. Current Status of Research on Narrow-Gap All-Position GMAW

The all-position welding process of pipelines generally refers to the welding from the flat position to the vertical position and then to the overhead position. To address the issues of sidewall lack of fusion and interlayer lack of fusion, it is necessary to study the formation patterns and influencing factors of narrow-gap GMAW all-position welding seams, and explore methods to optimize seam formation. Currently, research by scholars both domestically and internationally on the formation of narrow-gap welds primarily focuses on three aspects: droplet transition behavior, arc morphology, and molten pool behavior.

2.1. Droplet Transition Behavior in Narrow-Gap GMAW

The migration process droplets from the tip of the welding wire to the molten pool is referred to as droplet transfer. The droplet transfer behavior plays a crucial role in determining spatter, arc stability, and molten pool behavior, which directly impacts the stability of the welding process and the quality of the weld seam [3,4]. In GMAW, there are three primary modes of droplet transfer: short-circuit transfer mode, globular transfer mode, and spray transfer mode [5]. Short-circuit transfer typically occurs at lower welding currents, where the molten droplet contacts the workpiece through the arc gap, forming a short circuit. This mode features low heat input and is suitable for thin plate welding. Globular transfer can be further divided into coarse droplet and fine droplet transfer. When the current is relatively small and the arc voltage is high, coarse droplet transfer forms, with the droplet diameter being larger than the wire diameter [6], resulting in significant spatter. Conversely, when the current is higher, fine droplet transfer occurs, characterized by minimal spatter and a stable arc, making it widely used in production. Spray transfer mode features high arc power, concentrated heat flow, strong penetration capability, and good weld bead formation quality. For pulsed gas metal arc welding (P-GMAW), there are three typical droplet transfer modes: one droplet multiple pulses (ODMP), one droplet per pulse (ODPP), and multiple droplets per pulse (MDPP). ODPP is considered the ideal droplet transfer mode by many scholars [7,8]. Regardless of the welding form, if the droplet transfer is unstable, the weld seam is prone to defects such as porosity, slag inclusion, or poor fusion. For all-position welding, the effect of gravity on droplet transfer varies with different welding positions: in the flat welding position, gravity acts as a promoting force for droplet transfer, whereas in the overhead welding position, gravity acts as a hindering force, as shown in Figure 1. A stable droplet transfer process can be obtained by optimizing the process parameters, which in turn ensures the high-quality of weld formation.

The effect of arc length on the droplet transition is reflected in three aspects: first, it determines the length of the droplet transition path; second, it affects the extent of magnetic bias blowing, which in turn affects the droplet force (especially in the position of the sidewall of the narrow bevel); and third, the arc length affects the magnitude of the welding current. Zhai P et al. [9,10] studied the characteristics of droplet transfer in GMAW at the flat welding position under different arc lengths. Their findings indicate that when the arc length is too short, a “multiple droplets per pulse” transfer mode tends to occur, leading to

short circuits and spatter. Conversely, when the arc length is too long, it is more likely to exhibit a "one droplet multiple pulses" transfer mode, leading to large droplet transfer and causing disturbance in the molten pool. Liu Wenji, Xiao Yu et al. [11] analyzed the effect of arc length correction on the transition of melt droplets in the narrow-gap P-GMAW at the overhead position and found that when the torch swings to the sidewall, the melt droplets will easily deviate from the wire axis to the other side of the wall transition, leading to a protrusion in the middle of the weld. Using a shorter arc is easier to control the arc shape, ensuring the droplets transition along the diameter of the wire to the molten pool. Since the wire axis is parallel to the sidewall of the narrow bevel, the longer the arc, the greaterthe effect of magnetic bias blowing, resulting more pronounced change in the arc morphology. As found in the literature [11], test results showed that when the arc length correction factor was 6, droplets even transferred to the right sidewall.

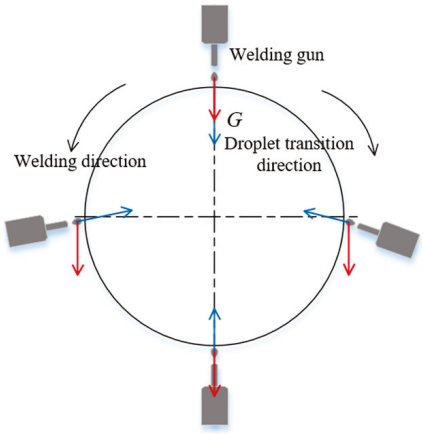

Figure 1. Schematic diagram of the effect of gravity on the transition of the melt drop for different welding positions (The red and blue arrows represent the direction of gravity and droplet transition direction).

Under the same welding wire diameter, the wire feeding speed (WFS) determines the magnitude of the welding current, and thus the impact of WFS on droplet transfer reflects the influence of welding current on droplet transfer. Dongqing Y et al. [12] observed the droplet transfer modes in GMAW at different wire feeding speeds. They found that when the WFS was between 3 and 8 m/min and the arc voltage was moderate, the droplet transfer was in a stable short-circuit transfer mode (as shown in Figure 2), leading to good weld seam formation; as the WFS increased, the droplet transfer became unstable, with more spatter; when the WFS exceeded 10 m/min, the droplet transfer mode shifted to spray transfer (as shown in Figure 3), resulting in poorer weld seam formation. Liu Wenji et al. [7] analyzed the impact of WFS on droplet transfer at the overhead welding position. They found that increasing the WFS helps to obtain smaller droplets and a higher transfer frequency, making it easier for droplets to reach the molten pool. However, under the effect of gravity, the molten pool struggles to flow towards the sides, easily forming a raised weld seam in the middle, which increases the amount of post-weld grinding work.

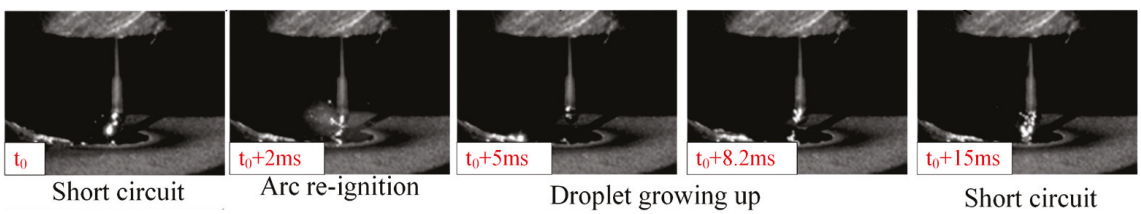

Figure 2. Short-circuit transfer (WFS = 6 m/min). Reprinted with permission from Ref. [12]. Copyright 2021, Elsevier.

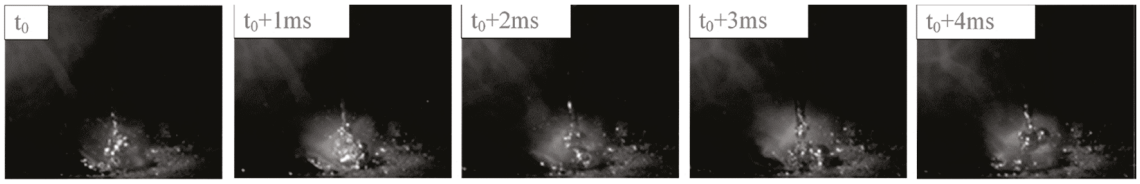

Figure 3. Spray transfer (WFS = 13 m/min). Reprinted with permission from Ref. [12]. Copyright 2021, Elsevier.

The effect of oscillation amplitude on droplet transfer essentially reflects the impact of sidewall constraints on the transfer mode. Bao Y et al. [13] recorded the droplet transfer during the overhead welding process of narrow-gap P-GMAW at different oscillation amplitudes using high-speed photography. As the oscillation amplitude increased, the droplet transfer mode changed from one droplet per pulse to multiple droplets per pulse (as shown in Figure 4), affecting the stability of the molten pool and leading to defects such as sidewall lack of fusion and undercutting. Wanghui X et al. [14] studied the influence of oscillating arc on the droplet transition. During upward welding, the effect of gravity on droplet transfer is reduced. When the welding wire oscillates toward the groove sidewall, the transfer frequency increases, manifesting as spray transfer; when the welding wire oscillates toward the center of the groove, droplet transfer becomes difficult, and as the droplet size increases, large droplet transfer eventually occurs; when the welding wire oscillates to the other side of the groove, the droplet transfer frequency increases and the droplet size decreases, reverting to spray transfer, as illustrated in Figure 5. During downward vertical welding, due to the downward flow of molten metal under the influence of gravity, the arc burns on the surface of the molten pool and the groove sidewall, and droplets are likely to contact the molten pool before completely detaching from the tip of the welding wire, leading to short-circuit transfer, which can cause spatter.

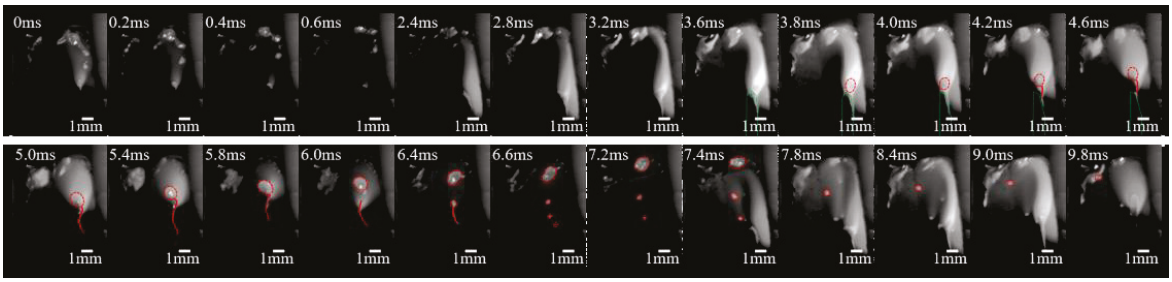

Figure 4. Droplet transport behavior of the right wall when the welding torch oscillated with 4.6 mm (The red circles indicates the droplet). Reprinted with permission from Ref. [13]. Copyright 2023, Authors.

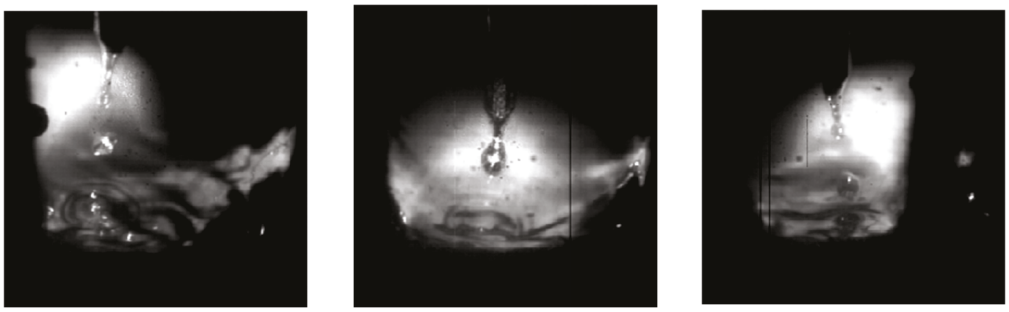

(**a**) (**b**) (**c**)

Figure 5. Droplet transfer in oscillating arc narrow gap welding: (**a**) left sidewall of the groove; (**b**) center of the groove; (**c**) right sidewall of the groove. Reprinted with permission from Ref. [14]. Copyright 2014, China Welding.

Furthermore, the assembly gap significantly influences droplet transfer behavior [15]. As the gap size increases (within the range of 0 to 4 mm), the droplet transfer mode in GMAW upward vertical welding evolves from short-circuit transfer to a special droplet transfer. This is because, with a larger gap, the arc can reach the root of the weld seam, causing most of the molten metal in the molten pool to fill the gap. At this point, droplets are pulled apart by an asymmetric magnetic field before they grow to the transfer size, forming what is known as "arc break transfer". In laser–arc hybrid welding, the laser-induced plasma alters the conductive path and forces acting on the molten droplet [16]. In laser–arc hybrid welding, pulse-induced laser [17,18] and the phase difference between the two wires in dual-wire P-GMAW [19] also affect the droplet transfer behavior, which in turn influences the weld bead formation.

2.2. Arc Behavior in Narrow-Gap GMAW

Welding arc is an electrically neutral, high-temperature plasma whose shape and stability have a crucial impact on weld seam formation and droplet transfer. The constraint of the narrow-gap groove on the arc differs significantly from that of V-groove and T-groove, thus exhibiting many unique characteristics. Studying the special arc features during the narrow-gap welding process and uncovering the mechanisms behind their formation is of great significance for improving the quality of narrow-gap welding and overcoming welding defects [20,21].

Wenji L et al. [22] discovered the phenomenon of arc "jumping" during the narrow-gap P-GMAW process and developed a weld seam tracking arc sensor based on this observation. They found that the arc interruption phenomenon occurring during the narrow-gap P-GMAW process follows a clear pattern, explaining the intrinsic mechanisms that cause arc interruption. The special constraints imposed by the narrow gap lead to changes in arc behavior and droplet transfer paths, which accumulate the necessary conditions for arc interruption. Their findings provide theoretical guidance for avoiding arc interruptions, contributing to the improvement of welding quality and reliability in narrow-gap welding applications. Additionally, when performing GMAW in narrow-gap, the arc appearance is significantly compressed. Without measures to alter the arc shape, there is a higher likelihood of generating numerous welding defects such as lack of fusion, porosity, and slag inclusion. However, by employing the method of laser thermal stabilization of the arc, although it can improve arc stability to some extent, the limitation of laser power becomes a concern. As the welding speed increases, inadequate heat distribution from the laser beam results in poor spreading of the molten metal and insufficient wetting at the weld toe [23], affecting the weld quality.

Bao Y et al. [13] investigated the influence of different oscillation amplitudes on arc behavior during the overhead welding process of narrow-gap P-GMAW. The arc takes on a trumpet-like shape, and as the oscillation amplitude increases, the angle at which the arc deflects toward the sidewall gradually increases (as shown in Figure 6). This leads to greater heat input to the sidewall, which is beneficial for ensuring sidewall penetration; however, excessive oscillation amplitude causes the arc pressure to push the molten metal in the molten pool back toward the center of the groove, forming a convex weld bead under the influence of gravity. Regarding the issue of sidewall lack of fusion, many scholars have conducted analyses from the perspective of arc behavior. Zhang G et al. [24] explained the process of arc climbing along the sidewall based on the self-regulating characteristics of the arc and the principle of minimum arc voltage. They found that the arc tends to climb onto the sidewall in narrow gaps, causing changes in the arc's electrical conductivity path, which leads to various droplet transfer modes and consequently affects weld seam quality. Ni Z et al. [25] studied the lack of fusion defects in narrow-gap GMAW upward vertical

welding with oscillating arcs, noting that sidewall lack of fusion typically occurs on the opposite sidewall after severe arc climbing. Within one oscillation cycle, if the arc climbs prematurely to the right sidewall, the temperature distribution and the state of the molten pool are affected, leading to a lack of fusion on the left sidewall.

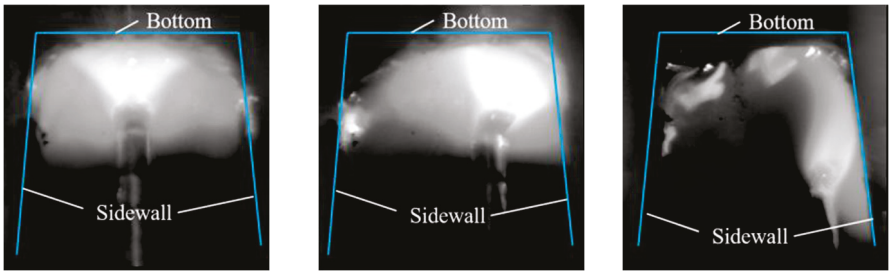

(**a**) (**b**) (**c**)

Figure 6. Arc characteristics for different oscillation widths: (**a**) 0 mm; (**b**) 2.6 mm; (**c**) 4.6 mm. Reprinted with permission from Ref. [13]. Copyright 2023, Authors.

2.3. Molten Pool Behavior in Narrow-Gap GMAW

During the narrow-gap all-position GMAW process, the melt pool is susceptible to flow phenomena under the influence of gravity. Sincebehavior of the molten pool is closely related to weld seam formation, understanding the patterns and causes of molten pool behavior in all-position GMAW is crucial for controlling the formation of the weld seam.

Gravity is a critical factor influencing the formation of all-position welds. Park J H et al. [26] used the P-GMAW process to weld in flat, vertical-down, and overhead positions, analyzing the behavior of the molten pool under the influence of gravity in different positions. As shown in Figure 7, during vertical-down welding, the molten pool flows downward due to gravity, accumulating at the center of the arc, which shortens the distance between the wire tip and the molten pool. When the droplet contacts the molten pool surface, short-circuiting transitions are likely to occur, leading to arc instability and spatter. In the overhead welding position, the combination of gravity and reverse flow causes the tail of the molten pool to experience strong reverse flow, leading to more molten metal accumulating at the tail of the molten pool (as shown in Figure 8). This increases the weld height and results in a weld shape with a central bulge. To mitigate the issue of molten pool flow, Cai X Y et al. [27,28] studied the behavior of the molten pool in the overhead welding position under the influence of gravity, based on all-position tandem narrow-gap GMAW. Most molten metal flows backward due to gravity, resulting in less molten metal beneath the arc. By adjusting the wire feed speed, they achieved high-quality welds suitable for the overhead welding position. Compared to laser welding, laser–arc hybrid welding offers higher robustness against welding defects but also results in greater weld penetration and wider weld beads [29]. Han R et al. [30] introduced a copper backing in laser–GMAW hybrid welding, which can accelerate the cooling and solidification process of the molten pool, particularly in vertical-up and overhead welding positions, thereby reducing the risk of molten pool downward flow.

Huang J et al. [31] revealed the effect of the current waveform on the solidification process of the molten pool during P-GMAW welding and investigated the dynamic behavioral characteristics of the molten pool (shown in Figure 9). The front of the molten pool is compressed, forcing the molten metal to flow towards the rear of the molten pool due to the obstruction at the bottom. Upon reaching the boundary at the rear, the molten metal is reflected. Meanwhile, the metal flow on the front surface of the molten pool is driven backward under the combined effects of impact force and surface tension, converging with the other stream of molten metal at the rear of the molten pool, leading to the accumulation

of molten metal. Wang L et al. [32] utilized high-speed photography and tracer particle technology to anlyze the characteristics of molten metal recirculation under different welding speeds and magnetic field excitation currents. Based on their findings, they proposed methods to suppress the formation of raised weld humping. Zhu C and colleagues [33] also investigated the effect of oscillating arcs on the behavior of the molten pool. An oscillating arc brings more heat to the side walls, causing the molten pool to oscillate with a large amplitude. This facilitates the rise of bubbles and helps reduce the formation of incomplete fusion defects.

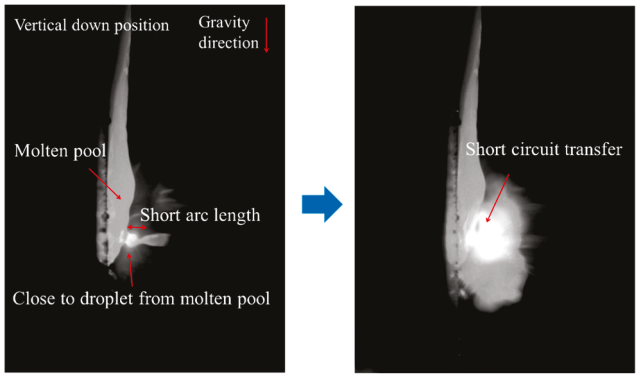

Figure 7. Short-circuit transition in the downward-facing weld position. Reprinted with permission from Ref. [26]. Copyright 2019, Authors.

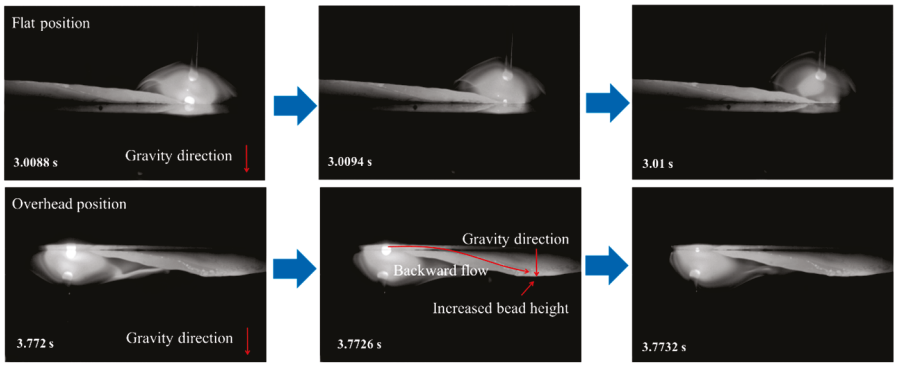

Figure 8. Melt pool characteristics for flat and overhead welding positions. Reprinted with permission from Ref. [26]. Copyright 2019, Authors.

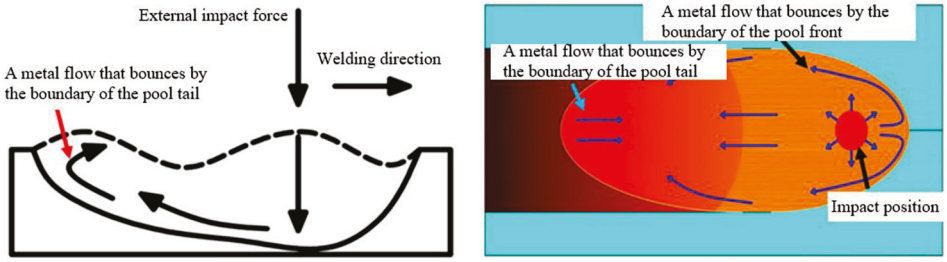

Figure 9. Schematic diagram of molten pool flow behavior. Reprinted with permission from Ref. [31]. Copyright 2023, Authors.

Numerical computation techniques have played a significant role in predicting molten pool flow and weld seam formation. Xu G et al. [34] found that during the GMAW vertical welding process, the size of the molten pool and the peak temperature of the molten metal significantly decrease, leading to an accelerated solidification rate of the molten pool, which is the primary factor responsible for suppressing weld pool sagging. Meanwhile, the upward component of the arc force and the enhanced support from the solidified

metal bulge help counteract the downward flow of the liquid metal. Hu Z [35] and Park J H [36] et al. studied the impact of gravity on the behavior of the molten pool at different welding positions through fluid dynamics models of the molten pool. Cho D W et al. [37,38] conducted numerical simulations to investigate the molten pool behavior under the one droplet per pulse mode during the GMAW process, as well as the molten pool flow patterns at different welding positions. These studies provide valuable insights into how external forces, for example the gravity, influence the molten pool dynamics and, consequently, the quality and formation of the weld seam.

2.4. Microstructure of Narrow-Gap GMAW

During the welding process, the base material undergoes alternating thermal cycles of rapid heating and cooling. The microstructure of the weld undergoes significant changes during solid-state phase transformations under different cooling rates, leading to notable differences in properties between the heat-affected zone (HAZ) and the base material [39].

The heat input involved in welding thermal cycles alters the microstructure of the base material, such as forming austenite grains, bainite, and martensite phases, which can result in reduced toughness in the HAZ at low temperatures [40]. Zhai P et al. [9] analyzed the optical microstructures of weld metals under three typical droplet transfer modes, finding that more uniform grain distribution was achieved under the ODPP condition. Lower heat input, combined with stronger stirring effects, facilitate the growth of finer and more uniform grains. Hang J et al. [31] found that liquid convection reduces the temperature gradient in the welding pool, intensifies compositional undercooling, and significantly alters the growth direction of primary austenite grains. Stronger impacts increase the proportion of proeutectoid ferrite in the weld microstructure and enlarge the grain size of proeutectoid ferrite and acicular ferrite, highlighting the importance of considering arc and droplet impingement for optimizing weld microstructures during welding process design.

Rapid cooling leads to the transformation of austenite into martensite in the weld and HAZ [41]. While martensite possesses high strength and hardness, it is brittle. Finite element analysis can be used to predict thermal history, deformation, residual stress and microstructure at any point in the material. Moreover, it has been identified that laser power has the greatest impact on thermal history during welding [39]. However, phenomena such as the movement of molten metal and latent heat released during solid-state phase transformations are often overlooked in numerical analyses. These factors affect temperature distribution and significantly influence the predicted microstructural composition [41,42]. Therefore, controlling welding parameters is crucial during welding process design to avoid excessive formation of brittle phases, thereby enhancing the overall performance of pipeline welds. According to related studies [29], lower brittleness microstructures were observed in the upper region of hybrid laser–arc welds, indicating that the heat source generated by the arc acts as a cooling inhibitor in the fusion zone. Thus, incorporating hybrid laser–arc welding in process design can effectively reduce weld brittleness and improve joint performance. Additionally, carbides play a critical role in the formation of weld microstructures [29]; excessive carbide content can adversely affect the microstructure, potentially causing localized hardening or embrittlement and increasing the risk of crack formation.

In narrow gap welding, a smaller groove angle can lead to uneven arc heating, making it easy to cause localized overheating or differences in cooling rates. These issues can further exacerbate problems such as inconsistent weld quality and increased risk of defects. It is essential to control these factors through appropriate welding procedures and heat treatment processes to avoid the occurrence of welding defects.

3. Methods to Improve Weld Bead Formation in Narrow-Gap GMAW

To address issues such as lack of side wall fusion and interpass lack of fusion that occur during the construction of all-position narrow-gap GMAW, researchers have explored several approaches, including optimizing welding process parameters, controlling arc shape using external magnetic fields, and combining with other heat sources. These investigations have yielded many important research findings.

3.1. Changing Process Parameters to Control Melt Pool Flow to Improve Weld Forming

Adjusting the angle of the welding torch or the workpiece can significantly influence arc force acting on the molten pool, thereby improving the weld bead formation. Yin T et al. [43] studied the effects of different torch tilting angles on the depth and width of the molten pool in vertical position metal active gas (MAG) welding of pipelines based on a dual-ellipsoid heat source model. Compared with the perpendicular and backward tilt torch postures, the forward-tilted torch resulted in a wider and shallower molten pool in welding (as shown in Figure 10). Lei Zhenglong et al. [44] investigated the suppression of moltn pool flow in laser–arc hybrid welding by altering the welding torch angle and utilizing the force of the shielding gas and the arc force acting on the molten pool. Zhang Yang et al. [45] studied the effect of workpiece inclination angle on the morphology of the welding molten pool in pulsed MAG welding. During uphill welding, increasing the workpiece inclination angle leads to a longer molten pool but a decreased width and surface area, leading to an accumulation of more metal at the rear of the molten pool and the formation of a depression at the front. When the inclination angle exceeds 60°, the weld seam essentially fails to form properly. In contrast, during downhill welding, as the workpiece inclination angle increases, the length of the molten pool decreases while the width increases. The molten metal flows forward due to gravity, resulting in a shape characteristic where the front of the molten pool is higher than the rear. However, when the inclination angle exceeds 75°, the welding process becomes unstable, and the spatter increases.

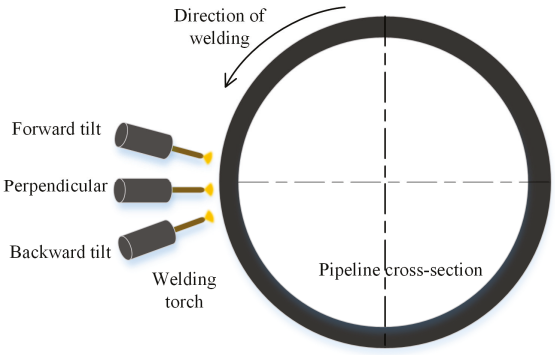

Figure 10. Schematic diagram of torch angle in vertical welding position.

An appropriate welding torch oscillation amplitude can helps balance the surface tension and heat input of the molten pool, leading to good weld seam formation. He Y et al. [46] employed the Taguchi method to investigate the influence of welding current, arc voltage, and welding speed on the side wall melt depth. They found that the primary cause of the formation of side wall unfused defects is the significant effect of temperature and oxides on the surface tension of the molten pool. Furthermore, they concluded that arc oscillation enhances heat transfer to the side walls, serving as an effective measure to eliminate side wall unfused defects. Bao Y et al. [13] investigated the impact of different oscillation amplitudes on the molten metal in the molten pool during overhead welding. Excessive oscillation amplitude can lead to a reduction in surface tension, making

the molten pool more prone to flow. Additionally, the arc pressure drives the molten metal in the molten pool back toward the center of the weld seam, and under the influence of gravity, a convex weld seam forms. On the other hand, an insufficient oscillation amplitude results in relatively higher surface tension, poor molten pool fluidity, and the formation of a deeper and narrower weld seam. Zhu C et al. [33] used computational fluid dynamics simulation to investigate the effect of arc oscillation on the molten pool behavior during narrow-gap GMAW. The results showed that changes in the arc oscillation frequency and amplitude significantly altered the fluid flow patterns within the molten pool. A larger oscillation amplitude promoted the rise of gas bubbles within the molten pool, improving side wall fusion. Although adjusting the oscillation amplitude can help to better fill the weld seam and reduce defects, dynamically adjusting the oscillation pattern to adapt to the changing real-time welding environment remains an unresolved problem, especially under complex working conditions.

The wire feeding speed also has an impact on the molten pool. In vertical and overhead welding positions, the molten pool is prone to flow due to gravity. Reducing the wire feeding speed leads to a decrease in welding current, thereby reducing heat input [47], which effectively controls the flow of the molten pool. However, in all-position welding, this would result in a thinner weld layer at that position, thus requiring an appropriate reduction in welding speed to ensure the height of the weld layer. Li Chenyang et al. [48] analyzed the changes in weld width and residual height at different wire feeding speeds during overhead welding. As the wire feeding speed gradually increases within the range of 3–5.5 m/min, both the weld width and residual height show an increasing trend. However, when the wire feeding speed exceeds 6.0 m/min, hump defects begin to appear. The study does not fully explore the impact of different welding positions on this conclusion. While optimizing process parameters can improve the weld bead quality in narrow-gap GMAW welding of pipelines to a certain extent, existing research mostly focuses on localized optimization under specific conditions, lacking systematic comparisons and validations across various conditions.

3.2. Improvement of Weld Forming by Applying a Magnetic Field to Control the Flow of the Molten Pool

The welding arc is a high-temperature plasma, and external magnetic fields have a significant impact on its behavior. By applying an external magnetic field, an electromagnetic force is generated on the arc or molten pool, opposingthe force of gravity. The shape of the arc and the force state of the molten pool can be altered, thereby improving weld seam quality. The improvement of molten pool behavior by electromagnetic forces can be categorized into two types: the first involves using electromagnetic forces to control the rotation or deflection of the arc at a certain angle, which serves to stir or support the molten pool; the second involves the direct action of the magnetic field on the molten pool, utilizing the electromagnetic force to counteract the gravitational force on the molten pool to improve its force state.

Guan Z Q et al. [49] generated a longitudinal magnetic field parallel to the welding torch axis using a magnetic generator installed on the welding torch. Under the influence of the Lorentz force F_X and the magnetic field B, charged particles in the arc undergo rotation (as shown in Figure 11), causing the arc to rotate at high speed, which increases the heated area and thereby controls the flow of the molten pool. Similarly, applying a transverse magnetic field uses the Lorentz force to deflect the arc, thereby changing the heat distribution on both sides of the groove and enhancing the quality of the weld seam formation [50]. To achieve sufficient sidewall fusion without significantly increasing the heat input, Wang J et al. [51] found that by applying an alternating magnetic field to assist arc welding, an alternating magnetic field can be formed in the arc burning zone,

periodically deflecting the welding arc within the pulse current cycle, which can provide more arc heat. However, the effectiveness of this method relies on precise adjustment of magnetic field parameters, which can be challenging to achieve in actual operation. Jian X et al. [52] established a mathematical computational model for narrow-gap tungsten inert gas welding to study the behavior of the welding arc and molten pool under the influence of an alternating longitudinal magnetic field. This research enhances the understanding of how external magnetic fields can be effectively utilized to control the welding process and improve weld seam quality. However, the model does not fully take into account the various complex conditions and interactions among variables that may occur during actual welding processes. Most existing studies focus on the impact of a single variable (such as magnetic field strength or frequency) on the welding process while neglecting the interactions among multiple factors and their overall effect on the welding outcome. For example, Yu J et al. [53] successfully achieved the joining of low-carbon steel Q235B using plasma-enhanced pulsed GMAW with an external magnetic field. Their research found that as the magnetic field current increased, the coupling of the dual arcs also increased. However, when the magnetic field current exceeded 1A, the changes in arc shape tended to level off. Changing the frequency of the applied alternating magnetic field can alter the shape of the welding arc, reducing the spatter rate and improving the appearance of the weld seam. Guan Z Q et al. [49] analyzed the effect of magnetic field frequency on GMAW arcs using high-speed camera techniques. Their analysis revealed that the shape and movement of the arc change with variations in the external magnetic field frequency. Below 60 Hz, the arc shape expands, leading to a deterioration in the weld bead appearance and mechanical properties. Conversely, above 60 Hz, the weld bead appearance and mechanical properties are significantly improved.

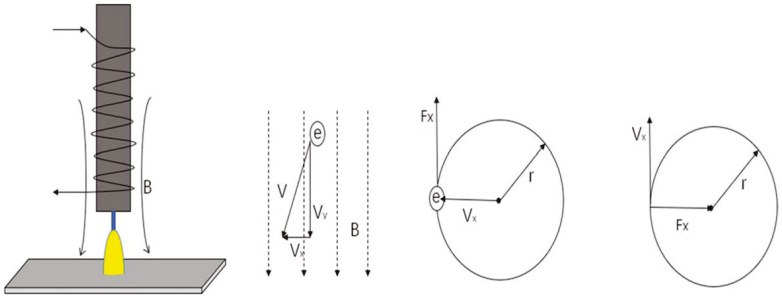

Figure 11. Motion and force of a charged particle in a longitudinal magnetic field (B, F_X and V_X indicate the longitudinal magnetic field intensity, Lorentz force and radial motion component.). Reprinted with permission from Ref. [49]. Copyright 2019, IOP Publishing.

Applying an external magnetic field to generate an upward electromagnetic force that counteracts part of the gravitational force on the molten pool can also control the flow of the molten pool in all-position welding. Yue Jianfeng et al. [54] proposed applying a high-frequency alternating magnetic field to the molten pool during downward vertical MAG welding (as shown in Figure 12). By applying a high-frequency alternating current to coil 0, coil 1, or coil 2, the generated magnetic field acts on the molten pool. The eddy current effect produced by this magnetic field generates an eddy current force that counteracts the gravitational component of the molten metal, overcoming the adverse effects of gravity on the formation of the molten pool. This method can be extended to vertical welding positions to enhance the versatility and flexibility of the welding process. Based on numerical simulations and experiments, Bachmann et al. [55] investigated the electromagnetic support effect on the molten pool during laser beam welding of austenitic stainless steel. Their research demonstrated that this electromagnetic support can prevent the sagging of the molten pool and detachment due to gravity. Shoichi M et al. [56]

proposed a method of applying an external electromagnetic field to generate an upward electromagnetic force to control the flow of the molten pool (as shown in Figure 13). The interaction between strong currents I and the magnetic field B_X produces an electromagnetic force in the opposite direction of gravity, thus suppressing the downward flow of the molten metal. This approach not only enhances the stability of the molten pool but also improves the quality and consistency of the weld seam. Wang et al. [57] developed an approach based on GMAW, wherein they controlled the fluid flow and its velocity distribution within the molten pool by applying an external magnetic field. They proposed that combining an appropriate electromagnetic field with a rear-tilted welding torch can yield high-quality welds without humping. Li Y et al. [58] applied an external magnetic field to the molten pool of low-carbon steel plates to generate a forward electromagnetic force, which breaks the reverse flow of molten metal. As a result, they achieved welds without humping. Given that low-carbon steel is a ferromagnetic material whose permeability changes significantly with increasing temperature, the behavior of the molten pool and its surrounding high-temperature regions under the influence of an external magnetic field becomes complex and difficult to predict. Consequently, research on utilizing external magnetic fields to control the dynamic behavior of the molten pool during the welding of low-carbon steel is relatively limited.

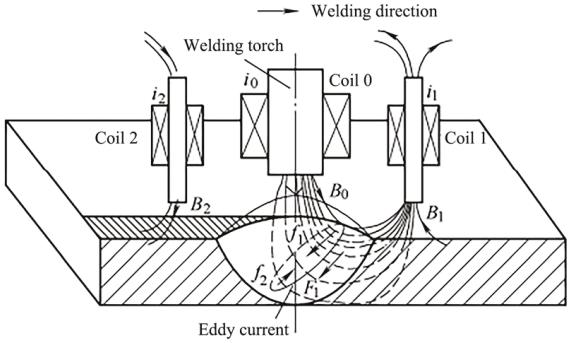

Figure 12. Principle diagram of the structure of the external high-frequency alternating electromagnetic field. Reprinted with permission from Ref. [54]. Copyright 2013, Journal of Mechanical Engineering.

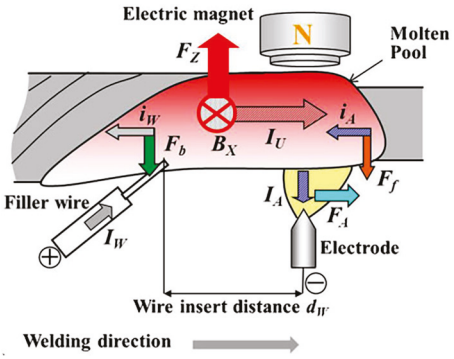

Figure 13. Schematic diagram of the electromagnetically controlled molten pool in the overhead position (F, I and B_X indicate the electromagnetic force, current flux density and magnetic flux density, respectively.). Reprinted with permission from Ref. [56]. Copyright 2013, Sage Publications.

Despite the significant improvement in weld bead quality that can be achieved by controlling arc shape and molten pool behavior through an externally applied magnetic field, this approach faces multiple challenges in practical application. Firstly, magnetic field parameters (such as intensity, frequency, etc.) need to be precisely regulated according to specific welding conditions, which pose higher demands on existing control systems. Secondly, different materials respond variably to magnetic fields, especially ferromagnetic materials whose permeability changes significantly with temperature, adding complexity

to magnetic control [59]. Furthermore, the interaction between magnetic field parameters and welding process parameters, as well as the feasibility of actual operation, are also issues that need to be addressed.

3.3. Improvement of Weld Formation by Combined Laser and Arc Welding Methods

Laser–arc hybrid welding is a welding technique that combines two heat sources: laser and arc. The high energy of the laser can rapidly heat the material, forming a deep and narrow molten pool, which significantly increases the welding speed [60]. The arc, on the other hand, serves as a compensatory element, enhancing the stability of the welding process. Additionally, during hybrid welding, the laser has the effect of attracting and stabilizing the arc [61]. When the arc and the laser are applied to the same molten pool, the welding process becomes more stable, effectively reducing issues such as side wall lack of fusion defects and thermal deformation of the weldment. Laser and arc welding can be simply divided into two methods. One of them is the laser-assisted arc welding process, which incorporates a low-power laser beam as an auxiliary heat source into traditional arc welding. This addition provides extra heating or preheating effects. However, the introduction of the low-power laser does not significantly impact the control of the weld penetration depth or changes in the welding speed [62]. Its application scope is limited. In contrast, arc-augmented laser welding uses high-power lasers as the primary heat source, complemented by an electric arc to broaden the molten pool width. This combination allows for achieving wide and deep weld beads at higher welding speeds, reducing the heat-affected zone and minimizing welding distortion [63–65].

The appropriate positioning of the laser beam relative to the arc (the light-wire spacing) can facilitate strong interactions and significantly increase the depth of penetration. When the laser beam irradiates the molten pool, the flow of the molten pool changes due to the influence of gravity, affecting the quality of the weld seam. A reasonable light-wire spacing can optimize the energy distribution of the laser on the molten pool [65], improving molten pool flow and reducing spatter. Research by Zhang Chen et al. [66] shows that as the distance varies from 0 to 4 mm (as shown in Figure 14), the greater the distance, the stronger the preheating effect of the laser on the molten pool, which enlarges the area at the front end of the molten pool and makes the process of droplet incorporation into the molten pool smoother. Conversely, Gui H and Liu S et al. [67,68] discovered that the laser has a compressing effect on the electric arc. The closer the laser's point of action is to the center of the arc, the stronger the interaction between the laser and the arc. This significantly compresses the arc, thus enhancing the penetration depth and stability of the molten pool.

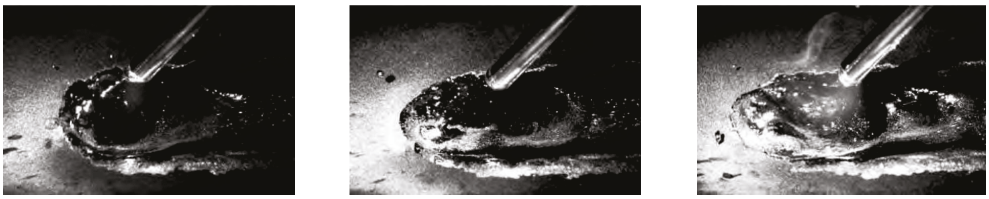

(**a**) (**b**) (**c**)

Figure 14. Melt pool state at different laser-to-wire distances: (**a**) 0 mm; (**b**) 2 mm; (**c**) 4 mm. Reprinted with permission from Ref. [66]. Copyright 2023, Aeronautical Manufacturing Technology.

Most existing studies focus on the impact of a single variable (such as laser-wire distance, laser power, current, etc.) on the welding process while neglecting the interactions among multiple factors and their overall effect on the welding outcome. For instance, Uemura T et al. [69] confirmed the weldability of hybrid laser–arc welding with a robot manipulator in the vertical-up position, but they did not fully consider the influence of gravity on the molten pool behavior under different welding positions. This oversight can

lead to an incomplete understanding and optimization of welding processes across various conditions, where multiple factors interact simultaneously, affecting the final weld quality and efficiency. To address the effects of gravity on the molten pool behavior caused by changes in welding position, Han R et al. [30] proposed laser-GMAW hybrid welding with a copper liner. This method supports the molten pool from the flat welding position to the vertical welding position, thereby preventing defects such as root sagging or burn-through at the root of the weld in this range. The interaction between the laser and the arc shows that the presence of the laser significantly enhances the degree of ionization of the arc plasma, reduces the resistance of the arc channel, and increases the density of free electrons and charged particles. These effects, in turn, promotes the stability and conductivity of the arc plasma.

However, full-position welding still faces many challenges, especially in the overhead welding position where the effect of gravity is significant. Composite heat sources can reduce the volume of the molten pool, effectively minimizing the impact of gravity and thus inhibiting the formation of concavities on the backside and hump defects on the front side of overhead welding joints. Liu Liming et al. [70] used a laser-MAG composite heat source to study the overhead welding position of 5 mm thick E36 high-strength steel. The results showed that this composite heat source could significantly improve the stability of the molten pool, ultimately achieving a well-formed overhead butt welding joint. Pang Fengyu et al. [71] conducted a study on the force analysis of the molten pool in all-position welding of 16 mm-thick X65 and 20 mm-thick X80 pipeline steels using low-energy laser–arc hybrid welding technology. The study found that heat input is the primary factor influencing the formation of internal concavity defects in root-pass welding. Research indicates that an increase in heat input leads to an enlargement of the molten pool volume, thereby increasing the gravitational force on the molten pool and enhancing its fluidity, which exacerbates the internal concavity defects in root pass welding. These findings highlight the importance of controlling heat input to manage the stability and quality of the molten pool in all-position welding processes.

4. All-Position Narrow-Gap GMAW Development Direction

In all-position pipeline GMAW, the molten pool is significantly affected by gravity, leading to issues such as side-wall lack of fusion and interlayer lack of fusion. Despite numerous studies indicating that the GMAW technique offers significant advantages in narrow-gap all-position welding, such as ease of automation and high productivity [72–74], there are some difficulties in ensuring the correctness of multiple welding parameters due to their relatively large number and strong interrelations [75]. In practical industrial applications, GMAW faces challenges like poor adaptability to complex geometries and difficulty in controlling heat input. Compared with other welding techniques, such as hybrid laser–arc welding and magnetic field-assisted welding, it is found that hybrid laser–arc welding offers several advantages, including reduced heat input, enhanced weld penetration, and improved process stability [61,76]. Additionally, by integrating solid-state phase transformation theories from materials science, a better understanding can be achieved regarding the impact of different cooling rates on weld quality. However, there remain some technical challenges that need to be overcome, including the complexity of welding equipment and the low level of intelligence in weld seam detection. Future technological development directions should focus on the following aspects:

1. Optimization methods for process parameters have overlooked the impact of interactions among multiple parameters on the overall weld bead formation. Future research should focus more on establishing comprehensive mathematical models or employing machine learning algorithms to predict and optimize the effects of multi-parameter

combinations. Developing intelligent all-position welding technology for pipelines can reduce reliance on the skill level of welders, ensuring consistency in welding quality. This includes technologies for online monitoring and quality assessment of the welding process, such as real-time detecting of sidewall lack of fusion, interlayer lack of fusion, and weld bead formation. It also involves dynamically adjusting process parameters based on real-time feedback, assessing potential defect locations, and providing guidance for post-weld inspection. By doing so, not only can welding quality be improved, but it also facilitates a more systematic approach to achieving high standards of weld integrity and performance.

2. In laboratory settings, ideal magnetic field control can be achieved; however, in actual industrial production, the stability of equipment and the convenience of operation are often limited. To overcome these challenges, future research should focus on developing intelligent control systems, optimizing the design of magnetic field generators, and integrating advanced sensing technologies with real-time monitoring systems. Ensuring consistent, high-quality weld seams across different welding positions requires robust solutions that can adapt to varying conditions.
3. Hybrid laser–arc welding offers advantages such as high welding efficiency and a small heat-affected zone, achieving notable research outcomes and seeing engineering applications. However, the introduction of a laser makes the equipment more complex, which limits its application in the field construction of pipelines. Developing compact, integrated hybrid laser–arc welding equipment is essential to promote the widespread use of this technology in all-position pipeline welding.

Author Contributions: Conceptualization, W.L. and Q.L.; methodology, W.L. and Q.L.; validation, W.L. and J.Y.; formal analysis, J.Y.; resources, P.Z.; data curation, B.L.; writing—original draft preparation, W.L. and Q.L.; writing—review and editing, W.L. and Q.L.; visualization, P.Z.; supervision, B.L.; funding acquisition, W.L. All authors have read and agreed to the published version of the manuscript.

Funding: This research was supported by the National Natural Science Foundation of China (Grant No. 51975410).

Institutional Review Board Statement: Not applicable.

Informed Consent Statement: Not applicable.

Data Availability Statement: The raw data supporting the conclusions of this article will be made available by the authors on request.

Conflicts of Interest: The authors declare no conflicts of interest.

References

1. Yin, T.; Wang, J.; Zhao, H.; Zhou, L.; Xue, Z.; Wang, H. Research on Filling Strategy of Pipeline Multi-Layer Welding for Compound Narrow Gap Groove. *Materials* **2022**, *15*, 5967. [CrossRef] [PubMed]
2. Baek, D.; Moon, H.S.; Park, S.-H. Development of an automatic orbital welding system with robust weaving width control and a seam-tracking function for narrow grooves. *Int. J. Adv. Manuf. Technol.* **2017**, *93*, 767–777. [CrossRef]
3. Zhang, X.; Gao, H.; Li, Z. Forces analysis of droplets and accurate control of metal transfer in GMAW by utilizing droplet resonance. *J. Manuf. Process.* **2021**, *70*, 121–131. [CrossRef]
4. Huang, J.; Pan, W.; Yang, W.; Xue, C.; Shi, Y.; Fan, D. The influence of bypass current on metal transfer in dual-bypass gas metal arc welding. *J. Manuf. Process.* **2019**, *38*, 179–186. [CrossRef]
5. Anzehaee, M.M.; Haeri, M. Estimation and control of droplet size and frequency in projected spray mode of a gas metal arc welding (GMAW) process. *ISA Trans.* **2011**, *50*, 409–418. [CrossRef] [PubMed]
6. Zhao, Y.; Chung, H. Numerical simulation of the transition of metal transfer from globular to spray mode in gas metal arc welding using phase field method. *J. Mater. Process. Technol.* **2018**, *251*, 251–261. [CrossRef]

7. Pal, K.; Pal, S.K. Effect of Pulse Parameters on Weld Quality in Pulsed Gas Metal Arc Welding: A Review. *J. Mater. Eng. Perform.* **2010**, *20*, 918–931. [CrossRef]
8. Reisgen, U.; Purrio, M.; Buchholz, G.; Willms, K. Possibilities of a control of the droplet detachment in pulsed gas metal arc welding: Droplet detachment control (DDC). *Weld. World* **2013**, *57*, 701–706. [CrossRef]
9. Zhai, P.; Xue, S.; Wang, J.; Tao, Y.; Chen, W.; Chen, T.; Ji, S. Comparative Study of Droplet Transfer Modes on Appearance, Microstructure, and Mechanical Properties of Weld during Pulsed GMAW. *Metals* **2020**, *10*, 611. [CrossRef]
10. Zhai, P.; Xue, S.; Wang, J.; Chen, W.; Chen, T.; Ji, S. Effects of Arc Length Adjustment on Weld Bead Formation and Droplet Transfer in Pulsed GMAW Based on Datum Current Time. *Metals* **2020**, *10*, 665. [CrossRef]
11. Liu, W.; Xiao, Y.; Yang, J.; Zhu, P. Influence factors and control methods of droplet transfer in narrow gap P-GMAW overhead welding position. *Trans. China Weld. Inst.* **2024**, *45*, 58–63. [CrossRef]
12. Dongqing, Y.; Hanying, X.; Yong, H.; Dejun, Y.; Dong, L.; Yong, P.; Kehong, W. Droplet transfer behavior and weld formation of gas metal arc welding for high nitrogen austenitic stainless steel. *J. Manuf. Process.* **2021**, *65*, 491–501. [CrossRef]
13. Bao, Y.; Xue, R.; Zhou, J.; Xu, Y. Effect of Increasing Oscillation Width on the Arc Characteristics and Droplet Transfer Behavior of X80 Steel in the Overhead Welding Position of Narrow Gap P-GMAW. *Metals* **2023**, *13*, 1314. [CrossRef]
14. Wanghui, X.; Chenglei, F.; Sanbao, L.; Chunli, Y. Research on droplet transfer in oscillating arc narrow gap GMA welding. *China Weld.* **2014**, *23*, 12–16. [CrossRef]
15. Wang, Z.; Zhang, S.; Yang, Z.; Yang, Y. Influence of gap on droplet transition of GMAW vertical welding and characteristics of temperature field. *Trans. China Weld. Inst.* **2019**, *40*, 89–94.
16. Zhang, W.; Hua, X.; Liao, W.; Li, F.; Wang, M. Behavior of the plasma characteristic and droplet transfer in CO2 laser–GMAW-P hybrid welding. *Int. J. Adv. Manuf. Technol.* **2014**, *72*, 935–942. [CrossRef]
17. Tao, X.; Ba, X.; Xu, G.; Liu, L. Effect of laser power on pulsed laser-induced MAG hybrid overhead welding of 4-mm-X70 pipeline steel. *Opt. Laser Technol.* **2023**, *164*, 109460. [CrossRef]
18. Li, J.; Sun, Q.; Kang, K.; Zhen, Z.; Liu, Y.; Feng, J. Process stability and parameters optimization of narrow-gap laser vertical welding with hot wire for thick stainless steel in nuclear power plant. *Opt. Laser Technol.* **2020**, *123*, 105921. [CrossRef]
19. Wu, K.; Yin, T.; Ding, N.; Zeng, M.; Liang, Z. Effect of phase on the behavior of metal transfer in double-wire pulsed GMAW. *Int. J. Adv. Manuf. Technol.* **2018**, *97*, 3777–3789. [CrossRef]
20. Ghosh, P.; Dorn, L.; Hübner, M.; Goyal, V. Arc characteristics and behaviour of metal transfer in pulsed current GMA welding of aluminium alloy. *J. Mater. Process. Technol.* **2007**, *194*, 163–175. [CrossRef]
21. Li, L.; Liu, W.; Gong, Q.; Xu, G.; Zhu, J.; Hu, Q.; Du, B. Numerical analysis of the dynamic behavior of arc by rotating laser-GMAW hybrid welding of T-joints. *Opt. Laser Technol.* **2023**, *167*, 109802. [CrossRef]
22. Wenji, L.; Liangyu, L.; Jianfeng, Y.; Peiyu, Y.; Xiaohui, L. Research on the "jump sidewall" behavior and its signal characteristics in narrow gap P-MAG welding. *Int. J. Adv. Manuf. Technol.* **2017**, *91*, 1189–1196. [CrossRef]
23. Yamba, P.; Zhenying, X.; Yun, W.; Rong, W.; Xing, Y. Investigation of humping defect formation in a lap joint at a high-speed hybrid laser-GMA welding. *Results Phys.* **2019**, *13*, 102341. [CrossRef]
24. Zhang, G.; Shi, Y.; Zhu, M.; Fan, D. Arc characteristics and metal transfer behavior in narrow gap gas metal arc welding process. *J. Mater. Process. Technol.* **2017**, *245*, 15–23. [CrossRef]
25. Ni, Z.; Dong, B.; Li, Y.; Cai, X.; Lin, S. Effects of processing parameters on molten behavior, arc stability, and defect forming in swing-arc narrow gap GMA vertical up welding. *J. Mater. Process. Technol.* **2023**, *321*, 118155. [CrossRef]
26. Park, J.-H.; Kim, S.-H.; Moon, H.-S.; Kim, M.-H. Influence of Gravity on Molten Pool Behavior and Analysis of Microstructure on Various Welding Positions in Pulsed Gas Metal Arc Welding. *Appl. Sci.* **2019**, *9*, 4626. [CrossRef]
27. Cai, X.Y.; Fan, C.L.; Lin, S.B.; Yang, C.L.; Bai, J.Y. Molten pool behaviors and weld forming characteristics of all-position tandem narrow gap GMAW. *Int. J. Adv. Manuf. Technol.* **2016**, *87*, 2437–2444. [CrossRef]
28. Cai, X.Y.; Lin, S.B.; Fan, C.L.; Yang, C.L.; Zhang, W.; Wang, Y.W. Molten pool behaviour and weld forming mechanism of tandem narrow gap vertical GMAW. *Sci. Technol. Weld. Join.* **2016**, *21*, 124–130. [CrossRef]
29. Silva, R.G.N.; de Paço, C.M.M.; Rodrigues, M.B.; de Sousa, J.M.S.; Pereira, M.; Ramos, B.B.; Schwedersky, M.B.; e Silva, R.H.G. A comparison between LBW and hybrid laser-GMAW processes based on microstructure and weld geometry for hardenable steels. *Int. J. Adv. Manuf. Technol.* **2020**, *110*, 2801–2814. [CrossRef]
30. Han, R.; Fan, X.; Wang, J.; Ren, D.; Song, G. Enhancing all-position weldability and weld quality via an innovative laser-GMAW hybrid welding technique with copper liner. *J. Manuf. Process.* **2024**, *124*, 697–707. [CrossRef]
31. Huang, J.; Chen, T.; Huang, D.; Xu, T. Study on the Effect of Pulse Waveform Parameters on Droplet Transition, Dynamic Behavior of Weld Pool, and Weld Microstructure in P-GMAW. *Metals* **2023**, *13*, 199. [CrossRef]
32. Wang, L.; Chen, J.; Wu, C.; Gao, J. Backward flowing molten metal in weld pool and its influence on humping bead in high-speed GMAW. *J. Mater. Process. Technol.* **2016**, *237*, 342–350. [CrossRef]
33. Zhu, C.; Cheon, J.; Tang, X.; Na, S.-J.; Lu, F.; Cui, H. Effect of swing arc on molten pool behaviors in narrow-gap GMAW of 5083 Al-alloy. *J. Mater. Process. Technol.* **2018**, *259*, 243–258. [CrossRef]

34. Xu, G.; Li, L.; Wang, J.; Zhu, J.; Li, P. Study of weld formation in swing arc narrow gap vertical GMA welding by numerical modeling and experiment. *Int. J. Adv. Manuf. Technol.* **2018**, *96*, 1905–1917. [CrossRef]
35. Hu, Z.; Hua, L.; Qin, X.; Ni, M.; Ji, F.; Wu, M. Molten pool behaviors and forming appearance of robotic GMAW on complex surface with various welding positions. *J. Manuf. Process.* **2021**, *64*, 1359–1376. [CrossRef]
36. Park, J.-H.; Cho, D.-W.; Moon, H.-S. CFD simulation of molten pool dynamic behavior on vertical-downward position in P-GMAW process. *Int. Commun. Heat Mass Transf.* **2022**, *132*, 105876. [CrossRef]
37. Cho, D.-W.; Park, J.-H.; Moon, H.-S. A study on molten pool behavior in the one pulse one drop GMAW process using computational fluid dynamics. *Int. J. Heat Mass Transf.* **2019**, *139*, 848–859. [CrossRef]
38. Cho, D.; Na, S.; Cho, M.; Lee, J. A study on V-groove GMAW for various welding positions. *J. Mater. Process. Technol.* **2013**, *213*, 1640–1652. [CrossRef]
39. Jardin, R.T.; Tuninetti, V.; Tchuindjang, J.T.; Hashemi, N.; Carrus, R.; Mertens, A.; Duchêne, L.; Tran, H.S.; Habraken, A.M. Sensitivity Analysis in the Modelling of a High Speed Steel Thin-Wall Produced by Directed Energy Deposition. *Metals* **2020**, *10*, 1554. [CrossRef]
40. Arora, K.S.; Pandu, S.R.; Shajan, N.; Pathak, P.; Shome, M. Microstructure and impact toughness of reheated coarse grain heat affected zones of API X65 and API X80 linepipe steels. *Int. J. Press. Vessel. Pip.* **2018**, *163*, 36–44. [CrossRef]
41. Kubiak, M.; Piekarska, W. Comprehensive model of thermal phenomena and phase transformations in laser welding process. *Comput. Struct.* **2016**, *172*, 29–39. [CrossRef]
42. Domański, T.; Bokota, A. The numerical model prediction of phase components and stresses distributions in hardened tool steel for cold work. *Int. J. Mech. Sci.* **2015**, *96*, 47–57. [CrossRef]
43. Yin, T.; Zhao, H.; Zhou, L.; Wang, H.; Wang, X.; Zhang, L. Welding Penetration Research on the Effect of Various Welding Torch Tilt Angles in All-Position Metal Active Gas Arc Welding. *Sci. Adv. Mater.* **2023**, *15*, 50–57. [CrossRef]
44. Lei, Z.; Yang, Y.; Li, F.; Chen, Y.; Zeng, H. Research on Weld Appearance of X70 Steel Joints Prepared by Laser-MAG Hybrid Welding Process for All-Position Root Welding. *Chin. J. Lasers* **2015**, *42*, 403002. [CrossRef]
45. Zhang, Y.; Lv, X.; Xu, L.; Jing, H. Effect of workpiece inclination on weld pool shape and weld forming in pulsed MAG welding. *Trans. China Weld. Inst.* **2019**, *40*, 9.
46. He, Y.; Tang, X.; Zhu, C.; Lu, F.; Cui, H. Study on insufficient fusion of NG-GMAW for 5083 Al alloy. *Int. J. Adv. Manuf. Technol.* **2017**, *92*, 4303–4313. [CrossRef]
47. Zhou, X.; Fu, Z.; Bai, X.; Tian, Q.; Fang, D.; Fu, J.; Zhang, H. Numerical simulation of the effect of wire feeding speed on the molten pool flow and weld bead morphology of WAAM. *Trans. China Weld. Inst.* **2023**, *44*, 109–116. [CrossRef]
48. Li, C.; Xu, Y.; Zhou, J.; Li, J. Effects of welding parameters on formation of overhead position MAG surfacing. *Weld. Join.* **2023**, 32–38.
49. Guan, Z.Q.; Zhang, H.X.; Liu, X.G.; Babkin, A.; Chang, Y.L. Effect of magnetic field frequency on the shape of GMAW welding arc and weld microstructure properties. *Mater. Res. Express* **2019**, *6*, 0865e5. [CrossRef]
50. Yue, J.; Xie, C.; Zhao, J.; Zhou, W.; Liu, W.; Huang, J. Arc heat input distribution of fillet welding of dissimilar steel with applied transverse magnetic field. *Trans. China Weld. Inst.* **2023**, *44*, 83–90. [CrossRef]
51. Wang, J.; Sun, Q.; Zhang, T.; Zhang, S.; Liu, Y.; Feng, J. Arc characteristics in alternating magnetic field assisted narrow gap pulsed GTAW. *J. Mater. Process. Technol.* **2018**, *254*, 254–264. [CrossRef]
52. Jian, X.; Wu, H. Influence of the Longitudinal Magnetic Field on the Formation of the Bead in Narrow Gap Gas Tungsten Arc Welding. *Metals* **2020**, *10*, 1351. [CrossRef]
53. Society, A.W.; Yu, J.; Zhang, H.; He, P.; Yang, X.; Teng, Y.; Wang, Q.; Wei, L.; Zhang, W. Arc Characteristics and Welding Process of Magnetic Field Assisting Plasma-GMAW-P. *Weld. J.* **2021**, *100*, 1–12. [CrossRef]
54. Yue, J.; Li, L.; Liu, W.; Wang, T. Downward Welding Pool Shape Control Based on Exterior High Frequency Alternative Magnetic Field. *J. Mech. Eng.* **2013**, *49*, 65–70. [CrossRef]
55. Bachmann, M.; Avilov, V.; Gumenyuk, A.; Rethmeier, M. Experimental and numerical investigation of an electromagnetic weld pool support system for high power laser beam welding of austenitic stainless steel. *J. Mater. Process. Technol.* **2014**, *214*, 578–591. [CrossRef]
56. Shoichi, M.; Yukio, M.; Koki, T.; Yasushi, T.; Yukinori, M.; Yusuke, M. Study on the application for electromagnetic controlled molten pool welding process in overhead and flat position welding. *Sci. Technol. Weld. Join.* **2013**, *18*, 38–44. [CrossRef]
57. Wang, L.; Wu, C.S.; Gao, J.Q. Suppression of humping bead in high speed GMAW with external magnetic field. *Sci. Technol. Weld. Join.* **2016**, *21*, 131–139. [CrossRef]
58. Li, Y.; Wu, C.S.; Wang, L.; Gao, J.K. Analysis of additional electromagnetic force for mitigating the humping bead in high-speed gas metal arc welding. *J. Mater. Process. Technol.* **2015**, *229*, 207–215. [CrossRef]
59. Zhang, F.; Liu, S.; Liu, F.; Zhang, H. Stability evaluation of laser-MAG hybrid welding process. *Opt. Laser Technol.* **2019**, *116*, 284–292. [CrossRef]

60. Neubert, J.; Keitel, S. Influence Of Tolerances on weld formation and quality of laser-GMA-hybrid girth welded pipe joints. *Weld. World* **2011**, *55*, 50–57. [CrossRef]
61. Acherjee, B. Hybrid laser arc welding: State-of-art review. *Opt. Laser Technol.* **2018**, *99*, 60–71. [CrossRef]
62. Le Guen, E.; Carin, M.; Fabbro, R.; Coste, F.; Le Masson, P. 3D heat transfer model of hybrid laser Nd:Yag-MAG welding of S355 steel and experimental validation. *Int. J. Heat Mass Transf.* **2011**, *54*, 1313–1322. [CrossRef]
63. Li, C.-L.; Fan, D.; Yu, X.-Q.; Huang, J.-K. Residual stress and welding distortion of Al/steel butt joint by arc-assisted laser welding-brazing. *Trans. Nonferrous Met. Soc. China* **2019**, *29*, 692–700. [CrossRef]
64. Sathiya, P.; Mishra, M.K.; Soundararajan, R.; Shanmugarajan, B. Shielding gas effect on weld characteristics in arc-augmented laser welding process of super austenitic stainless steel. *Opt. Laser Technol.* **2013**, *45*, 46–55. [CrossRef]
65. Huang, H.; Zhang, P.; Yan, H.; Liu, Z.; Yu, Z.; Wu, D.; Shi, H.; Tian, Y. Research on weld formation mechanism of laser-MIG arc hybrid welding with butt gap. *Opt. Laser Technol.* **2020**, *133*, 106530. [CrossRef]
66. Zhang, C.; Hu, P. Effect of arc on process stability of laser–arc hybrid welding of aluminum alloy. *Aeronaut. Manuf. Technol.* **2023**, *66*, 53–59. [CrossRef]
67. Gui, H.; Zhang, K.; Li, D.; Li, Z. Effect of relative position in low-power pulsed-laser tungsten-inert-gas hybrid welding on laser-arc interaction. *J. Manuf. Process.* **2018**, *36*, 426–433. [CrossRef]
68. Liu, S.; Zhang, F.; Dong, S.; Zhang, H.; Liu, F. Characteristics analysis of droplet transfer in laser-MAG hybrid welding process. *Int. J. Heat Mass Transf.* **2018**, *121*, 805–811. [CrossRef]
69. Uemura, T.; Gotoh, K.; Uchino, I. Expansion of laser–arc hybrid welding to horizontal and vertical-up welding. *Weld. World* **2022**, *66*, 495–506. [CrossRef]
70. Liu, L.; Chen, L.; Song, G. Weld Formation of high Strength Steels by low-power pulsed laser Induced mental active gas hybrid welding in overhead positions. *China Mech. Eng.* **2020**, *31*, 2137–2141. [CrossRef]
71. Pang, F.; Dai, P.; Song, G.; Fang, X.; Miao, Z.; Tang, Q.; Liu, L. All-position welding process and performance of pipeline steel by laser-induced arc hybrid welding. *Weld. Technol.* **2021**, *50*, 52–55. [CrossRef]
72. Ibrahim, I.A.; Mohamat, S.A.; Amir, A.; Ghalib, A. The Effect of Gas Metal Arc Welding (GMAW) Processes on Different Welding Parameters. *Procedia Eng.* **2012**, *41*, 1502–1506. [CrossRef]
73. Zeng, M.; Huang, J.; Zhang, Y.; Hu, P. Modeling for GMAW process with a current waveform control method. *J. Mater. Process. Technol.* **2016**, *240*, 404–413. [CrossRef]
74. Pinto-Lopera, J.E.; Motta, J.M.S.T.; Alfaro, S.C.A. Real-Time Measurement of Width and Height of Weld Beads in GMAW Processes. *Sensors* **2016**, *16*, 1500. [CrossRef] [PubMed]
75. Martínez, R.T.; Bestard, G.A.; Silva, A.M.A.; Alfaro, S.C.A. Analysis of GMAW process with deep learning and machine learning techniques. *J. Manuf. Process.* **2021**, *62*, 695–703. [CrossRef]
76. Huang, L.; Wu, D.; Hua, X.; Liu, S.; Jiang, Z.; Li, F.; Wang, H.; Shi, S. Effect of the welding direction on the microstructural characterization in fiber laser-GMAW hybrid welding of 5083 aluminum alloy. *J. Manuf. Process.* **2018**, *31*, 514–522. [CrossRef]

Disclaimer/Publisher's Note: The statements, opinions and data contained in all publications are solely those of the individual author(s) and contributor(s) and not of MDPI and/or the editor(s). MDPI and/or the editor(s) disclaim responsibility for any injury to people or property resulting from any ideas, methods, instructions or products referred to in the content.

MDPI AG
Grosspeteranlage 5
4052 Basel
Switzerland
Tel.: +41 61 683 77 34

Applied Sciences Editorial Office
E-mail: applsci@mdpi.com
www.mdpi.com/journal/applsci



Disclaimer/Publisher's Note: The title and front matter of this reprint are at the discretion of the Guest Editor. The publisher is not responsible for their content or any associated concerns. The statements, opinions and data contained in all individual articles are solely those of the individual Editor and contributors and not of MDPI. MDPI disclaims responsibility for any injury to people or property resulting from any ideas, methods, instructions or products referred to in the content.





Academic Open
Access Publishing

mdpi.com

ISBN 978-3-7258-8640-1